INFRARED EMISSION MEASUREMENTS OF RADIATION AND TRACE GAS VARIABILITY IN THE HIGH ARCTIC

Zen H. Mariani

A thesis submitted in conformity with the requirements for the degree of Doctor of Philosophy

Department of Physics
University of Toronto
Toronto, Ontario, Canada

September 2014

INFRARED EMISSION MEASUREMENTS OF RADIATION AND TRACE GAS VARIABILITY IN THE HIGH ARCTIC

Zen Mariani
Doctor of Philosophy
Department of Physics, University of Toronto
2014

ABSTRACT

The objective of this Ph.D. is to investigate the atmospheric radiative budget and composition in the high Arctic using a new (prototype) interferometer. The Canadian Network for the Detection of Atmospheric Change has equipped the Polar Atmospheric Environment Research Laboratory (PEARL) at Eureka, Nunavut (80ºN, 86ºW) with an Extended-range Atmospheric Emitted Radiance Interferometer (E-AERI), which was installed in October 2008 at the PEARL Ridge Lab (610 m a.s.l.).

The E-AERI measures the infrared (IR) thermal emission of the atmosphere in the 400-3000 cm^{-1} (3.3-25 μm) spectral region. An older AERI, the Polar AERI (P-AERI), was stationed in Eureka from 2006-2009 and was located at sea level. The impact of clouds and ice crystals on the radiative budget were investigated from two altitudes using these two AERIs. The increased radiance due to the presence of clouds was found to be larger at Eureka than at the Southern Great Plains (SGP), indicating that cloud cover plays an important role in the Arctic's radiative budget.

This thesis presents the first measurements of the two surface cooling-to-space windows (at 10 and 20 μm) in the high (> 75^{o} N) Arctic. Distributions of brightness temperatures were filtered based on cloud cover and do not vary in the summer, indicating that the 20 μm window is closed when water vapour is a maximum. Trends in downwelling radiance were found in

several spectral microregions corresponding to these cooling-to-space windows and meteorological conditions (temperature, water vapour, cloud cover). Trends at 10 μm during the winter were positive, in the opposite direction, and significantly larger (factor > 3) than any of the seasonal trends detected at the SGP, indicating that changes in the downwelling radiance are accelerated in the high Arctic compared to lower latitudes.

Spectra recorded by the E-AERI were also used to retrieve total column concentrations of O_3, CO, CH_4, and N_2O year-round to fill a gap in the PEARL data series, providing the first continuous ground-based trace gas measurements throughout polar night at Eureka. This work involved the implementation of the SFIT2 retrieval algorithm modified for emission spectra. E-AERI trace gas retrievals were characterized and comparisons to other spectrometers at Eureka are within uncertainties (1-9% differences). An investigation of the diurnal and seasonal cycle of CO was performed to highlight the usefulness of continuous, year-round measurements at Eureka.

ACKNOWLEDGEMENTS

I will be forever indebted to the many people I have worked with on this project; not just those at the University of Toronto, but also collaborators at other national and international institutions. None of this work would be possible without the assistance they provided to me; it is clear from this project that collaboration is an essential part of the scientific process. The extent of international collaboration that occurred during my Ph.D. is an obvious indication that climate change truly is a global issue.

First and foremost, I would like to take this opportunity to thank my supervisor, Dr. Kimberly Strong, for all her guidance and support over the past several years. The ideal supervisor, Kim's expertise has helped guide my research while also allowing me to take my own path. Through working with Kim over the past 5+ years, I have gained an in-depth perspective of exceptional leadership and project management skills that I can only hope to implement in the future; these will prove invaluable to my future career.

There is a long list of individuals without whom this work simply could not have been accomplished. I would like to thank Penny Rowe and Von Walden of the University of Idaho (now at Washington State University) for P-AERI data, analysis, and useful discussion of results. Most of the work involving SFIT2 trace gas retrievals would not have been possible if not for the help of Mathias Palm at the University of Bremen to introduce the emission add-on for SFIT2. I have worked with Mathias for 5 years now and his expertise in retrieval theory proved invaluable in pushing the new AERI trace gas retrievals forward. None of the long-term E-AERI measurements would be possible if not for the help of ABB engineers to bring the instrument back online after serious repairs were required; specifically I would like to thank Guillaume Gamache, who visited Eureka with me twice in 2011 to perform two service visits. Guillaume's expertise proved irreplaceable, restoring the E-AERI measurements to full capacity during a stressful time, all the while making the difficult work an enjoyable experience (even at -50 ^{o}C). Thanks also to Stephane Lantagne (ABB) for his work initially installing the E-AERI.

Thank you to all the researchers in Prof. Strong and Prof. Kaley Walker's research groups, particularly those who shared MP704A with me for 5 years; much of this work is a reflection of their support. I would like to thank Prof. Kaley Walker and the staff at the

Environment Canada Weather Station at Eureka for their support during my participation in the 2010, 2011 (twice), and 2013 ACE Arctic Validation Campaigns. Thanks to UW-SSEC for AERI calibration and PEARL site manager Pierre Fogal and CANDAC operators Ashley Harrett, Alexei Khmel, Paul Loewen, Oleg Mikhailov, Keith MacQuarrie and Matt Okraszewski who have helped with the E-AERI measurements at PEARL. Special thanks to Pierre Fogal for his guidance and help with all E-AERI repairs and maintenance. I would like to recognize the support given by Cyndi Whaley, Felicia Kolonjari, and Rodica Lindenmaier for their assistance with Matlab, Fortran, and IDL codes used to analyze some of the E-AERI data. Special thanks to Felicia Kolonjari who set up the Alopex server and helped install SFIT2+Emission on it. Thanks to David Hudak at Environment Canada for providing MMCR data. Thanks to Dan Weaver for his help with analyzing water vapour data, Simone Chaudhary for her help automating SFIT2, Greg Lusk for his insightful discussions on the philosophy of atmospheric measurements and modelling, and Ana Sousa for her help with logistics and organization. Thanks to my committee members, Prof. Kaley Walker and Prof. Dylan Jones, for their guidance on this project, and thanks to the Noble fund for supporting visits of my international collaborators. Finally, I would like to thank the Physics Department at the University of Toronto for implementing a variety of world-class seminar series that widened the breadth of my graduate experience and allowed me to practice a variety of essential presentation skills.

The high Arctic is a completely remote region with the harshest environment in Canada, which makes performing research there extremely difficult and expensive. The Polar Environment Atmospheric Research Laboratory (PEARL) is operated by the Canadian Network for the Detection of Atmospheric Change (CANDAC), which is led by Prof. James R. Drummond (Dalhousie University). CANDAC/PEARL funding partners are: the Arctic Research Infrastructure Fund, Atlantic Innovation Fund/Nova Scotia Research Innovation Trust, Canadian Foundation for Climate and Atmospheric Science, Canadian Foundation for Innovation, Canadian Space Agency (CSA), Environment Canada (EC), Government of Canada International Polar Year, Natural Sciences and Engineering Research Council (NSERC), Ontario Innovation Trust, Ontario Research Fund, Indian and Northern Affairs Canada, and the Polar Continental Shelf Program. Walden and Rowe acknowledge funding from NSF award ARC-1108451 for the P-AERI instrument. Spring visits to PEARL were made as part of the Canadian Arctic ACE Validation Campaigns, led by Kaley Walker and supported by CSA, EC, NSERC, and the Northern Student Training Program. This work was also supported by the

NSERC CREATE Training Program in Arctic Atmospheric Science, and I was personally awarded funds through the Centre for Global Change Science (CGCS), University of Toronto School of Graduate Studies, NSERC CGS-M fellowship, and an Environment Canada Meteorological Service of Canada Award.

Finally, I would like to thank my family for their continued and unwavering support during my time at the University of Toronto; they helped inspire me more than they can ever imagine.

ZEN MARIANI

University of Toronto
September 2014

CONTENTS

LIST OF TABLES

LIST OF FIGURES

1. INTRODUCTION

Why study the Arctic atmosphere? This remote expanse, segregated from almost all major population centres, is one of the most poorly understood regions of the world. The Arctic has often been referred to as 'Earth's early-warning system' since observed changes in the Earth's climate are more pronounced here than anywhere else on the globe; a phenomenon caused by Arctic amplification. Most of these changes in the Earth's climate are occurring in the Arctic first, and at significant levels, providing insight into the state of the planet's climate. Not surprisingly, the Arctic is often viewed as the canary in the coal mine. Because of its remoteness, very few research stations exist in the Arctic, which has created large geographic gaps in measurements of the atmospheric state. The new infrared (IR) emission measurements taken at the Polar Environment Atmospheric Research Laboratory (PEARL) presented in this thesis provide a unique dataset of the atmospheric radiative budget and composition year-round that can be used to improve our understanding of the Arctic atmosphere.

1.1 Climate Change in the Arctic

As has been noted by the Arctic Council and others [ACIA, 2004; IPCC, 2013], nowhere else on Earth is climate change more pronounced than in the Arctic. Continued increases in surface temperature and atmospheric water vapour in the Arctic are expected, with a corresponding increase in downwelling radiance [ACIA, 2004; Richter-Menge, 2006; Bekryaev *et al.*, 2010]. Currently, rising sea levels, an increase in global mean temperatures, and changes in precipitation patterns are but a few of the many characteristics of climate change [WMO, 2006; IPCC, 2013]. Due to the vast amount of ice in the Arctic, and the strong relationship between the ocean, land, and atmosphere, the Arctic is a region of particular significance when considering the Earth's climate.

The Arctic is typically defined to be north of 66^{o}N, and encompasses parts of Canada, Alaska, Greenland, Russia, Iceland, and several European countries. At such high latitudes, the intensity of the Sun's radiation is reduced compared to other regions of the planet, such as the tropics. This results in an extremely cold, dry climate so uninhabitable that trees, for instance, cannot grow throughout almost the entire Arctic region. It is home to diverse wildlife, most of which have been minimally affected by direct human activities. Indirectly, however, the wildlife of the Arctic has recently been negatively impacted due to the rapidly changing climate [Hinzman *et al.*, 2005; Jenssen, 2006]. This is ultimately caused by changes to the atmosphere's composition since the Industrial Revolution as a result of burning of fossil fuels [Andrews, 2000; IPCC, 2013].

There is a long list of evidence illustrating the different abrupt changes to the Arctic climate. The permafrost is warming, hydrological processes are changing, and biological and social systems are evolving in response to these changing conditions [Hinzman *et al.*, 2005; WMO, 2006; IPCC, 2013]. There has been extensive decline of Arctic sea ice since the 1970s, with record loss in September 2012. Figure 1.1 illustrates the extent of sea-ice loss in the Arctic since 1900, with observed sea-ice loss exceeding that of model predictions from the Intergovernmental Panel on Climate Change (IPCC). The annually averaged total column ozone (O_3) decrease is about 7% since 1979 in response to enhanced chlorine resulting from anthropogenic emissions of chlorofluorocarbons (CFCs) [WMO, 2006].

Solar radiation and the exchange of radiation between the land, ocean, and atmosphere determine the Arctic's climate. The land-ocean-atmosphere system's radiative transfer is affected by a number of factors, such as albedo, cloud cover, and composition of the atmosphere and ocean (concentration of greenhouse gases, degree of salinity in the oceans, etc.). The climate's equilibrium in the Arctic is sensitive to the stability of sea ice and snow cover, the continued melting of which has already been shown to produce sudden and far-reaching consequences [Maslanik *et al*., 1996; Rothrock *et al*., 1999; Brown *et al*., 2010]. This is because the sea ice and snow cover in the Arctic affect both the albedo of the planet, as well as the composition and temperature of the global ocean currents.

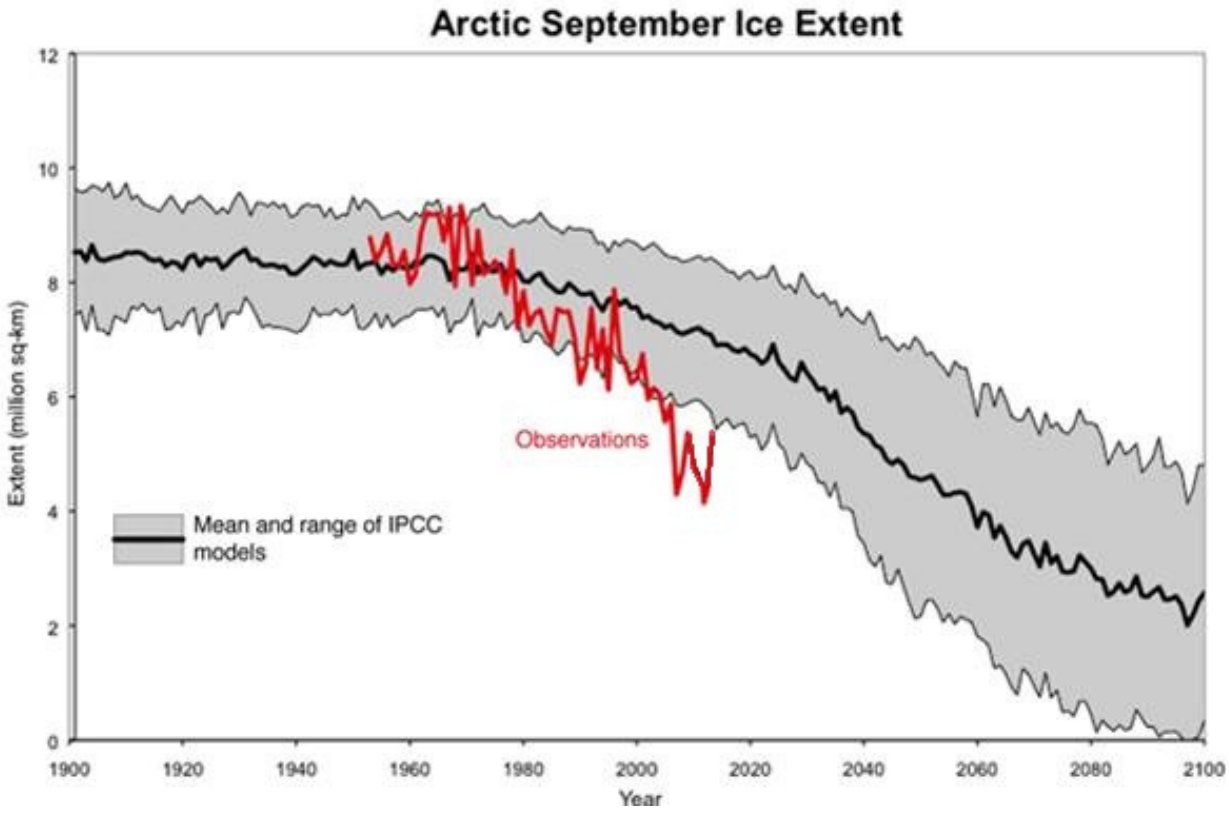

Figure 1.1: Total Arctic sea ice coverage in the month of September determined from satellite measurements (red) and the mean (black) and range of IPCC 2007 model predictions (grey). Image: National Snow and Ice Data Center (accessed February 2014).

During the summer months in the Arctic, there are 24 hours of daylight due to the tilt of Earth's axis of rotation. The high albedo of the Arctic surface (except during summer) results in a significant amount of solar radiation being reflected back into space. As the sea ice and snow cover decreases, the albedo also decreases, resulting in an increased amount of solar radiation absorbed by the land and ocean. This in turn causes an increase in temperature, resulting in the observed acceleration of the melting of sea ice and snow, causing further decrease in the albedo, achieving a runaway effect called the 'ice-albedo feedback' [Andrews, 2000; Francis and Vavrus, 2012; Screen and Simmonds, 2013] (note that ice is not only melting in the sea but also on land; in July 2012, 97% of the Greenland ice sheet experienced some form of surface melt, including the summits, which is causing a rise in the global sea level [Gregory, 2004; Vinas, 2012]). This process is also referred to as Arctic amplification (sometimes referred to as 'polar amplification') and there is debate as to whether this process is linked to extreme weather in mid-latitudes [Francis and Vavrus, 2012; Barnes, 2013; Screen and Simmonds, 2013]. Figure

1.2 illustrates the extent to which the Arctic is experiencing amplification via increasing temperatures (both on land and in the surrounding ocean) when compared to the rest of the globe. The radiation absorbed by the Earth's surface is re-emitted in the form of outgoing longwave radiation (mostly in the IR) from the ground into the atmosphere, where much of it will be absorbed and re-emitted once again. It was Jean Baptiste Joseph Fourier who studied this process and named it the "greenhouse effect" [Le Treut *et al.*, 2007]. This cyclic process intricately connects the Sun, ground, and atmosphere together; a small change in one affects the entire system, sometimes in a chaotic, runaway manner [Maslanik *et al*., 1996; Brown *et al*., 2010]. Determining the Earth's radiation balance is complicated for this very reason.

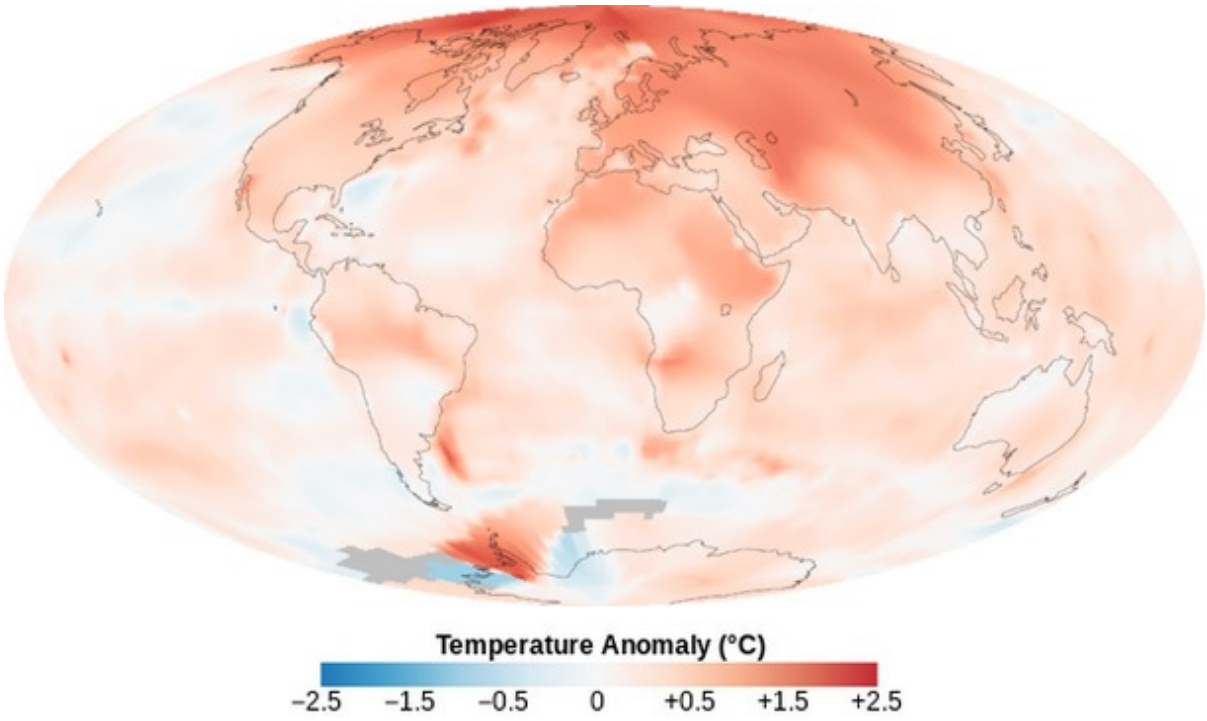

Figure 1.2: Surface temperature anomalies relative to 1951-1980 for 2000-2009 as measured by surface meteorological stations and analysed by the Goddard GISS Surface Temperature Analysis. Image: NASA/Goddard /Earth Observatory (accessed February 2014).

Almost the entire Arctic is covered in sea ice or snow; as such, it acts as a major 'reflector' for the entire planet. For a planet in equilibrium, without an atmosphere, all incoming shortwave radiation from the Sun is equivalent to all outgoing radiation from the planet's surface. However, with the presence of an atmosphere, not all of the Sun's radiation reaches the

surface – some gets absorbed in the atmosphere and roughly one-third of the incoming solar radiation is reflected back to space [Forster *et al.*, 2007]. For the Earth, about 10% of incoming solar radiation is absorbed by the atmosphere, and 80% of outgoing thermal radiation from the surface is absorbed [Andrews, 2000].

Greenhouse gases, such as CO_2, are responsible for absorbing this outgoing radiation. It is the composition and concentration of these gases in the atmosphere, along with the surface's albedo, that determine the amount of radiation that is absorbed by the surface of the Arctic. Thus the energy balance of the planet is altered by changing the concentration of greenhouse gases in the atmosphere.

There exists a multitude of evidence (from theoretical, to experimental, to model) that confirms that increasing greenhouse gas emission from fossil fuels significantly perturb the planet's climate. As will be shown in Sect. 2.3, there is a clear relationship between humankind's burning of fossil fuels and atmospheric composition. This impacts global surface temperatures, particularly in the Arctic due to Arctic amplification. This increase is, in turn, melting the sea ice and snow, causing a decrease in the planet's albedo, which is further increasing the surface and atmospheric temperatures, causing a positive feedback cycle.

1.2 Objectives

This work is part of the Canadian Network for the Detection of Atmospheric Change (CANDAC) goal to improve our understanding of the changes occurring to the Arctic atmosphere. CANDAC is a network of researchers formed in 2002 that established the Polar Environment Atmospheric Research Laboratory (PEARL) in the high Arctic to take measurements of various components of the Arctic atmosphere. Measurements taken at PEARL are combined with those from satellites and sondes (balloons) to give a comprehensive picture of the Arctic atmospheric and how it is changing. The main research themes of CANDAC are Arctic troposphere transport and air quality, waves and coupling processes, Arctic radiative environment: the impact of clouds, aerosols, and diamond dust, and Arctic middle atmospheric chemistry, the latter two being the focus of the work presented in this thesis.

One of the instruments at PEARL is the Extended-range Atmospheric Emitted Radiance Interferometer (the E-AERI). This instrument measures the absolute downwelling IR radiation spectrum for studies of the Arctic radiation budget and atmospheric composition, and is described in detail in Sect. 3. The main research objectives of this thesis are:

1) Validate the new E-AERI measurements, including performance evaluation, certification, analysis of first measurements, and comparisons with an existing, similar AERI instrument at Eureka.
2) Investigate the radiative impact of clouds and ice crystals at two different altitudes. Characterize the radiative forcing at two altitudes and how it changes due to different meteorological events that are unique to the Arctic, such as ice crystal events, and determine their impact on the IR spectrum. This addresses the question of what is the impact that clouds have on the radiative budget in the Arctic, and how is this different from other, more humid regions?
3) Investigate the Arctic's IR cooling-to-space windows. Compile downwelling radiances to investigate the extent to which a transition of regimes from cooling-to-space at 20 μm to cooling-to-space at 10 μm is occurring, and compare it with other available climatologies (described more in Sect. 2.1.3). This addresses the question to what extent are the two cooling-to-space windows changing in the Arctic and what is causing this change? How are these two windows different? The new combined Eureka AERI dataset comprises long-term downwelling radiance measurements in the Arctic that cover a large spectral region.
4) Use spectra recorded by the E-AERI to retrieve total column concentrations of trace gases in the Arctic year-round to fill a gap in the PEARL data series, providing insight into the state of the lower atmosphere throughout polar night. Perform comparisons between E-AERI trace gas retrievals and other spectrometers at Eureka during the sunlit months and perform validation of this new retrieval product that can be used with all AERI systems deployed across the globe. Retrieving total columns of O_3, CO, CH_4, and N_2O will address the questions how will stratospheric and tropospheric O_3 change in the future, and what is the state of the Arctic atmosphere during polar night?
5) Implement the SFIT2 retrieval algorithm, which is widely used in the Fourier Transform Infrared (FTIR) remote sounding research community, to retrieve total columns of O_3,

CO, CH_4, and N_2O using a new version that has been modified for emission spectra. Test and validate this algorithm, and examine and compare new retrieval parameters.

1.3 Contributions to This Work

The E-AERI was first managed by Mareile Wolff, a post-doctoral fellow at the University of Toronto. Responsibility for the instrument was transferred to me upon Mareile's departure from the University in September 2009. Sample E-AERI data sets were sent to Mathias Palm (University of Bremen) by Mareile to help test the SFIT2 emission retrieval code on the E-AERI data. A Matlab code to read raw E-AERI spectra files was written by Mareile. The core of this code is used in some of my Matlab scripts when analyzing E-AERI spectra (and has since been extensively modified). All modifications to the SFIT2 retrieval code were performed by Mathias Palm. Testing and troubleshooting of the algorithm were done by me. Implementation of the new binput files for SFIT2 was performed by me, with help from Felicia Kolonjari (University of Toronto) and Mathias Palm. Installation of the SFIT2+emission code on the Alopex server was done by Felicia Kolonjari.

A Matlab code used to produce profiles of height, pressure, and temperature (zpT files) from Eureka radiosondes was written by Rebecca Batchelor (University of Toronto). These codes were modified and implemented by myself. *A priori* climatologies used in the trace gas retrieval code were developed by Rodica Lindenmaier (University of Toronto) and Keeyoon Sung (University of Toronto); all modifications of these *a priori* profiles to extend the profiles down to 10 m for the Zero Altitude PEARL Auxiliary Laboratory (0PAL) retrievals were performed by me. The automation batch script used to run SFIT2_emission on Alopex was written by me with help from Simone Chaudhary (University of Toronto). Error analysis codes were written in IDL by Rebecca Batchelor. I modified these codes so they could be adapted to E-AERI spectra; they were used for all error analyses performed in this report. A Matlab code to calculate the residuals of spectra was written by Jeffrey Taylor (University of Toronto). These codes were modified and implemented by myself.

Initial testing and validation of the E-AERI instrument was performed by engineers and researchers at the University of Wisconsin Space Science and Engineering Centre (UW-SSEC). The daily operation and maintenance of the E-AERI instrument was performed by the

CANDAC operators at Eureka until 2012; after this point I assumed responsibility for the instrument's operation and condition via remote connection. Troubleshooting problems with the instrument was initially done by Mareile Wolff, Pierre Fogal (University of Toronto), the CANDAC operators, and Kimberly Strong (University of Toronto) in 2008. Pierre Fogal and the CANDAC operators assisted me with performing repairs and shipping parts of the instrument during the spring 2010 ACE Arctic Validation Campaign. Pierre Fogal also assisted me in June 2013 to perform repairs to the E-AERI's metrology laser. ABB engineer Guillaume Gamache accompanied me during two visits to Eureka, for the spring 2011 ACE Arctic Validation Campaign and again in October 2011, to perform on-site maintenance of the E-AERI; I would like to emphasize Guillaume's hard work and dedication during this stressful period. Remote retrieval of the E-AERI data has been made possible through the development of an automated FTP network created by Yan Tsehtik (Dalhousie University).

A number of collaborators have helped perform various calculations, the results of which have been included in some of the figures shown in this work. P-AERI spectra have been provided by Penny Rowe and Von Walden (University of Idaho, now University of Washington), and were used extensively in this work. Matlab codes to convert the P-AERI spectra into an SFIT2-readable format were created by myself. Penny Rowe used a retrieval algorithm (which she developed herself) to provide me with P-AERI total column amounts for CO that I used to compare with the SFIT2 results. Penny Rowe analyzed meteorological temperature and precipitable water vapour (PWV) measurements (with help from Dan Weaver, University of Toronto) at Eureka that I used to compare to E-AERI radiances in microwindows sensitive to temperature and PWV, performed a 41-year temperature analysis of Eureka's temperature trend, and calculated percentages of radiance lost to space in different atmospheric windows. Christopher Cox (University of Idaho) performed the calculations to convert E-AERI radiances to all-sky irradiance for a thin ice crystal cloud analysis. Glen Lesins (Dalhousie University) and Shawn Turner (Environment Canada) ran the Fast Line By Line Radiative Transfer Model that I used to do comparisons with E-AERI spectra.

1.4 Thesis Outline

The introduction to climate change in the Arctic and presentation of the scientific motivation for performing research in this region is given here in Chapter 1. The principles of atmospheric physics and chemistry that are applicable to this work are provided in Chapter 2, and a description of the E-AERI and P-AERI is provided in Chapter 3, including a description of the combined eight-year Eureka AERI dataset.

Chapters 4 through 8 present results using measurements from the E-AERI, as well as the P-AERI, instruments. Chapter 4 describes the E-AERI's initial measurements and comparisons with the P-AERI, including an investigation of the radiative budgets at two altitudes and comparisons to simulated radiances. Chapter 5 presents IR measurements of clear-sky vs. cloudy skies and a case study of the radiative impact of a thin, low-altitude ice-crystal cloud. Chapter 6 discusses the distributions of downwelling brightness temperatures sorted for clear-sky, thin-cloud, and thick-cloud conditions, and investigates trends in the measured downwelling radiance in the primary cooling-to-space windows as well as trends in the type of cloudiness, temperature, and precipitable water vapour. Chapter 7 discusses the retrieval theory used to perform trace gas retrievals, including the retrieval methodology implemented. Chapter 8 discusses the use of spectra collected by the E-AERI to derive concentrations of trace gases in the atmosphere above Eureka throughout polar night for the first time using a newly modified retrieval algorithm, including full error analysis, comparisons with other spectrometers at PEARL, and an investigation into the diurnal and seasonal trends of these trace gases. Chapter 9 summarizes the results of this thesis and outlines recommendations for future work.

2. ATMOSPHERIC PHYSICS AND CHEMISTRY

In order to understand observations of the atmospheric state, one must develop a theoretical background that is capable of explaining from first principles the methods used to obtain the measurements. For instance, by utilizing our understanding of physics that has been established over decades of research, one can explain how radiation emitted from the Sun travels through space, reaches the top of the Earth's atmosphere, interacts with the molecules and particles in the atmosphere, and reaches the surface. This understanding can be extended to understanding the radiative transfer on other planets. Since the Industrial Revolution, humans have altered the composition of the atmosphere, which dominates the radiative transfer processes. Thus we must combine two fundamental physical sciences, physics and chemistry, to obtain a more complete understanding of the atmospheric state.

2.1 The Earth's Radiation Budget

2.1.1 Atmospheric Radiative Transfer

The Earth's atmosphere appears as a thin blue line from space, reaching up to only ~120 km above sea level. The general structure of the atmosphere is illustrated in Figure 2.1. This highly variable structure must be considered when constructing the theoretical understanding of how radiation passes through it. The concept of a 'blackbody' helps describe how radiation is absorbed and emitted throughout the atmosphere. A blackbody is any material that absorbs all radiation falling on it, where its absorption and emission of radiation is in equilibrium. The E-AERI makes use of our understanding of blackbody radiation as it measures the downwelling spectral radiance emitted from the atmosphere at particular wavelengths, with spectral calibration achieved by comparison with two blackbodies at known temperatures.

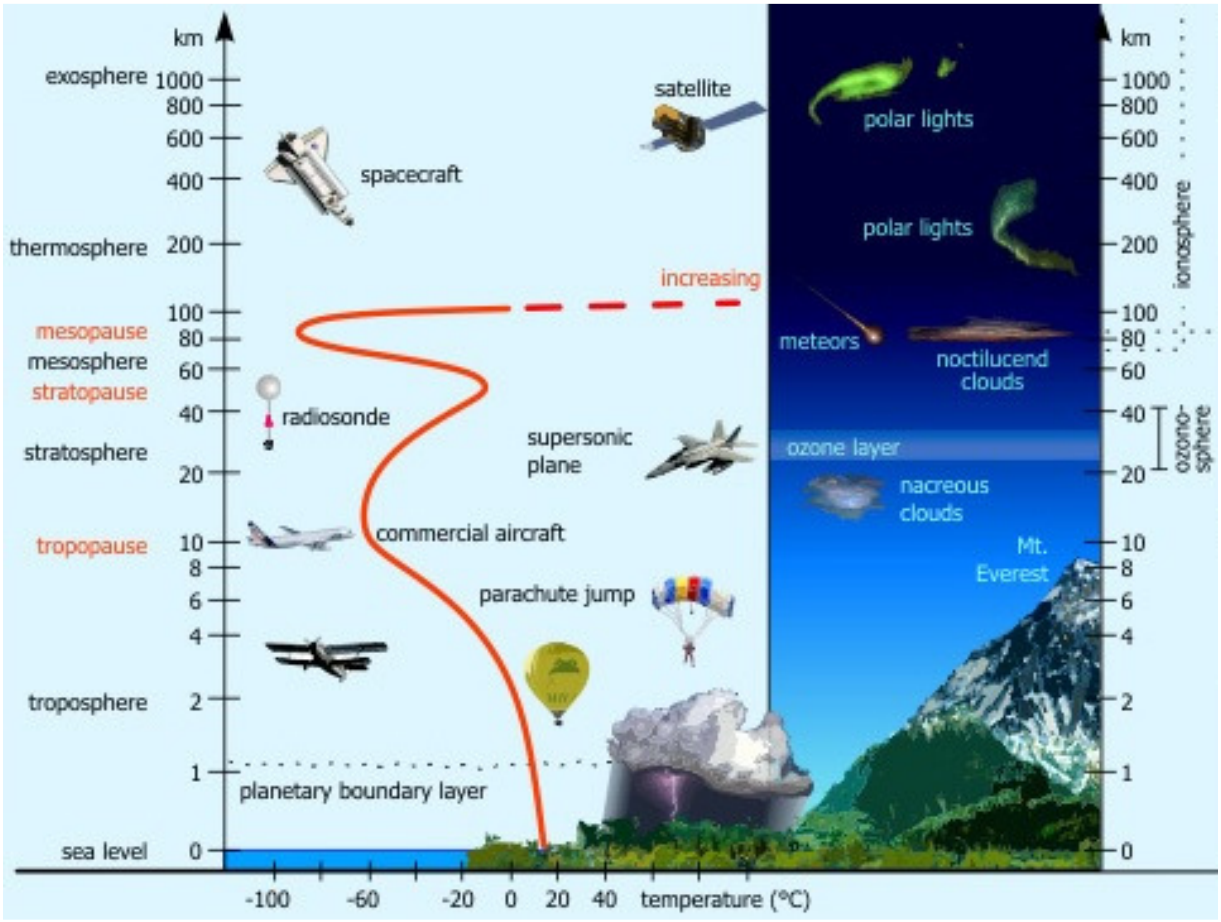

Figure 2.1: Structure of the Earth's atmosphere. An approximate temperature profile is shown in red as a function of height. Also labelled are approximate altitudes of various objects for reference. Image: [www.theozonehole.com, accessed May 2014].

Blackbody radiation is well understood via Planck's Law [Planck, 1901]. Planck's Law describes the spectral radiance emitted from a blackbody in thermal equilibrium at all wavelengths of the electromagnetic spectrum. Planck postulated that atoms behave like small electromagnetic oscillators that each oscillate at a specific frequency. The average energy emitted per oscillator is described by Planck's function, expressing the spectral radiance (also referred to as the intensity, or the 'source term'), $S(\tilde{\nu}, T)$, as:

$$S(\tilde{\nu}, T) = \frac{2h\tilde{\nu}^3 c^2}{e^{\left(\frac{hc\tilde{\nu}}{K_B \mathrm{T}}\right)} - 1} \qquad \textbf{(2.1)}$$

where T is the temperature, h is Planck's constant (6.26 x 10^{-34} Js), $\tilde{\nu}$ is the wavenumber [cm^{-1}; inverse wavelength], c is the speed of light (2.99 x 10^{8} m/s), and K_B is Boltzmann's constant (1.38 x 10^{-23} $m^2 kg\ s^{-2} K^{-1}$). Hence the spectral radiance S is the energy per unit time per unit surface area per unit solid angle per unit wavenumber. Eqn. **(2.1)** can be re-arranged to solve for T, now called the brightness temperature (sometimes referred to as 'radiance temperature' or 'apparent temperature'), via:

$$T = \frac{hc\tilde{\nu}}{K_B \ln\left(\frac{2h\tilde{\nu}^3 c^2}{S(\tilde{\nu})} + 1\right)} \quad \textbf{(2.2)}$$

The brightness temperature is the temperature a blackbody would need to have to yield the observed radiance at that wavenumber. By integrating Eqn. **(2.1)** over all wavenumbers and the solid angle, the energy flux, or the power emitted per unit area, can be obtained by:

$$F = \sigma T^4 \quad \textbf{(2.3)}$$

where F is the irradiance and σ is the Stefan-Boltzmann constant (5.67 x 10^{-8} $Js^{-1}m^{-2}K^{-4}$). Eqn. **(2.3)** is the Stefan-Boltzmann Law, which is essentially a measure of the total energy emitted per unit surface area per unit time of a blackbody. From Eqn. **(2.1)** it is evident that a blackbody will emit radiation at an amount that is dependent upon the frequency of the radiation and temperature as long as it remains in thermodynamic equilibrium. Both **(2.1)** and **(2.3)** can be applied to all molecules in the atmosphere below 70 km in altitude, as the temperature is considered uniform in an isotropic radiation field, permitting local thermodynamic equilibrium conditions [Liou, 2002].

Not all radiation reaches the surface of the Earth; when radiation interacts with matter, it can be scattered, absorbed, or emitted. The Beer-Bouguer-Lambert Law, or Beer's Law [Bouguer, 1729; Perrin, 1948], provides the expression for the decrease in radiation due to an absorbing homogeneous medium as:

$$I(z) = I(0)e^{-\int k\rho dz}$$

(2.4)

where I is the radiation intensity at a given height z, k is the absorption coefficient, and ρ is the density of the absorbing medium (gas). Beer's Law does not account for emission however, which can be described by the Planck function in Eqn. **(2.1)**. Schwarzschild's equation [Schwarzschild, 1914] describes the change in intensity of the radiation at a particular frequency through an absorbing and emitting medium as:

$$dI = -Ik\rho dz + Sk\rho dz\,.$$

(2.5)

The first term is called the sink function and represents the bulk of the atmosphere that absorbs radiation and transfers it into molecular energy (rotational, vibrational, electronic). The second term represents emission of radiation due to vibrational/rotational (for the IR) excited molecular states along the optical path. Note that this equation does not account for other removal processes in the atmosphere, such as scattering (discussed in more detail in the next Sections).

The plane parallel approximation of the atmosphere represents it as having many infinitesimally thin layers from the ground up to the top of the atmosphere. As explained in Liou [2002], on the basis of the energy conservation principle, the absorbed radiant energy heats the layer. This relationship is represented by:

$$\Delta F(z) = -\rho C_p \Delta z \frac{\partial T}{\partial t}$$

(2.6)

where $\Delta F(z)$ is the difference between the upward and downward radiation flux density at height z, C_p is the specific heat at constant pressure, T is the temperature and t is the time. By solving Eqn. **(2.5)** in its integral form and computing the difference between the upward and downward flux densities for a plane parallel atmosphere as shown in Liou [2002], the cooling-to-space term can be obtained:

$$\left(\frac{\partial T}{\partial t}\right)_{space} = -\frac{1}{\rho C_p}\pi S_{\tilde{\nu}}(z)\frac{d}{dz}T_v(z_\infty - z)$$

(2.7)

where $\left(\frac{\partial T}{\partial t}\right)_{space}$ is the cooling-to-space approximation and $S_{\tilde{\nu}}(z)$ is the Planck function (Eqn. **(2.1)**) evaluated for the temperature at height z. $T_v(z_\infty - z)$ is the layer transmission function from height z up to the top of the atmosphere (z_∞) and is equivalent to:

$$T_v = 2\int_0^1 e^{\frac{-\tau_v}{\mu}}\mu d\mu \tag{2.8}$$

where μ is the cosine of the zenith angle of the radiation incident on a plane parallel atmosphere and τ is the optical depth. The cooling-to-space term given in Eqn. **(2.7)** is sometimes referred to as the Newtonian cooling approximation, since it assumes an isothermal temperature profile such that local cooling rates are only produced from the emission of a local layer [Liou, 2002].

2.1.2 Clouds and the Earth's Energy Budget

Scattered solar radiation can have a large impact on the atmospheric radiative transfer. Radiation scattered by molecules in the atmosphere is described by Rayleigh scattering [Rayleigh, 1871] but has a negligible impact in the IR portion of the electromagnetic spectrum (< 1% of extinguished vertical radiation) [Houghton, 2002]. Radiation scattered by larger particles, such as clouds and aerosols, has a significantly larger impact in the IR portion of the spectrum however, and is described by Mie scattering [Mie, 1908].

Clouds play a significant role in atmospheric radiative transfer. This is illustrated in Figure 2.2 by both the magnitude and the number of mechanisms by which they affect the radiative budget of the Earth. Note that clouds play an even more significant role in the Arctic than what is illustrated in Figure 2.2 because they act as the primary source of downwelling radiation during polar night [Vavrus, 2004] (Figure 2.2 also omits other processes that are unique to the Arctic, such as large sensible and latent heat in the snow/ice pack and significantly higher albedo for the majority of the year). To complicate the matter, substantial uncertainties and sources of errors when measuring the Earth's global energy budget are due to cloud distribution and properties [Trenberth *et al.*, 2009]. Hence in order to reduce the uncertainties in our understanding of the Earth's global energy balance, we must improve our understanding of cloud radiative processes, including cloud cover distributions and trends.

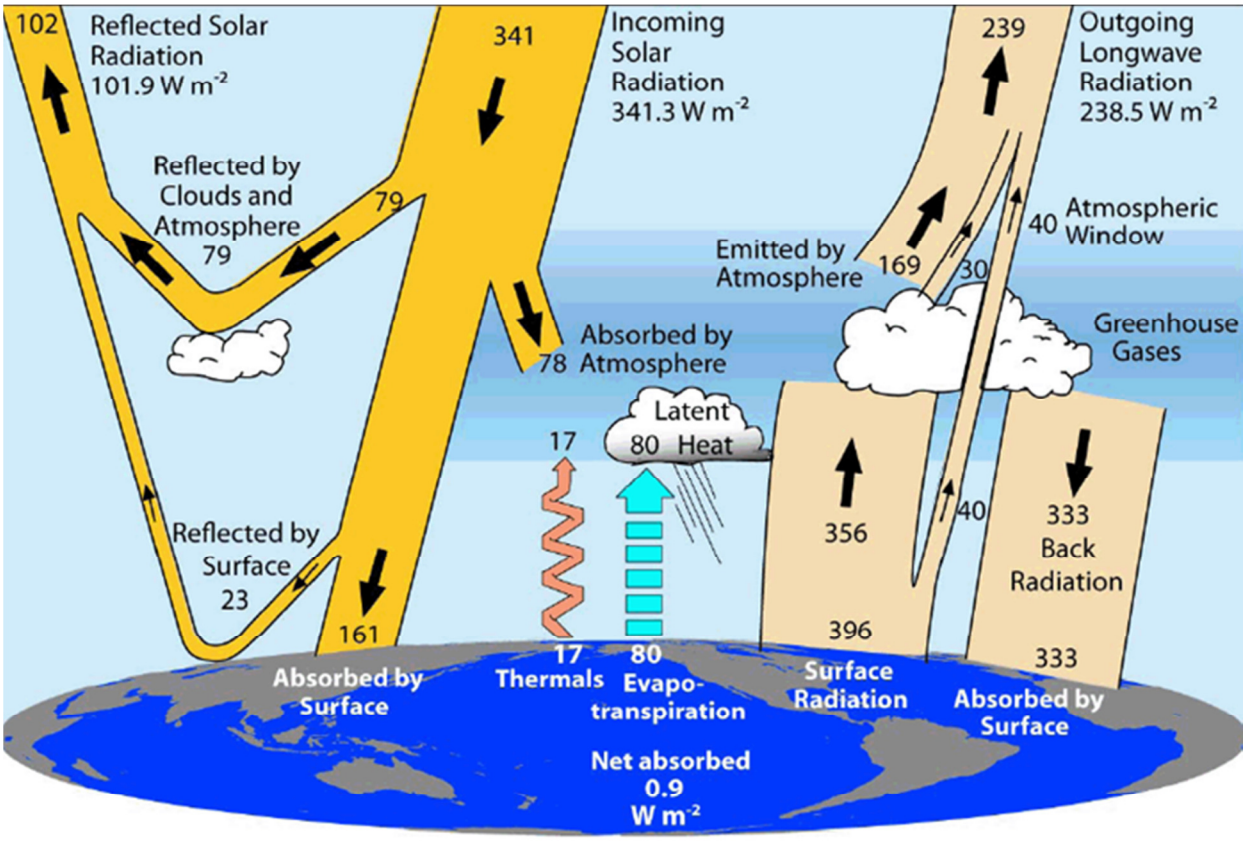

Figure 2.2: Visualization of atmospheric radiative transfer involving most general processes. Global annual mean budget is provided between March 2000 and May 2004. Image taken from Trenberth *et al*. [2009].

Certain changes in the Arctic climate have a corresponding increase in downwelling radiance [ACIA, 2004; Richter-Menge, 2006; Bekryaev *et al*., 2010]. As shown in Francis and Hunter [2007], the causes for the increase in the downwelling longwave flux density vary geographically and also depend on micro- and macrophysical cloud properties. The percentage increase in downwelling radiance due to a cloud has been shown to be more significant in the Arctic than in more humid regions [Tobin *et al*., 1999; Intrieri *et al*., 2002]. Given the frequency of cloud cover in the high Arctic (> 75^{o} N), this increase in surface radiative forcing due to clouds can have important consequences for the surface energy balance, as shown in Curry *et al*. [1996]. To characterize changes in downwelling radiance due to water vapour, temperature, and clouds, there is a need for long-term measurements of downwelling radiance in the high Arctic.

Long-term cloudy-sky radiation measurements are also essential for evaluating General Circulation Model (GCM) simulations. As argued in Webb *et al*. [2001], "if we are to have confidence in predictions from climate models, a necessary (although not sufficient)

requirement is that they should be able to reproduce the observed present-day distribution of clouds and their associated radiative fluxes." Since IR spectra can be generated from GCMs using radiative transfer models, ground-based measurements of downwelling radiance can be used to evaluate models as was done by the International Satellite Cloud Climatology Project [Klein and Jakob 1999; Webb *et al*. 2001].

While there are numerous satellite measurements of radiative fluxes, they do not directly measure surface radiative fluxes, making ground-based measurements critical for determining the effect of clouds on surface fluxes. In the Arctic, significant downwelling surface radiative forcing from different types of clouds was observed by a suite of ground-based instruments during the Surface Heat Budget of the Arctic (SHEBA) experiment, including an older extended-range AERI [Tobin *et al*., 1999; Uttal *et al*., 2002], but this campaign lasted less than one year. The longest relevant study was performed by Dong *et al*. [2010]; it used a decade of observations to determine the cloud fraction and radiative forcing over Barrow, Alaska (71^{o}N, 156^{o}W), where an earlier extended-range AERI was deployed in 1998 and continues to operate under the Atmospheric Radiation Measurement (ARM) program [Stokes and Schwartz, 1994; Stamnes *et al.*, 1999; Marty *et al.*, 2003; Knuteson *et al.*, 2004a]. Studies by Cox *et al*. [2012] and Cox *et al*. [2014] have used downwelling AERI radiances measured at Eureka from 2006 to 2008 to investigate clear and cloudy-sky fluxes and retrieve cloud properties. Significant differences between the longwave radiation flux were found between Barrow and Eureka [Cox *et al.,* 2012], indicating that surface measurements at more locations are needed to characterize surface radiative forcing across the Arctic – particularly since no long-term measurements of this type exist in the high (> 75^{o} N) Arctic. Thus measurements from the AERI, which can directly measure the radiative properties of clouds (described more in Sect. 3), can be used to improve our understanding of the impact of clouds on the radiative budget in the Arctic.

2.1.3 Surface Cooling-to-Space Windows

Evident in Figure 2.2 are the mechanisms by which the Earth cools itself; namely by emission of radiation to space. If the incoming energy is equivalent to the outgoing energy, then the Earth's radiation budget is in equilibrium. This isn't the case however, as 0.9 W/m^2 is absorbed by the Earth's surface as indicated in Figure 2.2; it is this imbalance that causes the observed increases in global temperatures [IPCC, 2007]. One of the important mechanisms by

which the Earth cools itself is by emitting thermal IR radiation from near the surface out to space through the atmospheric window. The atmospheric window occurs around 10 μm (~800 to 1250 cm^{-1}, or 8 to 12 μm) due to the absence of absorption features from any major greenhouse gas, as illustrated in Figure 2.3. For this reason, this window is considered the primary surface cooling-to-space window and as such is a crucial component in the Earth's global energy budget, particularly in relation to global warming. Measurements of radiation, such as those made by the AERI, can provide information about changes in the 10 μm surface cooling-to-space window. Note that 'cooling-to-space' refers to radiation emitted near the surface that reaches the top of the atmosphere; it occurs at all wavelengths, but cooling to space from the Earth's surface (as opposed to higher in the atmosphere) occurs primarily in this atmospheric window.

In the Arctic, significant IR surface cooling-to-space can also occur in the 20 μm 'dirty-window' (~400 to 600 cm^{-1}, or 17 to 25 μm), which is more transparent compared to lower latitudes, in the extremely cold and dry Arctic atmosphere [Tobin *et al.*, 1999]. At lower latitudes, surface cooling-to-space in the 20 μm window is generally much less significant due to strong absorption by water vapour; in the Arctic, the 20 μm window is semi-transparent and hence important for climate and energy balance [Tobin *et al.*, 1999]. The lower temperatures also shift the peak in the Planck function to longer wavelengths, increasing the impact of the 20 μm window in the Arctic [Tobin *et al.*, 1999]. The transition of regimes from surface cooling-to-space at 20 μm to surface cooling-to-space at 10 μm in the Arctic is of interest due to the possible impacts of continued warming, particular during the Arctic winter [Bintanja *et al.,* 2011].

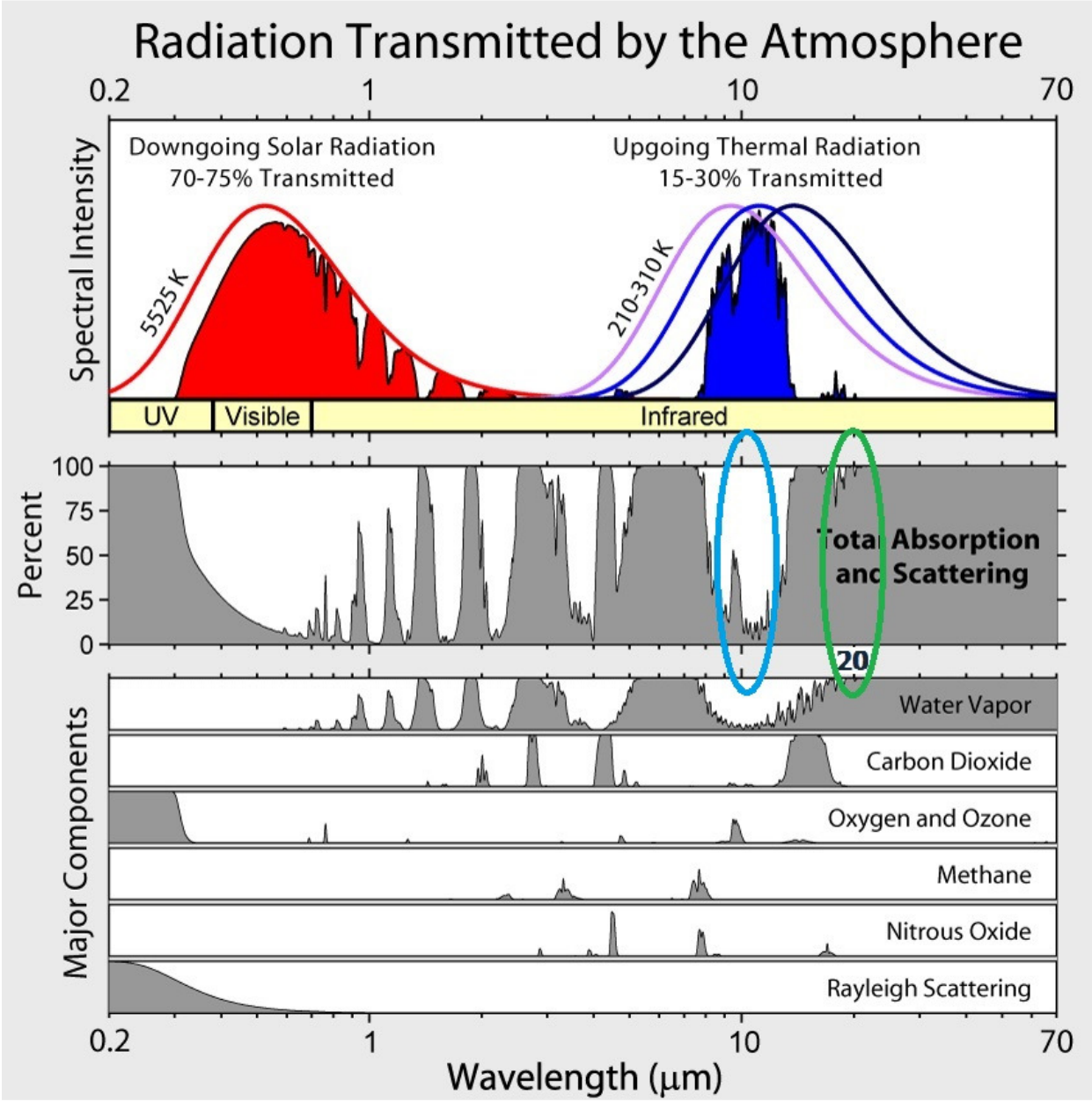

Figure 2.3: The transmission of downwelling solar radiation and upwelling thermal radiation (top panel) as a function of wavelength, the absorption bands in the Earth's atmosphere (middle panel), and the major individual contributors to atmospheric absorption, comprising greenhouse gases and Rayleigh scattering (bottom panel). The light blue oval indicates the 10 μm atmospheric window and the green oval indicates the 20 μm window. Note this figure was produced for non-Arctic conditions; the actual transmission at 20 μm is much greater in the Arctic. Image: R. Rohde [www.globalwarmingart.com/images/7/7c/Atmospheric_Transmission .png, accessed April 2014], modified by Zen Mariani.

AERIs perform thermal IR measurements with spectral ranges that cover both of these surface cooling-to-space windows of interest. The first AERI installed at Eureka was the Polar-AERI (P-AERI), whose spectral range includes both the 10 μm window and a portion of the

20 μm window from ~500 to 600 cm^{-1} (17 to 20 μm). In October 2008, installation of the Extended-range AERI (E-AERI) extended the range of the measurements in the 20 μm window down to 400 cm^{-1} (25 μm).

2.2 Fourier Transform Spectroscopy

2.2.1 Infrared Emission Spectroscopy

This work will focus on IR radiation, which is electromagnetic radiation with a wavelength longer than visible light, ranging from 700 nm to 1 mm. As previously discussed, the balance of absorbed and emitted IR radiation determines the Earth's climate. Combined with the advantageous fact that IR radiation interacts with matter (atmospheric trace gases) at numerous wavelengths, the reason for studying this spectral region is self-evident.

The internal molecular energy is quantized in electronic, vibrational, and rotational energy states. The internal energy of a molecule is described by solutions of the time-independent Schrödinger equation; while exact solutions are not possible, approximations can be made to produce accurate estimates of a molecule's energy levels. The energy associated with the internal motion of a molecule is manifested via vibrations or rotations of the molecule, corresponding to radiation in the microwave and IR portions of the electromagnetic spectrum. Molecules that have complex charge orientations, such as O_3, have electric dipole moments that permit the molecule to couple with the electric field, allowing the molecule to interact with – that is, absorb, scatter, and/or emit – IR radiation.

Quantum theory dictates that only discrete energy levels of a molecule can exist (as opposed to the classical view of a continuum). Thus there exist unique, discrete vibrational and rotational states associated with a molecule's rotational-vibrational structure, producing unique, discrete absorption or emission transitions in the IR. Photons are absorbed or released during a molecule's vibrational and rotational transitions, which can then be detected by FTIR spectrometers. In practice, discrete absorption/emission lines (of infinitesimal width) do not exist; instead there is some width (or spread in frequency) of the spectral line due to several effects described below.

Precise knowledge of the strength, width, and general shape of these spectral lines are required in order to extract specific molecular information from spectral lines, including the pressure of the molecule (which provides the altitude) and the molecular concentration (amount). The line strength, S, is directly related to the absorption coefficient, $k_{\tilde{\nu}}$, via:

$$S = \int_{-\infty}^{\infty} k_{\tilde{\nu}} d\nu$$

(2.9)

where $k_{\tilde{\nu}}$ is normalized. Precise measurements of the strength and shape of spectral lines can be analyzed in the inverse sense to infer the concentration of the molecule.

The spectral lineshape is broadened by the Doppler shift, collisions, and natural broadening. Natural broadening refers to the effect of the Heisenberg Uncertainty Principle [Heisenberg, 1927], whereby the relationship of the energy of a state, E, and its natural lifetime, Δt, is:

$$\Delta E \Delta t \geq \frac{h}{2\pi}$$

(2.10)

where h is Planck's constant. Planck's relation shows that changes between two adjacent energy levels, E_2 and E_1, gives rise to distinct frequencies of radiation, ν, via:

$$E_2 - E_1 = h\nu \,.$$

(2.11)

By combining Eqn. **(2.10)** with **(2.11)**, we achieve proof that the emitted radiation from a single transition can never be monochromatic and must have some width:

$$\Delta\nu \geq \frac{1}{2\pi\Delta t} \,.$$

(2.12)

Thus the half-width at half-maximum for natural broadening, α_N, is:

$$\alpha_N \geq \frac{1}{4\pi\Delta t}.$$

(2.13)

However, the typical half-width of an isolated molecule is < 3 x 10^{-4} cm^{-1} [Banwell, 1983], which is negligible in comparison to other sources of line broadening. Doppler broadening occurs below ~50 km and results from the frequency shift along a molecule's direction of motion (the Doppler effect). The Doppler-shifted frequency, ν, for a molecule travelling with velocity *v*, is given by:

$$\nu = \nu_0 \left(1 + \frac{\mathrm{v}}{c}\right)$$

(2.14)

for a molecule emitting radiation at the line centre frequency ν_0, where *c* is the speed of light. For a gas in local thermodynamic equilibrium, the Maxwell-Boltzmann distribution can be used to describe the Doppler lineshape [Liou, 2002], $f_{\mathrm{D}}(\nu - \nu_0)$, as:

$$f_{\mathrm{D}}(\nu - \nu_0) = \frac{1}{\alpha_D\sqrt{\pi}}\, e^{\left[-\left(\frac{\nu-\nu_0}{\alpha_{\mathrm{D}}{}^2}\right)^2\right]}$$

(2.15)

where α_D is the e-folding line width given by:

$$\alpha_{\mathrm{D}} = \nu_0 \left(\frac{2K_B\mathrm{T}}{mc^2}\right)^{\frac{1}{2}}$$

(2.16)

and *m* is the mass of the molecule, *T* is the temperature, and K_B is the Bolztmann constant. Note the e-folding width is commonly used for mathematical convenience; the half-width at half-maximum is $\alpha_{\mathrm{D}}\sqrt{\ln 2}$.

Spectral line broadening due to collisions, called Lorentz broadening, occurs below ~20 km and results due to the frequent collisions between molecules in the atmosphere, producing temporary deformations of the molecule. The distribution of the time between collisions behaves according to Poisson's Law [Lorentz, 1906] and can describe the Lorentz lineshape, $f_{\mathrm{L}}(\nu - \nu_0)$, as:

$$f_{\mathrm{L}}(\nu - \nu_0) = \frac{\alpha_L}{\pi(\nu - \nu_0)^2 + {\alpha_L}^2} \tag{2.17}$$

where α_{L} is the half-width at half-maximum:

$$\alpha_L = \alpha_0 \left(\frac{p}{p_0}\right)\left(\frac{T_0}{T}\right)^{\frac{1}{2}} \tag{2.18}$$

where p_0 and T_0 are the standard pressure and temperature, and the half-width at half-maximum at standard pressure and temperature, α_0, is equivalent to ~0.1 cm^{-1}. Lorentz line broadening dominates in the wings of spectral lines, whereas the Doppler lineshape is stronger in the centre of the line and weaker in the wings. The Lorentz lineshape is not dominant for molecules radiating at lower pressures due to its inherent pressure-dependence, unlike the Doppler lineshape. For the region of the atmosphere where both Lorentz and Doppler lineshapes are applicable, approximately 20 to 50 km, these lineshapes can be convolved to produce the Voigt lineshape [Huang and Yung, 2004], $f_{\mathrm{V}}(\nu - \nu_0)$:

$$f_{\mathrm{V}}(\nu - \nu_0) = f_{\mathrm{L}}(\nu - \nu_0) * f_{\mathrm{D}}(\nu - \nu_0)\,,$$
$$f_{\mathrm{V}}(\nu - \nu_0) = \frac{\alpha_{\mathrm{L}}}{\pi^{\frac{3}{2}}\alpha_D}\int_{-\infty}^{\infty} \frac{1}{(\nu' - \nu_0)^2 + {\alpha_{\mathrm{L}}}^2}\, e^{\left[-\left(\frac{\nu' - \nu_0}{{\alpha_{\mathrm{D}}}^2}\right)^2\right]} d\nu'\,. \tag{2.19}$$

This Voigt lineshape is commonly used in spectroscopy as a representation of a radiating molecule's spectral absorption/emission lines.

2.2.2 Interferometry

Fourier transform spectroscopy (FTS: also used for Fourier transform spectrometer) is the spectroscopic method used by many research areas that require a combination of high spectral resolution, precision, fast acquisition, and high signal-to-noise ratio (SNR). Invented by Albert Michelson in the 1880s, Fourier transform interferometry remains the core component of many IR spectrometers today [Michelson, 1887; Bell, 1972]. All wavelengths of radiation are

collected simultaneously in a FTIR. A FTIR spectrometer is based on a Michelson Interferometer (MI); a basic illustration of the typical MI design is shown in Figure 2.4. The typical MI consists of two mirrors (one translating back and forth, one stationary), a detector, and a beamsplitter. The MI creates an Optical Path Difference (OPD) between the stationary and moving mirrors due to the different distances the radiation travels. This in turn creates a phase difference between the two beams of radiation. When the two beams are recombined at the beamsplitter, they create an interference pattern, which is a pattern of bright and dark fringes due to the introduced phase difference.

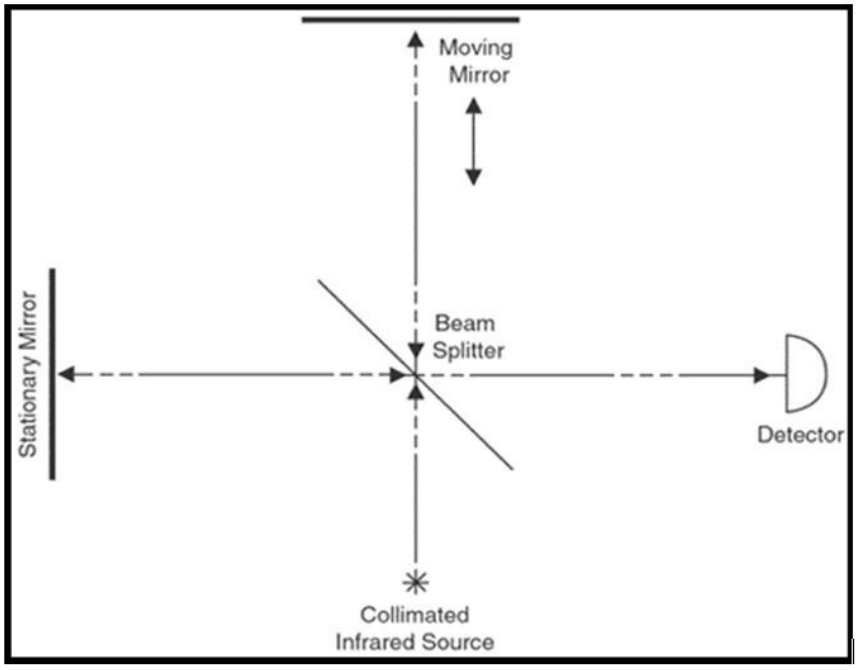

Figure 2.4: Illustration of a Michelson interferometer. Radiation from a source first passes through a beamsplitter, sending radiation to both mirrors. The moving mirror creates an optical path difference, which when recombined creates an interference pattern on the detector. Image: [www.cluin.org /programs/21m2/openpath/op-ftir/] accessed January 2014.

Note the actual design of the E-AERI's interferometer is more complicated; the MI design illustrated in Figure 2.4 is modified to use two cube-corner mirrors joined together in a 'wishbone' design such that both mirrors move at the same time, as illustrated in Figure 2.5. This design decreases the physical space required to create the OPD. The E-AERI's beamsplitter is made of potassium bromide (KBr) and transmits half of the radiation and reflects the remaining half, ensuring an equal portion of radiation reaches both mirrors. The fixed and

moving mirrors reflect the radiation back to the beamsplitter, where again half the radiation is reflected and the remaining half is transmitted.

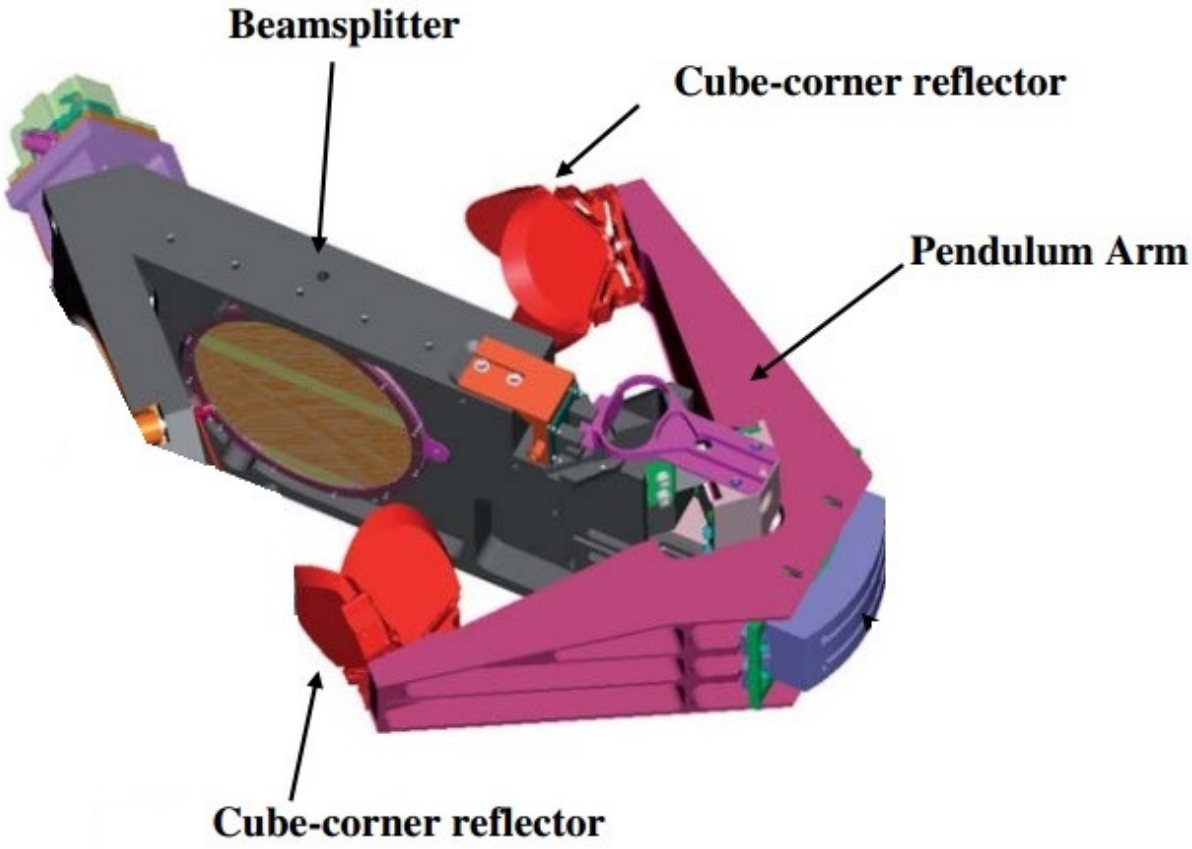

Figure 2.5: Illustration of the E-AERI interferometer. Two cube-corner reflectors (red) mounted on a pivoting 'wishbone' structure (purple) are used as moving elements to create the OPD. Image modified from Fu *et al.* [2007].

The FTIR spectrometer's detector records the interferogram, which can be translated into an absorption/emission spectrum using the Fast Fourier Transform (FFT) algorithm. When the incident wave of radiation is split by the beamsplitter, reflected, ψ_r, and transmitted, ψ_t, beams are produced. When these beams reflect off the stationary and scanning mirrors, they return to the beamsplitter via:

$$\psi_r = |r||t|A_0 e^{i(\omega t - 2kx_1 + 2\pi\varphi_r + 2\pi\varphi_t)} \quad \textbf{(2.20)}$$

$$\psi_t = |r||t|A_0 e^{i(\omega t - 2kx_2 + 2\pi\varphi_r + 2\pi\varphi_t)}$$

(2.21)

where A_0 is the amplitude of the wave, x_i is the optical path, k is the wavenumber ($k = 2\pi\tilde{\nu}\hat{k}$) in the $\hat{k}$ direction, $\tilde{\nu}$ is the wavenumber (reciprocal of the wavelength), |r| is the reflection coefficient, |t| is the transmission coefficient, t is time, ω is the angular frequency, φ_r is the phase shift due to reflection, and φ_t is the phase shift due to transmission. Thus the detector receives the re-combination of these two beams:

$$\psi_{tot} = \psi_t + \psi_r ,$$
$$\psi_{tot} = |r||t|A_0 e^{i(\omega t + 2\pi\varphi_r + 2\pi\varphi_t)}\left[e^{2ikx_1} + e^{2ikx_2}\right].$$

(2.22)

It is assumed that the beamsplitter is ideal and splits the beam evenly and compensates for any phase-induced changes upon reflection or transmission, such that:

$$|r|^2 = |t|^2 = \frac{1}{2}$$

(2.23)

$$\varphi_r = \varphi_t = 0 .$$

(2.24)

If we define the OPD, Δx, as $\Delta x = x_2 - x_1$ and substitute Eqn.**(2.23)** and **(2.24)** into **(2.22)**, we achieve:

$$\psi_{tot} = \frac{A_0}{2} e^{i\omega t} e^{2ikx_1}\left[e^{2ik\Delta x} + 1\right].$$

(2.25)

The corresponding intensity, *I(x)*, can be found by taking the square modulus:

$$I(x) = \psi_{tot}\psi_{tot}^{*} ,$$
$$I(x) = \frac{{A_0}^2}{4}(1 + cos[2k\Delta x]) ,$$
$$I(x) = I_0(1 + cos[2\pi\tilde{\nu}x])$$

(2.26)

where I_o is the constant background signal (equivalent to $\frac{A_0{}^2}{4}$) and, for simplicity, the OPD is now expressed as x rather than $2\Delta x$. Upon initiation of a scan, the two corner cube mirrors are an equal distance from the beamsplitter such that the OPD = 0. This is known as the point of Zero Path Difference (ZPD). As the scan continues (one corner cube moves towards the beamsplitter, the other moves away from the beamsplitter), the OPD increases and the interferogram can be recorded as a function of the moving mirror's position. For a polychromatic source of radiation, the intensity, *I*, at each position *x* consists of all wave frequencies superimposed. This results in a significantly more complex looking function than a single sinusoid, which would be expected if only a single wavelength of radiation was present. Hence the amplitude, I_o, is composed of spectral intensities that depend on all wavenumbers and the expression must be integrated:

$$I(x) = \int_0^\infty B(\tilde{\nu})\, cos(2\pi\tilde{\nu}x)\, d\tilde{\nu} \tag{2.27}$$

where $B(\tilde{\nu})$ is the wavenumber-dependent spectral intensity and I_o has been left out for simplicity [Pinkus, 1999]. Since the signal at the detector is a superposition of multiple sine waves, the signal is additive and continuous, allowing the use of Fourier decomposition to extract the spectral intensity as a function of wavenumber. Hence the spectrum resulting from the Fourier transform of the interferogram is given by:

$$B(\tilde{\nu}) = \int_0^\infty I(x)\, cos(2\pi\tilde{\nu}x)\, dx\,. \tag{2.28}$$

Through the use of the MI, FTIR spectroscopy utilizes the coupled vibrational and rotational transitions that occur in the mid-IR region to produce high-resolution spectra [Jacob, 1999]. Defining the spectral resolution of FTIR spectrometers involves several different criteria and can be calculated using multiple methods; a detailed discussion of this is provided in Lindenmaier [2012]. Because the resolution depends on the resolution criterion applied as well as the apodization function, for the purposes of this work 1/(max OPD) is chosen as the 'nominal resolution' of the FTIR.

2.2.3 Advantages and Limitations of Fourier Transform Spectroscopy

In general, the interferometers used in FTS have several advantages over other designs, such as diffraction grating or prism spectrometers. About 200 times more power can be sent through the interferometer compared to a grating spectrometer, where the power is limited by the entrance slit [Jacquinot and Dufour, 1948]. Interferometers have large resolving power; the longer the scanning arm is, the greater the OPD, the higher the resolution [Michelson, 1887; Connes, 1987]. Combined with the calibration advantage of the interferometer, which arises from the highly accurate wavenumber sampling that requires no interpolation or wavenumber calibration (unlike in grating or prism spectrometers) [Erickson, 1979; Connes, 1970], this permits interferometers to attain the very high-resolution measurements necessary for high-precision trace gas measurements. Additionally, interferometers receive information from a broad range of spectral wavelengths during each element of a scan, whereas older grating or prism spectrometers receive information only from a very narrow band of wavelengths that reach the exit slit of the instrument at a particular time during each element of the scan [Fellgett, 1951; 1958]. Multiple FTS scans can be co-added together in a relatively short period of time, increasing the measurement's SNR. Thus FTS spectra can be measured relatively quickly.

The derivation provided in Sect. 2.2.2 is for an ideal system; in reality this isn't the case. For instance, it was assumed that any phase changes induced by the beamsplitter are compensated for; this does not occur in practice and phase errors usually occur, resulting in a slightly asymmetric interferogram relative to the ZPD. The OPD is also not infinite, creating the need for an apodization factor that imposes the limits of the scan mirror on the Fourier transform [Davis *et al.*, 2001]. The field-of-view (FOV) of the FTS in an ideal case is zero (entrance aperture is infinitely small and located at the focus of the collimator) when in reality the entrance aperture is finite, allowing divergent rays of radiation to enter the spectrometer. The FOV must be known in order to correct for this effect and mitigate the errors it causes (broadening of spectral lines, reducing the resolution). Despite these disadvantages, it is clear that the advantages of a MI FTS are so powerful that today the MI design has been widely adopted and used in applications requiring spectroscopic measurements, from astronomy to atmospheric physics to industry.

2.3 Atmospheric Composition

2.3.1 Overview of the Earth's Atmospheric Composition

The atmosphere consists of 78% nitrogen and 21% oxygen; a portion of the remaining 1% consists of several different trace gases. Greenhouse gases, such as ozone (O_3), nitrous oxide (N_2O), methane (CH_4), carbon dioxide (CO_2), and water (H_2O) absorb and re-emit a significant amount of this thermal radiation in the atmosphere when compared to other gases, and cause the greenhouse effect.

Several different greenhouse gases are produced as by-products of complete/incomplete combustion of fossil fuels (e.g., by running your car engine) and can be transported to the Arctic atmosphere. Many of these greenhouse gases have long lifetimes (on the order of years, decades, or centuries); hence once released into the atmosphere they have a long impact on the atmospheric chemistry and radiative transfer. The concentrations of many greenhouse gases, particularly CO_2, have drastically changed since the Industrial Revolution, which started in the 1800s [Andrews, 2000; IPCC, 2013]. Figure 2.6 illustrates the sharp increase in CO_2 emissions in the late 1800s, causing an increase in the atmospheric CO_2 concentration. The connection between humankind's fossil fuel burning and current changes in climate exhibits such statistical significance that the IPCC's Fifth Assessment Report states that "it is extremely likely (95% confidence) more than half of the observed increase in global average surface temperature from 1951 to 2010 was caused by the anthropogenic increase in greenhouse gas concentrations and other anthropogenic forcings together" [IPCC, 2013].

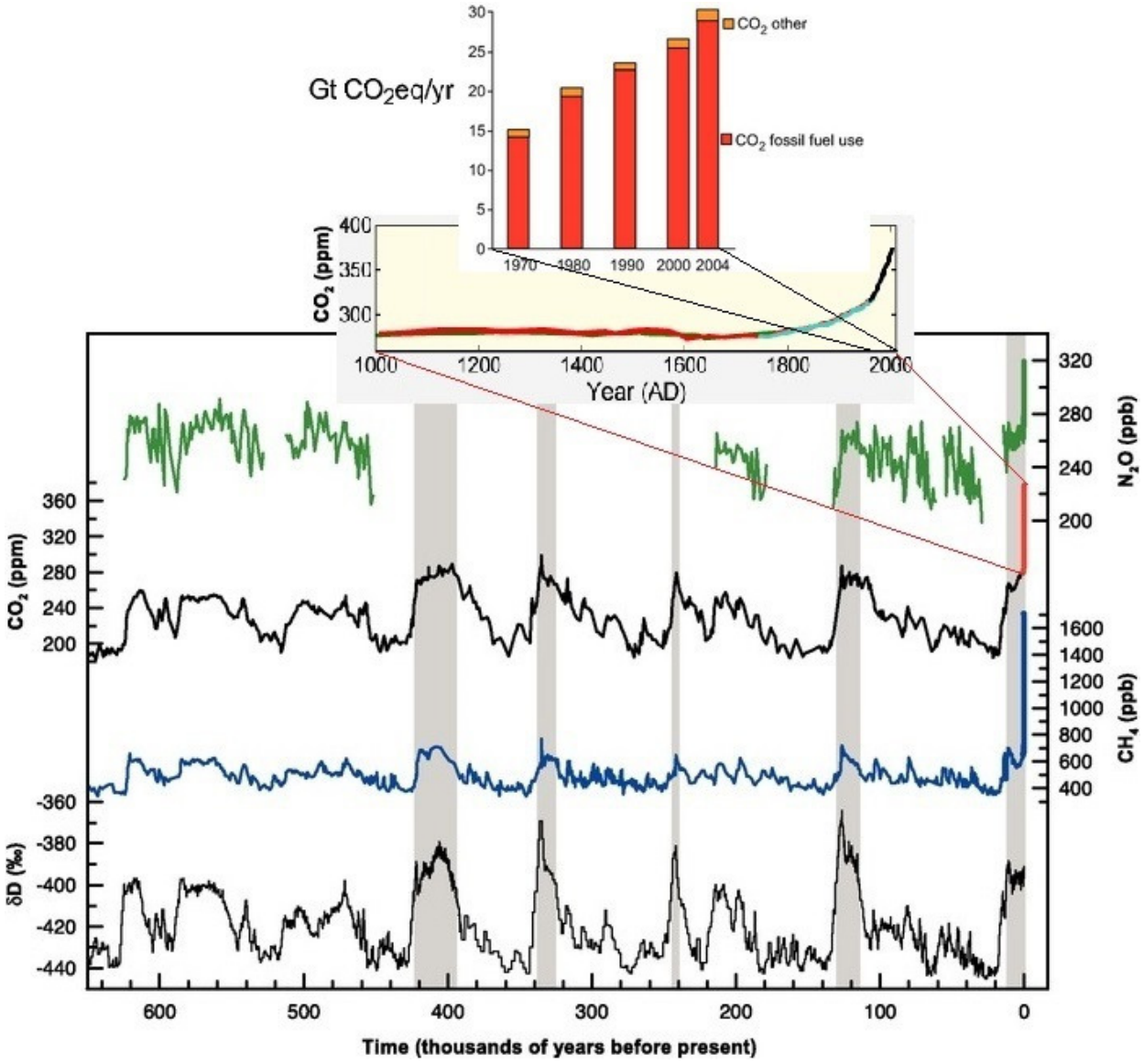

Figure 2.6: From top to bottom: insert of CO_2 emissions by fossil fuel (red bars) and other sources (yellow bars) since 1970 in units of Gigatonnes; CO_2 concentration during the last 1000 years (different colored lines represent measurements from different sites); and 650,000 years of Antarctic ice core data showing atmospheric concentrations of the greenhouse gases N_2O (green), CO_2 (black), and CH_4 (blue) in air trapped within the ice cores and from recent atmospheric measurements. Variations of deuterium (δD; black) are also shown at the bottom, which is a proxy for local temperature. Shaded regions indicate current and previous interglacial warm periods. Image: modified from IPCC [2007].

Due to the limited population in the Arctic, local emissions of greenhouse gases (including ozone-destroying CFCs) are very low. However, in general the Brewer-Dobson circulation transports stratospheric air in the north-south and vertical directions across the globe. The Brewer-Dobson circulation describes how tropospheric (between 0-15 km in alt.) air parcels

at low latitudes move upward into the stratosphere (between about 15-50 km), where they then move poleward. Once these parcels reach the poles, they descend back into the troposphere [Andrews, 2000]. Aside from the Brewer-Dobson circulation, lower-altitude transport of trace gases from northern Eurasia provides the dominant source of pollution measured at the Arctic surface during the winter [Stohl, 2006].

2.3.2 The Importance of Measuring Trace Gases in the High Arctic

There are many gases present in the Earth's atmosphere at extremely low concentrations – these are referred to as trace gases. Despite their smaller concentrations, their ability to significantly affect the radiative balance of the planet warrants their extensive monitoring. Two of the four "*grand challenges in atmospheric chemistry*" identified in the IGOS Atmospheric Chemistry Theme Report are "*stratospheric chemistry and ozone depletion*" and "*chemistry-climate interactions*" [IGOS, 2004]. O_3 is well known as a strong absorber of solar UV-B radiation, which is the main source of heating in the stratosphere. Stratospheric O_3 has declined significantly since about 1980 in response to enhanced chlorine resulting from anthropogenic emissions of CFCs [Solomon, 1999; WMO, 2006]. This is particularly true in the Arctic, where the annually averaged O_3 loss is about 7% since 1979 and, recently, the most severe chemical O_3 loss over the Arctic was recorded in February and March 2011 [Manney *et al.*, 2011; Adams *et al.*, 2012b; Lindenmaier *et al.*, 2012].

A gradual recovery of global stratospheric O_3 is expected due to the signing of the Montreal Protocol and its subsequent amendments to regulate the production of CFCs [Austin *et al.*, 2003; WMO, 2006; IPCC, 2013]. However, a vital remaining question pertains to increasing greenhouse gas concentrations and their impact on climate change, particularly with respect to long-term changes in the formation of polar stratospheric clouds (PSCs) and the polar vortex, requiring ongoing monitoring of stratospheric O_3 recovery [e.g., Shindell *et al.*, 1998; 2001; Schnadt *et al.*, 2002; Schnadt and Dameris, 2003; Rex *et al.*, 2004, Kim and Flatau, 2010]. Thus the impact of climate change on Arctic O_3 recovery remains uncertain; understanding this evolution is the overall goal of CANDAC's Arctic Middle Atmosphere Chemistry theme mentioned in Chapter 1.2.

Long-term observations are thus essential to address the question of what is the composition of the Arctic atmosphere and how is it changing with time? Eureka is an excellent

location for various scientific studies, ranging from polar ozone depletion, to satellite validation, to characterizing long-range transport. Measurements of other trace gas species measured at Eureka are imperative in order to characterize polar ozone depletion, including N_2O, which is an important greenhouse gas and has been shown to be one of the most important ozone-depleting substance emitted today [Ravishankara *et al.*, 2009]. Measurements of O_3 and the products of N_2O, particularly during the winter-time formation of the polar vortex, can provide insight into chemical and dynamical processes occurring in this rapidly changing region.

Such monitoring at Eureka started in 1993 with the installation of a Bomem DA8 FTIR by Environment Canada [Fast *et al.*, 2011] with regular intensive monitoring using the 125HR (and other) spectrometers beginning in 2006 after the establishment of PEARL [Fraser *et al.*, 2009; Batchelor *et al.*, 2009; Fogal *et al*., 2013]. PEARL is uniquely situated in close proximity to frequent measurements by polar-orbiting satellites, such as the Atmospheric Chemistry Experiment (ACE), making ground-based measurements at this site particularly useful for satellite validation purposes [e.g., Batchelor *et al*., 2010; Adams *et al*., 2012a]. The products of biomass burning over northern Eurasia, which has increased significantly over the past 100 years due to human activities, can also be transported to the Arctic and result in CO (among other) total column enhancements [Stohl, 2006; Warneke *et al*., 2010; Viatte *et al*., 2014]. This provides a growing source of chemically and radiatively active gases such as CO_2, CH_4 and other hydrocarbons that can be measured by ground-based spectrometers such as the E-AERI. Photochemistry has a noticeable effect on the budget of trace gases above Eureka: polar night (24-hr darkness) occurs from mid-October to mid-February and rapidly transitions to polar day (24-hr sunlight) from late-April to late-August.

The seasonal variability of these trace gases is measured by the E-AERI at PEARL; for instance, the polar vortex is frequently above Eureka in the spring, with vortex dynamics playing a key role in the ozone budget, whereas in the summer the variability in trace gases is largely dependent on transport from lower latitudes, solar radiation, and chemical reactions. The E-AERI trace gas measurements have been (and will continue to be) integrated with other chemical, dynamical, and cloud/aerosol measurements made at Eureka. The wide range of measurement capabilities that are implemented at Eureka enable the contributions of these interconnected processes to be unravelled.

The new E-AERI trace gas measurement products described in Chapters 7 and 8 complement the ground-based solar-absorption measurements at Eureka, such as the Bruker

125HR at the PEARL Ridge Lab. E-AERI measurements are taken every seven minutes year-round, including polar night when the solar-viewing spectrometers at PEARL are not operated. This allows E-AERI measurements to fill the gap in the PEARL dataset during the four months of polar night, as illustrated in Figure 2.7. Measurements throughout polar night also permit the quantification of the diurnal and seasonal cycle of trace gases for the first time at Eureka, as will be shown. During sunlit periods, the combination of the E-AERI and solar-absorption FTIR measurements enable improved temporal resolution, comparison studies, and measurements from different altitudes (during the E-AERI's measurements at 0PAL) to improve our understanding of the lower-tropospheric composition (which is of interest for investigating biomass burning events and other pollution plumes that are transported to the high Arctic from southern latitudes) as well as stratospheric composition. The next two subsections describe the chemical processes pertaining to the four trace gases, O_3, CO, CH_4, and N_2O, that were measured by the E-AERI.

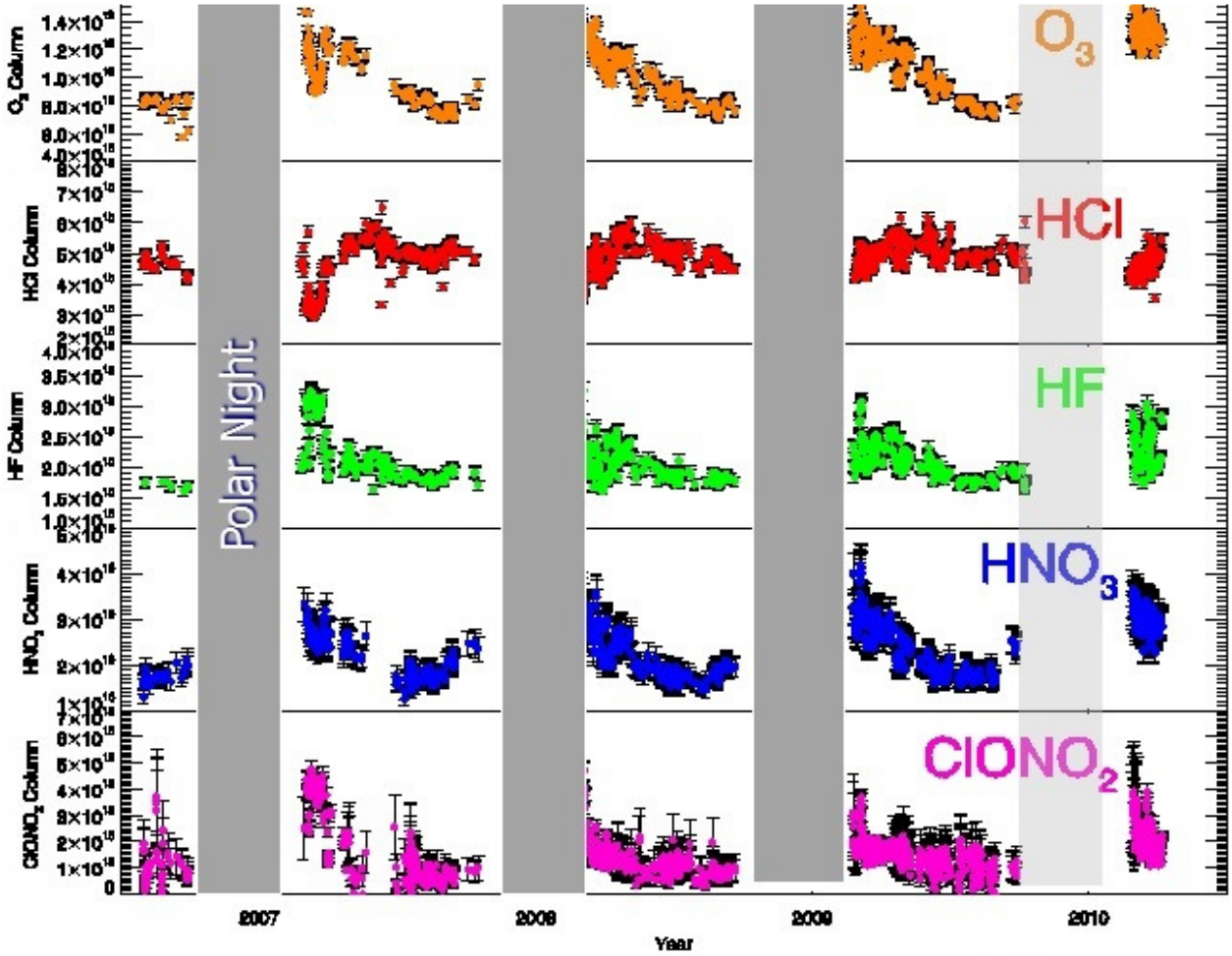

Figure 2.7: Sample time series of the Eureka Bruker 125HR trace gas measurements at PEARL of O_3 (orange), HCl (red), HF (green), HNO_3 (blue), and $ClONO_2$ (magenta) from 2006 to 2011. Gaps in the measurement record (grey vertical bars) indicate periods of Polar night when the Bruker 125HR (and all other ground-based solar-absorption spectrometers at Eureka) cannot take measurements. Image: Rodica Lindenmaier (modified by Zen Mariani).

2.3.3 Stratospheric Ozone in the Arctic

O_3 is a pollutant in the troposphere with harmful effects on the respiratory system, yet beneficial in the stratosphere where it acts as a powerful absorber of harmful UV radiation. The conditions in the Arctic stratosphere can be favorable for the heterogeneous reactions that deplete O_3, particularly in the midst of the cold air found in the Arctic polar vortex. The vortex is a large-scale asymmetric cyclonic circulation pattern that occurs during the northern hemisphere winter as a result of the temperature difference between the equator and the pole. It stretches from the upper troposphere to the lower mesosphere, forming in the fall and disintegrating in the spring. It is important to conduct measurements of O_3 prior to, during, and

after the formation and breakup of the polar vortex to quantify the chemical and dynamical processes that occur in and around this continually-shifting region, particular with respect to the O_3 loss.

Ozone is naturally generated and destroyed in the stratosphere via the Chapman mechanism [Jacob, 1999]:

$$O_2 + h\nu \rightarrow O + O \quad \textbf{(2.29)}$$

$$O + O_2 + M \rightarrow O_3 + M \quad \textbf{(2.30)}$$

$$O_3 + h\nu \rightarrow O_2 + O(^1D) \quad \textbf{(2.31)}$$

$$O_3 + O \rightarrow 2O_2 \quad \textbf{(2.32)}$$

where $h\nu$ = UV photon, M = third body molecule, and $O(^1D)$ = excited state O atom. The observed ozone loss in the stratosphere over the Arctic is not explained by only these reactions (**(2.29)** to **(2.32)**) – it is mainly caused by the heterogeneous chemistry that occurs in PSCs as a result of CFCs and other ozone-depleting substances [Solomon, 1999].

The northern hemisphere winter results in an increase in both halogen reservoirs (due to the absence of solar radiation to break them apart) such as hydrogen chloride (HCl) and chlorine nitrate ($ClONO_2$), and chlorine activation (conversion of chlorine reservoir species into an ozone-depleting form) [Hanson and Ravishankara, 1995; Danilin and McConnell, 1995; Jacob, 1999; WMO, 2006]. If long periods of cold temperatures (< 195 K) are maintained during the winter, PSCs consisting of liquid and solid nitric acid (HNO_3), H_2O, and sulfuric acid (H_2SO_4) can form. PSCs provide surfaces for the heterogeneous chemistry of ozone depletion to occur at polar sunrise in the spring.

When the sinks for stratospheric O_3 dominate, the result is the creation of an O_3 hole, such as that found over the South Pole in 1985 (and every year since). O_3 depletion permits excess solar radiation to reach the surface of the Arctic, particularly in the ultra-violet (UV) [Andrews, 2000; WMO, 2006]. To date, springtime ozone loss has been less severe over the Arctic than over Antarctica because Arctic stratospheric temperatures are generally higher, resulting in less frequent formation of PSCs, which are necessary for the heterogeneous chemistry that leads to O_3 destruction.

2.3.4 Tropospheric Chemical Processes in the Arctic

In the upper troposphere, O_3 acts as a greenhouse gas, absorbing some of the IR radiation emitted by the Earth (though much less than CO_2, for instance) [Forster *et al.*, 2007]. It is produced through oxidation of CO, CH_4, and other Non-Methane Volatile Organic Compounds (NMVOCs) in the presence of NO_x (NO and NO_2) via:

$$CO + OH \rightarrow CO_2 + H \quad \textbf{(2.33)}$$

$$H + O_2 + M \rightarrow HO_2 + M \quad \textbf{(2.34)}$$

$$HO_2 + NO \rightarrow OH + NO_2 \quad \textbf{(2.35)}$$

$$NO_2 + h\nu \xrightarrow{O_2} NO + O_3 \quad \textbf{(2.36)}$$

$$\overline{Net: CO + 2O_2 \rightarrow CO_2 + O_3} \quad \textbf{(2.37)}$$

The major sink of tropospheric ozone arises from reactions with HO_2 and OH, and dry deposition. The effect of net reaction **(2.37)** is creation of the greenhouses gases CO_2 and O_3.

Fossil fuel combustion and biomass burning are major sources of CO; its major sink is tropospheric oxidation by OH [Jacob, 1999]. CH_4's major sink is oxidation by OH and its major sources are wetlands, natural gas, livestock and rice paddies. CH_4 is of particular interest due to its long lifetime (~12 years) and large global-warming potential (23 times more effective than CO_2) [IPCC, 2013].

The primary source of stratospheric NO_x, which can deplete stratospheric ozone, is N_2O. Because it is very stable (~112 year lifetime) and is generally unreactive in the troposphere, it eventually gets transported to the stratosphere where the majority is converted to N_2 + O via photolysis. N_2O is a strong greenhouse gas that is emitted from the Earth's oceans, soils, incomplete combustion and agriculture. Thus N_2O acts as a carrier of reactive nitrogen to the stratosphere and, given its increasing anthropogenic emissions [IPCC, 2013], is of particular interest.

3. THE EXTENDED-RANGE ATMOSPHERIC EMITTED RADIANCE INTERFEROMETER

Precise, accurate, and well-calibrated instruments are the cornerstone of science. For hundreds of years, instrumentation has served as one of the greatest tools to discern the falsifiability of a scientific theory. Yet with exponential increases in technology come increasingly intricate and complicated scientific instruments that require increasingly stringent and detailed operation and validation. In order to determine the extent of the changing climate, one must utilize a suite of reliable scientific instruments capable of measuring different properties of the atmosphere to a high degree of accuracy over a continuous, long period of time. As the demand for these types of measurements has risen, so has the implementation of new, state-of-the-art, prototype instruments (and their successors) that measure specific aspects of the changing climate to an unprecedented level of accuracy and reliability.

Portions of this Chapter have been published in Mariani et al. (2012a, 2012b, and 2013).

3.1 Measurement site: Eureka, Nunavut

CANDAC has equipped PEARL at Eureka, Nunavut (80ºN, 86ºW) for measurements during International Polar Year (IPY, project 196) and beyond. Eureka is isolated and remote (there is no town within hundreds of km) and is only populated by eight staff members from Environment Canada's Eureka Weather Station.

There are two additional laboratories at Eureka besides the PEARL Ridge Lab (at 610 m a.s.l.): 0PAL located at 10 m above sea level near Environment Canada's Eureka Weather Station (15 km away from the PEARL Ridge Lab), and the Surface and Atmospheric Flux, Irradiance and Radiation Extension (SAFIRE), located two km from the Weather Station. There are over two dozen instruments installed at these three laboratories that measure a variety of atmospheric properties, and additional meteorological measurements are taken at Environment Canada's Eureka Weather Station [Fogal *et al.*, 2013].

The E-AERI was installed in October 2008 and acquired one full year of measurements at the PEARL Ridge Lab. In September 2009, the E-AERI was moved to 0PAL, where it has remained. The geography surrounding the two measurement sites is seen in Figure 3.1. Measurements of downwelling radiance from an altitude of 10 m continue to be taken at 0PAL to determine concentrations of trace gases and investigate IR cooling in the 20 μm region.

Figure 3.1: Satellite composite image of Eureka on Ellesmere Island (insert: highlighted in red, black diamond is Eureka), Nunavut, Canada in the early summer. Right photos are of the PEARL Ridge Lab (top, photo: Paul Loewen) and 0PAL (bottom, photo: Zen Mariani) in winter. The PEARL Ridge Lab and 0PAL are separated by 15 km and their locations are indicated on the left image. Left image: © 2013 Google, © 2013 TerraMetrics. Left insert: © 2013 Wikipedia.

3.2 Description of the E-AERI

3.2.1 Generations of AERI Instruments

AERI instruments were developed at the University of Wisconsin Space Science and Engineering Centre (UW-SSEC) from 1989 to 1998 using an MR100 spectroradiometer developed from an MB-120 interferometer designed for industrial applications by ABB Bomem Inc. of Quebec, Canada [Collard *et al.*, 1995]. A suite of AERI instruments was then developed for the ARM program [DOE, 1990] Climate Research Facility sites in the Southern Great Plains (Oklahoma), the North Slope of Alaska, and the Tropical Western Pacific [Stokes and Schwartz, 1994, Knuteson *et al.*, 2004a]. In addition to the downwelling radiance measurements, measurements of the atmospheric state (e.g., radiosonde profiles) are made at these sites, allowing for radiance simulations [Ellingson and Wiscombe, 1996]. These AERI systems have collected over a decade of data at the ARM sites and have been used to generate climatologies in downwelling IR radiance [Turner and Gero, 2011] and to investigate long-term trends [Gero and Turner, 2011]. In addition to the ARM AERIs, other AERI instruments include the Marine AERI (M-AERI) [Minnett *et al.*, 2001], the University of Denver's high-resolution AERI-X deployed at the PEARL Ridge Lab from 1994-2002 [Olson *et al.*, 1996], and the University of Idaho's Polar AERI (P-AERI) [Walden *et al.*, 2005, Rowe *et al.*, 2008]. The current network of AERI systems deployed around the globe is illustrated in Figure 3.2.

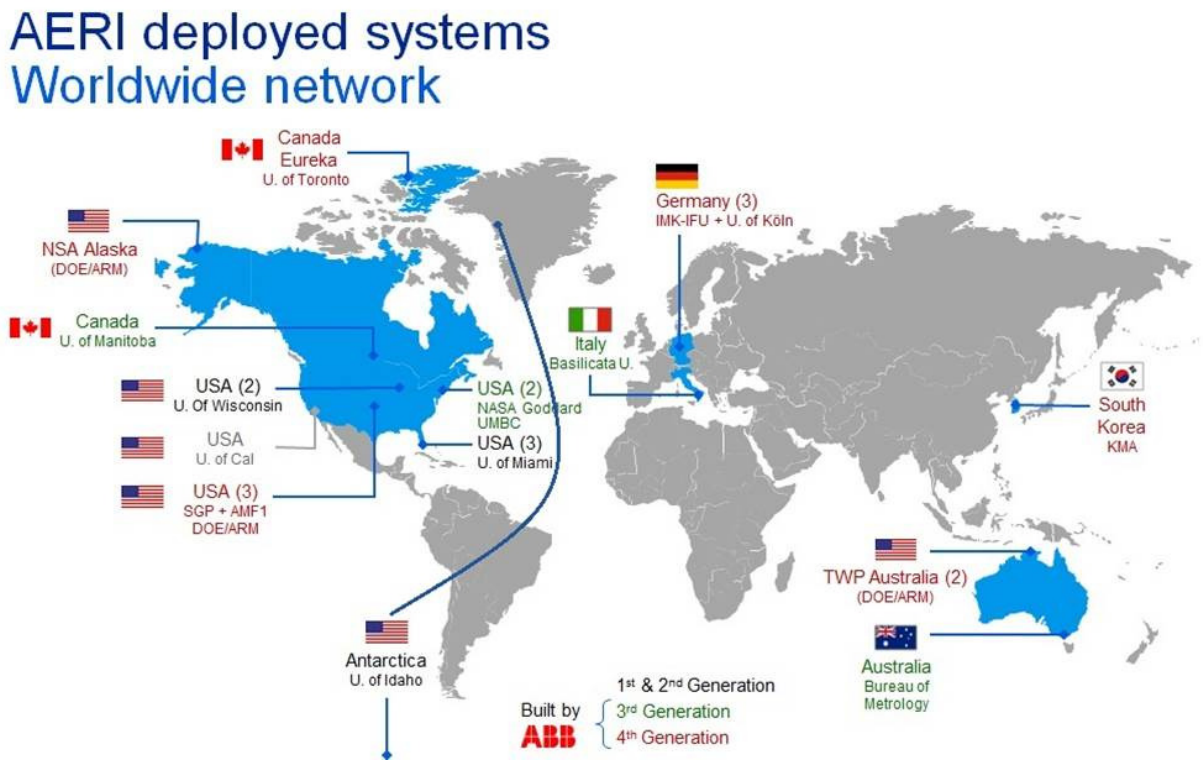

Figure 3.2: Location, affiliation, and generation of all AERI systems deployed across the globe as of September 2012. Regions in blue have permanent AERI installations (Original image: ABB; modified by Zen Mariani).

The newest (4th) generation AERI (e.g., the E-AERI installed at PEARL) was developed by ABB under commercial license from UW-SSEC. These AERIs incorporate the newest generation of ABB Bomem's FTIR spectroradiometer, a UW-SSEC blackbody cavity, the latest signal conditioning units, and a new detector/Stirling cooler with an extended lifetime (compared to its predecessor). The new AERI configuration allows in-field replacement of the Stirling cooler and metrology laser. The software has been updated with a combination of ABB software for data acquisition and instrument communication/control interface, and UW-SSEC software for post-processing and atmospheric science functions to ease future evolution of hardware and software by each party. The new AERIs also include front-end and back-end enclosures that protect against atmospheric precipitation and temperature variation, respectively. In addition to these modifications, the E-AERI extends the spectral coverage range of a standard AERI (520-3000 cm^{-1}) to 400-3000 cm^{-1}. The spectral range of the E-AERI covers the so-called "dirty window" (around 400 cm^{-1}, or 25 μm), where much of the IR cooling currently occurs in the dry air of the Arctic.

The emitted thermal radiance measured by the E-AERI is primarily dependent on the water vapour content and temperature of the atmosphere in cloud-free scenes. Therefore, temperature and humidity profiles of the planetary boundary layer can be retrieved from AERI and E-AERI spectra, as demonstrated in Feltz *et al.* [1998], Smith *et al.* [1999], and Turner *et al.* [2000]. This allows for high-temporal-resolution records and analyses of temperature and water vapour changes due to mesoscale meteorological features. The sampling interval of approximately seven minutes allows the study of short-term meteorological phenomena in the lower atmosphere, e.g., inversion developments, cloud effects, and front passages.

3.2.2 Instrument Design

The E-AERI measures radiance by the use of a FTS, calibrated with two blackbodies. It is composed of three distinct parts: the front-end (housing the input optics), the back-end (housing the electronic modules and interferometer), and the computer (standard off-the-shelf laptop). The front-end optics consists of two blackbodies and the scene mirror. The scene mirror has a gold reflecting surface and is mounted at 45° to the motor rotation axis, which is in turn positioned coincident with the interferometer input optical axis. This configuration allows different views: nadir, zenith (sky), Ambient Blackbody (AB) and Hot Blackbody (HB). Steady air flow is provided by a fan within the front-end enclosure to push dust and dirt particles away from the scene mirror. Seasonal cleaning of the scene mirror is performed by on-site operators to remove any accumulated dust and dirt, maintaining the mirror's reflectivity. The scene mirror directs IR radiation through an IR-transmitting optical window into the interferometer at the back-end portion of the instrument. Temperature, pressure, relative humidity, and rain/Sun sensors are also monitored to obtain complete knowledge of the measurement conditions.

The interferometer is an MR-300 series FTS that measures a double-sided interferogram, installed in the back-end portion of the instrument. The maximum OPD is 1 cm, providing a spectral resolution of 1 cm^{-1}. Two IR-detecting channels are supported by an extended-range photoconductive mercury cadmium telluride (MCT) detector coupled with a photovoltaic indium antimonide (InSb) detector mounted in a sandwich configuration. The detectors are housed in a dewar and cooled below 70 K by a linear Stirling-cycle cryo-cooler. Electronic modules (signal conditioning electronics, blackbody temperature controller, and Stirling cooler

support electronics) are mounted in the back-end. The temperatures of the back-end components are kept stable through a temperature control unit.

The instrument is designed to be configured as stand-alone or mounted thru-wall. An enclosure protects the instrument against Sun, rain, snow, wind, sand, etc. Currently, the instrument is removed from its mobile base for thru-wall installation and is fixed on a mounting platform. The photographs in Figure 3.3 were taken after the E-AERI was installed using the thru-wall configuration in a penthouse on the roof of the PEARL Ridge Lab. The front-end is outside the building, detached from the back-end and sealed to the external wall (see arrow in left side of Figure 3.3), while the back-end is inside the building (right side of Figure 3.3). A schematic of the E-AERI illustrates the instrument's thru-wall configuration and several key components in Figure 3.4.

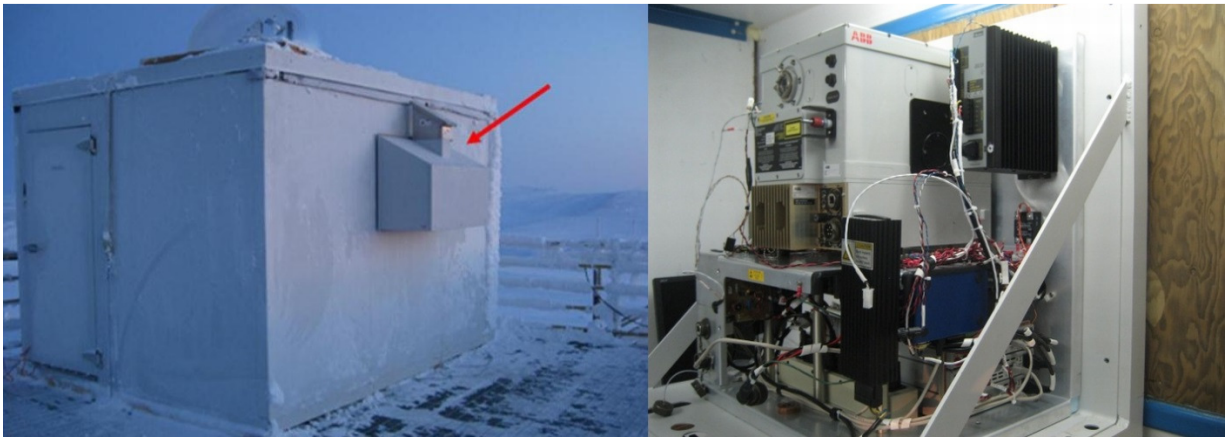

Figure 3.3: Exterior [left, red arrow] and interior [right] views of the E-AERI installed on the roof of the PEARL Ridge Lab using the thru-wall configuration. [Left]: Front-end portion of the E-AERI instrument housing the optics; the hatch is closed during precipitation events (photo: Stephane Lantagne). [Right]: The back-end portion of the E-AERI instrument with its internal protective enclosure temporarily removed to show the MR-300 series interferometer housing and electronic modules (photo: Zen Mariani).

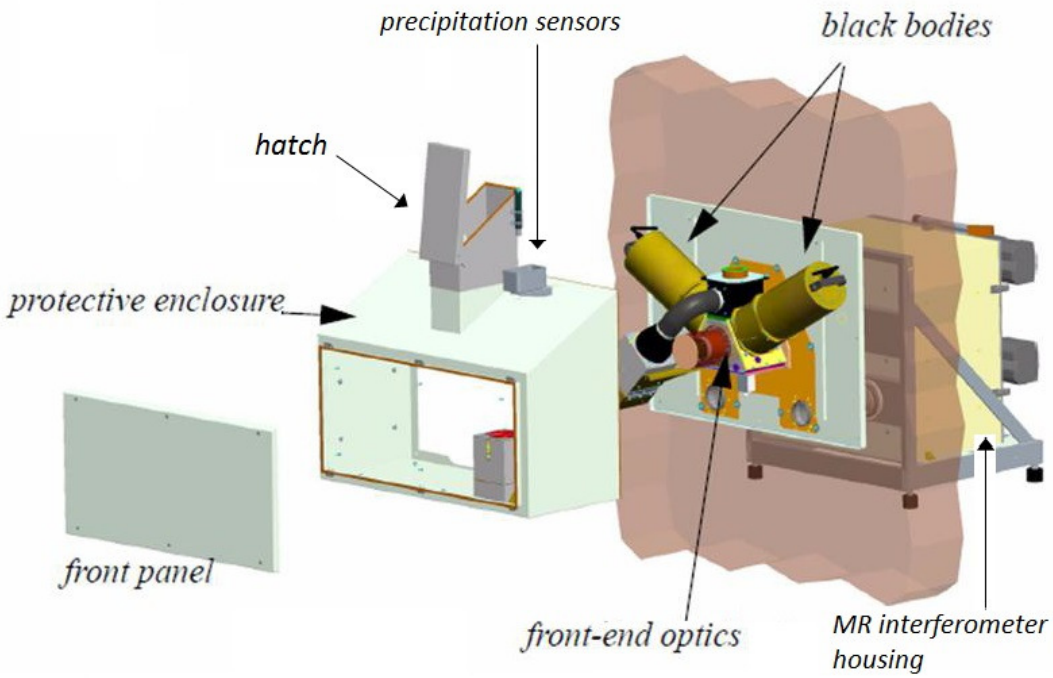

Figure 3.4: Thru-wall configuration of the E-AERI used at PEARL and 0PAL. Original schematic: ABB (modified by Zen Mariani).

The electronics and the FTS contained within the back-end enclosure (shown opened in Figure 3.3) can operate between -30°C and +40°C. A temperature control unit maintains it at a constant temperature. The front-end enclosure protects against precipitation (both rain and snow) but is not stabilized in temperature; it is free running near the ambient temperature. Two Vaisala DRD11A precipitation sensors (one elevated and one flush with the enclosure) detect any precipitation occurring. A hatch, actuated by the precipitation sensors or directly by the user or instrument commanding script, can be closed to protect the input optics, or opened to look at the atmosphere (these components are labelled in Figure 3.4). In the presence of precipitation, the system will automatically close the hatch and turn itself off in a self-protection mode that does not allow sky measurement. After the precipitation ends, the system returns to normal acquisition mode. Temperature, pressure, relative humidity, and Sun sensors are also monitored in the enclosure to obtain knowledge of the measurement conditions.

3.2.3 Instrument Measurements

One measurement cycle includes a zenith-sky measurement as well as calibration measurements of the blackbodies to ensure accurately calibrated zenith-sky spectra. Measurements are independent of sunlight or moonlight and are only interrupted during precipitation events to prevent damage of the optics. The E-AERI is designed to operate on two different repeating scene-mirror schedules in which the downwelling IR radiation is bracketed by views of the reference blackbodies. Rapid sampling mode is used in order to follow very short-term changes due to variable cloud-cover. In this mode, the E-AERI scene mirror pivots such that the instrument looks at the HB, AB, and then Sky View (SV) in the following order: HB AB SV SV SV SV SV SV SV SV AB HB. This is useful for quick measurements of the sky to detect changes in frontal passages. However, in the time between blackbody measurements, the ambient and instrument temperatures can drift during the calibration period, resulting in mis-calibrated spectra [Knuteson *et al.*, 2004b]. For this reason, the E-AERI is usually operated in slow sampling mode, following the pattern: HB AB SV AB HB. This method sandwiches each SV measurement between blackbody measurements, improving the calibration of the spectra.

The instrument performs two Michelson mirror sweeps (forward and backward) for each spectrum. Co-adding spectra for the blackbodies takes about two minutes each, and for the sky view it takes about three minutes, such that 127 co-adds are performed for each blackbody measurement and 248 co-adds are performed for each SV measurement. Co-adding spectra is a common technique employed to increase the SNR by adding successive spectra to create the mean spectra corresponding to an individual sky dwell period [Knuteson *et al.*, 2004b]. Spectral information will add up faster than the noise, allowing an increase in the SNR by a factor of $\sqrt{n}$, where n = number of co-adds.

The standard E-AERI data product consists of calibrated downwelling radiance spectra from the two detectors: 400-1800 (MCT) and 1800-3000 cm^{-1} (InSb). Combined, these form a continuous spectrum from 400-3000 cm^{-1}. Two data description files and one summary file contain measurement time, instrument parameter metrics, mean radiance, imaginary radiance, corrective offset, responsivity, brightness temperature (sometimes referred to as radiance temperature), blackbody temperature drift, and scene Noise Equivalent Spectral Radiance (NESR) from each detector for each seven-minute sampling interval. The radiance data are automatically processed using instrument-related corrections such as those described in

Knuteson *et al.* [2004b], resulting in calibrated radiances with a standardized spectral scale in real time.

3.2.4 Comparisons to Other Ground-based Emission Spectrometers

The E-AERI has been designed to record emission measurements over a broad region of the IR spectrum that includes atmospheric trace gas emission lines and the so-called 'dirty window' around 400 cm^{-1} where much of the near-surface IR cooling to space occurs in the Arctic (this spectral region becomes more transparent due to the extremely cold and dry Arctic atmosphere) [Clough *et al.*, 1992; Tobin *et al.*, 1999]. Other ground-based emission spectrometers are used to study near-IR the emission spectroscopy of distant stars [e.g., Waldmann *et al.*, 2012] or are designed to measure different atmospheric trace gases (for instance, millimeter-wave radiometers (MWRs) such as the Kiruna millimeter-wave radiometer (KIMRA) [Raffalski *et al.*, 2005]). Aside from the spectral region measured, MWRs differ from the E-AERI in that they require their detectors to be cooled to significantly lower temperatures (< 35 K) than the E-AERI (< 70 K) in order to detect the faint millimeter-wave emission lines. MWRs typically measure weaker emission signals but have higher spectral resolution than the E-AERI. The E-AERI is also zenith-viewing, permitting measurements directly above the site's location, whereas many emission spectrometers (including some MWRs and older generations of the AERI system) use a slant path to increase the emission signal. The E-AERI software system performs all necessary data calibration and quality control in real-time and, like most MWRs, is fully automated and can be controlled remotely.

Emission spectrometers can be deployed off the ground and utilize different viewing geometries. For instance, the Michelson Interferometer for Passive Atmospheric Sounding (MIPAS) instrument on Envisat and its balloon-borne version (MIPAS-B) measure vertical profiles of trace gases using IR limb-emission sounding [Fischer and Oelhaf, 1996]. The Spectroscopy of the Atmosphere using Far InfraRed Emission - Airborne (SAFIRE-A) operates in the far-IR spectral region, making limb sounding observations of atmospheric emission from high-altitude aircraft [Bianchini *et al.*, 2003]. The Scanning Infrared Gas Imaging System (SIGIS) is a ground-based thermal emission IR spectrometer that measures volcanic SO_2 and SiF_4. To do this, SIGIS (and other instruments that measure volcanic emissions) uses the radiation of the volcanic gas itself, allowing for continuous monitoring day and night of the

volcanic plume [Stremme *et al.*, 2012 and references therein]. Compared to the E-AERI, some other ground-based IR emission spectrometers used in the past, such as the Bruker IFS-120M and the Radiation Explorer in the Far InfraRed-Prototype for Applications in Development (REFIR-PAD) [Becker and Notholt, 1997; Bianchini *et al.*, 2010], have had a narrower spectral range but greater spectral resolution. For all these instruments, the spectra are calibrated using one or more blackbodies. Where one blackbody is used (such as with MIPAS-B), the instrument views cold space as the cold source and the blackbody as the hot source. Since the E-AERI cannot view cold space from the ground, it uses two blackbodies (ambient and hot) for its calibration.

3.2.5 The Combined Eureka AERI Dataset

The installation of the E-AERI at PEARL was preceded by a similar AERI, which was deployed at 0PAL from March 2006 to June 2009 (and was subsequently deployed in Summit, Greenland). The University of Idaho's Polar Atmospheric Emitted Radiance Interferometer (P-AERI) was deployed at 0PAL from March 2006 to June 2009. The two instruments are similar, but the P-AERI does not provide spectral coverage below 500 cm^{-1}. Thus from October 2008 to June 2009 there were two AERI instruments operating at Eureka at two altitudes. P-AERI measurements were recently used to identify significant differences in downwelling fluxes between Barrow and Eureka [Cox *et al.*, 2012]. There were only two data gaps during this measurement period (occurring in June 2007 and April/May 2008), resulting in good temporal coverage from 2006-2009. The P-AERI is an older, 2nd generation AERI instrument with a spectral range of ~500 to 3000 cm^{-1} (3.3 to 20 μm); however, careful analysis of calibration accuracy indicates that although noise begins to increase rapidly below 500 cm^{-1}, P-AERI spectra are well calibrated down to 494 cm^{-1} [Rowe *et al.*, 2011a, 2011b] and therefore the spectral region from 494 to 500 cm^{-1} can be used as long as spectral and/or temporal averaging is performed to reduce the noise. The instrument has been deployed on numerous field campaigns at different remote sites and extensively characterized, and its data has undergone quality control [Walden *et al.*, 2005; Town *et al.*, 2005, 2007; Rowe *et al.*, 2008, 2011a, 2011b].

The radiometric calibration absolute accuracy is < 1% of the ambient blackbody radiance for both AERIs [Knuteson *et al.*, 2004b]. Thus it is possible to determine whether the instrument's noise level or sensitivity has changed significantly over time; both instruments'

noise-equivalent radiances were relatively constant over their respective measurement periods, indicating consistency throughout the dataset. The usefulness of this approach with respect to combining measurements from different AERIs for a single long-term dataset is discussed in more detail in Turner and Gero [2011]. Coincident E-AERI and P-AERI radiances are discussed in Sect. 4.1 of this thesis; measured radiances agreed within noise and indicated consistency between the two instruments.

The P-AERI operates in rapid sampling mode, which produces calibrated spectra every ~40 s. Since the E-AERI operates in a slower sampling mode (every ~7 minutes), the P-AERI spectra were averaged within each simultaneous E-AERI measurement to match the temporal resolution of the E-AERI, which matches the approach used to produce the Southern Great Plains (SGP) climatology in Turner and Gero [2011]. Thus we can combine the two AERI datasets into a single eight-year (and continuing) Eureka AERI dataset that consists of over 250,000 quality-controlled 7-minute-averaged spectra starting in March 2006 with the P-AERI and extending to August 2013 (in this work) with the E-AERI, as illustrated in Figure 3.5. A detailed description and time series of E-AERI issues are provided in the Appendix and are useful for future AERI users as a reference for troubleshooting AERI issues and a guide for other new 4th-generation AERI systems.

The gaps in the dataset are discussed in the Appendix; as a result of these measurement gaps, the E-AERI dataset is not as evenly distributed as the P-AERI: 51%, 31%, and 18% of P-AERI measurements occurred during winter, summer, and fall/spring, respectively, whereas 60%, 24%, and 16% of E-AERI measurements occurred during these same periods. Seasons are defined (see Sect. 5.3) so that winter, summer, and fall/spring take up 58%, 25%, and 17% of the year.

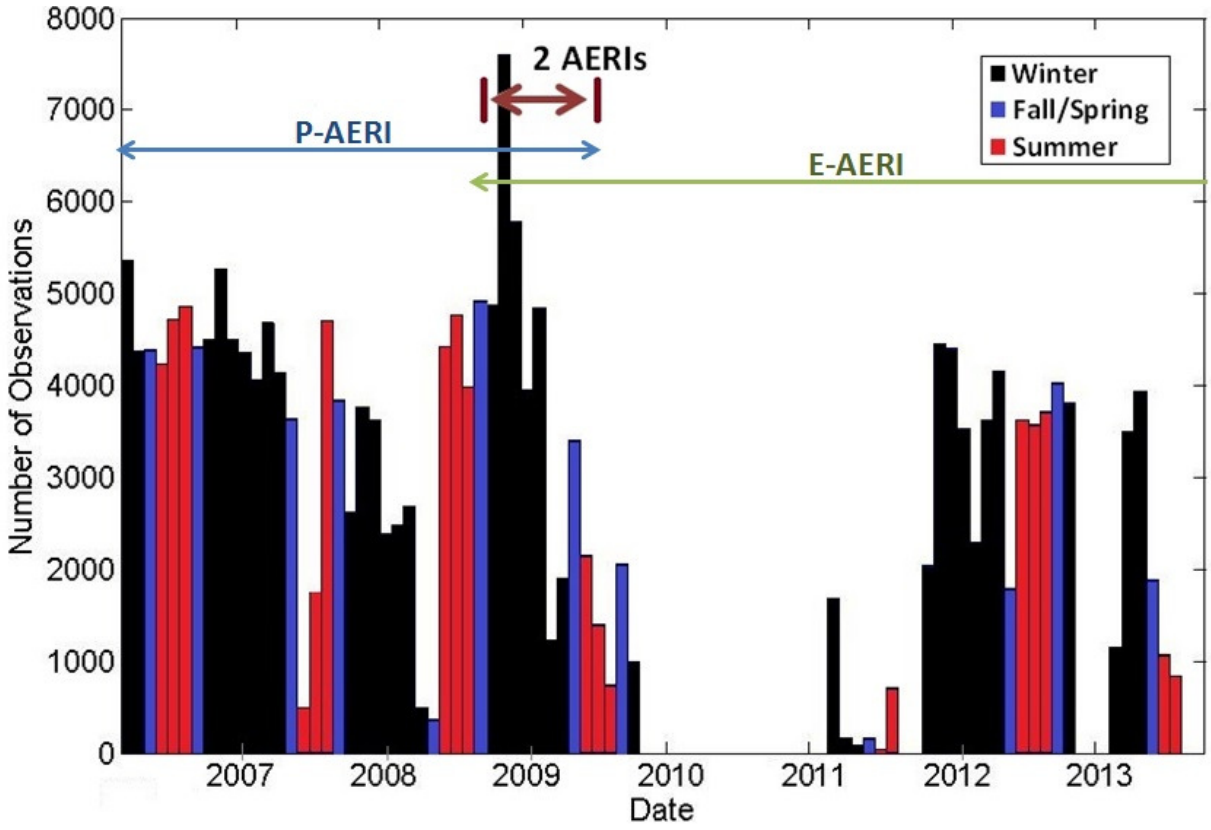

Figure 3.5: Number of AERI observations for each month in the combined Eureka AERI dataset ending August 2013. Bars are coloured black for winter (October – April), blue for fall/spring (May and September), and red for summer (June – August) months. The overlap period where two AERIs operated at two altitudes is indicated in the region with arrows. Gaps exist due to instrument repair or maintenance, as outlined in Table A.1.

3.3 Blackbody Calibration

Measurements of the emission from the two blackbodies are used to calibrate the sky-view measurement. The two calibration blackbodies are of identical construction, each consisting of a thermally isolated cavity that is painted with a high-emissivity diffuse black paint. The emissivity of both blackbodies is > 0.999 $\pm$ 0.1%. Each cavity contains a heater, a feedback thermistor and three thermistor sensors. Each blackbody's temperature can be set using the instrument's software. For operation at PEARL, the HB is set at 310 K and the AB operates at the outside temperature.

The E-AERI calibration methodology uses a pair of HB/AB views bracketing the SV measurements. The blackbody temperatures are fit to a linear function of time to account for changes in the instrument temperature during a calibration sequence. Similarly, a linear interpolation to the centre of the SV time is performed for each HB and AB measurement. The approach shown here for radiometric calibration of the E-AERI system is based on that of Revercomb *et al.* [1988]. Using the Planck Function (Eqn. **(2.1)**), the HB and AB radiance at temperature *T* can be calculated:

$$B_{\tilde{\nu}}^{H} = \epsilon_{\tilde{\nu}}^{H} B_{\tilde{\nu}}(T^{H}) + (1 - \epsilon_{\tilde{\nu}}^{H}) B_{\tilde{\nu}}(T^{R}) \quad \textbf{(3.1)}$$

$$B_{\tilde{\nu}}^{A} = \epsilon_{\tilde{\nu}}^{A} B_{\tilde{\nu}}(T^{A}) + (1 - \epsilon_{\tilde{\nu}}^{A}) B_{\tilde{\nu}}(T^{R}) \quad \textbf{(3.2)}$$

where H = Hot blackbody, A = Ambient blackbody, $B_{\tilde{\nu}}{}^{x}$ = calculated Planck function radiance for the HB/AB, $\epsilon_{\tilde{\nu}}^{x}$ = emissivity spectra for HB/AB, $B_{\tilde{\nu}}(T^{x})$ = Planck function radiance at observed temperature T^{x}, and T^{R} = reflected temperature (radiative temperature of the environment that enters the blackbody cavity). T^{R} is estimated using the blackbody support structure temperature.

Using Eqns. **(3.1)** and **(3.2)**, the calibrated radiance, $N_{\tilde{\nu}}$, at wavenumber $\tilde{\nu}$ can be found:

$$N_{\tilde{\nu}} = \left(B_{\tilde{\nu}}^{H} - B_{\tilde{\nu}}^{A}\right) R_{E} \left[\frac{(S_{\tilde{\nu}}^{S} - S_{\tilde{\nu}}^{A})}{(S_{\tilde{\nu}}^{H} - S_{\tilde{\nu}}^{A})}\right] + B_{\tilde{\nu}}^{A} \quad \textbf{(3.3)}$$

where R_E = real part of the complex argument, $S_{\tilde{\nu}}^{S}$ = scene view of the sky (zenith-viewing), $S_{\tilde{\nu}}^{A}$ = scene view of the AB (when radiation from the blackbody is directed into the spectrometer), and $S_{\tilde{\nu}}^{H}$ = scene view of the HB. Because of the complex exponential in the definition of the Fourier transform, the spectra will have both real and imaginary parts. The imaginary part of the complex argument (not shown in Eqn. **(3.3)**) is zero within the instrument noise [Knuteson *et al.*, 2004b]. Calibrated radiances for each sweep direction (forward and backward Michelson mirror sweeps) are averaged, creating the mean calibrated radiance for each SV period. Details of the instrument's operating software, which permits fully-automated measurements to take place, are described in the Appendix.

3.4 Certification Procedure

To validate its performance, the entire E-AERI underwent calibration and certification testing according to UW-SSEC standards and procedures. The E-AERI has undergone certification tests three times: one initial certification test after the instrument was constructed took place in September 2008 at UW-SSEC, and two calibration and acceptance tests performed on-site at Eureka by Guillaume Gamache (ABB) and me in February 2011 and again in November 2011 to ensure instrument performance stability and measurement reliability. All three times, the E-AERI has successfully passed UW-SSEC certification standards, with the exception of performing a side-by-side clear-sky comparison the latter two times with an additional AERI (since no additional AERI was available at Eureka). The certification procedure is labour-intensive, requiring several days' worth of measurements, complete disassembly/reassembly of the instrument (in order to access certain ports, etc.), and additional equipment (a third BB, mapping equipment, etc.) from UW-SSEC. All test results are recorded and sent to UW-SSEC personnel for inspection and approval. The general certification procedure for a 4th generation AERI instrument is:

a) Disassemble E-AERI from thru-wall configuration and reassemble as stand-alone.
b) NESR measurement: described below.
c) Nonlinearity test: described below.
d) Radiometric calibration verification test: described below.
e) Resistance test: use 2 external resistance boxes (from UW-SSEC) to test the E-AERI's multimeters and other electronic equipment to ensure reliable electronics using certification software from ABB.
f) Spectral stability test: described below.
g) Wavenumber calibration: use ABB certification software to find an effective laser wavenumber value for the HeNe laser that provides the best spectral match for regions of regular spectral lines.
h) Disassemble E-AERI as stand-alone configuration and re-assemble as thru-wall.
i) FOV mapping: Use a pinhole white light and map instrument's signal using Excel software from ABB (described in more detail below).
j) Submit results to UW-SSEC for inspection.

The performance characteristics of the E-AERI are summarized in Table 3.1. Items with a '*' indicate performance metrics verified during calibration at UW-SSEC. Initial measurements of the NESR were performed in Quebec City (before shipping to Eureka) and again at Eureka immediately after its arrival in October 2008. The root-mean-square (RMS) of the variation in the calibrated radiances from 284 spectra of the HB determines the NESR. NESR measurements taken at Eureka are shown in Figure 3.6. The observed increase in noise at 667 cm^{-1} and from 2300-2400 cm^{-1} is due to CO_2 absorption inside the instrument, which reduces responsivity. For both the long wavelength (LW; MCT) and short wavelength (SW; InSb) bands, the NESR is well below the specified requirement; about one-half and one-third of the specification for the LW and SW, respectively. One exception is in the region around 400 cm^{-1}; the new detector installed in November 2011 decreased the noise in this region to below the specified requirement, as shown in Figure 3.7. Additional information about the certification procedure and results is available at: https://groups.ssec.wisc.edu/groups/aeri/cal-vals/e-aeri-001/nov-2011-post-repair-acceptance-testing/aeri-101-nov.-2011-post-repair-acceptance-testing.

Table 3.1: E-AERI instrument performance. Items with a '*' indicate performance metrics verified during calibration at UW-SSEC in September 2008.

Item	Performance
General System Elements	• ABB Bomem MR-300 Michelson interferometer with PC computer interface • Full-aperture temperature-controlled calibration reference sources • Automated system for providing sequential views of the sky (zenith) and two blackbodies (one at ambient temperature, one at 37°C) for radiometric calibration • Environmental Monitoring System, for blackbody temperature data • Computer and Data Handling System, for sequencing all E-AERI operations and data handling, including acquisition, processing, display, and networking
*Spectral range	400-3000 cm^{-1} (3.3-25 μm)
*Spectral resolution	1.0 cm^{-1}, unapodized maximum optical path difference [OPD] of 1 cm
*Spectral line stability	< 10 ppm change in the 1918 cm^{-1} water line concentration
*Spatial and angular FOV	46 ± 1 mrad full angle
*Radiometric calibration absolute accuracy	< 1% of ambient blackbody radiance
*Reproducibility	< 0.2% of ambient blackbody radiance
*Blackbody cavity characterization	• Temperature Knowledge: ± 0.1°C of absolute temperature • Emissivity knowledge: better than ± 0.1% • Temperature stability: better than 0.05°C over viewing period (» 120 s)
*Nonlinearity knowledge	Better than 0.1%
*Polarization	Scene mirror imposes < 0.1% polarization on incident unpolarized radiation
*Wavelength calibration	Channel wavenumber knowledge: better than 0.01 cm^{-1}
*Noise (RMS for 2-min blackbody view)	<0.4 mW $(m^2\ sr\ cm^{-1})^{-1}$ for 420-1400 cm^{-1} (except 667 cm^{-1}, where CO_2 in the instrument reduces responsivity) <0.015 mW $(m^2\ sr\ cm^{-1})^{-1}$ for 2000-2600 cm^{-1} (except 2300-2400 cm^{-1}, where CO_2 in the instrument reduces responsivity)
Temporal sampling	Repeat cycle: ≈ 7 min Interferometer scan period: <2 s
Detectors	Two detectors are mounted in sandwich configuration covering two spectral regions: Channel one (400-1800 cm^{-1}): extended-range photoconductive mercury cadmium telluride (MCT) Channel two (1800-3000 cm^{-1}): photovoltaic indium antimonide (InSb)
Beamsplitter	Potassium bromide (KBr)
Operational requirement	Automatic control system hardware contains these features: • Scheduled sequencing of the following operations: – Scene switching between sky and blackbody views – Interferometer and housekeeping data acquisition and transfer • Capability of remotely changing the operation listed above • 24-hour continuous operations with data output at 7-min intervals • Linear stirling-cycle cryo-cooler keeps detectors cooled down below 70 K • Real-time display with flags for out-of-limit conditions
Operating environment	Operating temperature: • Spectroradiometer (back-end) enclosure: -30° to +40°C • Input and calibration (front-end) enclosure: -70° to +40°C
Data products	Primary (required for scientific use): • Calibrated spectra • Standard deviation for blackbody and sky views • Calibration coefficient and blackbody temperature Secondary (auxiliary information for real-time monitoring and quality control): • Ambient air temperature • Ambient pressure • Ambient humidity • Instrument housekeeping data

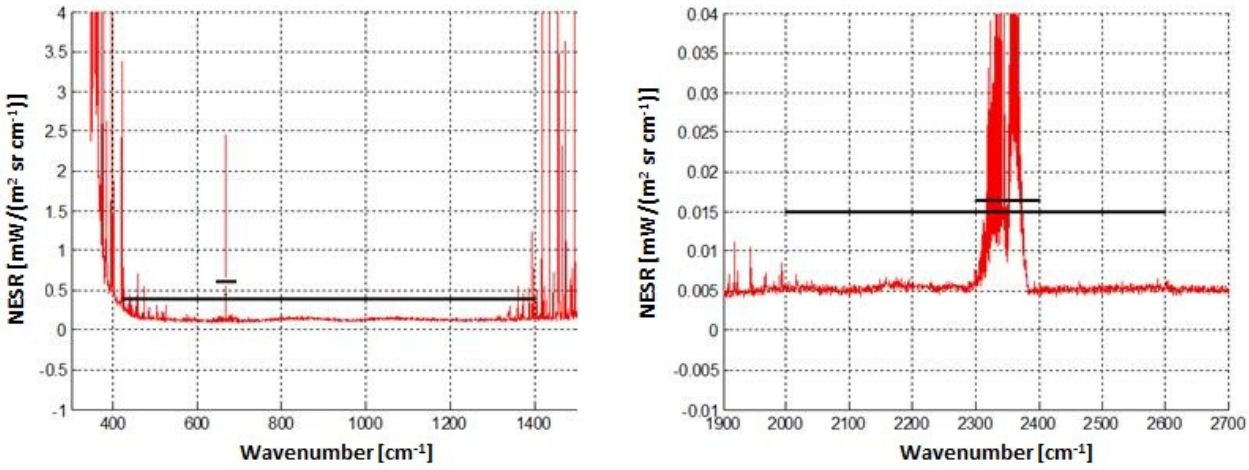

Figure 3.6: NESR test for the MCT [left] and InSb [right] detectors performed in October 2008 in Eureka. The solid black line indicates the specified requirement for the NESR test. The elevated black line indicates the spectral region where the NESR is expected to increase due to CO_2 in the instrument.

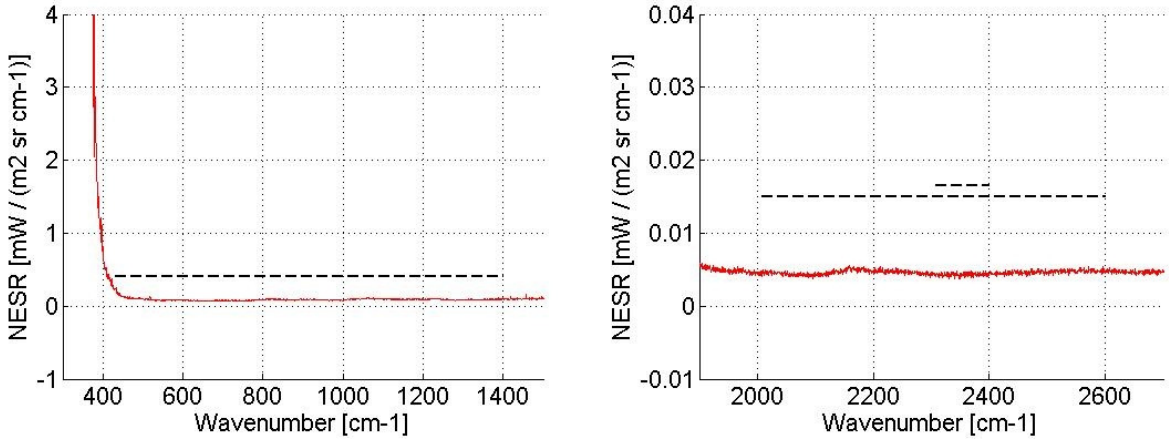

Figure 3.7: NESR test for the MCT [left] and InSb [right] detectors performed in November 2011 in Eureka. The dashed black line indicates the specified requirement for the NESR test.

A four-body nonlinearity test was performed using the AB, HB (set to 330 K for these tests), an intermediate blackbody (temperature between AB and HB, around 318 K), and an Ice-Blackbody (IB) at 273 K. The intermediate blackbody and IB are used as external reference sources to verify blackbody temperature knowledge. These external reference sources are calibrated using the same National Institute of Standards and Technology traceable approach as used for the other blackbodies. During the test period, the scene mirror views each blackbody to measure the blackbody temperatures over several hours to ensure stability and reduce the noise level. A nonlinear correction factor is then applied to the E-AERI BB calibration

Examples of the radiometric calibration verification test results are shown in Figure 3.8 for the intermediate body and IB. Water vapour has strong absorption between 1450 and 1800 cm^{-1} and CO_2 has strong absorption around 667 and 2380 cm^{-1}, resulting in the observed discrepancies in these regions. The IB measurement has an offset of 0.2 K; this is comparable to the error of $\pm$ 0.2 K for other AERI systems [Knuteson *et al*., 2004a]. This error can be due to incorrect placement of the ice-body (too far away or not exactly centred).

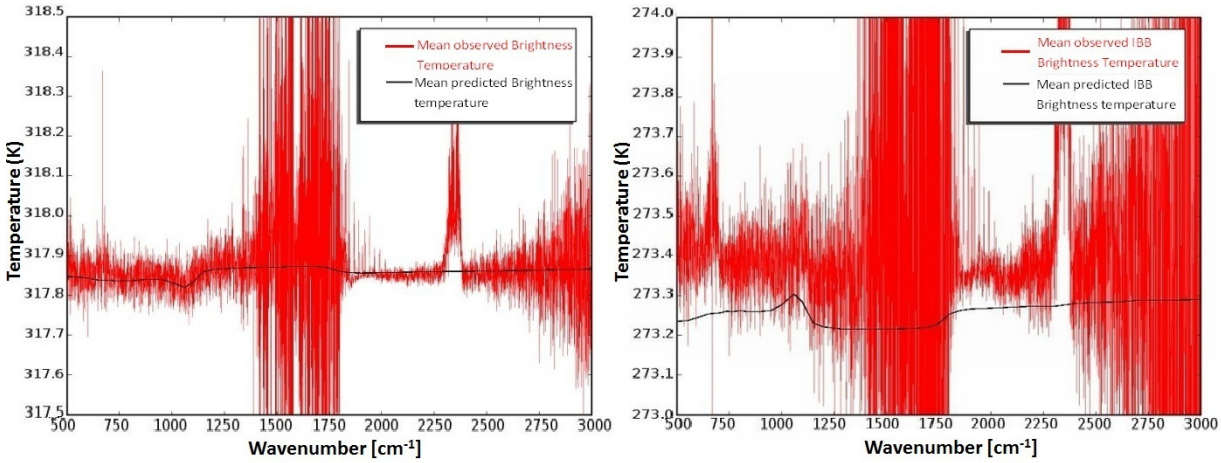

Figure 3.8: Laboratory radiometric calibration verification 'four-body' test results conducted at UW-SSEC on September 27, 2008 before deployment to Eureka. [Left]: Intermediate black-body brightness temperature spectrum. [Right]: IB brightness temperature spectrum. The measured spectrum (red) is the temporal-averaged calibrated radiance converted to equivalent blackbody brightness temperature. Note the y-axis range in both panels is 1 K. The black line indicates the predicted blackbody temperature.

A side-by-side comparison with two UW-SSEC AERI systems, the AERI-07 (with an extended-range detector) and the AERI-Bago (AERI-03), was performed as shown in Figure 3.9. These instruments have been employed in numerous measurement campaigns and are considered reliable benchmarks for measurement inter-comparison purposes [Knuteson *et al*., 2004a]. Results from these comparisons indicate that agreement between the E-AERI and the other two instruments is comparable to the agreement between the AERI-07 and AERI-Bago, as shown in Figure 3.10, verifying the accuracy of the E-AERI radiances [UW-SSEC, 2008].

Figure 3.9 Side-by-side comparisons of the E-AERI at UW-SSEC in September 2008 with two similar AERIs (Photo: UW-SSEC).

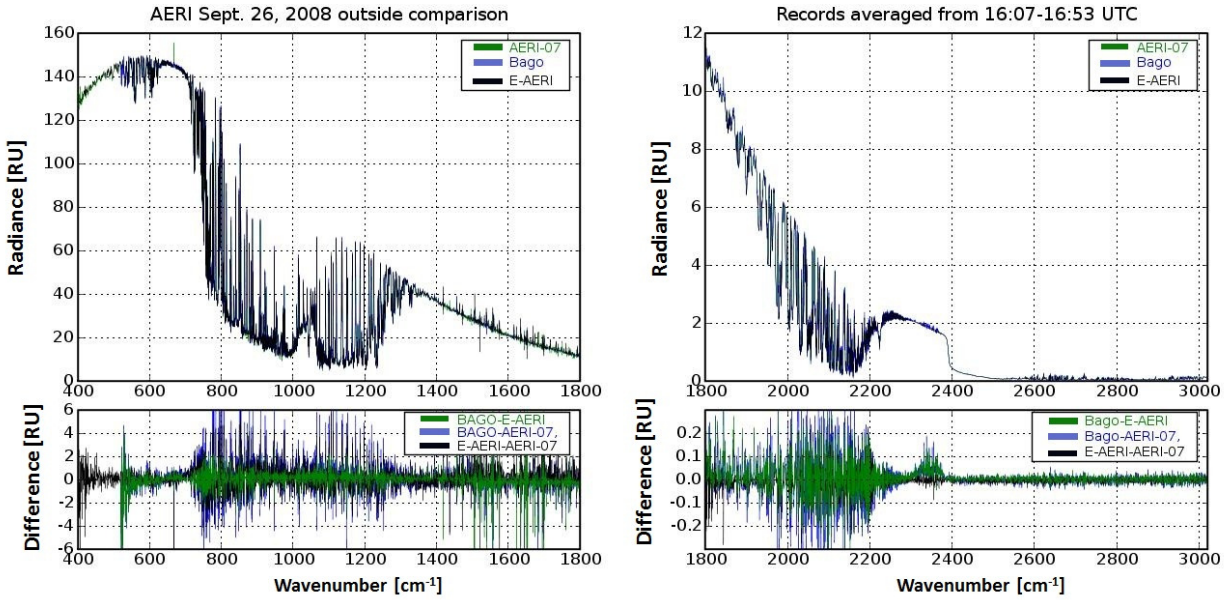

Figure 3.10: Radiance measurements during two outside side-by-side tests performed at UW-SSEC. Top panels display measured radiance (RU = mW/(m^2 sr cm^{-1})) with residuals in the bottom panels.

The instrument's FOV is carefully mapped using a pinhole light to correct for the small effects of instrument self-apodization on the Instrument Line Shape (ILS). The result is an 'ideal' sinc function ILS, which is described in more detail in Knuteson *et al.* [2004b] along with the correction methodology used on the spectra. Three FOV tests were performed on the zenith-sky, HB, and AB views and confirmed proper optical alignment of the source and reference blackbody cavities. Figure 3.11 illustrates the FOV mapping for the HB. All values on the periphery are zero, indicating that the FOV has a clear path to the HB. Similar results were obtained for the zenith-sky and AB tests. The wavenumber knowledge was found to be 0.0018 cm^{-1}, which is better than the 0.01 cm^{-1} requirement. A spectral line stability test was performed by tracking any shift in the peak of the 1918 cm^{-1} water line during the ambient blackbody measurements for 600 minutes. The spectral line stability meets the requirement of < 10 ppm, as shown in Figure 3.12.

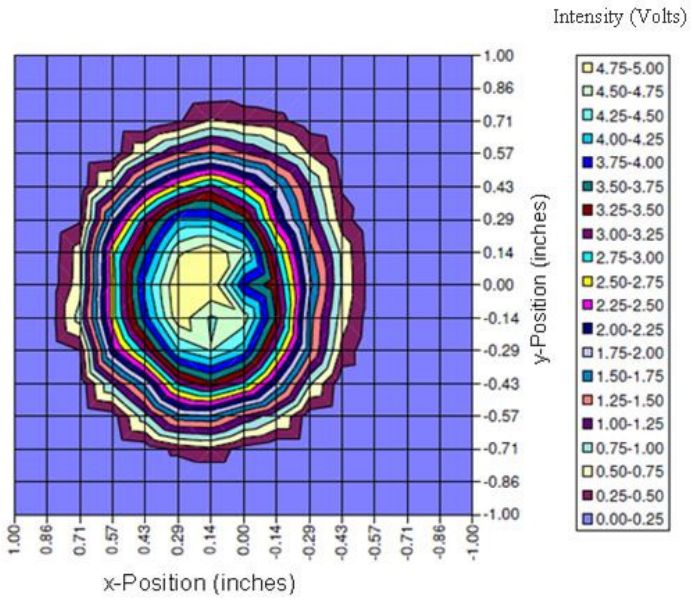

Figure 3.11: Typical radiometric FOV mapping of the aperture of the E-AERI HB. Values around the periphery are zero, verifying optical alignment. Similar results are obtained for the AB and zenith-sky FOV. This FOV test was conducted in September 2008 at UW-SSEC.

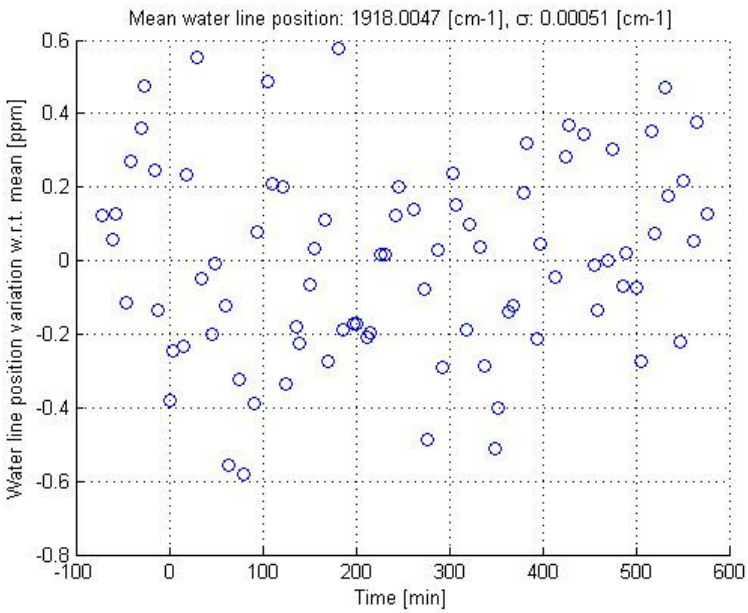

Figure 3.12: Spectral line stability test conducted February 19, 2011 during the E-AERI's second validation per UW-SSEC standards. The deviation of the 1918 cm^{-1} water line peak's position was tracked over 600 minutes to confirm the instrument's frequency stability.

3.5 Summary of the Extended-range Atmospheric Emitted Radiance Interferometer

This chapter outlined the details of the E-AERI instrument, as well as its predecessor at Eureka, the P-AERI. The University of Toronto was the first institution to receive the new 4th-generation AERI system, which at the time was a prototype. The history of the AERI instruments was outlined in this chapter, along with a description of the changes pertaining to the E-AERI's new design and performance characteristics. A description of the type of measurements the E-AERI makes, as well as a summary of the measured spectra's quality control, was presented. Combining the existing P-AERI dataset with the E-AERI was made possible after extensive characterization of both instruments and side-by-side comparisons (shown in next Chapter) ensured consistency between both AERI's measurements. Details of the BB calibration methodology, including the theoretical formulation for this calibration, and instrument certification procedure have been described in this chapter. The E-AERI's automated

measurements are an absolute necessity for this project when considering the remoteness of the measurement site, particularly post-2012 when CANDAC operators were no longer on-site at PEARL year-round. The UW-SSEC certification procedure, considered a benchmark for AERI performance standards and necessary for all AERI instruments to ensure measurement reliability and stability, was described in detail along with results from the three times the E-AERI underwent calibration and acceptance testing.

4. INITIAL MEASUREMENTS AND COMPARISONS

In order to optimize the precision and accuracy of scientific results, one must possess reliable, well-characterized, and validated tools to obtain the result. The use of a newly designed prototype interferometer can be a high-risk high-reward scenario: operating a new instrument with unpredictable difficulties in order to gather new scientific data. Since the E-AERI was untested in the field, validation was necessary to ensure the nominal scientific accuracy and precision of the instrument was correct. This was also important for the commercial success of this new 4th-generation AERI system. Fortunately a similar, older-generation AERI was already installed at Eureka, permitting side-by-side comparisons. Having two AERIs operating at two altitudes also provided an opportunity to investigate differences in the radiative budgets at these two altitudes at Eureka – something never done before in the Arctic.

Portions of this Chapter have been published in Mariani et al. (2012a).

4.1 Side-by-side Comparisons at Sea Level

Prior to its installation at the PEARL Ridge Lab, the E-AERI was operated side-by-side with the P-AERI at 0PAL for several days (Sept. 28 to Oct. 1, 2008). The P-AERI has been extensively characterized [Walden *et al*., 2005, Rowe *et al*., 2008] and the data at Eureka have been quality controlled [Rowe *et al*., 2011a,b]. The E-AERI was installed in a stand-alone configuration on the back of a truck parked directly outside the 0PAL container, placing the two AERIs side-by-side. This was the first field deployment of a 4th-generation AERI system. The two AERIs acquired continuous coincident measurements during this intercomparison period, providing an opportunity to compare the two instruments and evaluate the new E-AERI spectra.

Coincident E-AERI and P-AERI radiances recorded on October 20, 2008 are shown in Figure 4.1 for the P-AERI spectral range of 500 to 3000 cm^{-1}. Strong trace gas absorption can also cause large errors in calibrated sky spectra; these spectra are corrected as part of the post-processing as discussed in detail by Rowe *et al*. [2011b]. The radiances agree within $\pm$ 1 $mW/(m^2\ sr\ cm^{-1})$ for the MCT detector and $\pm$ 0.2 $mW/(m^2\ sr\ cm^{-1})$ for the InSb detector with the exception of the 1450-1800 cm^{-1} spectral region. These results are comparable to the AERI-07 and AERI-03 (Bago) comparisons with the E-AERI and are close to the magnitude of the NESR provided in Table 3.1.

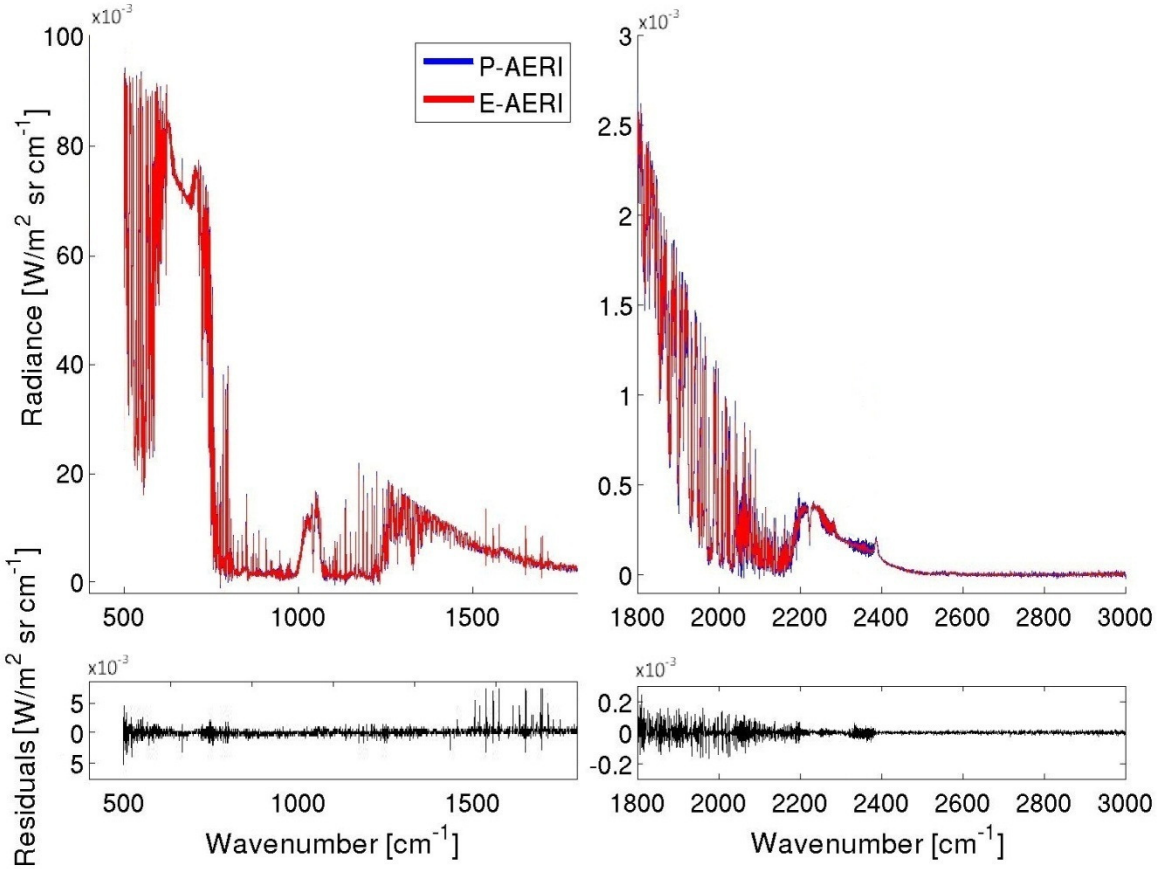

Figure 4.1: Side-by-side comparisons between the E-AERI (red) and P-AERI (blue) instruments within the P-AERI spectral range on October 20, 2008. Top panels display measured radiance with residuals in the bottom panels.

Larger emission lines are visible in the E-AERI (but not P-AERI) spectra in the 1450-1800 cm^{-1} spectral region as shown in Figure 4.2. These emission lines correspond to emission

by water vapour. Figure 4.2 [right] is a similar radiance measurement taken by the E-AERI several months later on April 4, 2009 at the PEARL Ridge Lab. Hence the October 20, 2008 spectrum was recorded before the instrument had time to dry out – it took approximately eight days for the E-AERI to dry out (diffusion of H_2O) to a point where the larger emission lines were not detectable. The consistency between AERIs permits the two datasets to be combined, constructing a single continuous eight-year (and growing) Eureka AERI dataset as discussed in Sect. 3.2.5.

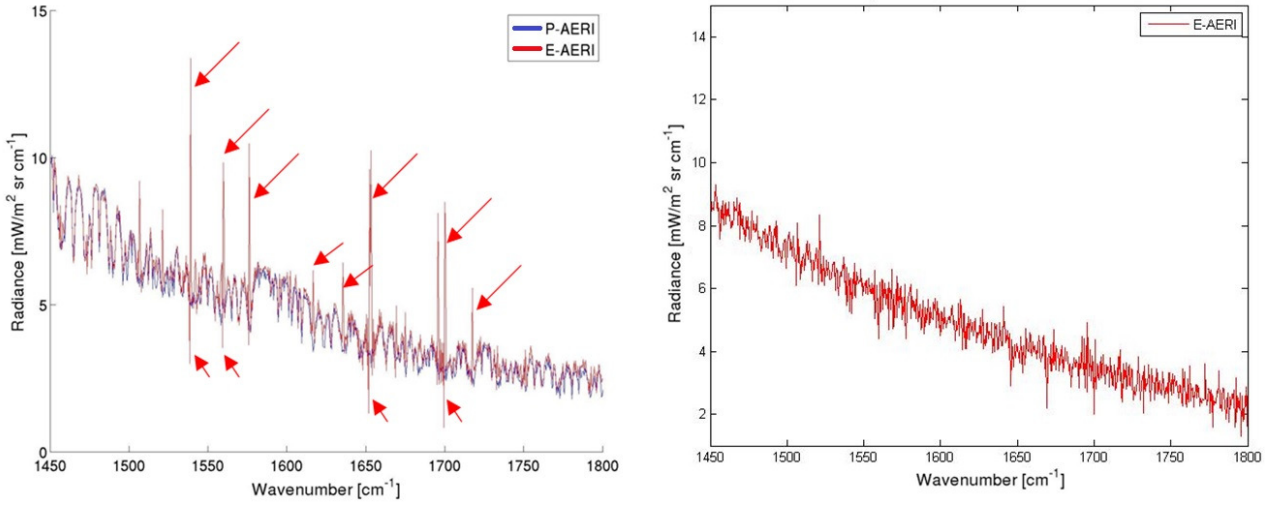

Figure 4.2: Measured radiance in the 1450–1800 cm^{-1} region on October 20, 2008 [Left] and April 4, 2009 [Right]. Larger emission lines in the E-AERI observations (red arrows) do not exist in the P-AERI spectra due to reduced humidity in the P-AERI. The complete absence of such large emission lines in the E-AERI spectra is observed several months later once the instrument had time to dry out [Right].

4.2 Investigation of the Lower Tropospheric Radiative Budget at Eureka

E-AERI measurements (at 610 m) were recorded at the PEARL Ridge Lab from October 2008 to September 2009, providing an overlap period with the P-AERI (at 10 m) ending when the P-AERI was removed from 0PAL in June 2009. Since the two measurement sites are located

only 15 km apart, this provides a unique opportunity to compare the IR radiative budgets at these two altitudes at Eureka. The extremely cold and dry Arctic atmosphere is also dense and heavy, resulting in an increased number density of trace gases in the lower troposphere compared to lower latitudes. From a climatology of radiosonde water vapour data, 10-20% (winter-summer) of the water vapour column at Eureka resides in the first 610 m (not shown).

Comparisons between temporally coincident E-AERI and P-AERI measurements of radiance from October 2008 to April 2009 are shown in Figure 4.3. Radiances were averaged on an hourly basis and used to calculate radiance differences. Each column of Figure 4.3 corresponds to a single coincident hourly-averaged P-AERI – E-AERI spectrum. The 600 m difference between the two sites has a large impact on the measured radiance, such as differences in the CO_2 band around 667 cm^{-1} due to a temperature inversion and – most notably – H_2O saturation between 400-800 cm^{-1}.

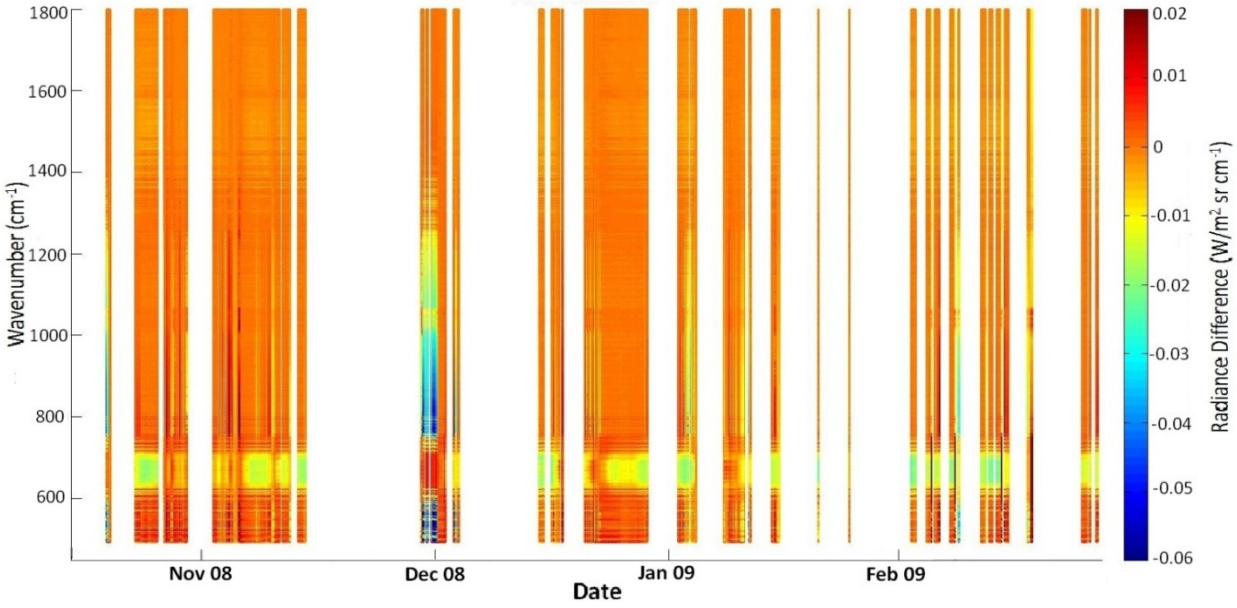

Figure 4.3: Hourly-averaged coincident radiance difference measurements (P-AERI – E-AERI) from October 22, 2008 to April 5, 2009. Only the longwave radiances are shown for clarity. White spaces correspond to periods with no measurement overlap due to precipitation or instrument maintenance.

Temperature profiles for the high Arctic frequently exhibit temperature inversions (due to the extremely cold surface) for the first two kilometers above the surface; thus temperatures at the Ridge Lab can be ~20 K warmer than at 0PAL depending on the time of year. This is reflected in the 600-800 cm^{-1} CO_2 band (which is where large differences in Figure 4.3 occur),

corresponding to warmer temperatures at the Ridge Lab and a smaller CO_2 column (due to the 600 m elevation difference) resulting in greater E-AERI radiances. Other periods with large differences between the instruments correspond to the occurrence of ice crystals, high aerosol concentrations, fog or low cloud cover. For instance, the large radiance differences (red bands) in February occur on days for which low-level clouds were present above Eureka. For the low-level clouds that exist below 610 m, only the P-AERI can measure the increased emission from the cloud particles; hence the radiance difference increases for such days. Thus the difference between the downwelling radiance at two altitudes is shown to be highly variable during the measurement overlap period for different spectral regions due to meteorological changes, such as cloud cover and temperature. This will be illustrated more clearly later in Sect. 5.2.

4.3 Comparisons with Simulated Radiances

4.3.1 The Fast Line-by-Line Radiative Transfer Model

In order to further validate E-AERI (as well as P-AERI) radiances, comparisons were made between AERI spectra and simulated spectra at the same altitudes. Furthermore, investigating differences between the simulated spectra and the measured spectra at each altitude provides insight into the limitations of the radiative transfer model. Radiances measured on April 4, 2009 by both AERIs were simulated using a Fast Line-By-Line Radiative Transfer Model (FLBLRTM) for an altitude of 10 m (P-AERI) and 610 m (E-AERI). The FLBLRTM is a faster version of a standard Line-By-Line Radiative Transfer Model (LBLRTM), as developed in Clough *et al*. [2005]. This is achieved by replacing the computationally expensive section of the LBLRTM code that calculates absorption coefficients directly from a spectral database with absorption coefficient lookup tables set on a wavenumber, pressure, and temperature grid. Although the absorption coefficient has an absorber amount dependency, it is generally insignificant for atmospheric cases [Turner, 1995]. Water vapour is an exception and is treated differently in that two lookup tables are required to represent it instead of one as with other absorbers. In addition to speeding up the calculation, the use of tables also reduces the amount of code and hence enables the model to be relatively easy to tailor to a specific problem.

For this work, absorption coefficient tables for H_2O, CO_2, O_3, N_2O, CO, CH_4, O_2 and N_2 were created by D. S. Turner (Environment Canada) for the spectral region from 400 to 3000

cm^{-1} on a grid interval of 0.005 cm^{-1}. The spectral line data are taken from the High Resolution Transmission Molecular Absorption Database (HITRAN) 2008 [Rothman *et al.*, 2009]. The H_2O continuum is accounted for by the CKD2.4 continuum model [Clough *et al*., 1989] and in all cases the Voigt line shape is assumed. The CKD2.4 continuum is compatible with HITRAN86; the new H_2O spectral lines in updated versions of HITRAN are generally very weak and do not affect the end result, particularly for a lower-resolution instrument such as the E-AERI. The radiances are computed for clear skies (April 4, 2009 had clear skies during this analysis period) with no aerosols. Temperature, pressure, and relative humidity data from Vaisala radiosondes launched near 0PAL were interpolated to 00:08 Universal Time Coordinated (UTC) on April 4, 2009 and included in the model calculations.

4.3.2 Comparing AERI Radiances and Simulated Radiances

Clear-sky comparisons between the E-AERI and P-AERI measurements at 00:08 UTC on April 4, 2009 are shown in Figure 4.4a, with the differences (P-AERI – E-AERI) in Figure 4.4d. Large negative residuals in the 600-800 cm^{-1} and 1600-1800 cm^{-1} spectral regions correspond to differences >14% and >33%, respectively. Such differences are expected due to the large temperature and humidity difference at the two sites and the absorption by CO_2 and H_2O, emphasizing the dependence of the radiative budget on the atmospheric temperature and relative humidity profile. Positive residuals typically occur in more transparent spectral regions where CO_2 absorption does not occur; they are positive due to the additional 600 m of atmospheric emission measured by the P-AERI. The measured radiance differences provide insight into the spectral regions that experience increasing or decreasing downwelling radiance at different altitudes.

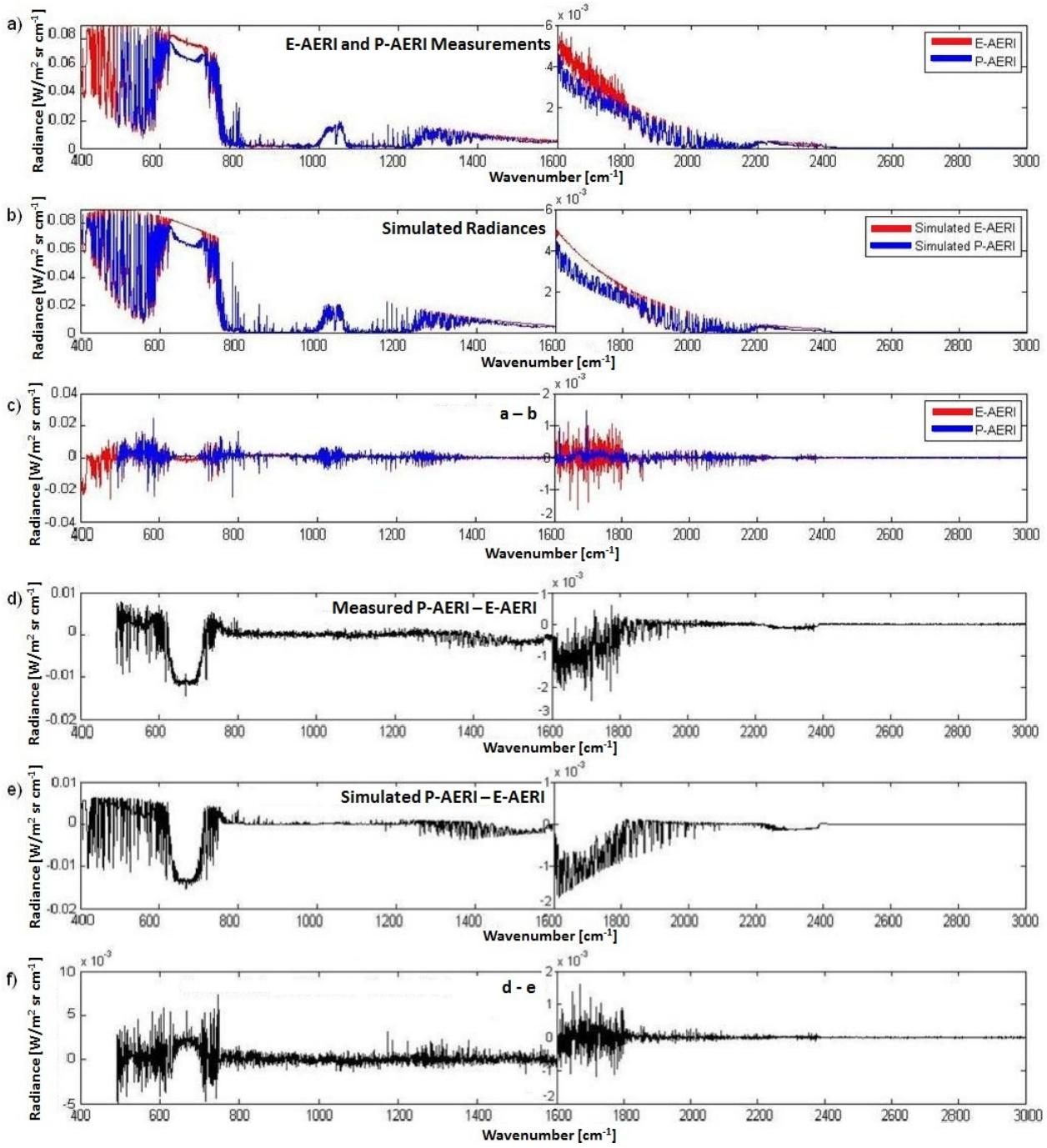

Figure 4.4: (a) E-AERI (red) and P-AERI (blue) measured radiances at 00:08 (UTC) on April 4, 2009 with (b) simulated spectra shown below. (c) Differences between the measured and simulated spectra for each instrument (a – b). (d) Measured differences (P-AERI – E-AERI) with (e) simulated differences shown below. (f) Differences between the measured and simulated radiance differences (d – e).

Results from the model simulations are shown in Figure 4.4b and agree with E- and P-AERI radiances within $\pm$ 20 mW/(m^2 sr cm^{-1}). The simulated E-AERI spectrum in the 1600-

1800 cm^{-1} region is significantly smoother than the measured E-AERI spectrum. Model simulations at altitudes varying from the surface to 3 km indicate emission and absorption features in this spectral region become quickly saturated as altitude increases. Model simulations also indicate that the simulated radiances are very sensitive to changes in temperature and H_2O for the lowest 3 km of the atmosphere. Radiosonde H_2O profiles have lower accuracy (10-20%) at the low humidities encountered in the Arctic, causing large biases in the radiosonde profile [Schneider *et al.*, 2010]. When the H_2O profile is uniformly decreased by 20% in the model simulation, the emission and absorption features are no longer saturated and the spectrum in this spectral region is less smooth (akin to the E-AERI's spectrum). The radiosonde temperature profile used to produce the simulated radiances also has small errors of < 2 K. Changing the temperature profile by $\pm$ 1, $\pm$ 2, and $\pm$ 5 K in the model simulations results in a shift in the baseline radiance. Hence biases in the radiosonde temperature and H_2O profiles used in the simulation cause the simulated radiances to saturate and deviate from the true state, resulting in the observed discrepancy.

Differences between the measured radiances (Figure 4.4a) and simulated radiances (Figure 4.4b) are shown in Figure 4.4c and have good agreement with the exception of the wings of the 600-800 cm^{-1} CO_2 band. Differences between the measured P-AERI – E-AERI radiance differences (Figure 4.4d) and the corresponding simulated radiance differences (Figure 4.4e) are shown in Figure 4.4f and indicate agreement for the majority of the spectrum with slightly larger differences around the 600-800 cm^{-1} CO_2 band, further suggesting small errors in the radiosonde temperature profile. The differences between the simulated and measured spectra indicate the model`s reliance on accurate radiosonde temperature profiles in order to accurately describe Arctic radiances. Large errors in the 400-600 cm^{-1} (> 29%) region also indicate the model's reliance on accurate relative humidity profiles. Thus the FLBLRTM used to simulate clear-sky radiances at two altitudes agrees with E- and P-AERI radiances for the majority of the spectrum; the largest differences between measured and simulated radiances occur in spectral regions that are strongly influenced by atmospheric temperature and/or water vapour, illustrating the model's dependence on accurate meteorological data from radiosondes as inputs.

4.4 Summary of AERI Validation and Comparisons

This chapter presented a first look at the new E-AERI measurements of downwelling radiance. It has been ensured that spectra measured by the E-AERI are consistent with the P-AERI by performing side-by-side comparisons and comparing measured spectra to simulated spectra. This measurement consistency and reliability validates the combination of two AERI's datasets to create a single eight-year Eureka AERI dataset, as described in Chapter 3. Differences between the E- and P-AERI during side-by-side clear-sky comparisons were within measurement error, with the exception of one spectral region (1450 to 1800 cm^{-1}) sensitive to humidity. However, once the E-AERI had time to dry out, spectra from the E-AERI matched that of the P-AERI. This is an important caveat to consider for future users of AERI data when they move an AERI from a humid climate to a dry one, and provides an estimate (around eight days) for when the AERI's MR interferometer will be completely dried-out.

The difference between the radiative budget at two altitudes (610 m and 10 m) was investigated, with large differences occurring in specific spectral regions that are representative of the temperature difference between the two altitudes. Other differences in the radiative budgets at these two sites were attributed to different meteorological conditions (clouds vs. no clouds) between them. These differences were relatively consistent throughout the nine-month measurement overlap period (i.e. there are no outliers) and indicate no seasonal bias. Finally, comparisons between E- and P-AERI measured radiances during clear-sky conditions and simulated radiances using a FLBLRTM indicate good agreement. Differences between the E- and P-AERI radiances occur in the same spectral regions identified during the investigation of the different radiative budgets at two altitudes. Differences between the simulated radiances and measured radiances occur at spectral regions strongly sensitive to changes in water vapour and temperature, indicating the importance of accurate radiosonde profiles for the simulations.

5. RADIATIVE IMPACT OF CLOUDS

The radiative properties of clouds are among the most poorly understood aspects in atmospheric radiative transfer. For experimentalists and climate modellers alike, the impact of clouds on the Earth's radiative budget – and how this impact will change in the future – remains largely unknown. There is disagreement among climate scientists as to how clouds will react and influence a warming planet. This is because clouds are inherently complicated: they form at varying altitudes, they can be of varying thicknesses and types, they can have different compositions (from sub-zero liquid water to water to ice), it is difficult to predict their location, and they can appear/disappear suddenly through numerous complicated and interconnected processes. Given the Arctic's frequent cloud cover and the AERI's ability to directly measure cloud radiative forcing, a unique opportunity to measure and quantify the radiative properties of clouds is presented.

Portions of this Chapter have been published in Mariani et al. (2012a).

5.1 Impact of Clouds on the Radiative Budget

Clouds affect radiative transfer in numerous ways, as illustrated in Figure 2.2. The ability of AERI systems to detect the presence of clouds and provide information about cloud properties has been well demonstrated [e.g., Collard *et al*., 1995; DeSlover *et al*., 1999; Shaw *et al*., 2005; Turner 2005]. Other instrumentation at 0PAL that provides information for cloud studies includes the Millimeter Wave Cloud Radar (MMCR), which measures equivalent radar reflectivity, Doppler velocity, spectral width, and Doppler spectra over 2-second intervals, and the University of Wisconson's Arctic High Spectral Resolution Lidar (AHSRL), which was

deployed in August 2005 and measures aerosol backscatter cross section and particulate circular depolarization ratio [Eloranta, 2005]. These can be used to determine cloud heights, thicknesses, composition, internal structure and vertical motions with high vertical and temporal resolution.

Figure 5.1a shows E-AERI measurements made on April 16, 2009 at 00:08 UTC and 17:57 UTC. The MMCR indicates that on April 16, early-morning clear skies were followed by a thick cloud layer above Eureka for the remainder of the afternoon and evening (Figure 5.2). The top panel of Figure 5.2 shows the measured equivalent radar reflectivity [dBZ], the middle panel shows the measured Doppler velocity [m s^{-1}], and the bottom panel shows the measured spectral width [m s^{-1}]. This figure shows slowly descending cirrus clouds. The cloud is mostly ice until around 09:00 UTC; then the spectral width increases (as indicated by the appearance of green shading), which may be due to the presence of liquid water. The E-AERI radiance increases after 04:00 UTC in the 400-600 cm^{-1} and 750-1400 cm^{-1} regions due to emission by cloud particles, correlating with the MMCR's detection of a low-altitude, relatively thick (~2 km) cirrus cloud that first appeared above Eureka at 04:00 UTC. Figure 5.1b displays the brightness temperature measured by the E-AERI throughout the day. Periods of increased brightness temperature correlate with increased cloud cover above Eureka. The averaged radiance over 750-1200 cm^{-1} increases from 4.4 to 21.6 mW/(m^2 sr cm^{-1}), almost 500%, and the brightness temperature increases 44%.

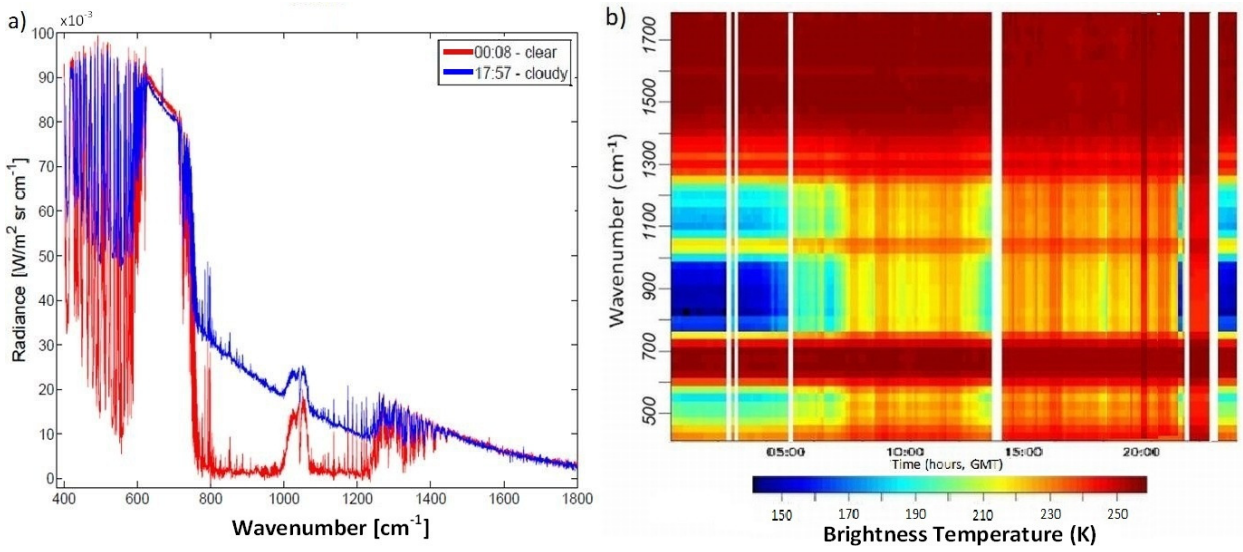

Figure 5.1: [a] E-AERI measurements of radiance on April 16, 2009 at 00:08 UTC (red) and 17:57 UTC (blue). [b] Brightness temperatures measured throughout April 16, 2009. White spaces correspond to periods of no measurement (instrument reboot, precipitation). Only the longwave spectral region (up to 1800 cm^{-1}) is shown for clarity.

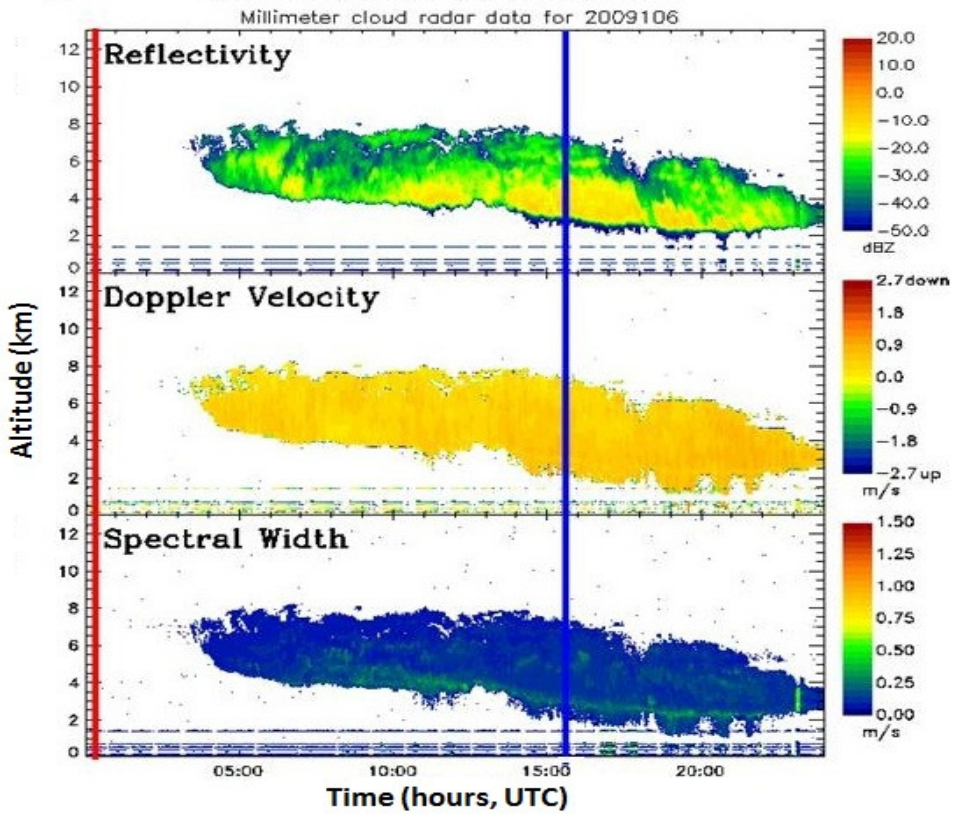

Figure 5.2: MMCR reflectivity, Doppler velocity, and spectral width plots for April 16, 2009. Red and blue vertical bars correspond to the time of E-AERI measurements, at 00:08 UTC and 17:57 UTC, respectively, shown in Figure 5.1.

Measurements made by an AERI instrument at the SGP Cloud and Radiation Testbed show relatively smaller increases (typically an increase from ~10 to ~30 mW/(m^2 sr cm^{-1}) averaged over 750-1200 cm^{-1}) in the presence of similarly thick clouds [Turner *et al*., 2000], while previous measurements in the high Arctic taken at SHEBA show increases similar to or larger than those seen by the E-AERI in Eureka (typically > 40% increase in brightness temperature averaged over 750-1200 cm^{-1}) [Turner, 2005]. Thus the impact of clouds on the radiation budget is greater in the Arctic than in other more humid regions due to the extremely cold and dry Arctic air and hence to the main atmospheric window being more transparent. This coincides with model results suggesting that the impact of clouds on the radiative budget is most pronounced for the Arctic [Vavrus, 2004]. Such large increases in radiance and brightness temperatures in these spectral regions provide a proxy for cloud detection and enable analysis of cloud optical depth, phase, and particle size [e.g., Turner, 2005]. Cloud detection is crucial in the post-processing of E-AERI data since temperature and trace gas retrievals using SFIT2 are significantly more difficult in cloudy scenes.

5.2 Radiative Impact of an Ice-crystal Cloud

A low-level ice crystal cloud was present on the last measurement overlap day shown in Figure 4.3 (April 5, 2009), as reported throughout the day by a meteorological technician at the Eureka Weather Station. It is possible that this thin ice cloud was the result of blowing snow, as frequently occurs at Eureka (e.g., Lesins *et al.* [2009]). A 10-minute interval (20:30-20:40 UTC) was selected from this day since the ice crystals were concentrated below 610 m at this time. This provides a unique opportunity to assess the impact of ice crystals on the radiative budget at two altitudes; one above the ice crystals (E-AERI) and one below (P-AERI). Figure 5.3 shows backscatter cross-section and depolarization ratios measured by the AHSRL, which was operated throughout the period of interest. The circular particulate depolarization ratio was > 20% below ~700 m (indicating ice crystals), and the backscatter cross-section above the ice crystal cloud was $< 10^{-6}$ m^{-1} sr^{-1} (indicating that liquid water clouds or precipitation were not associated with the ice crystal event); both of these conditions pass the criteria used to screen for ice crystals in Lesins *et al.* [2009].

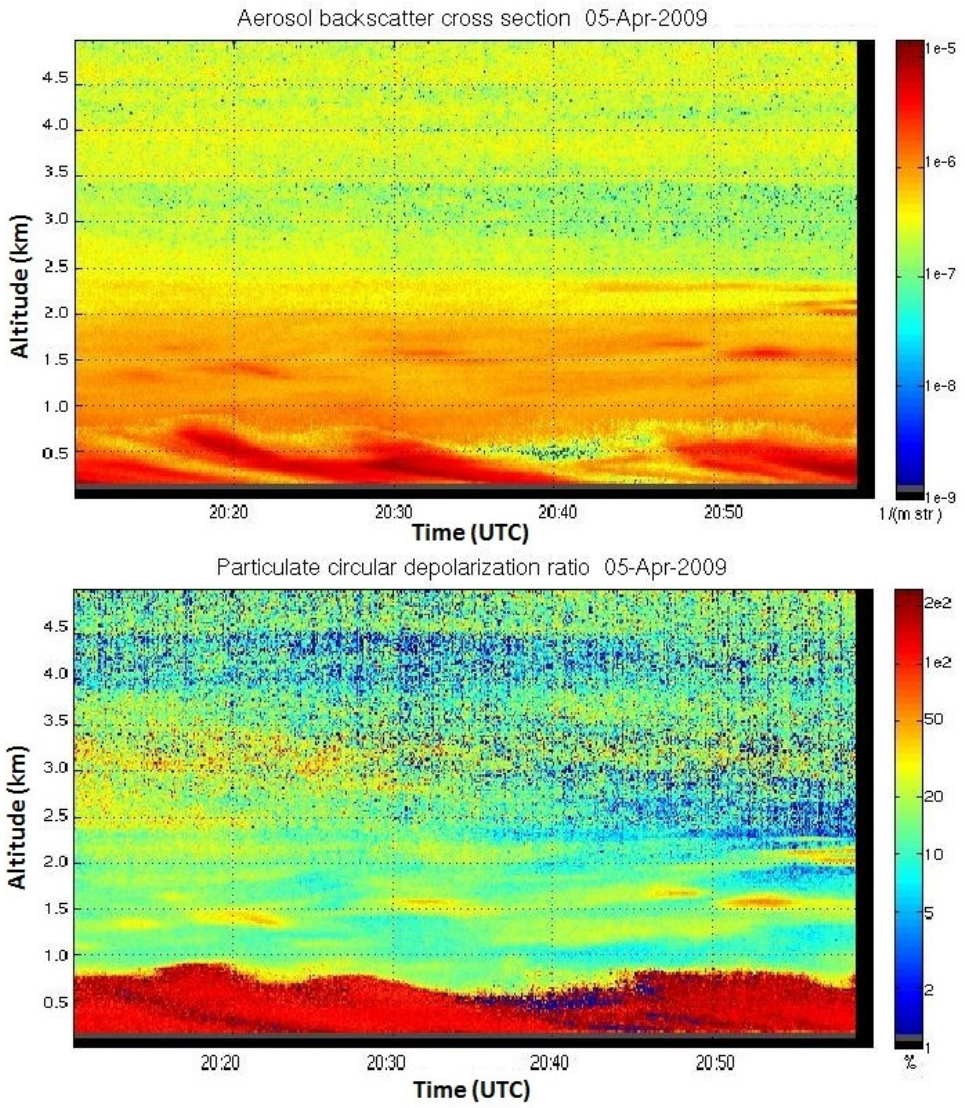

Figure 5.3: AHSRL measurements of backscatter cross section [top] and particulate circular depolarization ratio [bottom] between 20:10 and 21:00 UTC on April 5, 2009. From 20:30-20:40, the top of the ice crystal cloud was ~610 m, where the E-AERI is located.

Ice crystal radiances were compared to clear-sky radiances measured the day before (April 4, 2009) at 0:08-00:18 UTC, as shown in Figure 5.4. The temperature difference between the two measurement times (April 4 – April 5) was -4 K at 0PAL and +3 K at the PEARL Ridge Lab, accounting for differences in the 600-800 cm^{-1} CO_2 band (radiation emitted by ice crystals on April 5 also contribute to differences in this region but this change is not visible from the AERIs' altitudes). This temperature difference is shown in the radiosonde temperature profiles for April 4 and 5 in Figure 5.5 [left]. Radiosonde relative humidity profiles are also shown in Figure 5.5 [right]. The temperature at the top of the ice crystal cloud (~ 610 m) was -26.0 ^{o}C and

the temperature at the surface (10 m) was -33.9 ^{o}C. Brightness temperatures at the top of the ice crystal cloud are greater than at the bottom due to the strong temperature inversion illustrated in Figure 5.5 [left]. Radiance measurements made during these two ten-minute time intervals were averaged, and both instruments' differences (ice – clear) are shown in the bottom two panels of Figure 5.4. The P-AERI measured the largest increases in radiance in the cloud sensitive 'atmospheric window' (750-1000 cm^{-1}) since it was located below the ice crystal cloud and received emission from the ice particles. For instance, the largest ice crystal – clear sky difference increase in this spectral region was > 175% for the P-AERI and < 50% for the E-AERI (when averaged over 10 cm^{-1} bins).

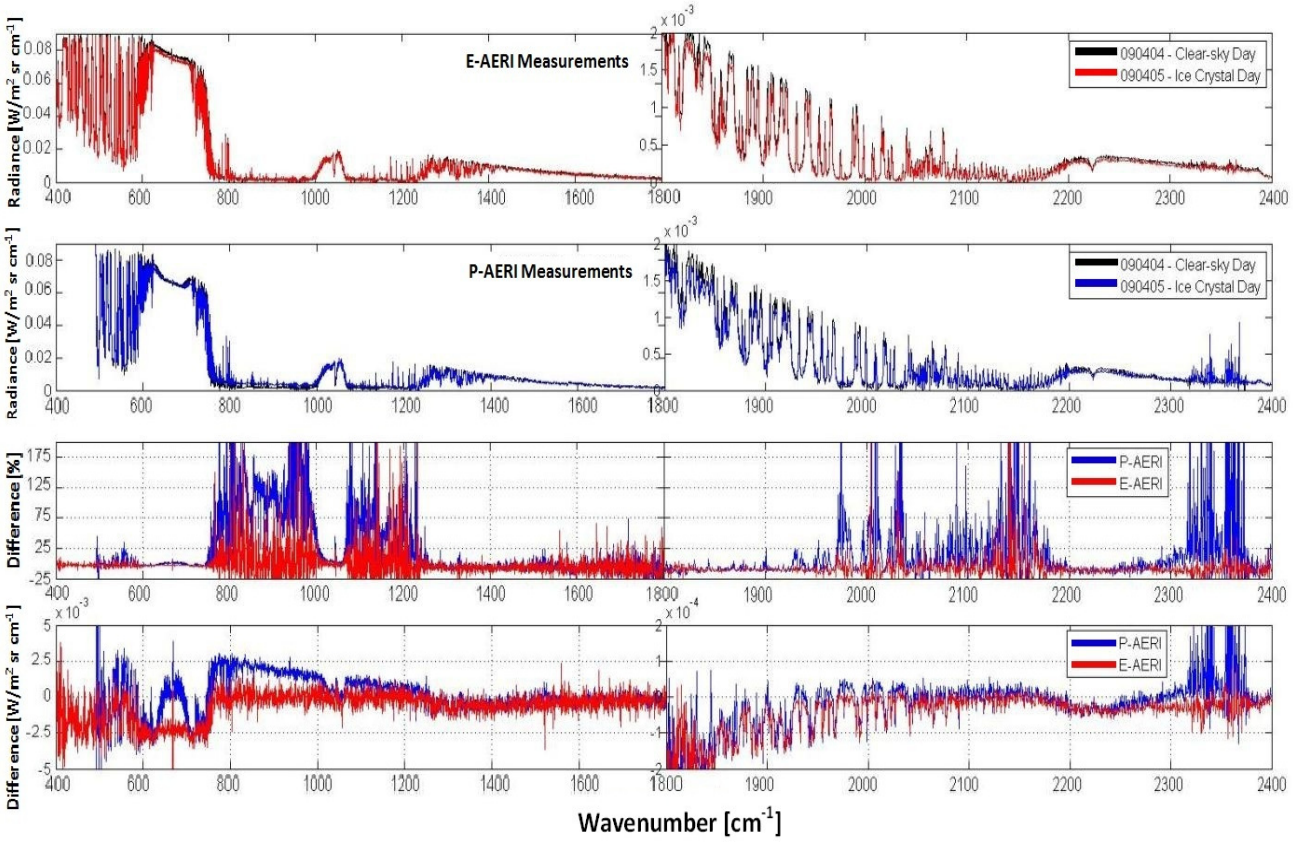

Figure 5.4: Radiance measurements for April 4, 2009 (00:08-00:18 UTC) and April 5, 2009 (20:30-20:40 UTC) for the E-AERI [top panel] and P-AERI [second panel]. Bottom two panels are differences between the ice crystal and clear-sky radiances, given as a percentage (ice crystal – clear sky / clear sky) and in radiance for both instruments, respectively.

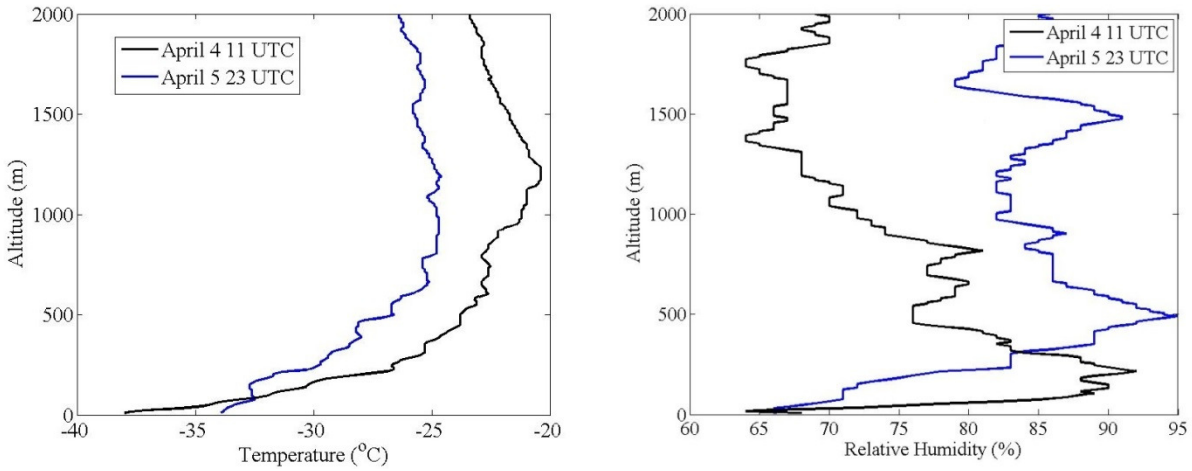

Figure 5.5: Radiosonde air temperature [left] and relative humidity [right] profiles extending to 2000 m for 11:00 UTC April 4, 2009 (black; clear-sky case), and 23:00 UTC April 5, 2009 (blue; ice crystal cloud case).

Longwave downwelling radiances during the April 5 case were converted to longwave downwelling all-sky irradiance based on the method of Cox *et al*. [2011]. This method models the portion of the IR spectrum not measured by the AERI and accounts for the radiance anisotropy associated with the viewing zenith angle. The model requires vertical profiles of temperature and humidity, which were obtained by interpolation between the two radiosondes that bracket the times of the AERI measurements. This is important to avoid inclusion of irradiance contributions in spectral regions (such as 600-800 cm^{-1}) associated with the temperature structure and not the cloud. For the atmospheric profile associated with the E-AERI, only the radiosonde measurements above 610 m were used and the 610-m temperature was set to the brightness temperature near the centre of the 600-800 cm^{-1} CO_2 band, which is a good approximation of the near-surface air temperature.

Calculated longwave downwelling all-sky irradiance was similar for both instruments (~140 to 141 W/m^2). As previously stated, the colder air temperature measured by the P-AERI below the ice crystal cloud results in less radiance in the 600-800 cm^{-1} CO_2 emission band; this reduces the longwave downwelling all-sky irradiance. The increase in radiance measured by the P-AERI in the normally transparent atmospheric window (the emission from the ice crystal cloud) represents an increase in longwave downwelling all-sky irradiance. To determine the magnitude of this increase, the longwave downwelling irradiance from the ice crystal cloud was obtained by differencing the cloudy-sky and clear-sky irradiances; the clear-sky irradiance was obtained from an LBLRTM calculation [Clough *et al.*, 1992] using the interpolated radiosonde

temperature and H_2O profiles. The longwave downwelling irradiance from the ice crystal cloud was found to be 7.8 ± 2 W m^{-2} as measured by the P-AERI (5 W/m^2 greater than measured by the E-AERI). This is equivalent to a 6 ± 1% increase in longwave downwelling irradiance from the ice crystal cloud as measured by the P-AERI (below the cloud) compared to a negligible percent increase measured by the E-AERI (above the cloud). A 6 ± 1% irradiance increase for this thin cloud (< 600 m thick) is in agreement with the measured surface forcing of up to 36% of the downwelling longwave irradiance from thicker (> 2 km) ice clouds found in Lesins *et al.* [2009], whereas previous results at the SHEBA station suggested ice crystals had no significant impact on the surface radiative forcing [Intrieri and Shupe, 2004]. Given the relatively high frequency of ice crystal events at Eureka described in Lesins *et al.* [2009], this can have important consequences for the surface energy balance in the high Arctic region.

5.3 Creation of a Cloud Filter

The sensitivity of the AERI radiance to cloud radiative forcing provides information about the presence and various properties of clouds, as demonstrated in a number of studies [Rathke *et al*., 2002; Turner, 2005; Cox *et al*., 2012, 2013]. Measurements of radiance from the AERI can be grouped based on cloud cover to ascertain the corresponding forcing produced by different types of cloud cover. The cloud radiative forcing can be quantified either across the entire spectrum as a flux density (W/m^2) or over a specific spectral region of interest, such as the cooling-to-space regions for the Arctic. As demonstrated, a distinct and clear increase in radiance occurs during the presence of clouds. Hence it is possible for the AERI system to independently identify the presence of clouds, providing an additional 'retrieved' data product for the instrument for which there are many applications: for instance, automated long-term measurements of cloud cover type on a basic scale (clear sky/thin cloud/thick cloud) can eventually provide a climatology of cloud cover type above Eureka.

Currently no cloud climatology exists at Eureka (MMCR data provides cloud information in graphical format but not a simple sky classification scheme). Environment Canada archives cloud data, but the format is relatively ambiguous (e.g., "clear sky/moderately cloudy/cloudy", approximate cloud cover fraction) and subject to the interpretation of the

individual Weather Station operator taking the measurement. Future investigation of the radiative budget at Eureka, separated based on different seasons or different spectral regions, for instance, can also be correlated with this automated sky view scene classification data product. Additionally, retrievals of trace gases when clouds are present are difficult due to the increased emission from cloud particles, as will be discussed in Sect. 7.4.2. Thus cloudy spectra must be filtered out in order to perform retrievals only on clear-sky spectra. Including a cloud filter increases the data products of the AERI instrument; a reliable metric for the meteorological conditions at Eureka every seven minutes is generated and can be used by other researchers.

Increases in AERI radiances have been correlated with the type of cloud cover above Eureka, allowing AERI measurements to independently identify the presence of clouds. Emission by cloud particles causes the observed cloud radiative forcing, increasing the radiance in the cloud-sensitive region (750-1200 cm^{-1}) as discussed in Sect. 5.1. Cloudy measurement periods are filtered using a maximum radiance threshold criterion, which is season-dependent, within the cloud-sensitive region. These cloudy scenes can be further separated to classify cloudy scenes as thin (optically thin or high-altitude) or thick (opaque or low-altitude) clouds consistent with the approach of Turner and Gero [2011]. Note this approach introduces ambiguity between cloud thickness (height) and cloud thickness (optical depth) – for the purpose of this study, as in Turner and Gero [2011], clouds are not separated solely based on cloud optical depth due to the large impact that the temperature (height) of the cloud has on the downwelling radiance and brightness temperature distribution.

Characterizing sky scenes using AERI spectra is simplified in the extremely dry and cold atmosphere of the Arctic. Figure 5.6 illustrates the sensitivity of the E-AERI to clouds at Eureka in the 850 to 950 cm^{-1} region; radiances measured on November 1, 2008 are shown for early morning thin-cloud cover, mid-day clear skies, and evening thick-cloud cover. Hence the average radiance over the 850-950 cm^{-1} spectral region was used to determine the sky scene since it is within the spectral window that is highly sensitive to clouds and it has limited interfering species (i.e., away from the O_3 band around 1050 cm^{-1}). This method allows optically thick and/or low-altitude 'warm' clouds and optically thin and/or high-altitude 'cold' clouds to be distinguished by the AERI using a set of radiance thresholds provided in Table 5.1.

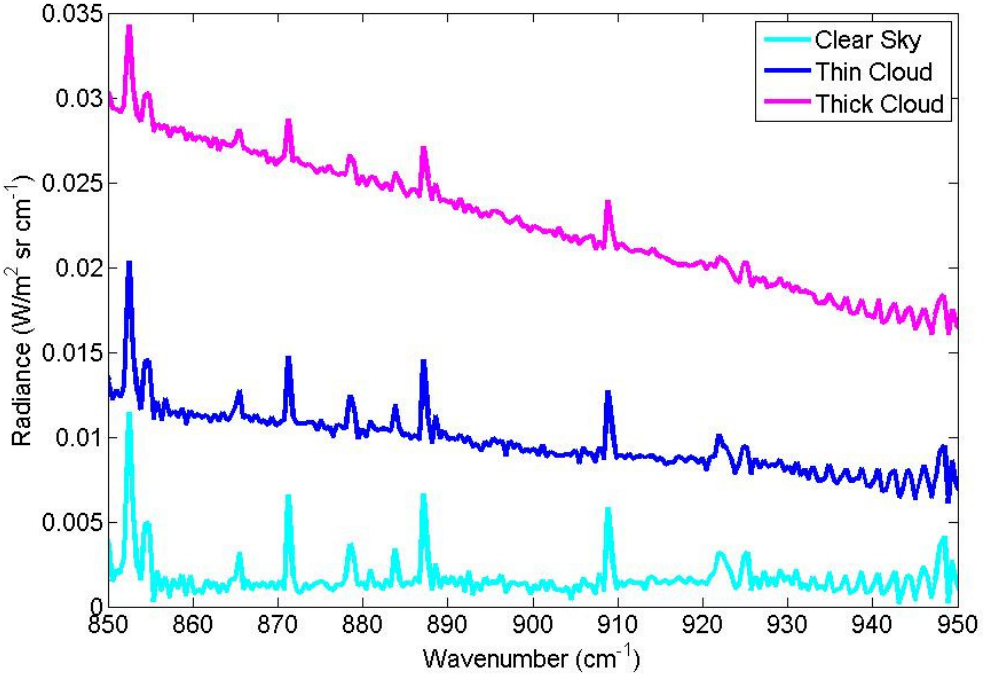

Figure 5.6: E-AERI radiances measured on November 1, 2008 during clear-sky (cyan), thin-cloud (blue), and thick-cloud (magenta) conditions. The 850-950 cm^{-1} spectral range shown here is used to classify cloud thickness.

Table 5.1: Average radiance thresholds in the 850-950 cm^{-1} region used to determine clear sky vs. thin cloud vs. thick cloud AERI spectra. Thresholds change depending on season, corresponding to changes in temperature and water vapour at Eureka.

Season	**Designation**	**Average Radiance (W/[m^2 sr cm^{-1}])**
Winter (October-April)	Clear sky	< 0.0015
	Thin cloud	0.0015 - 0.009
	Thick cloud	> 0.009
Fall/Spring (May/September)	Clear sky	< 0.007
	Thin cloud	0.007 - 0.02
	Thick cloud	> 0.02
Summer (June-August)	Clear sky	< 0.015
	Thin cloud	0.015 - 0.045
	Thick cloud	> 0.045

Radiance thresholds were determined using two instruments available at Eureka capable of detecting and determining cloud properties: the AHSRL and the MMCR [Eloranta, 2005]. Utilizing these datasets (from 2006-2013) permitted fine-tuning radiance thresholds on AERI spectra to determine the type of sky scenes. Radiance thresholds were adjusted

(increased/decreased) until they produced the correct cloud thickness classification that matched measurements from the AHSRL and MMCR for each season. It is important to note that the clear-sky classification will include clouds that are too thin to be seen by the MMCR.

Results from the entire AERI cloudy scene designation dataset were compared to AHSRL, MMCR, and Eureka Weather Station operator observations throughout the entire eight-year measurement period to verify the accuracy and stability of the sky scene characterization. The accuracy of our cloud classification based on these thresholds is found to be > 95% when compared to the MMCR and AHSRL dataset. An example of the verification exercise is shown for one day (November 1, 2008) in Figure 5.7 where AERI sky classifications are compared to cloud measurements by the MMCR. Precisely discerning 'clear' from 'thin clouds', and 'thin clouds' from 'thick clouds' is difficult and somewhat arbitrary using MMCR data but still allows one to cross-check the sky scene classification output and confirm that no outliers exist. For the purposes of this study, 'thin' clouds correspond to clouds that are either semitransparent in the IR, high-altitude (and hence colder) opaque clouds, or low-altitude clouds that were only partially in the AERI's FOV during the sky measurement period [Turner and Gero, 2011]; the latter introduces some, albeit very few, cases where the wrong designation was given. Since the AERI automatically closes the hatch and does not take measurements during precipitation, a small fraction of precipitating (presumably thick) clouds are excluded from this analysis.

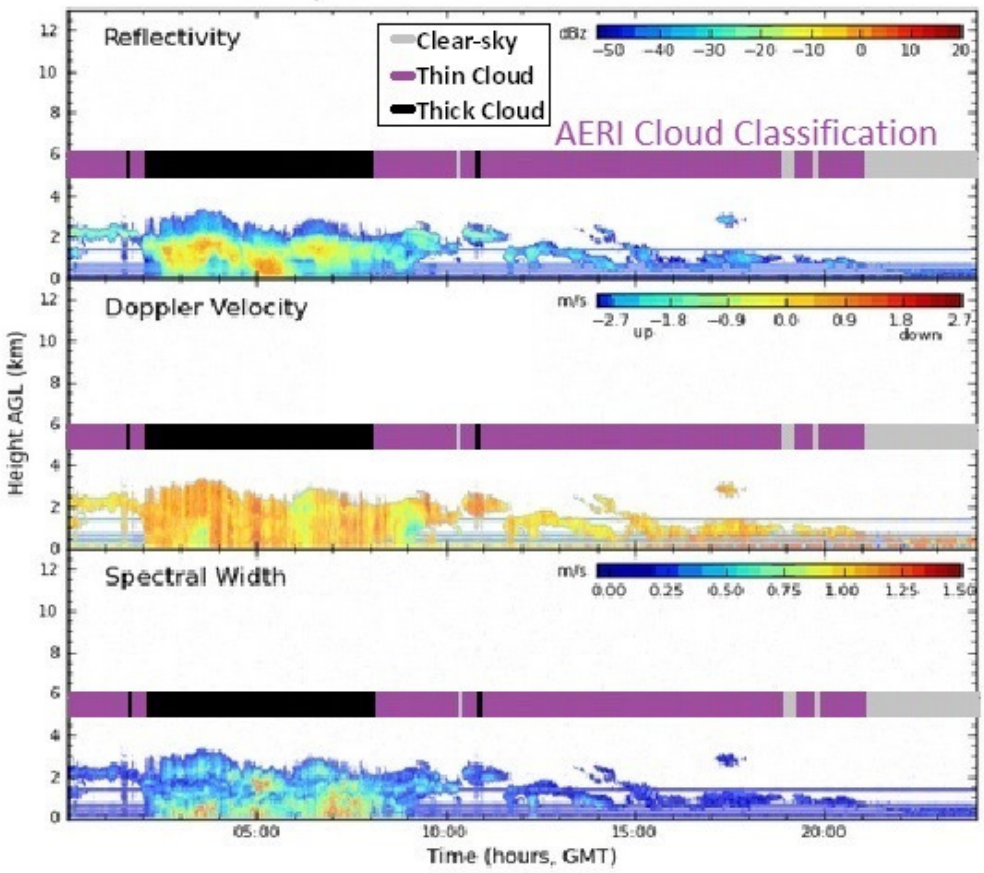

Figure 5.7: Example of AERI cloud classification scheme validation using MMCR observations. Results from the AERI cloud classification scheme are shown as a bar in each panel (clear sky = grey / thin cloud = purple / thick cloud = black), with the corresponding cloud cover measured by the MMCR shown below. Measurements were taken November 1, 2008 using spectra from the E-AERI.

The average radiance thresholds within the 850 to 950 cm^{-1} window listed in Table 5.1 change with season; the timing of these changes is closely correlated with changes in precipitable water vapour (PWV) measured by a MWR at Eureka (sharp increase/decrease in May/September) to reflect the increase/decrease in background continuum emission due to changes in water vapour as well as temperature. As a result, the seasons are not of equal length; this reflects the unique environmental conditions experienced in the high Arctic (a long cold and dry winter followed by a rapid transition to a short summer). Radiance thresholds that change with the season (according to the PWV) also reduce the ambiguity in IR spectra between thin clouds and water vapour. Note that the conclusions drawn from using these thresholds are insensitive to small (< 5%) changes in the radiance thresholds.

The percentage of each type of cloud cover that occurred since 2006 provides insight into the variability of cloud cover in the Arctic and is shown in Table 5.2. Note that only measurements at 0PAL were included in this study and some of the year-to-year variability is due to the uneven measurement distribution and the AERI's hatch being closed during (presumably thick) precipitating clouds. Despite this, the cloud coverage determined by AERI measurements is in very close agreement with other studies of cloud cover performed at Eureka, indicating the reliability of this method. For instance, a study performed by Lesins *et al*. [2009] using AHSRL measurements found that in January, February, March and December 2006, cloudy skies existed 65% of the time at Eureka, while our method indicates 66% cloud coverage during this same period. Note that actual cloudiness is likely to be higher, as the AERI instrument does not take measurements during precipitation events. Furthermore, most clear skies are found to occur in the summer and spring/fall periods, which is in agreement with the annual cycle of cloud cover for Eureka described in Shupe *et al*. [2011]. The large number of thin clouds observed during winter months is in agreement with a study of simulated and observed Arctic cloud cover in winter that found a large increase in high-altitude clouds (which would be classified as 'thin' in this study) as well as consistent nearly-overcast conditions [Vavrus *et al*., 2004].

Table 5.2 Clear-sky, thin-cloud, and thick-cloud coverage at Eureka for each year as determined by AERI measurements at 0PAL using the radiance thresholds in Table 5.1. Also shown are the percentages of each type of cloud cover during each season from 2006-2013. Percentage is calculated as the number of times the given cloud designation existed divided by the total number of AERI seven-minute spectra in that time period. Measurements from PEARL were not included in this analysis.

Year	Clear sky (%)	Thin cloud (%)	Thick cloud (%)
2006	31	28	41
2007	42	34	24
2008	34	35	31
2009	26	23	51
2010	N/A	N/A	N/A
2011	42	30	28
2012	24	30	46
2013	38	25	37
All measurements	33	31	36
Summer Months	49	19	32
Spring/Fall Months	40	12	48
Winter Months	25	41	34

5.4 Summary of Radiative Impact of Clouds

This chapter presented measurements of the surface radiative forcing due to the presence of clouds, including a case study of a low-altitude thin-layer ice-crystal cloud. The impact of clouds on the radiative budget was measured from two altitudes using two AERIs, and the difference between the radiative forcing at these two sites was analyzed. The E-AERI's measured radiance has been shown to increase by almost 500% in the 750-1200 cm^{-1} region in the presence of clouds, correlating with the MMCR and AHSRL's detection of clouds above Eureka. This increase is relatively larger for the Arctic than in other more humid regions, indicating that cloud cover plays a crucial role in the Arctic's radiative budget.

In a case study analyzing the radiative impact from a thin (< 600 m thick) ice cloud, a 6 $\pm$ 1% increase in longwave downwelling irradiance was measured by the P-AERI (below the cloud) while the increase measured by the E-AERI (above the cloud) was negligible. This is in agreement with previous measurements of significant surface forcing due to ice crystals shown in Lesins *et al.* [2009], and in disagreement with earlier results found at the SHEBA station, which suggested ice crystals had no significant impact on the surface radiative forcing [Intrieri and Shupe, 2004]. This demonstrates the usefulness of the E-AERI and P-AERI measurements for investigating the impact of clouds on the Arctic radiation budget. Future detailed investigation of periods of large differences in the P-AERI – E-AERI radiances is planned to further investigate the impact of different meteorological events on the radiative budget in the high Arctic.

This chapter also described the creation and implementation of an empirical cloud filter created for AERI spectra that made use of the increases in radiance during the presence of different types of clouds. The extremely dry and cold Arctic atmosphere allows for clear distinctions (large increases in radiance) between spectra during different types of cloud cover. Average radiance thresholds in the 850-950 cm^{-1} region were empirically determined and used to classify clear sky vs. thin cloud vs. thick cloud spectra. Thresholds change depending on season, corresponding to changes in temperature and water vapour at Eureka. Results from the cloud filter were compared to AHSRL, MMCR, and Eureka Weather Station cloud data to verify the cloud filter's accuracy; after fine-tuning of the radiance thresholds was performed, AERI cloud flags matched results from the AHSRL and MMCR consistently (>95 %). Clear-

sky, thin-cloud, and thick-cloud coverage at Eureka for each year and the percentages of each type of cloud cover during each season from 2006-2013 was provided and agrees with existing studies. This cloud filter may be used for performing studies correlating radiative forcing to cloud cover type, automated long-term measurements of cloud cover type to produce climatologies, and trace gas retrievals (which must be performed during clear skies) and is used in several sections in the remainder of this thesis.

6. MEASUREMENTS OF SURFACE COOLING-TO-SPACE WINDOWS

The Earth cools itself by emitting IR radiation from near its surface. The cooling-to-space windows (mentioned in Sect. 2.1.3) are where the atmosphere is mostly transparent; however these windows can become less transparent as climate change alters atmospheric composition; clouds can also affect their radiative properties. This Chapter outlines a study performed using the 8+ year Eureka AERI dataset in which the downwelling brightness temperatures and radiances in several microregions of interest were analyzed to determine their distributions and trends, respectively. Comparisons to a climatology of similar measurements of downwelling radiative forcing due to clouds at the SGP, produced using AERI measurements, was also performed, providing a direct comparison to a southern, more humid, climate. This permits one to draw conclusions about the differences between the high Arctic and the mid-latitude atmospheric processes.

Portions of this Chapter will be published in Mariani et al. in preparation.

6.1 The Arctic's Primary Surface Cooling-to-Space Atmospheric Windows

The transition of regimes from cooling-to-space at 20 μm to cooling-to-space at 10 μm in the Arctic is of concern due to the possibility of significant warming, yet there is no published downwelling radiance climatology in the high Arctic (> 75^{o} N) to monitor such a transition. As

described in Sect. 2.1.3, these two spectral regions are of particular interest due to their impact on the Earth's energy budget. In order to make use of both the E-AERI (which has measurements that cover the entire 20 μm window) and the P-AERI (which can take measurements down to 500 cm^{-1}, covering part of the 20 μm window) measurements in the combined Eureka AERI dataset, radiances in small spectral regions of interest, called microregions (sometimes referred to as 'microwindows'), were selected within the 10 and 20 μm windows (described in Sect. 6.2).

Determining the downwelling radiation variability for each season over the several years of AERI measurements can be used to evaluate GCMs relative to datasets, such as done in the International Satellite Cloud Climatology Project [Klein and Jakob 1999; Webb *et al*. 2001]. In addition, measurements of the 20 μm window are of particular interest since this window is heavily influenced by the concentration of water vapour, causing it to be more variable than the 10 μm window. Aside from measuring radiances for the purpose of monitoring this cooling-to-space window, the far IR is also important for cloud thermodynamic phase determination, as demonstrated by Rathke *et al.* [2002].

A climatology of the downwelling 10 μm brightness temperatures separated based on cloud cover, and trends in the downwelling radiance, have been provided for the SGP in Turner and Gero [2011] and Gero and Turner [2011]. A further goal of this work is to present a similar analysis for the high Arctic, permitting a direct comparison between the high Arctic and the mid-latitude conditions.

6.2 Microregions of Interest

Measurements of radiance by the AERI were grouped based on cloud cover to ascertain the corresponding forcing produced by different types of cloud cover, as described in Sect. 5.3. Cloudy scenes were classified as thin (optically thin or high-altitude) or thick (opaque or low-altitude) using the cloud filter described in Sect. 5.3. With cloud types defined for each season, radiances in each microregion of interest can be analyzed.

Radiances were averaged in four microregions to determine the brightness temperature and averaged radiance. These four microregions illustrated in Figure 6.1 are: (1) 529.9-532 cm^{-1}, which is within the 20 μm window where emission is primarily due to water vapour and clouds, (2) 985-998 cm^{-1}, which is within the 10 μm window, matches the window used to produce the SGP climatology in Turner and Gero [2011], and is where emission is primarily due to water vapour and clouds, (3) 784-785 cm^{-1}, which is a strong but unsaturated water vapour line sensitive to water vapour, and (4) 674-679 cm^{-1}, which is completely opaque due to strong CO_2 absorption, providing a good estimation of the near-surface air temperature. It is important to note that microregions (1) and (2) are meant to be representative of the entire 10 and 20 μm cooling-to-space windows, since brightness temperatures can vary by tens of K within these windows. Microregions (3) and (4) allow investigation of trends related to water vapour and surface temperature in addition to trends associated with cloudiness. Due to the strong sensitivity of microregions (3) and (4) to surface conditions, only measurements at 0PAL were used in trend analyses. Note that the main conclusions drawn from using these microregions are insensitive to small changes in their spectral location or width (tests not shown).

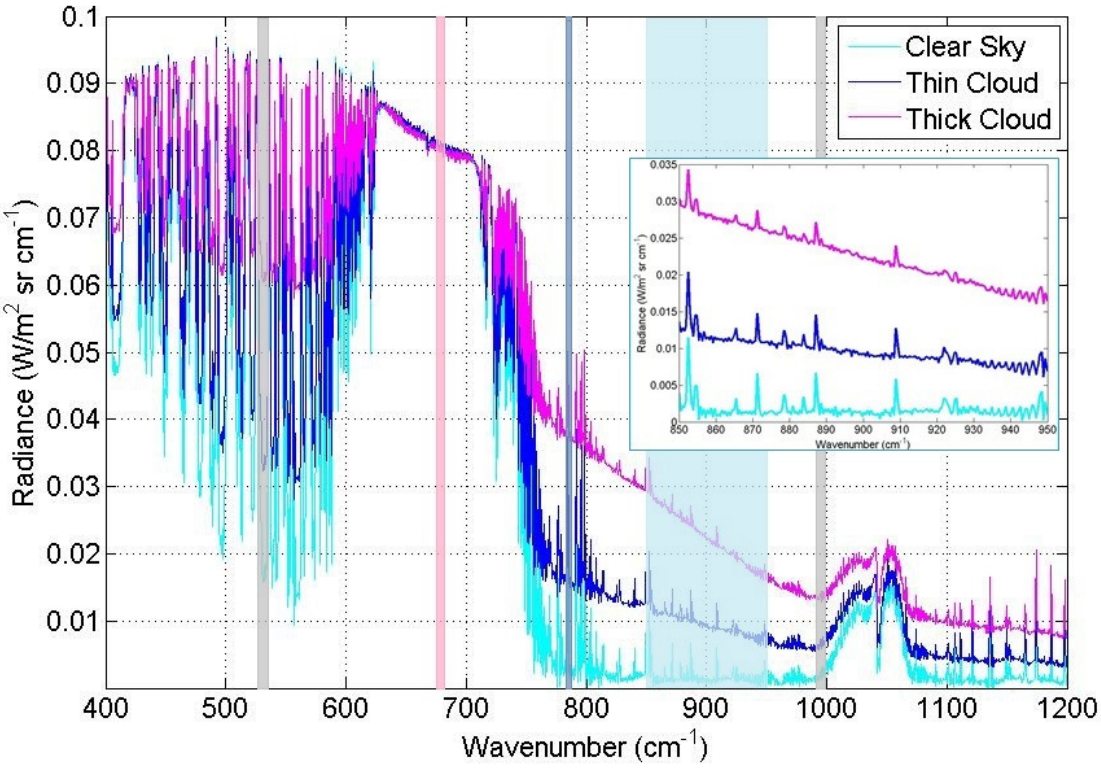

Figure 6.1: E-AERI radiances measured from the Ridge Lab on November 1, 2008 during clear-sky (cyan), thin-cloud (blue), and thick-cloud (magenta) conditions. Grey regions indicate the 20 and 10 µm (529.9-532 and 985-998 cm^{-1}) cooling-to-space windows. The shaded red and blue regions indicate the surface temperature (674-679 cm^{-1}) and water vapour (784-785 cm^{-1}) microregions of interest, respectively. The shaded light-blue region indicates the 850-950 cm^{-1} spectral range (enlarged in inset panel; Figure 5.6) used to classify cloud thickness.

6.3 Distributions of Downwelling Brightness Temperatures

6.3.1 Distributions at Eureka

The distribution of the Eureka AERI brightness temperatures for both the 10 and 20 µm surface cooling-to-space windows is provided in Figure 6.2. These distributions have been further separated into their sky scene classification using the method described in Sect. 5.3. Both the 10 and 20 µm distributions exhibit a bi-modal character for all-sky, clear-sky, and (to a lesser extent) thin-cloud classifications, in keeping with the bimodal distribution in downwelling

all-sky flux found at Eureka by Cox *et al.* [2014]. Both distributions have a single mode for thick clouds peaking at 260 K (at 10 μm) and 270 K (at 20 μm). However, there are distinct differences between these two cooling-to-space windows. The 20 μm window has broader distributions than the 10 μm window with a larger spread in temperatures. The difference between the 10 and 20 μm distributions in the low-temperature range is likely due to either ozone emission or the well-known positive bias between 985 and 998 cm^{-1} in AERI spectra (likely due to a small contribution inside the instrument not accounted for in the instrument's calibration) [Turner, 2003; 2008; Delamere *et al*., 2010], which prevents the brightness temperatures here from falling below ~160 K. The difference in the high-temperature range is indicative of enhanced water vapour emission in warmer atmospheres affecting the 20 μm window more than the 10 μm window.

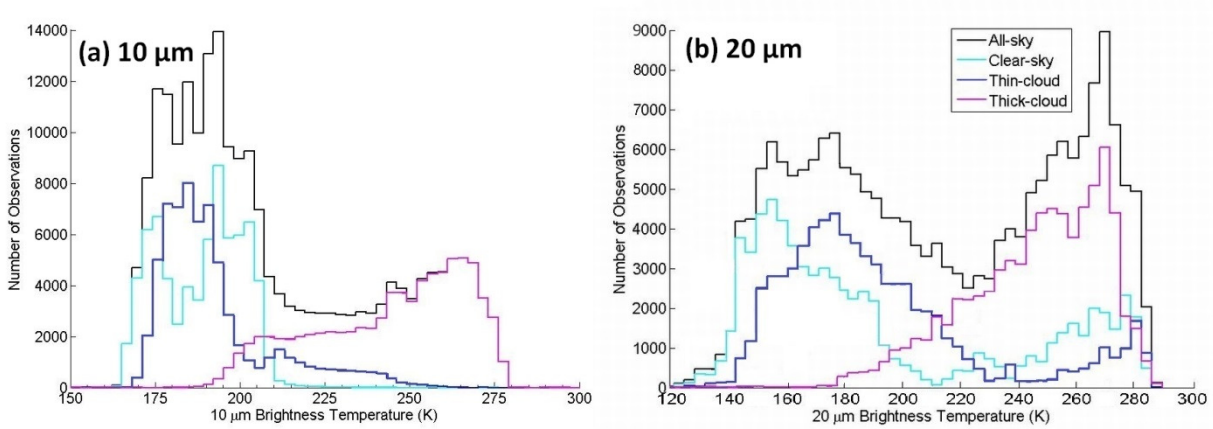

Figure 6.2: The distribution of brightness temperatures measured at 10 μm (985-998 cm^{-1}, left) and 20 μm (529.9-532 cm^{-1}, right) from the combined Eureka AERI dataset. Histograms of all-sky conditions (black), clear-sky (cyan), thin cloud (dark blue), and thick cloud (magenta) are shown. Note the scale of the y-axis is different for the 20 μm brightness temperatures since there are fewer measurements in the far IR.

The distributions are further separated based on season and are shown as a percentage of occurrence (number of *X* occurrences at that brightness temperature / sum of all *X* occurrences in that season, where *X* = all sky, clear sky, thin cloud, or thick cloud) in Figure 6.3. A distinct increase in brightness temperatures is observed from winter to fall/spring to summer for both the 10 and 20 μm windows. For instance, the distribution of thick clouds is wide and smoothed out in the winter (~5% occurrence from 200-250 K for 10 μm, 5-8% from 200-260 K for 20 μm) while it peaks much more sharply in the summer months (15% at 270 K for 10 μm, 30% at 275 for 20 μm). This indicates a sharp transition between these two seasons, typical of the high

Arctic atmosphere, which experiences a sudden and large increase in surface temperature and water vapour (by ~75 K and a factor >10, respectively from winter to summer, according to Eureka climatologies). In Figure 6.2 and Figure 6.3, the relative sizes of the two modes differ for the two windows, with generally more cases in the high-temperature mode for the 20 μm window relative to the 10 μm window.

There is almost no separation of brightness temperatures among sky scenes in the 20 μm window during the summer months in Figure 6.3f (even in the fall/spring a clear separation is difficult), indicating that the 20 μm window is saturated and essentially closed during this time. Since water vapour is the most radiatively active gas in these window regions, during peak PWV periods the transparency in the 20 μm region is decreased, resulting in a narrow distribution of downwelling brightness temperatures at 20 μm (all of which are > 250 K) independent of sky cover. This behaviour is analogous to the 20 μm window being opaque, as is the case at lower latitudes. The variability of temperature and water vapour at Eureka is illustrated in Figure 6.4 and is consistent with seasonal changes in the observed downwelling brightness temperature distributions. Given the long-term trend of increasing temperatures in the Arctic (not illustrated in Figure 6.4's limited timeframe) and the consequent increase in H_2O during prolonged Arctic summers [ACIA, 2004; Richter-Menge, 2006; Bekryaev *et al*., 2010; Lesins *et al*., 2010], it is anticipated that the surface radiative forcing will continue to increase due to the increased H_2O, which will have long-term consequences for the Arctic's energy balance.

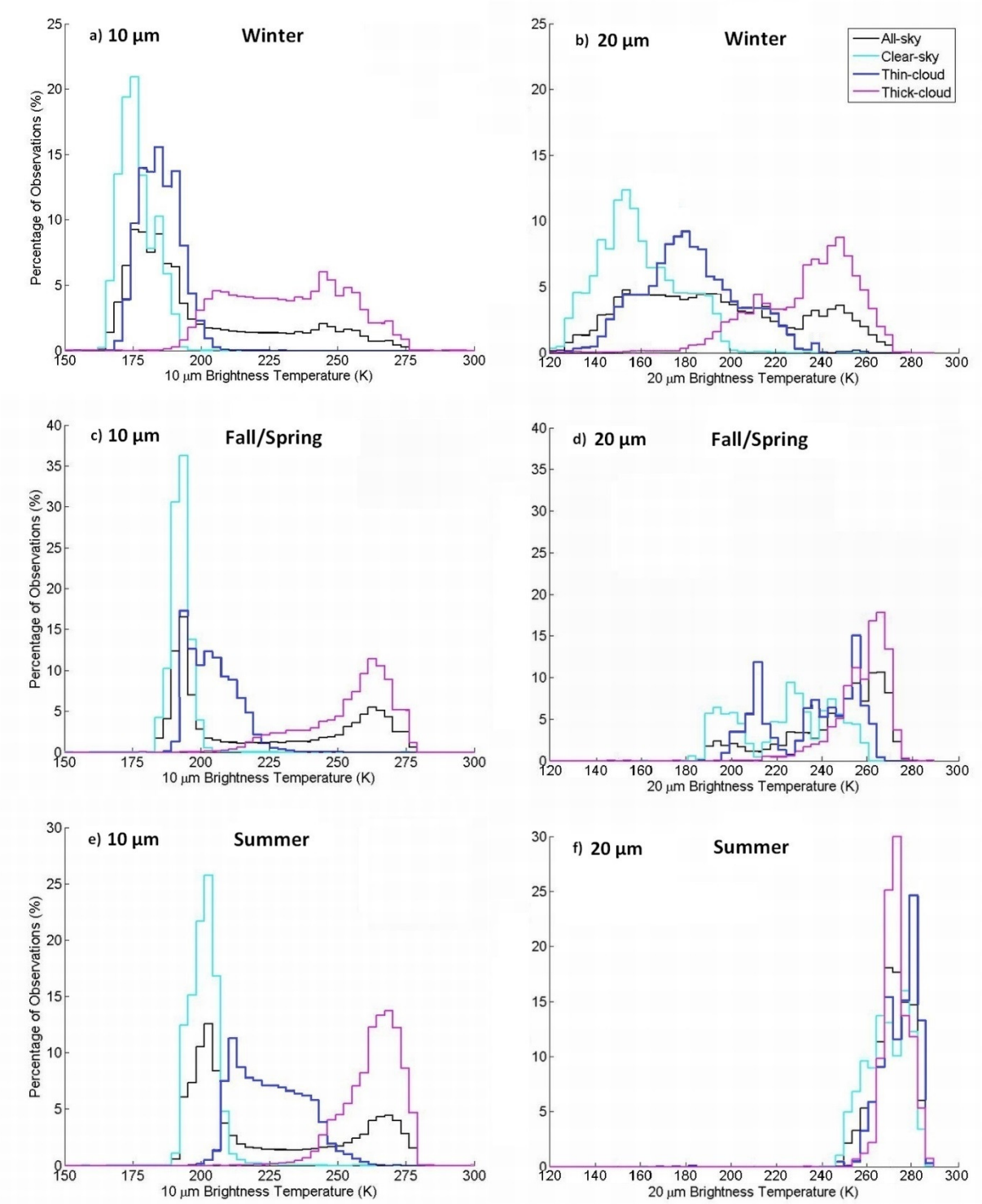

Figure 6.3: The same as Figure 6.2, except shown as a percentage of occurrence (number of *X* occurrences at that brightness temperature / sum of all *X* occurrences in that season, where *X* = all sky, clear sky, thin cloud, or thick cloud) and separated by season: winter (top row), fall/spring (middle row), and summer (bottom row).

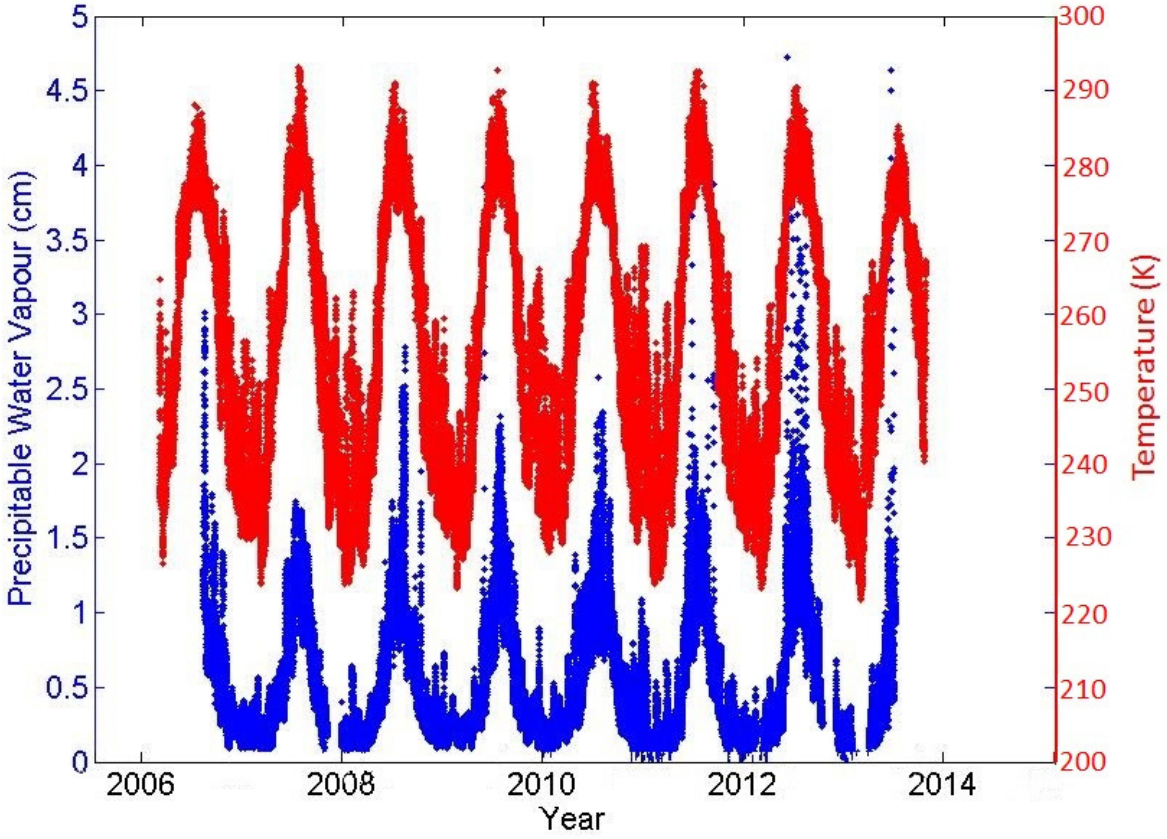

Figure 6.4: MWR PWV (blue, left y-axis) and Environment Canada surface temperature (red, right y-axis) records taken at Eureka from 2006-2013.

6.3.2 Comparison of Eureka and SGP 10 μm Downwelling Brightness Temperatures

The SGP climatology, which used similar measurements by AERIs around the Oklahoma (36° N, 97° W) region as part of the Department of Energy's (DOE) ARM program [Stokes and Schwartz, 1994], is an excellent dataset with which to perform direct comparisons. While efforts were taken to ensure that the methodology performed in this study matched those performed to produce the SGP climatology (e.g., same spectral range was used for the 10 μm window), there exist some minor differences. A threshold value of 250 K in brightness temperature (corresponding to 0.043 to 0.055 W/[m^2 sr cm^{-1}]) over a 70-minute period was used to separate thin from thick clouds in the SGP climatology described in Turner and Gero [2011], but given the colder temperatures experienced in the high Arctic, a new set of radiance thresholds was developed (Table 5.1). Secondly, to distinguish between clear skies and thin or thick clouds at

the SGP where the high humidity obscures clouds, a neural network algorithm was applied to AERI spectra [Turner and Gero, 2011]. At Eureka, however, the atmosphere is sufficiently cold and dry that even very weak cloud emission (including haze) is detectable with an AERI.

There exist notable similarities between the SGP and Eureka 10 μm distributions, as well as unique differences. First, both the clear-sky and thin-cloud brightness temperatures exhibit somewhat bi-modal distributions in the Eureka dataset, similar to the SGP. Second, Eureka brightness temperatures are lower since it is colder in the Arctic than at the SGP. Third, Figure 6.3 reveals that, unlike at the SGP, at Eureka the peaks of the fall/spring clear-sky and winter thin-cloud distributions are narrow. Fourth, the SGP 10 μm all-sky classification distribution is tri-modal while at Eureka it is bi-modal (black line in Figure 6.2). This is due to thin-cloud cases filling in the gap between the clear-sky modes at Eureka, turning the two colder modes into one wide cold mode, resulting in a net bi-modal distribution.

6.4 Trends in Downwelling Radiances

6.4.1 Radiance Trends at Eureka

Despite the combined Eureka AERI dataset's short length compared to natural variability and variability in the temporal distribution, statistically significant trends have been detected in downwelling radiance at Eureka between 2006 and 2013. Only AERI measurements taken at 0PAL were used in this trend analysis. Radiances have been separated based on seasonal averages to reduce the effects of seasonal variation, as done in Gero and Turner [2011]. The average radiance within each season for each year is shown in Figure 6.5. Applying a linear regression to each seasonal average quantifies the trends, shown in Table 6.1, in the two surface cooling-to-space windows (all-sky) and two microregions sensitive to water vapour and temperature (clear-sky). Only clear-sky observations are included for water vapour and temperature microregions to avoid the influence of clouds. Included in Table 6.1 are the measured surface temperature and PWV trends at Eureka, as measured by the Eureka Weather Station and MWR, respectively (shown separately in Figure 6.4).

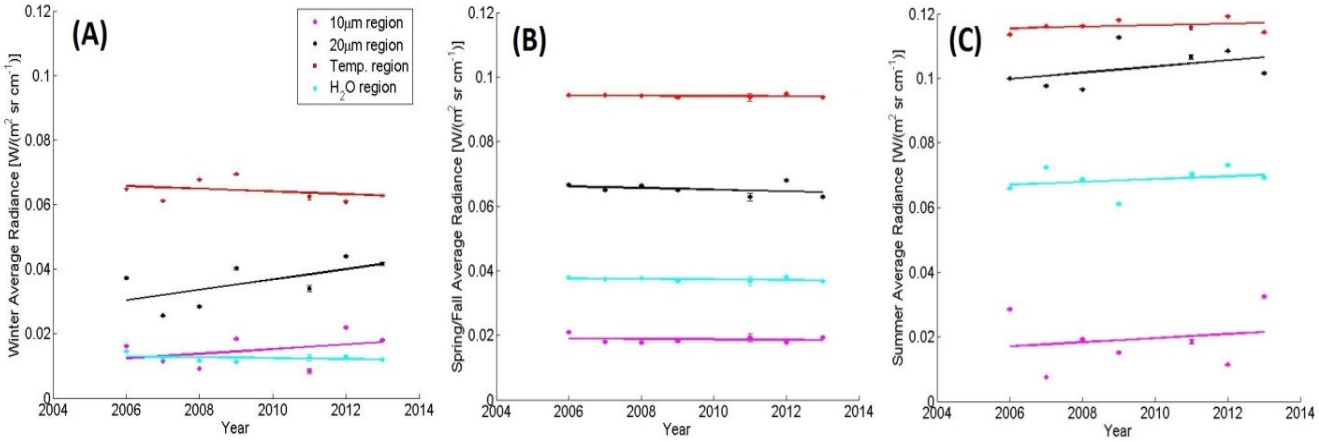

Figure 6.5: AERI measurements at 0PAL of downwelling radiance in the 10 μm (985-998 cm^{-1}; magenta) and 20 μm (529.9-532 cm^{-1}; black) cooling-to-space windows, as well as the microregions sensitive to temperature (674-679 cm^{-1}; burgundy) and water vapour (784-785 cm^{-1}; cyan). Radiances have been averaged over the three seasons (A) winter (Oct. to Apr.), (B) spring/fall (May/Sept.), and (C) summer (June to Aug.). Straight lines indicate the linear fit and error bars correspond to the standard error on the mean (standard deviation / square root of the number of observations).

Table 6.1: Seasonal AERI radiance and cloud type trends (percentage per year) using the microregions illustrated in Figure 6.1. Surface meteorological temperature measurements and PWV measurements by the MWR at Eureka are included for comparison. Errors are calculated to a 95% confidence interval using the method of Weatherhead *et al*. [1998]. Statistically significant trends are in bold.

Measurement	**Sky Conditions**	**Trend (% / yr)**		
		Winter (Oct.-Apr.)	**Spring/Fall (May/Sept.)**	**Summer (June-Aug.)**
10 μm (985-998 cm^{-1})	All-sky	**+4.9 ± 4.5**	-0.4 ± 0.6	+3.4 ± 7.0
20 μm (529-532 cm^{-1})	All-sky	**+4.6 ± 2.6**	**-0.4 ± 0.3**	**+1.0 ± 0.8**
Temperature microregion (674-679 cm^{-1})	Clear-sky	-0.7 ± 0.7	-0.1 ± 0.1	**+0.2 ± 0.1**
Surface Temp. (met. obs.)	All-sky	-0.3 ± 0.7	-0.2 ± 0.8	-0.1 ± 1.5
Water vapour microregion (784-785 cm^{-1})	Clear-sky	**-1.2 ± 1.0**	-0.2 ± 0.2	+0.7 ± 0.9
Precipitable Water Vapour (MWR)	All-sky	-2.5 ± 3.5	+0.4 ± 0.5	+2.5 ± 7.8
Clear-sky Observations	Clear-sky	-1.8 ± 2.4	-0.5 ± 0.8	+1.6 ± 2.1
Thin-cloud Observations	Thin cloud	**-6.1 ± 4.5**	-0.4 ± 1.0	+4.6 ± 6.0
Thick-cloud Observations	Thick cloud	**+7.2 ± 4.7**	**+0.8 ± 0.6**	-6.3 ± 6.3

The uncertainties in these trends were calculated to a 95% confidence interval using Eqn. 2 in Weatherhead *et al*. [1998], which is based on the length of the time series (number of years of time series data), the autocorrelation of the noise (which may be the result of various natural factors which give rise to somewhat smoothly varying changes), and the standard deviation of the noise. The linear model's noise, described as the unexplained noise of the measurement data in the Weatherhead method, can be obtained from the deseasonalized and detrended time series as explained in Weatherhead *et al.* [1998].

Statistically significant trends exist between 2006 and 2013 for all seasons for the 20 μm window (4.6 $\pm$ 2.6% / yr in the winter, -0.4 $\pm$ 0.3% / yr in the spring/fall, and +1.0 $\pm$ 0.8% / yr in the summer) and during the winter for the 10 μm window (4.9 $\pm$ 4.5% / yr). Although surface temperature has been increasing overall at Eureka since 1941 (by about 2 K in December-February and by almost 1 K in March-May) as has humidity (according to meteorological measurements at the Eureka Weather Station and Lesins *et al*. [2010]), this is not reflected in Table 6.1 as trends in the AERI microregions sensitive to water vapour and temperature, and trends in the PWV and surface temperature are generally not statistically significant between 2006 to 2013. An exception is for the water vapour microregion during the winter, for which the trend is statistically significant, but negative, and therefore not able to explain increases seen in the 10 and 20 μm regions. By contrast, Table 6.1 shows that thick-cloud cover increased by 7.2 $\pm$ 4.7% / yr during the winter at the expense of thin-cloud cover and 0.8 $\pm$ 0.6% / yr during spring/fall from 2006 to 2013. This suggests that these cooling-to-space windows are closing due to increasing thick-cloud cover.

During the summer, trends at 10 μm and in cloud thickness are not statistically significant. However, there is a small, positive, statistically significant trend in the 20 μm region. As discussed previously, this 20 μm window is mostly closed during the summer, suggesting that this trend is due to increases in temperature. In support of this is a positive, statistically significant trend in radiance in the microregion sensitive to temperature (0.2 $\pm$ 0.1 % / yr), but no statistically significant trend in surface temperature (likely due to the short timespan).

Trends in AERI microregions sensitive to water vapour and temperature are similar to the trends in MWR measurements of PWV and surface temperature at Eureka shown in Table 6.1, but generally not statistically significant. In the temperature microregion (674 to 679 cm^{-1}) radiances depend almost entirely on temperatures very near the surface; differences between

AERI and meteorological surface temperature trends are most likely due to differences in sampling. In the water vapour microregion (784-785 cm^{-1}), radiances measured by the AERI are sensitive to the entire water vapour column, but are most sensitive to the near-surface humidity (unlike the MWR); thus small differences are expected.

6.4.2 Comparison of Trends in Eureka and SGP Downwelling Radiances

When comparing radiance trends at 10 μm, the trend at Eureka during the winter is larger in magnitude than at the SGP and is in the opposite direction. In the SGP, statistically significant negative trends in the downwelling radiance at 10 μm region are found for all seasons except spring (March-May) and are between -0.25 and -1.25% / yr in magnitude. Gero and Turner [2011] attribute the negative radiance trends measured at the SGP to changes in cloudiness and an overall decrease in PWV over the SGP site. For Eureka, the significant positive trends in the 10 μm window are the result of increasing thick-cloud cover during the winter at the expense of thin-cloud cover. Hence like the SGP, trends in downwelling radiance at Eureka are associated with changes in cloud cover; unlike the SGP, trends at Eureka are not associated with PWV (although over a longer period of time this is plausible given the Arctic's long-term warming). The positive trend at 10 μm at Eureka during the winter is also much larger (factor > 3) in magnitude than during any season for the SGP. This indicates that changes in the downwelling radiance at 10 μm are accelerated in the high Arctic compared to lower latitudes during the seven months of Arctic winter, just as the changes in other atmospheric conditions such as temperature are more pronounced in the Arctic than other parts of the globe. There is thus evidence of change occurring in the surface energy budget at Eureka.

6.5 Summary of Measurements of Primary Cooling-to-Space Windows

Downwelling radiance and brightness temperature measurements were collected by AERI instruments in the Canadian high Arctic over an eight-year period. The consistency and reliability of this combined AERI dataset was verified, providing measurements of the two surface cooling-to-space windows at 10 μm and at 20 μm (the 'dirty window') in the high (> 75^{o} N) Arctic. Since an increase in emission allows for a clear distinction between spectra recorded during clear skies and spectra recorded when thin or thick clouds are present, radiance thresholds that change with each season (and, hence, PWV) were used to characterize the sky scene. This sky-scene characterization was tested and applied to AERI spectra, permitting designation of three distinct meteorological conditions: (1) clear skies, (2) thin clouds (optically thin or high-altitude), and (3) thick clouds (opaque or low-altitude). This dataset was compared to a similar dataset for the SGP and can be used to assess GCM simulations of brightness temperature distributions, cloud cover, and trends in radiance for the high Arctic's two surface cooling-to-space windows.

Distributions of brightness temperatures at 10 μm at Eureka were similar to those found at the SGP, with Eureka distributions shifted to colder temperatures. When separated by season, a distinct increase in brightness temperatures over Eureka was observed from winter to fall/spring to summer for both cooling-to-space windows. When water vapour is a maximum during the summertime, many scenes in the 20 μm microregion were warm independent of sky cover; hence distributions are narrow and do not vary with cloud thickness, indicating that this cooling-to-space window is mostly opaque (or "closed") in the summer. If the Arctic continues to warm at its current pace [ACIA, 2004; Richter-Menge, 2006; Bekryaev *et al*., 2010], the consequent increase in water vapour will increase the duration of the 20 μm window being closed, with important implications for the Arctic's energy balance; a shift towards warmer, 'summer-like' brightness temperatures will occur for other seasons, resulting in a net increase in year-round downwelling brightness temperatures regardless of cloud cover.

The distribution of clear-sky and thin-cloud brightness temperatures measured at 10 μm was similar to the distribution found at the SGP in Turner and Gero [2011] with a minor

difference in the all-sky distribution. Eureka brightness temperatures were found to occur at lower temperatures, as the second (warmer) mode of the bi-modal distributions is shifted to colder temperatures relative to the SGP, since it is colder in the Arctic than at the SGP.

The downwelling radiance in both the 10 and 20 μm cooling-to-space windows exhibited strong seasonal variability for all cloud thicknesses as a result of changes in temperature and water vapour. Despite the Eureka AERI dataset's short length compared to natural variability and variability in the temporal distribution, statistically significant trends were detected using the Weatherhead *et al.* method [1998] during the same time period. Radiance trends in seasonal averages at 20 μm existed for all seasons during this time period. Trends in seasonal averages at 10 μm during the winter were positive, in the opposite direction, and significantly larger (factor > 3) than any of the seasonal trends detected at the SGP, indicating that changes in the downwelling radiance are accelerated in the high Arctic compared to lower latitudes. This statistically significant increase (> 4% / yr) in radiance at 10 and 20 μm during the winter is mainly attributed to the increased prevalence of thick clouds at the expense of decreased thin clouds. It will be interesting to monitor these trends to determine whether they will continue, given that these trends are only for a short, eight-year period. Continued measurements are necessary to determine statistically significant correlations between the two cooling-to-space windows and surface measurements of temperature and PWV. A long-term record of integrated radiances throughout the entire 20 μm window (17-25 μm) could be compared to the entire 10 μm window (8-12 μm) to determine the effects of climate change on the Arctic's energy balance, particularly as the 20 μm window closes, and provide additional data for comparisons to climate models.

7. TRACE GAS RETRIEVAL TECHNIQUE

Emission spectra measured by the AERI can be used for more than radiative studies of the Earth's atmosphere. It is possible to infer the concentration of atmospheric gases by analyzing the shape and strength of the measured emission lines. Each molecule has a unique 'spectral fingerprint' in the form of discrete emission lines at particular wavelengths (or wavenumbers). Once the molecular fingerprints are characterized (via laboratory measurements), the measured emission spectra can be analyzed using a retrieval algorithm in order to determine the concentration of a particular gas in the atmosphere. This concept in spectroscopy has been long-established and applied to a range of phenomena, from investigating the composition of distant stars to quantifying pollution levels in a crowded city. The recent explosion in computing power has enabled us to perform these retrievals, which are inherently non-linear, complex, and hence computationally expensive, for a hundreds of atmospheric species in a matter of minutes using a retrieval algorithm in conjunction with remote sensing instruments (such as the AERI), which do not require the instrument to move or physically 'touch' the gas as with *in situ* measurements. The technique to perform these retrievals is presented in this Chapter.
Portions of this Chapter have been published in Mariani et al. (2013).

7.1 Retrieval Theory

7.1.1 The Optimal Estimation Method

The spectra derived from the interferograms recorded by the E-AERI can be analyzed to obtain the concentrations of specific trace gases in the atmosphere. This process, referred to as the 'inverse problem,' can be difficult to achieve if the mathematical formulation is ill-conditioned, ill-posed, or nonlinear, which is often the case since the atmosphere is not a controlled environment. The retrieval problem for trace gases using emission spectra is more

nonlinear than using solar absorption spectra (and hence more difficult) due to the addition of the emission term in the radiative transfer equation (described in Sect. 7.3.2) and decreased SNR (particularly in spectral regions with near-zero emission). In order to solve this ill-posed problem, optimizing the information content for each measurement can be achieved by combining observations with known quantities (called the *a priori*). This technique, known as the Optimal Estimation Method (OEM) as developed by Rodgers [1976, 1990, 2000], is commonly used in the atmospheric research community for retrievals from absorption and/or emission spectra from various types of FTSs.

To examine the information content, the atmosphere is described by measurements in a vector **y** and the unknowns sorted into a state vector **x**. Hence for E-AERI observations, measured radiances will occupy **y** while volume mixing ratios (VMRs) of the trace gases will occupy **x**. Measurements are described by a forward model, **F(x, b)**, which describes the physics of the measurement process via:

$$\mathbf{y} = \mathbf{F(x, b)} + \boldsymbol{\varepsilon} \tag{7.1}$$

where $\boldsymbol{\varepsilon}$ is the measurement error and **b** contains all parameters which influence the retrieval but are not retrieved (e.g., profiles of temperature and pressure). The forward model captures our entire understanding of the physics of the measurement, **y**.

As previously mentioned, with the OEM observations are combined with our best estimate of the true state. Hence it is necessary to use an *a priori* estimate of the atmospheric state, $\mathbf{x_a}$, and our best estimate of the model parameters, $\hat{\mathbf{b}}$, in conjunction with Eqn. **(7.1)**. To simplify this problem, it is convenient to linearize the model by performing a Taylor Series expansion about these estimates:

$$\mathbf{F}(\mathbf{x}, \mathbf{b}) = \mathbf{F}\left(\mathbf{x}_a, \hat{\mathbf{b}}\right) + \frac{\partial \mathbf{F}}{\partial \mathbf{x}}(\mathbf{x} - \mathbf{x_a}) + \frac{\partial \mathbf{F}}{\partial \mathbf{b}}\left(\mathbf{b} - \hat{\mathbf{b}}\right) + \cdots + \boldsymbol{\varepsilon} \ . \tag{7.2}$$

Since it is assumed that the forward model is linear over the range of the *a priori* and true state spaces, the higher-order terms in Eqn. **(7.2)** (expressed as "…") can be neglected. If it can be assumed that the forward function is invertible, then an inverse function, **R**, maps values from measurement space into the atmospheric state space:

$$\hat{\mathbf{x}} = \mathbf{R}\left(\mathbf{y}, \hat{\mathbf{b}}, \mathbf{x}_a, \mathbf{c}\right),$$
$$\hat{\mathbf{x}} = \mathbf{R}\left[\mathbf{F}(\mathbf{x}, \mathbf{b}) + \boldsymbol{\varepsilon}, \hat{\mathbf{b}}, \mathbf{x}_a, \mathbf{c}\right] \tag{7.3}$$

where $\hat{\mathbf{x}}$ is the retrieved state vector and **c** is the vector containing any additional parameters used in the retrieval that do not appear in the forward model. By substituting Eqn. **(7.2)** into Eqn. **(7.3)**, we achieve:

$$\hat{\mathbf{x}} = \mathbf{R}\left[\mathbf{F}\left(\mathbf{x}_a, \hat{\mathbf{b}}\right) + \frac{\partial \mathbf{F}}{\partial \mathbf{x}}\left(\mathbf{x} - \mathbf{x}_\mathbf{a}\right) + \frac{\partial \mathbf{F}}{\partial \mathbf{b}}\left(\mathbf{b} - \hat{\mathbf{b}}\right) + \boldsymbol{\varepsilon}, \hat{\mathbf{b}}, \mathbf{x}_a, \mathbf{c}\right],$$
$$\hat{\mathbf{x}} = \mathbf{R}\left[\mathbf{F}\left(\mathbf{x}_a, \hat{\mathbf{b}}\right) + \mathbf{K}\left(\mathbf{x} - \mathbf{x}_\mathbf{a}\right) + \mathbf{K}_\mathbf{b}\left(\mathbf{b} - \hat{\mathbf{b}}\right) + \boldsymbol{\varepsilon}, \hat{\mathbf{b}}, \mathbf{x}_a, \mathbf{c}\right] \tag{7.4}$$

where $\hat{\mathbf{x}}$ is the retrieved best estimate of the true atmospheric state. **K** is the weighting function matrix and $\mathbf{K_b}$ is the parameter space weighting function matrix. The sensitivity of the forward model to the true atmospheric state and true model parameters is provided by the weighting function matrices, which are defined in general as:

$$\mathbf{K_{ij}} = \frac{\partial \mathbf{F_i}(\mathbf{x})}{\partial \mathbf{x_j}} \ . \tag{7.5}$$

Next, the inverse equation given in Eqn. **(7.4)** can be linearized by performing a Taylor Series expansion with respect to $\mathbf{F}\left(\mathbf{x}_a, \hat{\mathbf{b}}\right)$ to produce:

$$\hat{\mathbf{x}} = \mathbf{R}\left[\mathbf{F}\left(\mathbf{x}_a, \hat{\mathbf{b}}\right), \hat{\mathbf{b}}, \mathbf{x}_a, \mathbf{c}\right] + \frac{\partial \mathbf{R}}{\partial \mathbf{y}}\left[\mathbf{K}\left(\mathbf{x} - \mathbf{x}_\mathbf{a}\right) + \mathbf{K}_\mathbf{b}\left(\mathbf{b} - \hat{\mathbf{b}}\right) + \boldsymbol{\varepsilon}\right],$$
$$\hat{\mathbf{x}} = \mathbf{x}_a + \mathbf{G}\mathbf{K}\left(\mathbf{x} - \mathbf{x}_\mathbf{a}\right) + \mathbf{G}\mathbf{K}_\mathbf{b}\left(\mathbf{b} - \hat{\mathbf{b}}\right) + \mathbf{G}\boldsymbol{\varepsilon} \tag{7.6}$$

where **G** is called the gain matrix and represents the sensitivity of the retrieved state to the measurements. Eqn. **(7.6)** can be generalized into an expression solely for the atmospheric state space:

$$\hat{\mathbf{x}} = \mathbf{x}_a + \mathbf{A}\left(\mathbf{x} - \mathbf{x}_\mathbf{a}\right) + \boldsymbol{\varepsilon}_\mathbf{x} \tag{7.7}$$

where $\boldsymbol{\varepsilon_x}$ represents all error terms and **A** is the averaging kernel matrix formulated as:

$$\mathbf{A} = \mathbf{GK} \tag{7.8}$$

$$\mathbf{A} = \frac{\partial \hat{\mathbf{x}}}{\partial \mathbf{y}} \frac{\partial \mathbf{y}}{\partial \mathbf{x}} = \frac{\partial \hat{\mathbf{x}}}{\partial \mathbf{x}} \tag{7.9}$$

which represents the sensitivity of the retrieved state to the true atmospheric state. The averaging kernel describes the subspace of the state space where the retrieval exists. Hence the rows of **A** characterize the relationship between the retrieval and the true state [Rodgers, 2000]. The rows can be summed to obtain the sensitivity of the measurement, which indicates the fraction of the retrieval that is derived directly from the measurement as opposed to the *a priori*.

The averaging kernel matrix is also capable of quantifying the vertical resolution of the retrieval, called the Degrees Of Freedom for Signal (DOFS). The DOFS represents the number of independent quantities that can be determined from a single measurement, and is expressed as:

$$\text{DOFS} = tr(\mathbf{A}) \tag{7.10}$$

where *tr*(**A**) is the trace of the matrix **A**. Since DOFS is a measure of information, it allows one to quantify the information content of each measurement.

7.1.2 Applying Bayes' Theorem

The best estimate of the atmospheric state is acquired by combining the true state with *a priori* information. This is necessary since **x** in Eqn. **(7.7)** is unknown. Performing measurements maps the state into the measurement space according to the forward model. However, a point in state space maps into a region in measurement space that is determined by the Probability Density Function (PDF) of $\boldsymbol{\varepsilon}$ because it is only known statistically; thus one must select an approach based on statistical methods in order to combine the true state with the *a priori*. The Bayesian Inference is used to determine the *Maximum A Posteriori* (MAP) estimator in order to determine the retrieval's weight towards the *a priori* vs. the weight towards

the measurements. The MAP estimator chooses the most likely (or mean) state averaged over the PDF.

According to Bayes' Theorem [Bayes, 1763]:

$$P(\mathbf{x}|\mathbf{y}) = \frac{P(\mathbf{y}|\mathbf{x})P(\mathbf{x})}{P(\mathbf{y})} \tag{7.11}$$

where $P(\mathbf{x})$ is the PDF of the *a priori*, or state $\mathbf{x}$ (and similar for $\mathbf{y}$), $P(\mathbf{y}|\mathbf{x})$ is the PDF of the observation and depends on the experimental error and forward function, or the PDF of $\mathbf{y}$ given $\mathbf{x}$, and $P(\mathbf{x}|\mathbf{y})$ is the conditional PDF of $\mathbf{x}$ given $\mathbf{y}$, also known as the *a posteriori* estimate [Rodgers, 2000]. It is $P(\mathbf{x}|\mathbf{y})$ that we want to maximize in Bayes' Theroem. It is assumed that there is a linear relationship between $\mathbf{x}$ and $\mathbf{y}$ ($\mathbf{y} = \mathbf{K}\mathbf{x}$) and the PDF distributions are Gaussian, such that:

$$P(\mathbf{y}) = \frac{1}{(2\pi)^{n/2}|\mathbf{S_y}|^{1/2}} e^{-\frac{1}{2}(\mathbf{y}-\bar{\mathbf{y}})^{\mathrm{T}}\mathbf{S_y}^{-1}(\mathbf{y}-\bar{\mathbf{y}})},$$

$$-2\ln[P(\mathbf{y})] = (\mathbf{y} - \bar{\mathbf{y}})^{\mathrm{T}}\mathbf{S_y}^{-1}(\mathbf{y} - \bar{\mathbf{y}}) + 2\ln\left[(2\pi)^{\frac{n}{2}}|\mathbf{S_y}|^{\frac{1}{2}}\right],$$

$$-2\ln[P(\mathbf{y})] = (\mathbf{y} - \bar{\mathbf{y}})^{\mathrm{T}}\mathbf{S_y}^{-1}(\mathbf{y} - \bar{\mathbf{y}}) + C_y \tag{7.12}$$

where $\bar{\mathbf{y}}$ is the mean of the observation, $\mathbf{y}$, n is the number of elements in the vector, $\mathbf{S_y}$ is the measurement error covariance matrix, and C_y is a constant term. Using this approach, $P(\mathbf{x})$ and $P(\mathbf{y}|\mathbf{x})$ can be expressed as:

$$-2\ln[P(\mathbf{x})] = (\mathbf{x} - \mathbf{x_a})^{\mathrm{T}}\mathbf{S_a^{-1}}(\mathbf{x} - \mathbf{x_a}) + C_x \tag{7.13}$$

$$-2\ln[\mathrm{P}(\mathbf{y}|\mathbf{x})] = (\mathbf{y} - \mathbf{F}(\mathbf{x},\mathbf{b}))^{\mathrm{T}}\mathbf{S_\varepsilon^{-1}}(\mathbf{y} - \mathbf{F}(\mathbf{x},\mathbf{b})) + C_{yx} \tag{7.14}$$

where $\mathbf{S_a}$ = *a priori* covariance matrix $(\mathbf{x}-\mathbf{x_a})(\mathbf{x}-\mathbf{x_a})^{\mathrm{T}}$, and $\mathbf{S_\varepsilon}$ = error covariance matrix. The maximum probability for $\mathbf{x}$ is equal to the expected value $\bar{\mathbf{x}}$ because the PDF, assumed to be Gaussian, is symmetric about $\mathbf{x} = \bar{\mathbf{x}}$ [Rodgers, 2000]. Note that $P(\mathbf{y})$ is considered a normalizing

factor; as such it is neglected when calculating $P(\mathbf{x}|\mathbf{y})$. To obtain a MAP estimator, the derivative of Eqn. **(7.11)** is set to equal zero:

$$\nabla_{\mathbf{x}}\{-2\ln[P(\mathbf{x}|\mathbf{y})]\} = \nabla_{\mathrm{x}}[(\mathbf{y} - \mathbf{F}(\mathbf{x},\mathbf{b}))^{\mathrm{T}}\mathbf{S}_{\boldsymbol{\varepsilon}}^{-1}(\mathbf{y} - \mathbf{F}(\mathbf{x},\mathbf{b}))] + \nabla_{\mathbf{x}}[(\mathbf{x} - \mathbf{x}_{\mathbf{a}})^{\mathrm{T}}\mathbf{S}_{\mathbf{a}}^{-1}(\mathbf{x} - \mathbf{x}_{\mathbf{a}})] = 0 \quad \textbf{(7.15)}$$

from which we define the cost function, $\mathbf{J}(\mathbf{x})$ to be:

$$\mathbf{J}(\mathbf{x}) = \big(\mathbf{y} - \mathbf{F}(\mathbf{x},\mathbf{b})\big)^{\mathrm{T}}\mathbf{S}_{\boldsymbol{\varepsilon}}^{-1}\big(\mathbf{y} - \mathbf{F}(\mathbf{x},\mathbf{b})\big) + (\mathbf{x} - \mathbf{x}_{\mathbf{a}})^{\mathrm{T}}\mathbf{S}_{\mathbf{a}}^{-1}(\mathbf{x} - \mathbf{x}_{\mathbf{a}})\,. \quad \textbf{(7.16)}$$

Clearly, the *a priori* and its covariance matrix must be carefully selected due to their large impact on the retrieval's outcome. The MAP solution occurs when $P(\mathbf{x}|\mathbf{y})$ is a maximum, or $\mathbf{J}(\mathbf{x})$ is a minimum. Since it is assumed that the problem is moderately linear, Newtoninan iteration is used to solve $\nabla_{\mathbf{x}}\mathbf{J}(\mathbf{x}) = 0$ via:

$$\mathbf{x}_{i+1} = \mathbf{x}_i - [\nabla_{\mathrm{x}}\nabla_{\mathrm{x}}\mathbf{J}(\mathbf{x}_i)]^{-\mathbf{1}}\nabla_{\mathrm{x}}\mathbf{J}(\mathbf{x}_i)\,. \quad \textbf{(7.17)}$$

By substituting Eqn. **(7.16)** into Eqn. **(7.17)** and setting $\mathbf{x}_{\mathbf{a}}$ as the initial step ($i = 0$), the optimal solution is:

$$\mathbf{x}_{i+1} = \mathbf{x}_{\mathbf{a}} + (\mathbf{S}_{\mathbf{a}}^{-1} + \mathbf{K}_{\mathbf{i}}{}^{\mathrm{T}}\mathbf{S}_{\boldsymbol{\varepsilon}}^{-1}\mathbf{K}_{\mathbf{i}})^{-1}\mathbf{K}_{\mathbf{i}}{}^{\mathrm{T}}\mathbf{S}_{\boldsymbol{\varepsilon}}^{-1}\big[\big(\mathbf{y} - \mathbf{F}(\mathbf{x}_{\mathbf{i}})\big) - \mathbf{K}_{\mathbf{i}}(\mathbf{x}_{\mathbf{a}} - \mathbf{x}_{\mathbf{i}})\big] \quad \textbf{(7.18)}$$

where $\mathbf{K}$ is called the Jacobian matrix and expressed as $\mathbf{K} = \frac{\partial \mathbf{y}}{\partial \mathbf{x}} = \nabla_{\mathbf{x}}\mathbf{F}$. Analogous to solving $\nabla_{\mathbf{x}}\mathbf{J}(\mathbf{x}) = 0$ numerically as above, we can obtain the analytical solution:

$$\hat{\mathbf{x}} = \mathbf{x}_{\mathbf{a}} + (\mathbf{K}^{\mathrm{T}}\mathbf{S}_{\boldsymbol{\varepsilon}}^{-1}\mathbf{K} + \mathbf{S}_{\mathbf{a}}^{-1})^{-1}\mathbf{K}^{\mathrm{T}}\mathbf{S}_{\boldsymbol{\varepsilon}}^{-1}(\mathbf{y} - \mathbf{K}\mathbf{x}_{\mathbf{a}})\,,$$
$$\hat{\mathbf{x}} = \mathbf{x}_{\mathbf{a}} + \mathbf{G}(\mathbf{y} - \mathbf{K}\mathbf{x}_{\mathbf{a}}) \quad \textbf{(7.19)}$$

where the expressions for the gain matrix and averaging kernel matrix become:

$$\mathbf{G} = \mathbf{S}_{\mathbf{a}}\mathbf{K}^{\mathrm{T}}(\mathbf{K}\mathbf{S}_{\mathbf{a}}\mathbf{K}^{\mathrm{T}} + \mathbf{S}_{\boldsymbol{\varepsilon}})^{-1} \quad \textbf{(7.20)}$$

$$\mathbf{A} = (\mathbf{S_a^{-1}} + \mathbf{K}^T\mathbf{S_\varepsilon^{-1}}\mathbf{K})^{-1}\mathbf{K}^T\mathbf{S_\varepsilon^{-1}}\mathbf{K}\,.$$

(7.21)

7.2 Error Analysis

Error estimates of trace gas total columns are essential when reporting final results. The error analysis is a vital part of the documentation of any retrieved data set as it helps identify characteristics of retrievals that can be optimized [Rodgers, 2000]. The uncertainty in the measured total columns is determined following the method described in Rodgers [2000], which has been implemented for many other instruments (e.g., the PEARL 125HR SFIT2 retrievals [Batchelor *et al*., 2009]). The error expression can be derived by including all the errors in the measurements and model parameters in Eqn. **(7.6)** to produce:

$$\hat{\mathbf{x}} = \mathbf{x}_a + \mathbf{A}(\mathbf{x} - \mathbf{x_a}) + \mathbf{G}\mathbf{K_b}\left(\mathbf{b} - \hat{\mathbf{b}}\right) + \mathbf{G}\Delta\mathbf{f}(\mathbf{x}, \mathbf{b}, \mathbf{b}') \; + \mathbf{G}\boldsymbol{\varepsilon}$$

(7.22)

where $\mathbf{b}'$ is the parameters of the forward function **f** that have been ignored when constructing the forward model **F(x,b)**. Thus $\Delta\mathbf{f}(\mathbf{x}, \mathbf{b}, \mathbf{b}')$ is the error in the forward model relative to the real physics. The individual error components can be extracted by subtracting the true state from the retrieved state and rearrangement of Eqn. **(7.22)**:

$$\hat{\mathbf{x}} - \mathbf{x} = \underbrace{(\mathbf{A} - \mathbf{I})(\mathbf{x} - \mathbf{x_a})}_{\text{smoothing error}} + \underbrace{\mathbf{G}\mathbf{K_b}\left(\mathbf{b} - \hat{\mathbf{b}}\right)}_{\text{model parameter error}} + \underbrace{\mathbf{G}\Delta\mathbf{f}(\mathbf{x}, \mathbf{b}, \mathbf{b}')}_{\text{forward model error}} + \underbrace{\mathbf{G}\boldsymbol{\varepsilon}}_{\text{retrieval noise}}$$

(7.23)

where **I** is the unity matrix (used to manipulate Eqn. **(7.22)** to achieve the form of $\hat{\mathbf{x}} - \mathbf{x}$) and the error components are labelled below each term. Since the true state is unknown, error covariance matrices over an ensemble of states are used to determine the total error via:

$$\mathbf{S_s} = (\mathbf{A} - \mathbf{I})\mathbf{S_a}(\mathbf{A} - \mathbf{I})^T$$

(7.24)

$$\mathbf{S_f} = \mathbf{G}\mathbf{K_b}\mathbf{S_b}\mathbf{G}^T{\mathbf{K_b}}^T$$

(7.25)

$$\mathbf{S_m} = \mathbf{G}\mathbf{S_\varepsilon}\mathbf{G}^T \tag{7.26}$$

where $\mathbf{S_s}$ is the smoothing error covariance, $\mathbf{S_f}$ is the model parameter error covariance, $\mathbf{S_b}$ is the error covariance matrix of **b**, and $\mathbf{S_m}$ is the retrieval noise error covariance. Note the forward model error is usually neglected since it is systematic and attempting to calculate it without knowing the true state, **x**, or the non-retrieved retrieval parameters, **b**, is computationally expensive and difficult. Previous work has shown that errors arising from forward model ray-tracing errors are < 1% [Schneider *et al.*, 2005]. The smoothing error is introduced by interpolating the true profile (which is an infinite-layer grid) onto a finite (*N*-layer) grid. The model parameter error covariance is caused by biases in the forward model parameters and contains both random and systematic errors.

The smoothing error ($\mathbf{S_s}$) and measurement error ($\mathbf{S_m}$) are added in quadrature with the model parameter errors ($\mathbf{S_f}$), forward model error, and interference errors. Model parameter errors are determined using a perturbation method for temperature, $\mathbf{S_{temp}}$, and the largest estimates of the uncertainties provided in HITRAN 2008 for $\mathbf{S_{lint}}$ (line intensity) and $\mathbf{S_{lwidth}}$ (air-broadened half-width) [Rothman *et al.*, 2009]. If the uncertainty is not provided in HITRAN 2008, a 20% uncertainty is assigned. The interference errors, $\mathbf{S_{intspec}}$ and $\mathbf{S_{intret}}$, are the errors in the retrieved column due to the constraint posed on the jointly retrieved quantities. The latter includes instrument lineshape, wavelength shift, background slope and curvature, phase error and zero level shift; their combination is described in Rodgers and Connor [2003]. Hence the total error, $\mathbf{S_{tot}}$, can be expressed as:

$$\mathbf{S_{tot}} = \sqrt{\mathbf{S_s}^2 + \mathbf{S_m}^2 + \mathbf{S_{temp}}^2 + \mathbf{S_{lint}}^2 + \mathbf{S_{lwidth}}^2 + \mathbf{S_{intret}}^2 + \mathbf{S_{intspec}}^2} \tag{7.27}$$

The smoothing error ($\mathbf{S_s}$) is a systematic error on short timescales, but random on long time scales (when $\mathbf{S_a}$ becomes a covariance over the large ensemble of atmospheric states) [Lindenmaier, 2012]. The uncertainty due to measurement noise ($\mathbf{S_m}$) is considered to be random, and the uncertainty due to spectroscopic parameters ($\mathbf{S_{lint}}$ and $\mathbf{S_{lwidth}}$) is mostly systematic, although a clear division between systematic and random uncertainties is not absolute. Since the different error sources are uncorrelated among each other, these errors have been added in quadrature, as recommended by the International Organization of Standardization

[1993]. The calculation of the covariance matrices discussed above is described in more detail in Sect. 8.1.

7.3 The SFIT2 Retrieval Algorithm

7.3.1 The SFIT2 Retrieval Algorithm

In order to retrieve concentrations of trace gases, spectra collected by the E-AERI must be analyzed using a retrieval algorithm. SFIT2 is a radiative transfer and profile retrieval algorithm based on the OEM of Rodgers [1976; 1990; 2000]. SFIT2 is widely used in the IR remote sounding community and has undergone extensive validation exercises [e.g., Hase *et al*., 2004]. The algorithm was originally created by C. P. Rinsland (NASA Langley Research Centre) and B. J. Connor (National Institute of Water and Atmospheric Research, New Zealand) and is used to calculate the concentration of a target trace gas from measured spectra. It is widely used in the Network for the Detection of Atmospheric Composition Change (NDACC) Infrared Working Group (IRWG) (e.g., the PEARL 125HR retrievals use SFIT2). To do this, it produces a calculated spectrum (with the same spectral resolution as the spectrometer) that is fitted to an observed spectrum by adjusting the trace gas volume mixing ratio profiles [Pougatchev *et al*., 1995; Rinsland *et al*., 1998]. The solution is found iteratively, and the iteration is performed until the iteration converges. Convergence is normalized (over the number of spectral points) such that if it converges to the level of noise, convergence = 1. The tolerance, which is the change in the convergence value (from 1.2 to 1.1, for instance), is set to 0.1. Once the change in convergence is less than 0.1, it stops the iteration and claims convergence. This entire process is illustrated in Figure 7.1. SFIT2 can be used in conjunction with FTIR spectra to retrieve more than 25 trace gases.

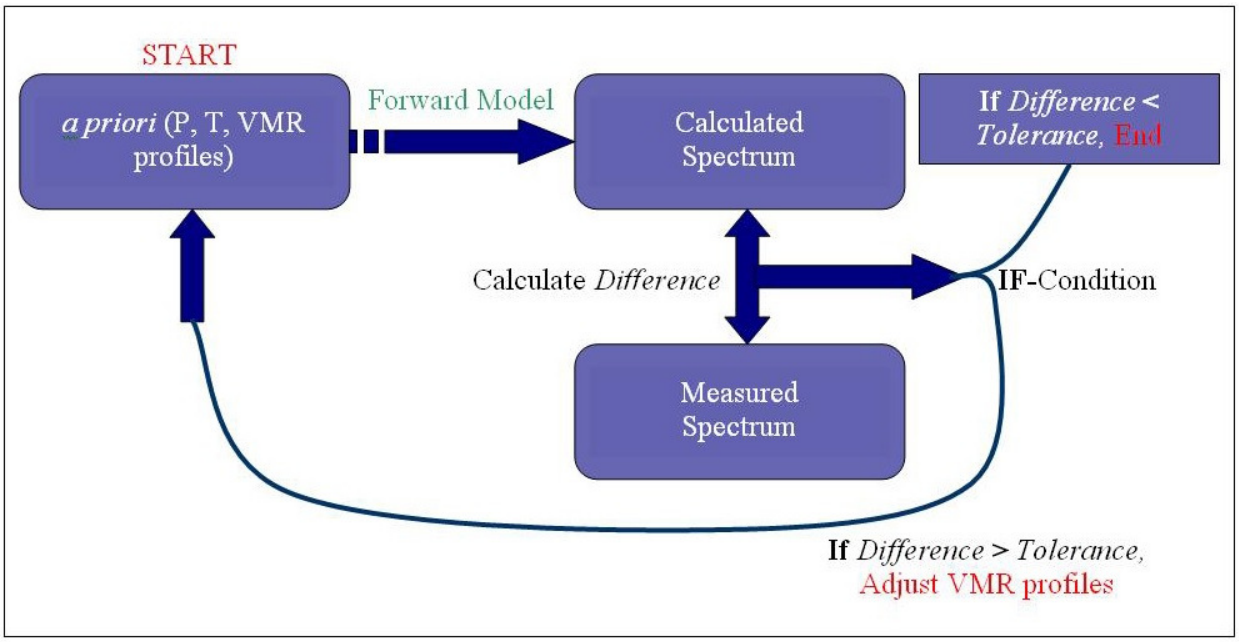

Figure 7.1: Simplified flow-chart diagram of the OEM implemented in SFIT2.

The forward model is a multispecies, multilayer, line-by-line radiative transfer model. The model assumes the Voigt lineshape function, local thermodynamic equilibrium, and homogeneous layers of the atmosphere. The *a priori* VMR profiles for the target trace gas, *a priori* covariance matrix, $\mathbf{S_a}$, and *a priori* interfering species VMR profiles are required inputs for the OEM SFIT2 uses. Additionally, SFIT2 requires instrument parameters to characterize its forward model (such as instrument FOV) and the section of the spectrum sensitive to the target trace gas to be fit (called 'miniwindows' or 'microwindows,' described in Sect. 7.5). SFIT2 is used in conjunction with HITRAN 2008 [Rothman *et al*., 2009], which provides spectral line parameters for line-by-line calculations of the atmospheric spectrum, and a model atmosphere is created via refractive ray-tracing and airmass path calculations computed using the FASTCODE (also referred to as FSCATM) algorithm [Meier *et al*., 2004]. FASTCODE provides the air mass distribution (the number of molecules as a function of altitude) and converts twice-daily radiosonde profiles of pressure, temperature, and *a priori* VMR profiles (described in Sect. 7.4.3) on a 61-layer grid to a density-weighted grid used by SFIT2. The number of layers of the density-weighted retrieval grid is specified by the user and can be altered at any time. With the OEM, the retrieved profile can be expressed as a linear combination of the *a priori* and the true state with error contributions.

Emission spectra are converted into ASCII file format prior to the retrieval. A *binput* file, in ASCII format, is created and used to specify: a) target trace gas, b) interfering trace gas species, c) the retrieval altitude grid, d) site information (lat/lon, elevation, etc.), e) instrument parameters (including FOV, maximum OPD, etc.), f) forward model parameters, g) *a priori* and uncertainties, h) information for the miniwindow (end points), and i) covariance matrices ($\mathbf{S}_{\varepsilon}$, $\mathbf{S}_{\mathbf{a}}$). Details on the construction of these input parameters are provided in Sect. 7.4.1.

7.3.2 The SFIT2+Emission Add-on

The SFIT2 retrieval code has recently been modified so that it can be applied to IR emission spectra, such as those recorded by the E-AERI. The SFIT2 retrieval code (along with its predecessors) was designed to use solar absorption measurements from an FTIR as input to the forward model. Hence modifications to the original SFIT2 (v. 3.93) code were required in order to adapt the algorithm to be used with emission spectra, such as those produced by the E-AERI. In this new emission add-on (SFIT2 v. 3.93+Emission), the retrieval code has been modified with an extension to calculate the full radiative transfer. The radiative transfer is given by Eqn. **(2.5)** and its integral form is:

$$I_{\tilde{\nu}}(z) = S_{\tilde{\nu}}(z_{\infty})e^{-\tau_{\tilde{\nu}}(0,z_{\infty})} + \int_{\infty}^{0} S_{\tilde{\nu}}(z)\frac{de^{-\tau_{\tilde{\nu}}(0,z)}}{dz}dz \qquad \textbf{(7.28)}$$

where $\tau_{\tilde{\nu}}(0, z_{\infty})$ denotes the opacity from the ground to the top of the atmosphere, $\tau_{\tilde{\nu}}(0, z)$ denotes the opacity from layer z to the observer at 0 and is equivalent to $\int_0^z k_{\tilde{\nu}}\rho(z)\,\mathrm{d}z$, $S_{\tilde{\nu}}(z_{\infty})$ is the source term for the background (top of atmosphere) radiation and equivalent to $I_{\tilde{\nu}}$ in Eqn. **(2.4)**, and $S_{\tilde{\nu}}(z)$ is the source term (Eqn. **(2.1)**) of the layer z. While in solar absorption spectroscopy, the rightmost term in Eqn. **(7.28)** can normally be neglected (except for optically thick regions of the atmosphere) due to the negligible emission of the atmosphere compared to the Sun, in emission spectroscopy this is the main source of radiation. The numerical iteration scheme used to find the zero of the gradient of the cost function in the OEM (Eqn. **(7.16)**) has also been changed from Gauss-Newton to Levenberg-Marquardt, which is more efficient in finding nonlinear solutions when the true solution is far from the current iteration point, as for weakly nonlinear problems [M. Palm; personal communication].

When SFIT2 is run, the model atmosphere is used in each iteration step to calculate the IR emission spectrum for the target and interfering trace gas species in the defined miniwindow. The original automation code, called *zephyr2* [Wood *et al.*, 2000], is incompatible with the new file system format used in SFIT2+Emission; hence a new automation code was written to achieve automation of the SFIT2 analysis on the extremely large (over 200,000 spectra) E-AERI dataset. The automation code, titled 'loop_SFIT2', is a bash script that can be used on any emission spectra in conjunction with SFIT2+Emission. E-AERI total column retrievals of O_3, CO, CH_4 and N_2O have been performed year-round using this new version of SFIT2 and are described in more detail in this Chapter. This new emission version of SFIT2 has been implemented in the next version of the code, SFIT4, by M. Palm (U. Bremen) and was released in early 2014.

7.4 Retrieval Implementation

7.4.1 E-AERI SFIT2 Retrievals

Due to the relatively low spectral resolution of the E-AERI, profile-scaled retrievals were performed (rather than full profile retrievals) in which the entire *a priori* profile of the trace gas is uniformly shifted (increased/decreased) by a scaling factor to match the true state. The scaled retrievals have DOFS just below 1 (> 0.9) per species and provide only the total column concentration. For this work, spectra collected in a one-hour window are averaged to produce a dataset of hourly-averaged radiances to improve the SNR; typically eight spectra are averaged in a one-hour window.

Attempts to perform retrievals on a multi-layer grid (i.e. 'profile retrievals,' such as performed for spectra recorded with the higher-resolution Bruker 125HR) resulted in convergence problems, likely due to the lack of vertical sensitivity in the lower-resolution E-AERI spectra. Extensive work went into attempting to achieve profile retrievals using E-AERI spectra: profile retrievals of O_3, CO, CH_4, and N_2O were originally attempted using relatively wide miniwindows which include a range of radiances but encountered several difficulties and overall did not perform as well as the scaled retrievals (spectral fits were worse, convergence problems were encountered, and comparisons to other ground-based spectrometers at Eureka

were far worse). An example of the result of performing scaled retrievals is provided in Figure 7.2; the retrieval produces an increased O_3 column (compared to the *a priori*) as indicated by the increased VMR profile, which is in agreement with the expected O_3 concentration at that time of year (February). The possibility of performing profile retrievals remains the basis of future work with the implementation of the new SFIT4 retrieval algorithm.

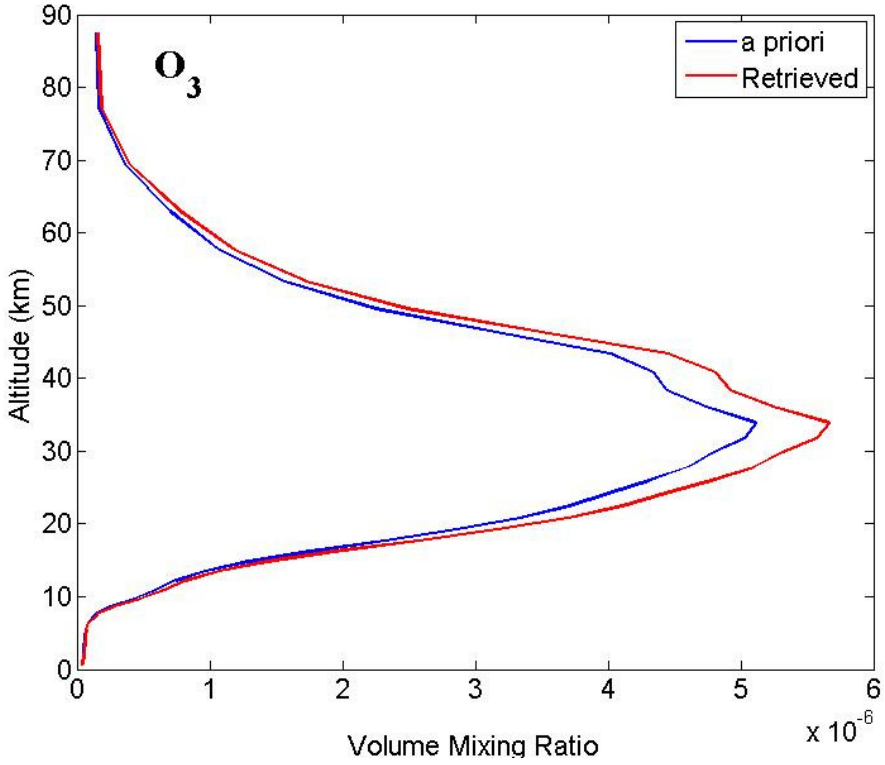

Figure 7.2 Sample E-AERI scaled O_3 retrieval. The *a priori* profile (blue) has been scaled by a factor of 1.1077 as a result of the SFIT2 retrieval, producing the retrieved profile (red). Retrieval was performed on hourly-averaged spectra on February 9, 2012, for 12:00-13:00 UTC.

An independent wavelength shift parameter for each miniwindow and the background slope (any offset of the spectrum) are fitted. The *a priori* VMR profiles of the interfering species were scaled simultaneously with the target trace gas during the retrievals. SFIT2 can incorporate a maximum of nine interfering species for each miniwindow, which, in effect, places a limit on the maximum size of the miniwindow. While column retrievals are usually well constrained and need no regularization, the fact that columns of multiple species (target and interfering) are retrieved in one inversion adds instability which is remedied by the use of OEM. Daily profiles of pressure and temperature were obtained from a combination of three sources: two daily

launches of radiosondes (6:15 a.m. and 6:15 p.m. EST) at Eureka were averaged to provide information up to 35 km, the National Centers for Environmental Prediction (NCEP) analyses from the NASA Goddard Space Flight Centre provided information from 35-50 km, and the 1976 US Standard Atmosphere was used above 50 km. When the retrieval has converged on a final solution, the result is the full vertical profile of the target gas (the state vector $\hat{\mathbf{x}}$ consisting of N target gas profile elements, where N is the number of layers in the retrieval grid), the scaling factors applied to the *a priori* profiles of interfering species, and the forward model parameters (i.e., background slope and curvature, wavenumber shift, phase error, etc.).

7.4.2 Implementing the Cloud Filter

Retrievals of trace gases when clouds are present are difficult due to the increased emission from cloud particles, causing a large increase in baseline radiance. This increased emission dwarfs the spectral signature from the trace gases of interest. Hence the cloud filter described in Sect. 5.3 was used to classify and eliminate all cloudy E-AERI spectra from retrievals. Spectra classified as having thin clouds (the lowest – and most conservative – radiance threshold) using the radiance thresholds in Table 5.1 were considered 'cloudy spectra' and filtered out. Thin clouds and aerosols can result in poorer spectral fits, reinforcing the requirement of the conservative cloud-filtering process. The impact of including spectra during thin clouds and/or periods of high aerosol concentrations on the retrieval will be discussed in more detail later in this Chapter. Spectra classified as having thick clouds were also (more obviously) filtered out due to their large impact on the baseline radiance. These relatively opaque clouds effectively limit the E-AERI sky scene observation up to the altitude of the cloud base height throughout much of the miniwindows, absorbing the emission from higher in the atmosphere. Hence only spectra classified as 'clear sky' by the cloud filter were used in all trace gas retrievals presented in this Chapter.

7.4.3 *a priori* Trace Gas Profiles

A priori estimates of trace gas VMR profiles at Eureka have been provided for 64 trace gases and used in previous studies involving SFIT2 retrievals [Batchelor *et al*., 2009; Lindenmaier *et al*., 2010]. These profiles were produced from a climatology of satellite, ground-

based, model, and balloon measurements. For the four gases studied in this work, over 7000 HALOE (lat > 65°N) profiles from 1991-2005 were used for CH_4 [Park *et al*., 1996]; the Eureka ozonesonde archive (1993-2005) and HALOE were used for O_3 (averaged ozonesondes up to 35 km alt., HALOE > 35 km) [Lindenmaier *et al*., 2010]; MkIV balloon measurements made at the high-latitude NDACC site at Kiruna, Sweden, were used for CO; and monthly mean VMRs reported in the SPARC2000 compilation (lat > 68°N) were used for N_2O [Randel *et al*., 2002]. The *a priori* profiles are zonally averaged mean VMR profiles of the climatological data sets (where latitude > 65°N) available. For more detail about these climatologies, see Lindenmaier [2012], Sect. 3.4. This same dataset was used to calculate the variance in the VMR profiles as a function of altitude. From these variances, the *a priori* covariance matrix, $\mathbf{S_a}$, can be calculated, as described in Sect. 8.1.

7.4.4 Retrievals at the PEARL Ridge Lab vs. at 0PAL

Clear-sky total columns of O_3, CO, CH_4, and N_2O from the PEARL Ridge Lab (610 m a.s.l.) were retrieved using hourly-averaged E-AERI spectra (described in Sect. 7.4.1 and 7.4.2) and the SFIT2 emission add-on retrieval algorithm (described in Sect. 7.3.2). The significance of measuring these particular trace gas species is described in Sect. 2.3. E-AERI measurements at the PEARL Ridge Lab commenced on October 22, 2008 and continued until September 10, 2009 and are not affected by local emissions of the Eureka Weather Station's power plant 15 km away.

Starting on February 16, 2011, the E-AERI resumed measurements closer to sea-level at 0PAL (10 m alt.). The 600 m difference between the two sites has a large impact on the measured radiance, such as differences in the CO_2 band between 600-800 cm^{-1} due to a temperature inversion and – most notably – H_2O saturation, as shown in Sect. 4.2. Increased occurrence of clouds at lower altitudes also results in more spectra being excluded due to cloud filtering. Depending on the season, 10 to 20% of the water vapour column is located below 610 m, increasing the amount of H_2O interference with the target trace gas. Retrievals were performed using a total column from 0.010 to 100 km. To perform comparisons with total column measurements made from the PEARL Ridge Lab, the first 600 m of the E-AERI total columns were removed (the scaled VMR profile is on a 39-layer altitude grid; the lowest layer of which is 0.010 to 0.610 km) to match them with those measured at the Ridge Lab, effectively

providing 0.610 to 100 km total columns. The additional error due to this removal, determined by generating simulated spectra and comparing the corresponding 'true' columns (with 600 m removed) with the retrieved columns (with 600 m removed), is small (< 1% for O_3 and < 2% for the other species).

7.5 Miniwindows

7.5.1 Investigation of Miniwindows

The choice of an appropriate microwindow is essential when performing retrievals. SFIT2 will analyze only the spectra within the microwindow; hence the selection of a microwindow can affect the retrieved profile's column amount, error, information content, and processing time. Because a trace gas will emit radiation at specific frequencies, it is important to determine which of these frequencies to include in the retrieval (typically the clearest and strongest) and which to leave out. Due to the lower spectral resolution of the E-AERI, the spectral regions that SFIT2 uses to fit the trace gas spectral lines must be significantly larger than those typically used in fitting high-resolution solar absorption spectra to incorporate sufficient spectral lines of the target trace gas. Since these fitted spectral regions are wider (10-25 times) than the standard microwindows used in NDACC IRWG SFIT2 retrievals, they will be referred to as 'miniwindows.' The maximum number of interfering species SFIT2 can incorporate into its retrieval is nine. The number of interfering species increases as the miniwindow size increases, placing a limit on the miniwindow's maximum size.

A detailed comparison of possible miniwindows was performed for each trace gas species. The goal is to achieve the lowest RMS residual of the fitted and measured spectra while still allowing the retrieval to converge on a final solution. Attempts were made to avoid spectral regions that have large H_2O emission features due to their large variability and capacity to dwarf emission features of the target gas. The H_2O continuum (resulting from numerous strong H_2O lines up to 700 cm^{-1}) in particular was avoided as much as possible due to the difficulty in its characterization. For each miniwindow analyzed, the list of interfering species must be adjusted to account for the presence of other trace gases emitting radiation within these regions. Column fits are performed for interfering gases since their emission features must be considered.

As an example, Figure 7.3 shows the four most accurate spectral fits when investigating different miniwindows for O_3. Other investigated miniwindows for O_3 not shown are 900 to 1300 cm^{-1}, 975 to 1005 cm^{-1}, and 1100 to 1300 cm^{-1}; all of which had higher RMS residual errors and/or convergence issues. An ideal miniwindow would incorporate as many strong O_3 emission lines in this spectral region as possible while limiting the number of interfering species to nine. The sample measurement day used for this test was April 4, 2009, which had clear skies with small variability in the measured radiances. From Figure 7.3 it can be determined that miniwindow (B) provides the smallest error in the fit with an RMS of 2.18% while permitting the retrieval to converge successfully. This result was confirmed using different spectra on April 4, 2009 as well as during another test day (December 25, 2011).

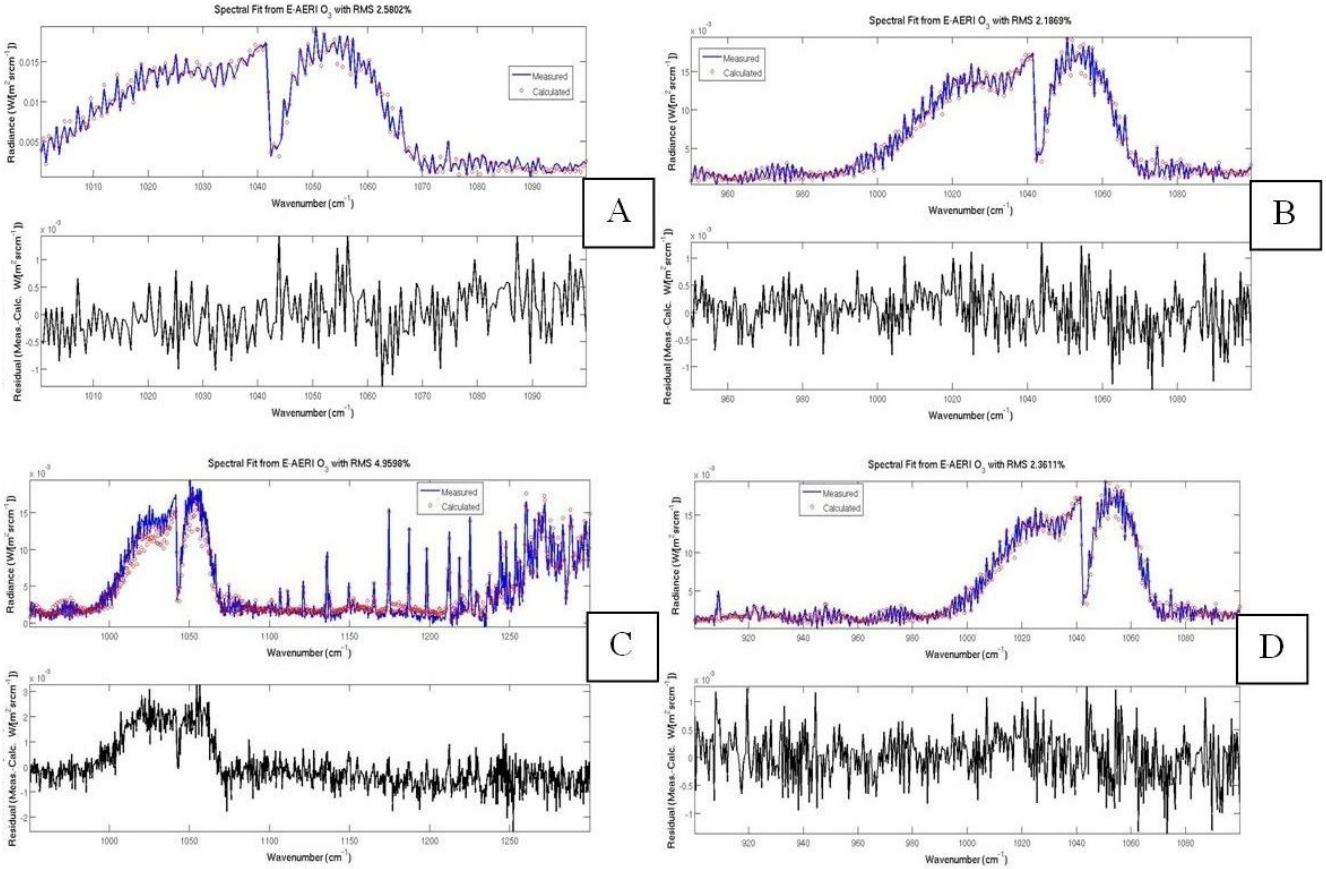

Figure 7.3: Plots of measured and calculated spectra (upper panels) with their residuals (lower panels) for four different O_3 miniwindows: (A) 1000-1100 cm^{-1} (RMS = 2.59%), (B) 950-1100 cm^{-1} (RMS = 2.18%), (C) 950-1300 cm^{-1} (RMS = 4.95%), and (D) 900-1100 cm^{-1} (RMS = 2.36%). Miniwindow (B) has the smallest residual and lowest residual. Measurements were taken from an hourly-averaged clear-sky spectrum at 12:00-1:00 UTC on April 4, 2009.

7.5.2 Selected Miniwindows and Spectral Fits

The process outlined in Sect. 7.5.1 was performed for the other trace gas species of interest in determining their miniwindows. Tests were also done during different seasons to ensure convergence stability regardless of changes in temperature and humidity at Eureka. Table 7.1 lists the miniwindow selected for each trace gas, the interfering species included in the retrieval, and the SNR and typical RMS residual in the spectral fit for the winter (December) and summer (June). The SNR provides the ratio of the maximum emission (radiance) to the noise for the given miniwindow, and increases in the summer when the thermal emission is a maximum.

Table 7.1: Retrieval specifications for each target trace gas: the retrieval miniwindow (spectral range), interfering species scale-fitted in each miniwindow, SNR, and typical RMS residual of the spectral fit for spectra measured in December (June).

Trace Gas	**Miniwindow (cm^{-1})**	**Interfering Species**	**SNR**	**Typical RMS ($W / [m^2\ sr\ cm^{-1}]$)**
O_3	950-1100	H_2O, CO_2, O_3^{667}, O_3^{676}, O_3^{686}, O_3^{668}	40 (80)	$2.7x10^{-4}$ ($5.9x10^{-4}$)
CO	2000-2200	O_3, N_2O, H_2O, OCS	50 (200)	$9.9x10^{-6}$ ($4.6x10^{-5}$)
CH_4	1150-1229	SO_2, H_2O, HDO, O_3, CCl_2F_2, HNO_3, CH_3D, N_2O	40 (90)	$2.3x10^{-4}$ ($6.5x10^{-4}$)
N_2O	1160-1300	CH_4, SO_2, H_2O, HDO, O_3, CCl_2F_2, HNO_3, CH_3D	35 (110)	$3.3x10^{-4}$ ($6.9x10^{-4}$)

Examples of the spectral fits and residuals for each trace gas listed in Table 7.1 are shown in Figure 7.4. A comparison between the fits in the summer (June) and winter (December) are provided using hourly-averaged E-AERI spectra and are typical for these two seasons. The spectral fits change depending on the season; for instance, larger emission features are found in the summer compared to the winter due to the increased temperature (resulting in increased thermal emission) as well as other factors (e.g., strong H_2O emission lines due to increased water vapour). Due to the difficulty in accurately fitting H_2O spectral lines, this slightly increases the RMS residual in the summer months (May-August) and decreases the RMS residual in the winter months (November-February). Meteorological events (i.e., ice clouds, fog, etc.) do not impact spectral fitting due to the cloud-filtering performed prior to the SFIT2 retrievals (described in Sect. 7.4.2).

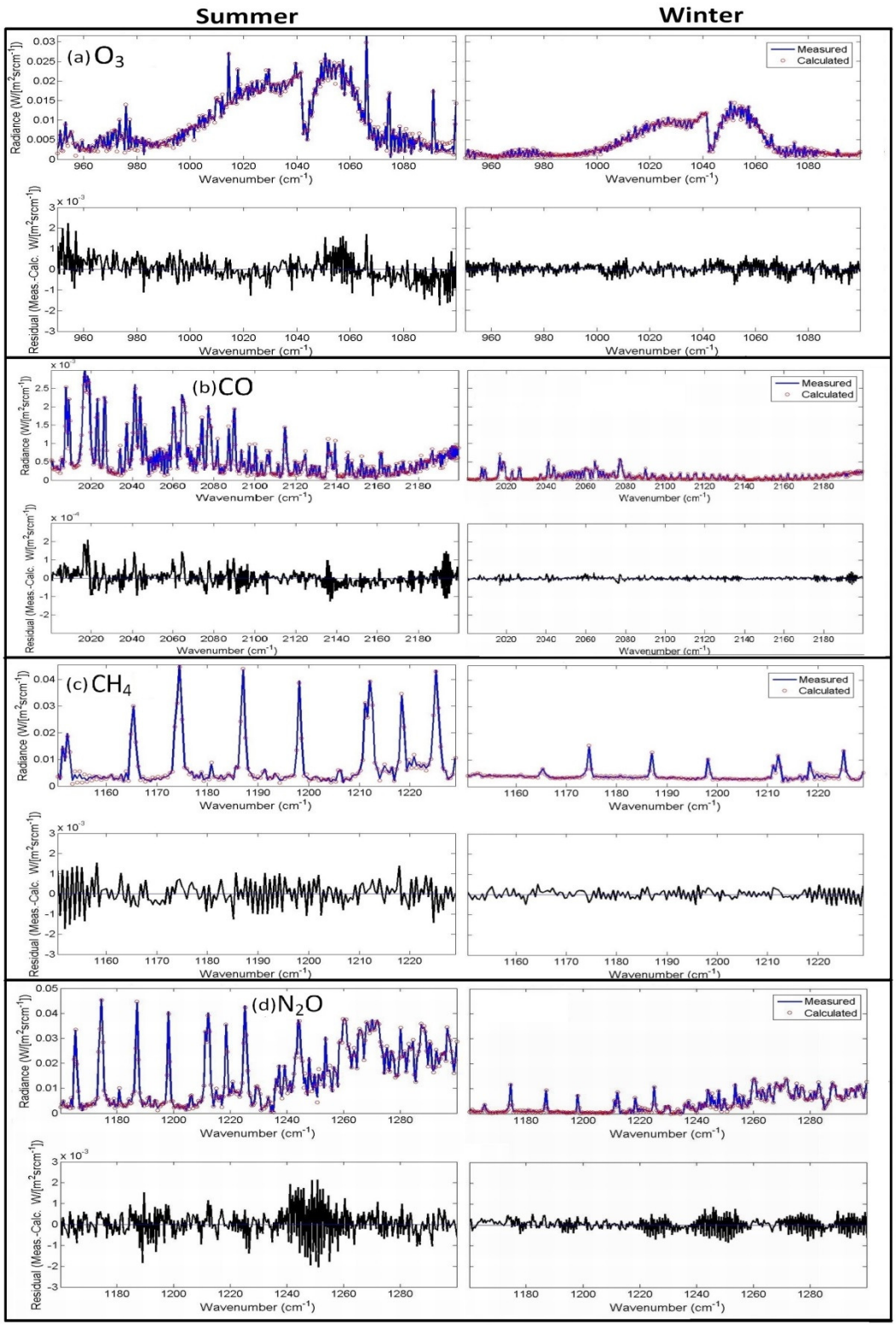

Figure 7.4 Sample summer (June 29, 2009; left column) and winter (December 31, 2008; right column) of spectral fits for retrievals of (a) O_3, (b) CO, (c) CH_4, and (d) N_2O. Top panels show the measured (blue) and fitted spectra (red circles), with their residuals shown in the bottom panels. Note the vertical scales are kept constant left-to-right while the residuals are on a finer scale. Retrievals were performed using SFIT2 and hourly-averaged E-AERI spectra.

7.5.2 Other Trace Gas Species Investigated

Several other trace gases were tested to determine if they could be retrieved from E-AERI spectra: HNO_3, H_2O, CO_2, HCN, NO, NO_2, C_2H_2, C_2H_6, and C_2H_4. Spectral fits were successful for CO_2 (miniwindow: 820 to 1060 cm^{-1}), HCN (miniwindow: 675 to 750 cm^{-1}), and C_2H_2 (miniwindow: 650 to 750 cm^{-1}), as shown in Figure 7.5. Despite the general usefulness in obtaining CO_2 columns, the estimated error (described in Sect. 8.1) on the CO_2 total column is 9.2% and, as such, is of questionable scientific value. Given the small seasonal variability of CO_2 and strict requirement for extremely precise CO_2 measurements, such as those done by the Total Column Carbon Observing Network (TCCON) which place a limit of <1% error on the CO_2 total column measurements, this large error on the E-AERI CO_2 total columns renders the product of little scientific use. The interfering species included in the CO_2 fit were: O_3, H_2O, O_3^{676}, O_3^{667}, O_3^{686}, O_3^{668}, CHF_2Cl, NH_3, and HNO_3. Similarly, HCN and C_2H_2 do not consistently converge due to numerical stability issues in the retrieval. Furthermore, large residuals were found for HCN and C_2H_2, indicating the spectral fits do not reproduce the observed spectra. Possible reasons for this include the molecule's low concentration (producing a small signal), inadequate interfering species included in the retrieval, etc. It appears that these trace gases can be retrieved when their concentrations are elevated in the atmosphere above Eureka, such as during biomass burning events, but more investigation into their retrieval performance is required. The interfering species included in these two retrievals were: HCN/C_2H_2, O_3, CO_2, H_2O, HNO_3, and C_2H_4. It is expected that retrievals of these two trace gases will perform better using the new SFIT4 algorithm, which has improved numerical stability [M. Palm; personal communication]. For these reasons, CO_2, HCN, and C_2H_2 retrievals have not been analyzed in further detail and are considered to be the focus of future work. The necessary setup parameters and *binput* files for retrievals of these trace gases have been created, allowing retrievals to be performed at any time, if desired.

Unfortunately the sensitivity of E-AERI measurements to NO, NO_2, HNO_3, C_2H_2, and C_2H_6, was too low for all investigated miniwindows, resulting in a retrieval of the *a priori* (which suggests no information content from the retrieval). While the spectral fits for HNO_3, for instance, were capable of matching the calculated spectrum to the measured spectrum, the signal from the HNO_3 emission line is simply too weak to be detected. This is a result of the low resolution of the E-AERI. H_2O retrievals had serious convergence issues (< 2% occurrence) and relatively large RMS errors. H_2O retrievals are believed to be possible using SFIT4, which is

more numerically stable, in conjunction with radiosonde H_2O profiles input as the *a priori* H_2O profile [M. Palm; personal communication]; this will be the focus of future work.

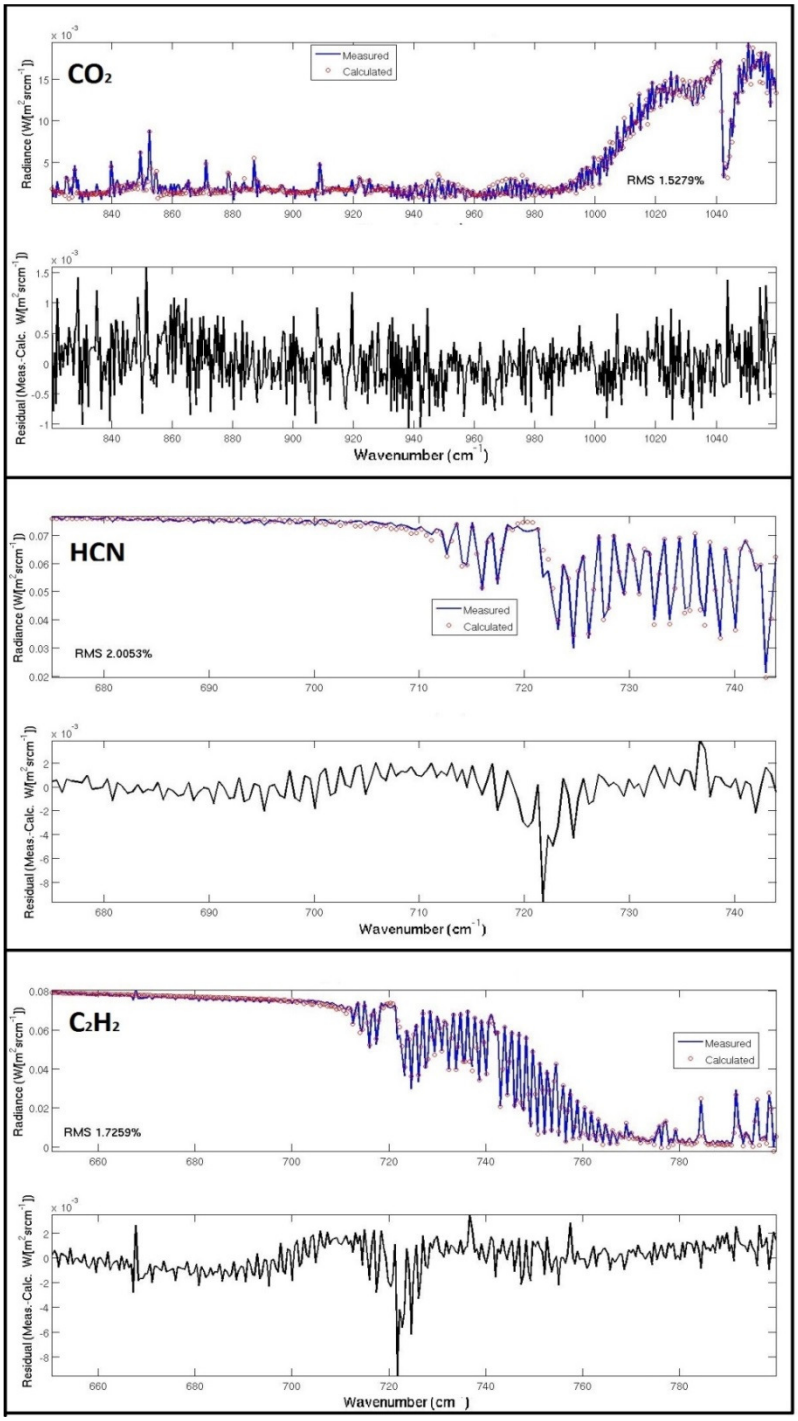

Figure 7.5: Sample spectral fits for retrievals of CO_2, HCN, and C_2H_2 (top to bottom). Top panels show the measured (blue) and fitted (red circles) spectra, with their residuals (on a finer scale) shown in the bottom panels. Measurements were taken from an hourly-averaged clear-sky spectrum at 00:00-1:00 UTC on April 4, 2009.

7.6 Summary of Trace Gas Retrieval Technique

The OEM retrieval theory was introduced in this Chapter. Following the formalism of Rodgers [2000], *a priori* information (e.g., previous climatological observations) is combined with measurements to produce a retrieved, or 'best estimate,' measurement of the atmospheric state. This process is necessary due to the moderately nonlinear and ill-posed problem (specifically, the fact that there are more unknowns than measurements) when trying to perform the inversion from measurement space (E-AERI spectra) to atmospheric state space (trace gas columns). In order to solve this inverse problem, the OEM uses Bayes' Theorem to find the MAP solution, providing the best estimate of the atmospheric state. The mathematical formalism outlining this theory was provided in this Chapter, along with a discussion of its implementation for E-AERI trace gas retrievals at Eureka. Details on the specific calculation of matrices are provided in the next Chapter. The OEM also permits one to estimate the errors on the retrieval: specific error contributions can be calculated separately and then combined to produce the total estimated error for each retrieval.

The SFIT2 trace gas retrieval algorithm was introduced in this chapter. SFIT2 employs the OEM and has undergone extensive validation and is widely used in the trace gas retrieval community. Previously SFIT2 was used solely for solar and lunar absorption spectra; a new, modified version of the SFIT2 algorithm that permits retrievals of emission spectra was created by M. Palm (U. Bremen) was introduced and used to perform all trace gas retrievals using E-AERI spectra. This permits the creation of a new data product for the E-AERI instrument and the first SFIT2 retrievals using AERI spectra. The modifications to the SFIT2 algorithm were outlined in this Chapter, including changes to the radiative transfer equation used in the SFIT2 algorithm.

The retrieval methodology for the four target trace gas species (O_3, CO, CH_4, and N_2O) was outlined, including the cloud filter (so as to only perform retrievals during clear-skies), *a priori* trace gas profiles, and the difference between E-AERI trace gas retrievals at PEARL vs. 0PAL. Miniwindows, required inputs for the SFIT2 algorithm, were characterized for each trace gas depending on their convergence and RMS error in the spectral fit, including the spectral range of each window and interfering species. Spectral fits indicate that SFIT2 is capable of accurately fitting the observed spectra, with RMS residuals consistent with the NESR level. The

performance of the spectral fits is equivalent at 0PAL, where there is 10-20% more water vapour. A comparison study of possible miniwindows was presented, describing the selection methodology for each miniwindow and quality of the spectral fits. Retrievals of HNO_3, H_2O, CO_2, HCN, NO, NO_2, C_2H_2, C_2H_6, and C_2H_4 were also investigated; only CO_2, HCN, and C_2H_2 had moderately successful retrievals due to issues with convergence, spectral fits, or large error estimates of the total column.

8. YEAR-ROUND TRACE GAS MEASUREMENTS AT EUREKA

What is driving the observed changes in the Arctic climate? The atmosphere's radiative transfer is sensitive to the slightest change in atmospheric composition of radiatively active gases, which has changed noticeably. Spectroscopy enables us to take regular, precise measurements of the atmospheric composition. Combined with our understanding of atmospheric chemistry, measurements of trace gas concentrations allow one to obtain an understanding of the processes involved in the Arctic atmosphere, from trace gases that are naturally created to those that are anthropogenic and/or are changing due to anthropogenic processes. As shown in the previous chapter, the OEM permits retrievals of trace gases. This Chapter presents the first trace gas measurements of O_3, CO, CH_4, and N_2O from 2008 to 2013 by the E-AERI instrument using the newly-modified SFIT2 and subsequent testing of the SFIT4 retrieval algorithms.
Portions of this Chapter have been published in Mariani et al. (2013).

8.1 E-AERI Total Column Error Estimates

The implementation of the error analysis described in Sect. 7.2 for E-AERI trace gas retrievals is described in this section, including a discussion of the calculation of the error covariance matrices (Eqns. **(7.24)** to **(7.26)**). This implementation follows the formalism developed by Batchelor *et al.* [2009]. An estimate of the instrument's noise is based on instrument RMS NESR tests performed by UW-SSEC as described in Sect. 3.5. The diagonals of the measurement noise covariance matrix, $\mathbf{S}_\varepsilon$, are equivalent to the noise squared, where noise is equal to the average of the NESR (which varies only slightly with wavenumber) throughout the miniwindow of the target trace gas. The diagonal elements of the *a priori* covariance matrix, $\mathbf{S}_a$, which constrains the retrieval to the *a priori*, were calculated based on an uncertainty of 30%

in the *a priori* VMR profile for each target gas; this value has been used for previous retrievals at Eureka as it represents the maximum tropospheric variability seen in the climatologies [Lindenmaier *et al*., 2012]. A conservative estimate of 100% was used as the uncertainty in the *a priori* total columns of the interfering species, with the exception of H_2O, where it was set to 300% due to H_2O's large seasonal variability at Eureka.

A conservative estimate of 20% was used where the uncertainty in the line parameters was unknown (e.g., O_3 line intensity for some lines). The maximum uncertainty within the quoted range from the radiosonde manufacturer (Vaisala) was used as the uncertainty associated with the atmospheric profiles of pressure ($\pm$1 hPa). In determining $\mathbf{S_{temp}}$ via perturbation, the uncertainties provided in the NCEP profiles were used (a more conservative estimate of 2 K was used below 30 km, 5 K between 30-35 km, 6 K between 35-40 km, 7 K between 40-50 km, and 9 K above 50 km). Since the E-AERI is zenith-viewing, errors in the solar zenith angle ($\mathbf{S_{SZA}}$) are zero. Several error sources ($\mathbf{S_{intret}}$, $\mathbf{S_{intspec}}$, $\mathbf{S_{temp}}$, and $\mathbf{S_s}$) vary from spectrum to spectrum and can be season-dependent. For instance, the interference from H_2O line-broadening decreases in the winter as the amount of water vapour in the troposphere decreases by over a factor of > 10 (compared to the summer). For this reason, actual total errors are typically slightly smaller in the winter.

Thin clouds can result in doubling of the RMS residual in the spectral fits, reinforcing the requirement of the conservative cloud-filtering process. The impact of aerosols on the retrieval is similar (albeit smaller) and is discussed in more detail in Sect. 8.3. A perturbation method was used to assess the error associated with using the wrong *a priori* VMR profile shape of the target trace gas; VMR concentrations were perturbed by 2% at one altitude grid and the change in the retrieved total column was calculated. The largest changes in the retrieved total column occur from perturbations to the lowermost altitudes of the troposphere for all species, indicating that E-AERI retrievals are dependent on the shape of the profile in the lower troposphere. This is discussed in more detail in Sect. 8.3. Table 8.1 lists the error components for each trace gas; retrievals performed on April 4, 2009 were used in the error analysis and are typical for the full dataset. The error bars in all graphs shown include all error sources ($\mathbf{S_{tot}}$).

Table 8.1: Error components for each retrieved trace gas total column. $\mathbf{S_{tot}}$ is determined from Eqn. **(7.27)**. Errors are based on a single spectrum on April 4, 2009; these errors are typical for other dates and decrease slightly in the winter and increase slightly in the summer as a result of decreased/increased H_2O emission (for instance).

Trace Gas	S_m (%)	S_s (%)	S_{temp} (%)	S_{lint} (%)	S_{lwidth} (%)	S_{intret} (%)	$S_{intspec}$ (%)	S_{tot} (%)
O_3	1.1	6.1	8.7	2.9	0.5	0.01	1.4	11.3
CO	8.0	11.9	3.4	0.2	0.1	0.01	0.1	14.7
CH_4	6.0	8.2	3.3	2.2	0.4	0.01	0.2	11.0
N_2O	6.5	6.7	4.7	2.6	0.5	0.02	0.5	10.9

8.2 Comparison Datasets

The E-AERI trace gas retrievals are a new data product for the AERI instrument (it is also the first time SFIT2 has been used to retrieve total columns of trace gases using emission spectra). Comparing E-AERI trace gas measurements with other ground-based spectrometers at Eureka provides a means of evaluating the E-AERI's new trace gas data product. The Bruker 125HR FTIR spectrometer is an NDACC instrument that has been used to make solar-absorption measurements at the PEARL Ridge Lab since 2006 and has been compared with other datasets in several studies [Batchelor *et al*., 2009; Lindenmaier *et al*., 2010; Adams *et al*., 2012a]. The 125HR provides partial and total column measurements of many trace gases during Sun-lit months, including the four gases measured by the E-AERI in this work. The viewing geometry of the 125HR is a Sun-pointing slant path. 125HR total column errors ($\mathbf{S_{tot}}$, comprising the smoothing error, measurement error, interference error, and forward model parameter error) are 4.3% for O_3, 1.8% for CO, 14.0% for CH_4, and 3.9% for N_2O [Lindenmaier, 2012], which are smaller than those of the E-AERI (10-15%, as shown in Table 8.1).

The remaining solar-absorption spectrometers at PEARL have been involved in numerous validation campaigns and provide total columns of O_3, and other trace gases. Three Environment Canada Brewer spectrophotometers (#021, #192, #069) deployed on the roof of the PEARL Ridge Lab use direct and scattered sunlight at UV wavelengths [Savastiouk and McElroy, 2005]. The viewing geometry of the Brewer spectrophotometers is a Sun-pointing slant path, like the 125HR. The standard Brewer algorithm was used to analyze Brewer data,

with small changes to the analysis parameters (e.g., maximum in the O_3 layer was set at 18 km instead of 22 km to better reflect conditions in the Arctic) [Lam *et al*., 2007]. The random error in Brewer total O_3 measurements is typically less than 1% [Savastiouk and McElroy, 2005].

The two UV-visible ground-based spectrometers (GBSs; both NDACC-certified) are very similar instruments and their measurements of zenith-scattered sunlight were analyzed using the same settings to retrieve O_3 total columns [Fraser *et al*., 2009; Adams *et al*., 2012a, b]. The two GBSs agree within 1% of each other and the total error of the O_3 column is 6.2% [Adams *et al*., 2012a]. An NDACC-certified SAOZ UV-visible grating spectrometer [Pommereau and Goutail, 1988] deployed on the roof of the PEARL Ridge Lab took zenith-sky measurements during the spring. The estimated error for SAOZ total O_3 measurements is 5.9% [Hendrick *et al*., 2011]. GBS and SAOZ total columns were retrieved independently, following NDACC guidelines, using the Differential Optical Absorption Spectroscopy (DOAS) technique [Platt and Stutz, 2008]. Both the GBSs and SAOZ are zenith-viewing and use scattered sunlight at sunrise/sunset to make measurements pointing to the azimuth angle of the Sun (which varies with the time of year).

Finally, the SFIT2+Emission retrieval algorithm can be used with any emission spectra, including other AERI instruments. This new retrieval method can be extended to other AERI instruments deployed across the globe shown in Figure 3.2, the demonstration of which is one of the goals of this Ph.D. project. The overlap period between the E-AERI at the PEARL Ridge Lab and the P-AERI, described in Sect. 3.2.5, at 0PAL in 2008-2009 provides an excellent opportunity to compare the trace gas retrievals between these two instruments at two altitudes and demonstrate the viability of extending this retrieval methodology to other AERIs.

8.3 2008-2009 Trace Gas Measurements from the PEARL Ridge Lab

8.3.1 Comparisons with Solar-absorption Spectrometers at Eureka

Clear-sky total columns of O_3, CO, CH_4, and N_2O from the PEARL Ridge Lab were retrieved using hourly-averaged E-AERI spectra (described in Sect.7.4.1) and the

SFIT2+Emission retrieval algorithm (described in Sect. 7.3). Figure 8.1 shows O_3, CO, CH_4, and N_2O total columns (from 0.610 to 100 km) measured at the PEARL Ridge Lab between October 24, 2008 and October 1, 2009. Also shown are measurements from the Bruker 125HR, Brewer, GBSs, and SAOZ spectrometers. Error bars are shown only for the E-AERI total columns for clarity. The pressure-temperature profiles and *a priori* VMR profiles for the E-AERI and 125HR are the same and SFIT2 was used to perform the retrievals for both instruments, making their measurements ideal for comparison purposes. Different retrieval algorithms and techniques were used for the Brewer, GBS, and SAOZ O_3 retrievals, as discussed in Sect. 8.2.

To compare the E-AERI data with the 125HR, a coincident time interval used the closest 125HR measurement recorded within $\pm$ three hours of an E-AERI measurement to maximize the number of coincident data points while minimizing the effect of measuring different air masses. All of the E-AERI and 125HR O_3 and CH_4 total column measurements agree within combined E-AERI and 125HR errors. For N_2O and CO, the agreement is slightly worse; 93% and 90% of the measurements, respectively, agree within combined errors. Comparisons between the two instruments can be quantified using the mean relative difference, which is the mean of the difference between the two instruments' measurements divided by their average, and the standard error on the mean, ($\sigma / \sqrt{N}$, where σ = standard deviation and N = number of data points).

The mean relative differences (100% x [E-AERI – instrument] / mean) between the E-AERI and the 125HR, Brewers, GBSs, and SAOZ are provided in Table 8.2. These differences are smaller than the total uncertainties ($\mathbf{S_{tot}}$) of the E-AERI total column measurements reported in Table 8.1, indicating good agreement. When the random error, $\mathbf{S_m}$, is removed from $\mathbf{S_{tot}}$, the differences are smaller than the uncertainty for all trace gases except CO. The results presented in Table 8.2 will be discussed in further detail in Sect. 8.5.1, once the 2011 total column measurements are presented.

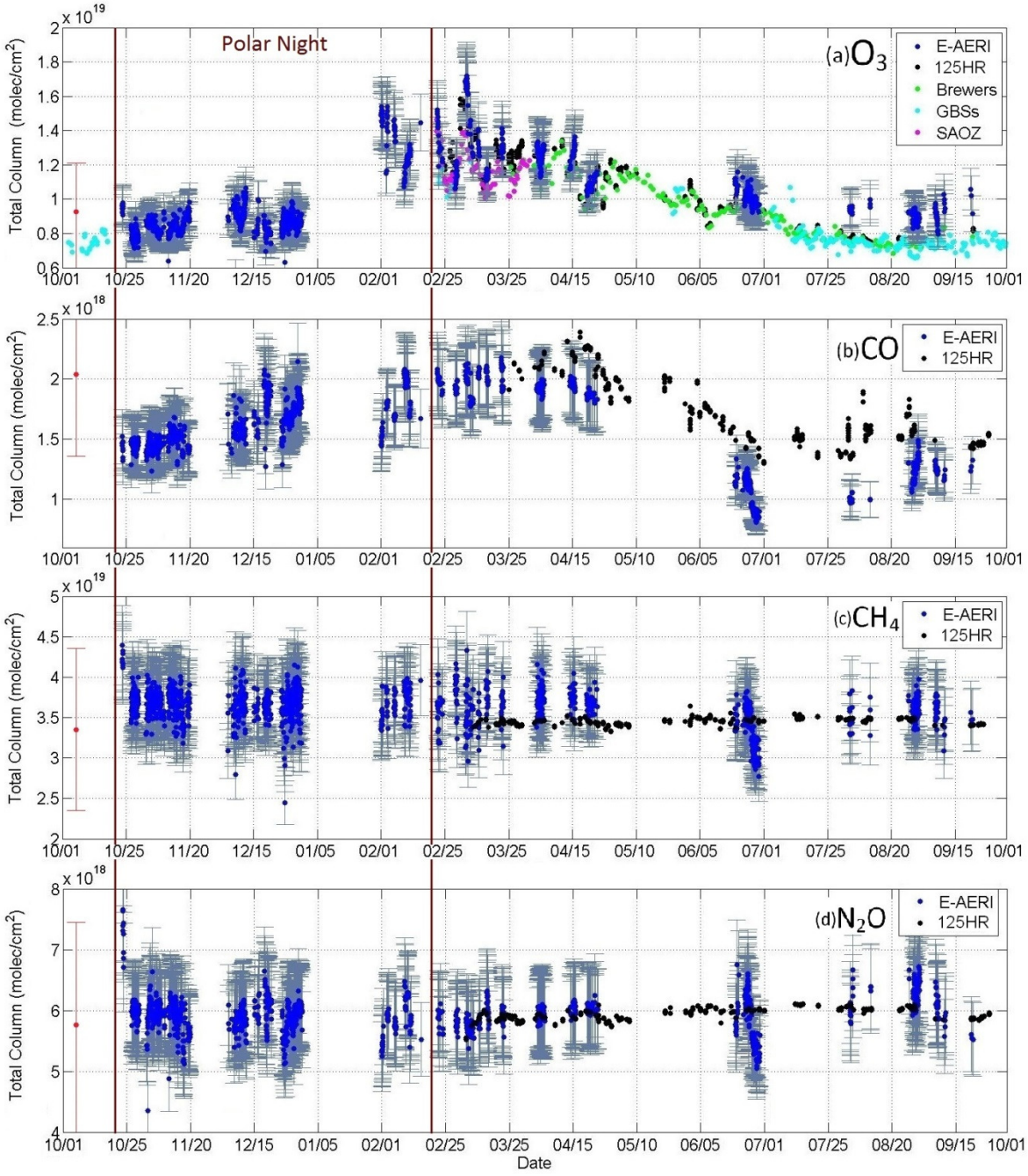

Figure 8.1: Total column measurements of (a) O_3, (b) CO, (c) CH_4, and (d) N_2O from the PEARL Ridge Lab. Dates are given as MM/DD from 2008-2009. E-AERI (blue), 125HR (black), three Brewers (green), two GBSs (cyan), and the SAOZ (pink) measurements are shown for comparison. Error bars are shown only for the E-AERI for clarity. The *a priori* column is shown for one day (red) with error bars corresponding to the square root of the diagonal of $\mathbf{S_a}$. Polar night is indicated between the brown vertical lines.

Table 8.2: O_3, CO, CH_4, and N_2O total column comparisons between the E-AERI and the 125HR (both unsmoothed and smoothed by the monthly E-AERI averaging kernels), Brewers, GBSs, and SAOZ for 2008-2009 and 2011. The Brewers, GBSs, and SAOZ cannot measure CO, CH_4, and N_2O. The mean relative difference (100% x [E-AERI – instrument] / mean) is given with the standard error ($\sigma / \sqrt{N}$) and the number of coincident data points (N) in brackets.

		Mean relative difference with the E-AERI (%)				
Year	**Trace Gas**	**125HR Unsmoothed**	**125HR Smoothed**	**Brewers**	**GBSs**	**SAOZ**
2008-2009	O_3	7.7 ± 0.3 (437)	4.0 ± 0.3 (437)	9.9 ± 1.6 (137)	-2.9 ± 1.0 (222)	8.4 ± 0.9 (188)
	CO	-14.4 ± 1.4 (366)	-8.7 ± 1.3 (366)	-	-	-
	CH_4	2.0 ± 0.3 (474)	1.7 ± 0.3 (474)	-	-	-
	N_2O	-1.2 ± 0.4 (514)	-1.0 ± 0.4 (514)	-	-	-
2011	O_3	8.1 ± 1.0 (123)	5.5 ± 0.9 (123)	N/A (0)	-9.4 ± 1.2 (27)	7.4± 1.9 (144)
	CO	-1.9 ± 0.6 (4)	-0.9 ± 0.6 (4)	-	-	-
	CH_4	-1.2 ± 1.4 (144)	-0.8 ± 1.3 (144)	-	-	-
	N_2O	-2.1 ± 0.9 (132)	-1.5 ± 0.8 (132)	-	-	-

To account for differences in vertical sensitivity between the E-AERI and 125HR, their averaging kernels must be considered. A typical February E-AERI total column averaging kernel, which was calculated using a perturbation method, is compared to a typical February 125HR averaging kernel in Figure 8.2. The E-AERI has high sensitivity to the four trace gases in the lower troposphere, with almost all sensitivity for CO coming from the surface concentration for instance. The E-AERI also has some sensitivity to stratospheric ozone, permitting it to detect changes in the ozone column where ozone depletion occurs (around 15 to 20 km). There are clearly large differences between the E-AERI and 125HR averaging kernels, and hence, in their vertical sensitivities. The 125HR sensitivity at higher altitudes in the atmosphere is due to its higher spectral resolution compared to the E-AERI.

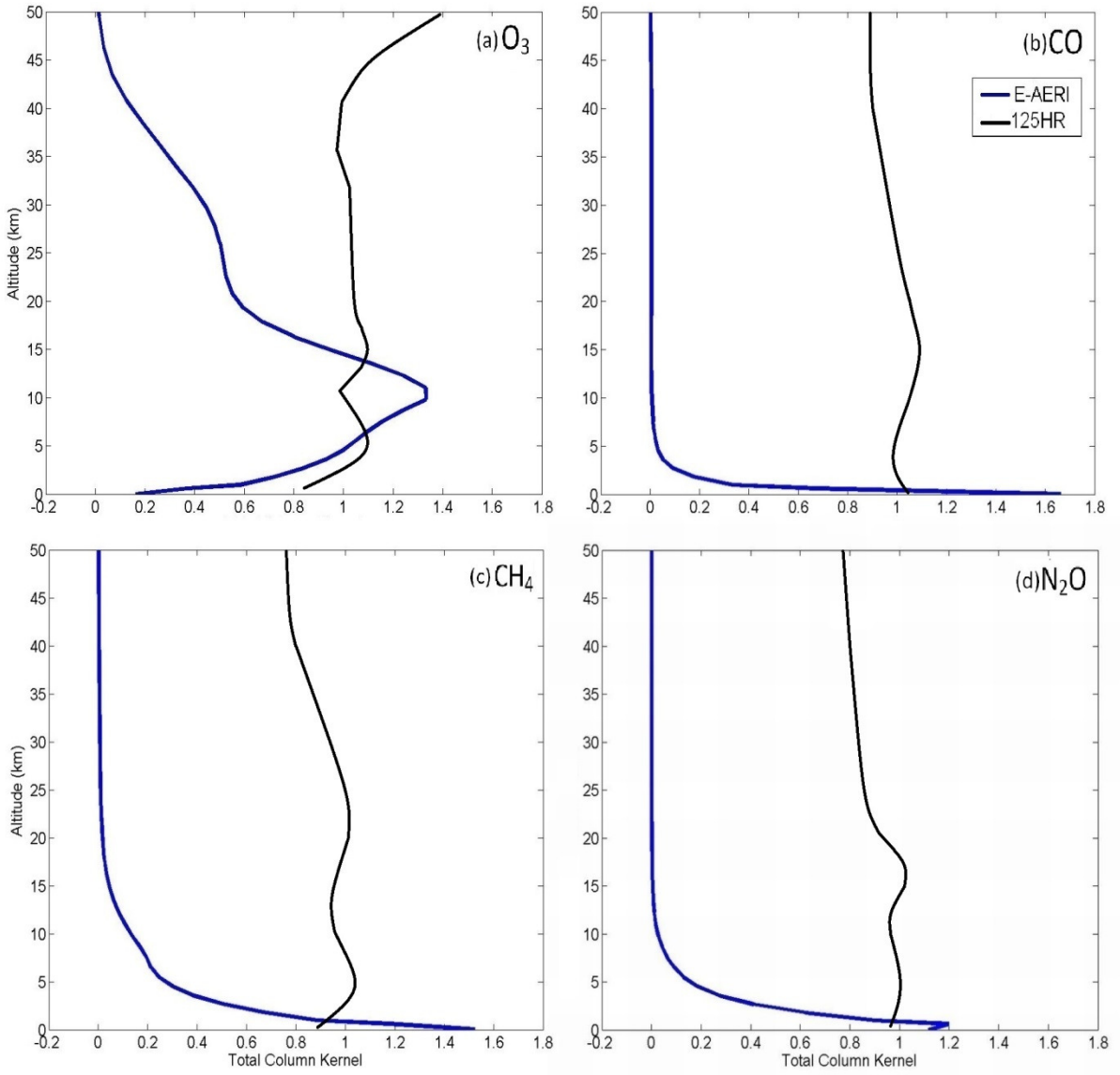

Figure 8.2 Typical E-AERI (blue) and 125HR (black) total column averaging kernels (molec. cm^{-2} / molec. cm^{-2}) in February for (a) O_3, (b) CO, (c) CH_4, (d) N_2O.

Using these averaging kernels, the 125HR profiles can be smoothed by the monthly mean E-AERI averaging kernels to produce smoothed 125HR total columns (from the smoothed profile). The smoothed measurement represents the profile the 125HR would measure if it had the same spectral resolution and vertical sensitivity as the E-AERI, and is computed using Eqn. (4) of Rodgers and Connor [2003]:

$$\mathbf{x_s} = \mathbf{x_a} + \mathbf{A}(\mathbf{x_h} - \mathbf{x_a}) \quad \textbf{(8.1)}$$

where $\mathbf{x_s}$ is the smoothed profile (125HR profile smoothed by the E-AERI averaging kernel) and $\mathbf{x_h}$ is the high-resolution profile (from the 125HR). After smoothing, the differences shown in Table 8.2 between the E-AERI and 125HR are less, particularly for O_3 and CO. Note the smoothed measurements are not shown in Figure 8.1 for clarity.

The larger difference for CO total columns is comparable to the differences (~13%) found between AERI CO retrievals and convolved *in situ* CO measurements by Yurganov *et al.* [2010], who attribute these discrepancies to the effect of aerosols on the measured radiances, which is not accounted for in their retrieval (nor in SFIT2). Collision-induced absorption (CIA) of N_2 contributes to the observed offset in the CO column year-round; this is discussed more in Sect. 8.4.1. The largest differences seen in Figure 8.1 occur in the summer months and are likely the result of increased H_2O and scattering of solar radiation from aerosols during this season. If the aerosol diameter is smaller than the wavelength (roughly), scattering can be neglected and the effect in the emission spectrum is primarily that of a broad emission feature in the spectra. Only for larger aerosols does scattering become important; this can have a larger impact on AERI spectra in the summer months due to increased scattering via a higher solar elevation angle and increased aerosol particle size [e.g., Turner 2005]. Additionally, as H_2O increases in the atmosphere, the intensity of H_2O emission lines increase, which makes them appear broader. The strong H_2O spectral lines dominate and interfere with the neighbouring spectral lines of the target trace gas, increasing the difficulty of distinguishing the emission signature of H_2O from that of the target trace gas. As a result, the H_2O concentration is over-estimated while the CO concentration is under-estimated for E-AERI CO retrievals in the summer.

The seasonal cycle of O_3 (maximum in the late winter), driven by the Brewer-Dobson circulation, can be seen by the E-AERI, as is evident in Figure 8.1. In addition, like the other spectrometers, the E-AERI observes a decrease in O_3 beginning in late February, which occurs as sunlight returns to Eureka. The seasonal cycle of CO (maximum in the winter) can also be observed, as previously demonstrated in Yurganov *et al*. [2010], and will be discussed in more detail in Sect. 8.4.2. Additional variation in the CO total column may be due to transport of biomass burning plumes and industrial emissions from lower latitudes to the Arctic [Stohl, 2006], with CO accumulating during the winter in the absence of OH oxidation. While most biomass burning events occur in the summer, dynamical transport from northern Eurasia into the

high Arctic occurs during the winter when only the E-AERI is operating [Stohl, 2006]. On average, E-AERI measurements of CH_4 and N_2O remain relatively constant throughout the year, as expected, yet individually they are more variable than those measured with the 125HR (although not significantly given the timescales). This is likely due to the E-AERI being sensitive to the surface concentration, whereas the contribution of the surface concentration in the 125HR total column is decreased since the 125HR has greater vertical sensitivity which includes the stratosphere as shown in Figure 8.2.

There are two key differences between the E-AERI and the other ground-based spectrometers' measurements that can also contribute to the differences in Figure 8.1. First, the E-AERI is zenith-viewing and samples air directly above PEARL, whereas the other spectrometers have different viewing geometries (as discussed in Sect. 8.2). Second, since the E-AERI measures thermal IR emission, a sensitivity analysis indicates measured radiances are highly sensitive to the lower troposphere. This is also indicated in Sect. 4.2 and is evident in the seasonal cycle characteristic of tropospheric CO, as seen in Figure 8.1. The other spectrometers are more sensitive to the stratosphere and thus to changes in the stratospheric concentration – for example, changes associated with chemical O_3 depletion. The E-AERI profile-scaled retrievals scale uniformly throughout the entire profile (the shape of the *a priori* profile cannot be altered), however, and are biased towards the concentration in the troposphere, contributing to the observed discrepancies.

The E-AERI and 125HR O_3 and CO measurements are highly correlated, as shown in Figure 8.3 with a correlation coefficient of 0.92 and 0.95, respectively (unsmoothed). As with the mean relative difference comparisons, a $\pm$ three-hour time interval was used to identify coincident measurements. Smoothed 125HR columns shown in Figure 8.3 result in stronger correlations, particularly for CO, as expected. E-AERI and Brewer, GBS, and SAOZ O_3 correlations (not shown) are not as strong ($r = 0.70$, 0.71, and 0.61 respectively), but given the different measurement techniques, this is expected. E-AERI and 125HR CH_4 and N_2O measurements are poorly correlated due to the lack of seasonal variability giving little dynamic range (not shown).

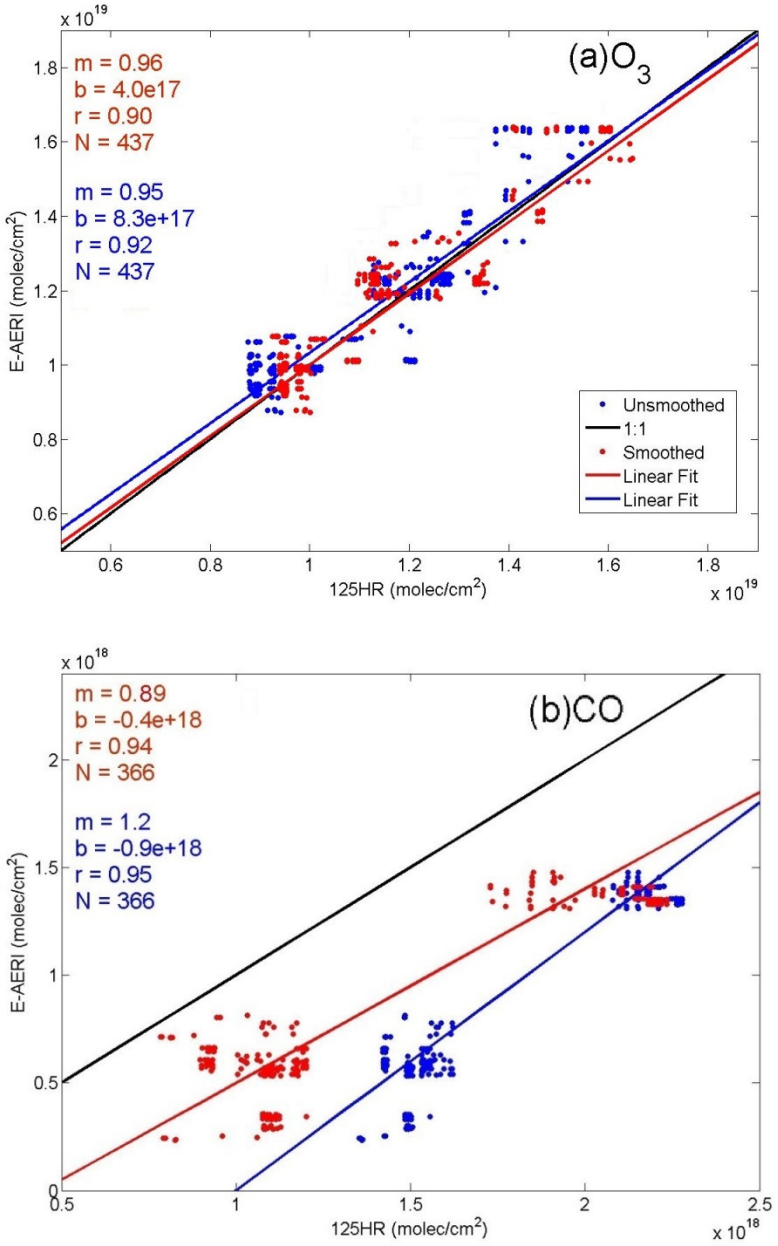

Figure 8.3: Total column comparisons for E-AERI vs. 125HR (a) O_3 and (b) CO using a $\pm$ three-hour coincidence criterion. The black line indicates the 1-1 line, the red (smoothed) and blue (unsmoothed) lines indicate the linear fit (m = fitted slope, b = fitted y-intercept, r = Pearson product-moment correlation coefficient, N = number of coincidences). 125HR total columns smoothed by the monthly E-AERI averaging kernel (Figure 8.2) are shown in red.

E-AERI O_3 columns are typically greater than those measured by the 125HR by 7% (averaged year-round), or by as much as 8-12% in the summer. E-AERI CO columns are systematically smaller than those of the 125HR with a systematic bias of approximately -14% (for unsmoothed columns averaged year-round), or by as much as 10-27% in the summer. This

bias accounts for the observed offset in the linear fit shown in Figure 8.3b, which is very similar to the bias in the AERI vs. vertically averaged convolved *in situ* CO measurements (~13%) in Yurganov *et al.* [2010], which has a comparable correlation ($m = 0.92$, $r = 0.76$). This indicates CO measurements from AERI instruments in general exhibit a systematic low bias compared to in-situ and other remote sensing instruments; this bias will be discussed more in Sect. 8.4.1.

8.3.2 Comparisons with the P-AERI

The emission add-on for the new SFIT2 retrieval algorithm was developed using E-AERI sample and simulated spectra. All tests performed on this emission version of the retrieval algorithm were only done using E-AERI spectra. Assessing the algorithm on a different instrument's data set is an essential test to the retrieval algorithm's versatility, particularly since one of the goals of this Ph.D. is to provide the trace gas retrieval methodology to other AERI users.

The P-AERI is the ideal instrument for this purpose. Because the P-AERI and E-AERI have the same spectral resolution, smoothing of profiles is not required in order to compare the two instruments. Since the P-AERI was installed at 0PAL (10 m a.s.l.), it 'sees' 600 m more of the atmosphere (the PEARL Ridge Lab has an altitude of 610 m). Hence the P-AERI total columns underwent the column adjustment described in Sect. 7.4.4, whereby the lower 600 m of the atmosphere is removed from the P-AERI total column. Since the two instruments are located close together are both zenith-viewing, it is assumed that the two instruments are observing almost the same airmass above Eureka.

While the P-AERI has the same measurement specifications as the E-AERI, its raw data format is different from the E-AERI. A conversion code was written to convert the P-AERI spectra into a usable format that SFIT2 can read. Identical parameters (e.g., $\mathbf{S_a}$ matrix, *a priori* profiles, etc.) were used for both instrument's retrievals. A comparison of both instruments' measurements of total column amounts on April 4, 2009 for spectra averaged between 12:00 to 13:00 UTC is shown in Table 8.3. The two instruments compare well with each other, as expected. The difference between the E-AERI and P-AERI total columns is below 6% for all trace gases, indicating good agreement.

Table 8.3: Retrieved total column amounts for four trace gases above Eureka on April 4, 2009 using hourly-averaged clear-sky radiances between 12:00 and 13:00 UTC from 610 m to 100 km by the E-AERI and P-AERI.

Trace Gas	SNR	Total Column (molec/cm^2)		Difference (%) 100*|(P-E)| / (0.5[P+E])
		E-AERI	P-AERI	
O_3	20	1.50×10^{19}	1.59×10^{19}	5.8
CO	47	2.55×10^{18}	2.53×10^{18}	0.8
CH_4	15	3.21×10^{19}	3.28×10^{19}	2.2
N_2O	16	5.86×10^{18}	5.65×10^{18}	3.7

Comparing these differences with the total errors listed in Table 8.1 shows that the total column differences between the two instruments are all within the total errors (even when $\mathbf{S_s}$ is not include in $\mathbf{S_{tot}}$) on the retrieved columns. This highlights the consistency of the E-AERI and P-AERI radiance measurements, as well as the stability of the new SFIT2 emission add-on. Particularly good agreement is found for CO (<1 % difference). The spectral fits for these retrievals (not shown) are almost identical (and resemble those in Figure 7.4), resulting in comparable RMS errors for the spectral fit of each trace gas. Hence it has been demonstrated that the new SFIT2 emission add-on works not only with E-AERI spectra, but also the P-AERI (and, hence, other AERI) spectra. There is no indication that the algorithm will not work with emission spectra from any other type of FTIR instrument.

8.4 A Closer Look at E-AERI CO Measurements

8.4.1 The Effect of Collision-induced Absorption of N_2 on CO Retrievals

From Figure 8.3b, there exists a clear low bias of the E-AERI CO total column compared to the 125HR. This large discrepancy in the CO total column measurement exists for another AERI, as shown in Yurganov *et al.* [2010], where AERI CO total column measurements were achieved using a different retrieval algorithm (similar to SFIT2) and compared to vertically averaged convolved in-situ CO measurements. Seeing as this study used a different retrieval algorithm and found the same bias, at first glance this seems to implicate the AERI instrument itself as experiencing a low bias in the spectral region where the CO retrieval was performed. While there are a number of factors that could contribute to this low bias as discussed in Sect. 8.3.1, a primary factor appears to be due to missing spectroscopic features in

the HITRAN 2008 and SFIT2 calculations; specifically, CIA by N_2 [G. Toon, M. Palm; personal communication].

CIA (and collision-induced emission) is the phenomenon by which spectral features caused by the inelastic collision between molecules in a gas appear; in this particular case, between N_2 molecules in the atmosphere. These inelastic collisions induce quantum transitions within the molecules, essentially causing the shape of the potential energy well to be distorted [Borysow and Frommhold, 1986; Brown and Tipping, 2003]. This produces a broad feature from the possible vibrational energies. While this effect is very small, due to the high concentration of N_2 and the high sensitivity of the E-AERI to the lower-troposphere, where N_2 is the densest, this broad feature results in absorption from 1% at 2100 cm^{-1} to > 10% at 2190 cm^{-1}. This is illustrated in Figure 8.4, where the transmittance of the atmosphere decreases as one moves from 2100 to 2200 cm^{-1} (where CO is retrieved) due in part to N_2 CIA. Note the broad shape of the N_2 CIA in comparison to the absorption spectra produced by other molecules.

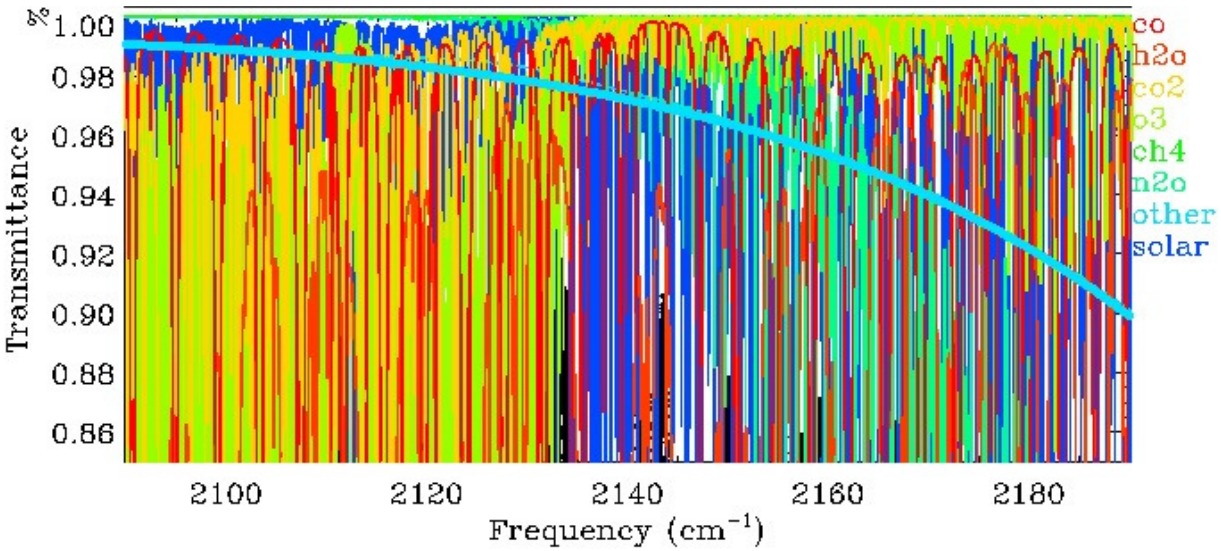

Figure 8.4: Simulated MkIV balloon-borne FTIR spectra in the spectral region where CO is retrieved. The broad cyan line labelled 'other' represents the N_2 CIA, where all other lines represent the amount of absorption by that particular molecule. Image: G. Toon (JPL), modified by Zen Mariani.

The N_2 CIA is not included in the HITRAN database, so this absorption/emission feature is not included in any SFIT2 retrievals. Following this discovery, M. Palm (U. Bremen) developed an ad-hoc, simplified N_2 CIA model for emission spectra in order to improve the E-AERI CO trace gas retrievals, with help from G. Toon (JPL). Adding an offset to the emission

spectra is not enough since the N_2 CIA is not constant; thus a constant absorption proportional to the air mass is used in conjunction with a slope in the absorption in the N_2 CIA model. This model will be implemented in the new SFIT4 retrieval algorithm, but for now remains a stand-alone prototype product for SFIT2+Emission users. As such, this N_2 CIA model encounters convergence, compatibility, and numerical stability issues, and hence cannot be fully automated until its implementation into SFIT4.

Preliminary results are provided in Table 8.4 and are encouraging. Test cases were performed of E-AERI CO retrievals using the N_2 CIA model on two different days occurring during two different seasons (winter and summer) and at two measurement sites (PEARL Ridge Lab and 0PAL). CO column retrievals on June 24, 2009 and December 25, 2011 were re-done using the N_2 CIA model; measurements in June had simultaneous 125HR measurements for comparison and were chosen because the original E-AERI CO measurements on this day had the largest difference with the 125HR CO total columns. E-AERI total columns of CO increased by 7.1% (summer) and 4.8% (winter) when the N_2 CIA model was implemented in the SFIT2+Emission retrieval, and spectral fits had slightly lower RMS errors (< 0.5 % change). This improves the comparison between the 125HR during the summer to within error of the E-AERI CO column. While no 125HR measurements took place in December for a direct comparison with the E-AERI CO column, the smaller increase in the E-AERI CO column using the N_2 CIA model reflects the typically smaller difference between the E-AERI and 125HR during the late winter months compared to the summer. Based on these preliminary results, it is suggested that a robust and fully-automated N_2 CIA model be included in the new SFIT4 version in order to improve the E-AERI CO retrievals.

Table 8.4: Comparison of retrievals of CO using the N_2 CIA model in conjunction with SFIT2+Emission. Percent differences were calculated as $(100*[x-y] /0.5[x+y])$. 125HR CO total columns are provided for comparison; no 125HR measurements were performed during December (polar night).

Date (UTC)	**E-AERI CO Total column without CIA (molec. / cm^2)**	**E-AERI CO total column with CIA (molec. / cm^2)**	**125HR CO total column (molec. / cm^2)**	**Change in E-AERI CO total column (%)**	**Difference between E-AERI and 125HR without CIA (%)**	**Difference between E-AERI and 125HR with CIA (%)**
June 24, 2009, 12:00-13:00	1.23e+18	1.32e+18	1.42e+18	+7.1	-15.4	-8.3
June 24, 2009, 13:00-14:00	1.22e+18	1.32e+18	1.42e+18	+7.1	-15.4	-8.3
December 25, 2011, 12:00-13:00	1.70e+18	1.7850e+18	N/A	+4.8	N/A	N/A

8.4.2 Diurnal and Seasonal Cycles of CO

The ability of AERI systems to measure the seasonal and 24-hour diurnal cycle of CO was demonstrated in Yurganov *et al*. [2010]. Given that there are no ground-based night-time measurements of CO at Eureka until now, quantifying the diurnal and seasonal cycles provides insight into the chemical and dynamical processes involving CO chemistry in the lower troposphere of the high Arctic. In general, the total column of CO is a minimum during Sun-lit periods and a maximum during the night due to dynamical transport and OH oxidation of CO, where OH is produced via photolysis. The 24-hour diurnal cycle of CO for the entire year and for three different seasons experienced in the high Arctic can be seen in Figure 8.5. The 24-hour cycle of CO total column during polar night (October 22 to February 19) is compared to the 24-hour cycle during polar day (April 22 to August 20) and the 24-hour cycle during 'equinoctial' months (March and September), which have roughly equal hours of Sun and night in each day.

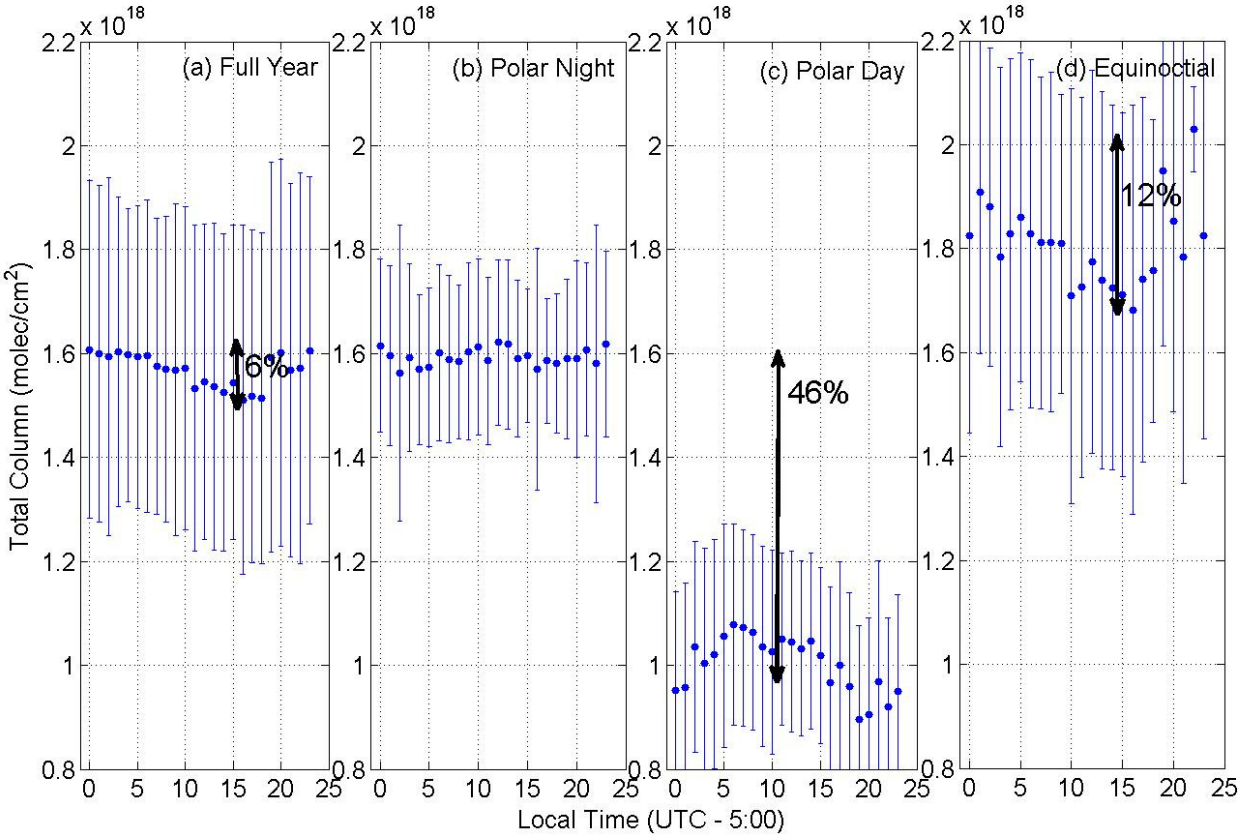

Figure 8.5: 24-hour diurnal cycle of CO during each season as measured by the E-AERI during 2008-2009: (a) averaged across the full year, (b) averaged during polar night (no Sun), (c) averaged during polar day (only Sun), and (d) March and September averaged during ~12 hours of sunlight (equinoctial). Error bars represent the standard deviation of the hourly means.

As observed in the full year and equinoctial panels (a and d), CO has a maximum around midnight as expected. The 24-hour diurnal cycle has an amplitude (maximum CO at night – minimum CO during the day / mean) of ~6% (indicated in panel a) for the full year; this is enhanced to ~12% (indicated in panel d) when filtered for the equinoctial months. Although the 24-hour equinoctial cycle is more variable (larger error bars are due to the larger standard deviation), the amplitude is enhanced as expected, as this is the only time the Arctic receives roughly 12 hours of sunlight each day. These are the first measurements of this kind at Eureka. Note that more measurements were obtained during the polar night and equinoctial months compared to polar day, which has the adverse effect of biasing the full-year results. These amplitudes (~6 and ~12%) are likely over-estimated given the sensitivity of AERI spectra to aerosols, the AERI CO low-bias discussed in Sect. 8.4.1, and the ~8% amplitude in the 24-hour

diurnal cycle of CO measured at the SGP found in Yurganov *et al*. [2010], which should have a larger amplitude than the high Arctic.

The average CO total column during the equinoctial months is greater than the average CO during polar night due to the lifetime of CO (~2 months). Almost all measurements during the equinoctial period were taken in March, when the concentration of CO is at a maximum (as indicated in Figure 8.1). Despite the Sun's return in February, CO was built up during polar night and a lag between the Sun's return and the depletion of CO due to OH oxidation occurs, resulting in the maximum occurring in March. Note that in order to quantify the impact of OH oxidation, the radiance contribution from scattered solar energy by aerosols in the summer, which has a larger signature in the CO miniwindow, will have to be removed (future work).

The amplitude of the 365-day seasonal cycle of CO is much larger than the 24-hour diurnal cycle. From Figure 8.1, the amplitude of the seasonal cycle of CO is ~57% (maximum CO in March – minimum CO in July / mean). As shown in Figure 8.5, CO columns during polar day are ~46% lower (indicated in panel c) than during polar night on average, consistent with the 24-hour OH oxidation in the summer. These are the first measurements of the 365-day seasonal cycle of CO in the high Arctic performed by an FTIR. Both of these amplitudes are larger than that in the SGP (~40%) [Yurganov *et al*. 2010], indicating a stronger 365-day seasonal cycle of CO at Eureka compared to mid-latitudes. Given the 24-hour darkness followed by 24-hour sunlight experienced in the Arctic, the increase in the amplitude of the 365-day seasonal cycle of CO is expected; however, given the larger bias of E-AERI CO vs. 125HR CO in the summer seen in Figure 8.1 and discussed in Sect. 8.4.1, this seasonal cycle may be overestimated.

8.5 Trace Gas Measurements from 0PAL

8.5.1 2011 Trace Gas Measurements and Comparisons

Starting on 16 February 2011, the E-AERI resumed measurements closer to sea-level at 0PAL. As discussed in Sect. 7.4.4, to account for the altitude difference between measurements at PEARL and 0PAL, the lower 600 m of the atmosphere was removed in all reported E-AERI

0PAL total columns. This effectively provides 0.610-100 km total columns, matching them with those measured at the Ridge Lab.

Figure 8.6 shows measurements of total columns in 2011 of the same four trace gases shown in Figure 8.1. Large gaps in the E-AERI data record are discussed in the Appendix and specifically outlined in Table A.1. The E-AERI total columns from 0PAL exhibit similar behaviour to those measured two years prior at the PEARL Ridge Lab, despite the additional H_2O. For instance, the seasonal cycle of CO can be resolved and the E-AERI CH_4 and N_2O total columns exhibit larger variability than the 125HR measurements, particularly in the summer. Persistent PSCs within the polar vortex resulted in severe chemical O_3 loss over Eureka in February and March 2011 [Manney *et al*., 2011; Adams *et al*., 2012b; Lindenmaier *et al*., 2012]. This O_3 loss is observed by the E-AERI, although not to the same magnitude (due to the difference in vertical sensitivity). O_3 columns a week prior to the start of solar absorption measurements in 2011 are available from the E-AERI. All of the E-AERI O_3, CO, and CH_4 total columns agree within error with coincident 125HR measurements; 96% of coincident measurements agree within error for N_2O.

The mean relative differences between the E-AERI and 125HR, Brewers, GBSs, and SAOZ for both 2008-2009 and 2011 are provided in Table 8.2. All mean relative differences are less than the uncertainties in the respective E-AERI total columns (see Table 8.1). Note that although the general agreement in 2011 is better than in 2008-2009, the number of coincident measurements is significantly smaller for all trace gases, with almost no coincident measurements occurring in the summer, where the largest discrepancies were observed in the 2008-2009 comparisons. Few ($N = 27$) coincident measurements between the E-AERI and the GBSs existed in 2011 (and no coincidences with the Brewers), likely causing to worse agreement for O_3 than in 2008-2009. The E-AERI O_3 measurements consistently have a positive bias compared to the 125HR, Brewers, and SAOZ throughout both measurement periods (2008-2009 and 2011), which is most prominent in the summer months (as with the 2008-2009 PEARL E-AERI retrievals). A negative bias relative to the GBSs is observed throughout both measurement periods, with very good agreement in 2008-2009.

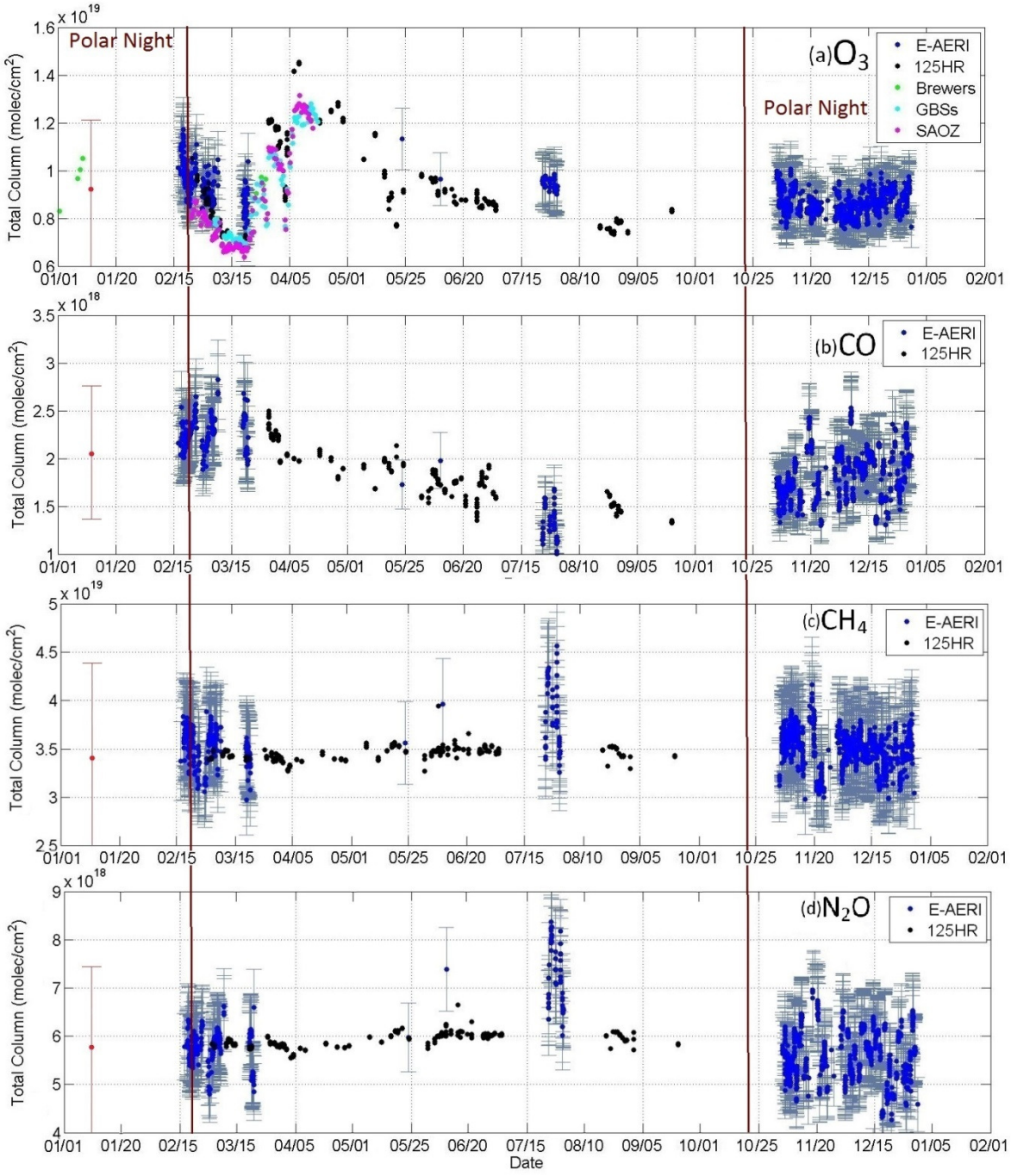

Figure 8.6: Same as in Figure 8.1, except for 2011. The E-AERI was located at 0PAL (10 m altitude) and retrieved total columns are from 0.61 to 100 km, while the other spectrometers were located at the PEARL Ridge Lab (610 m altitude). The *a priori* column is shown for one day (red) with error bars corresponding to the diagonal of $\mathbf{S_a}$. Polar night is indicated outside the brown vertical lines.

As seen in Figure 8.7, 2011 E-AERI and 125HR O_3 total column measurements are well correlated (r = 0.72 for smoothed 125HR columns), with weaker correlations between the E-AERI and the GBSs and SAOZ (r = 0.43 and 0.65, respectively, unsmoothed). There were no coincident measurements between the E-AERI and Brewers during 2011. While the correlations are not as strong as for the 2008-2009 measurements from the PEARL Ridge Lab, this is likely due to the increase of aerosols at lower altitude (which is not accounted for in SFIT2), a smaller seasonal sampling range, and fewer coincident measurements in 2011 than for 2008-2009. The apparent positive bias for CH_4 and N_2O total columns in summer 2011 compared to summer 2008-2009 is likely due to the enhanced influence that increased aerosols and water vapour concentrations have on the retrievals for lower measurement altitudes (0PAL vs. PEARL). As in 2008-2009, E-AERI O_3 columns are typically greater than the 125HR's (up to 5%). 125HR CO measurements did not commence until later in the spring, when the E-AERI was not operating. For this reason, there were too few coincidences (N = 4) between the E-AERI and 125HR to accurately determine their CO correlation. CH_4 and N_2O measurements are poorly correlated due to the lack of seasonal variability (not shown). Despite the additional water vapour at 0PAL, based on the results in Table 8.2, E-AERI trace gas retrievals are comparable to those obtained at the PEARL Ridge Lab.

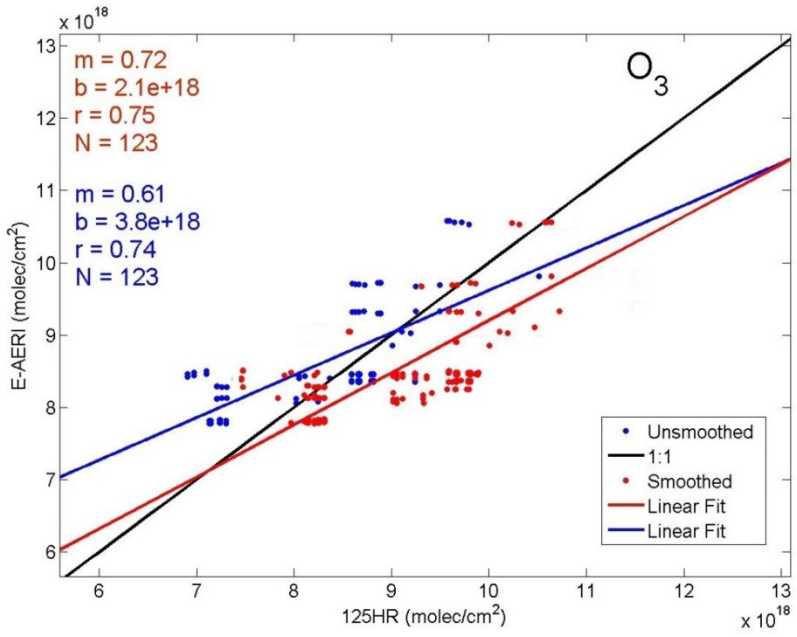

Figure 8.7: Same as Figure 8.3, but for 2011 O_3 total column comparisons for E-AERI vs. 125HR using a $\pm$ three-hour coincidence criterion.

8.5.2 January 2012 to July 2013 Trace Gas Measurements

The SFIT2 retrieval process has been fully automated to permit regular retrievals of O_3, CO, CH_4, and N_2O using E-AERI spectra. A shell script (batch code) was written by me in conjunction with several MATLAB codes that extract clear-sky E-AERI spectra, output spectra in a format required by SFIT2, perform all *a priori* calculations that are required, and then run SFIT2 on the spectra. As such, trace gas retrievals using E-AERI spectra are on-going; E-AERI total column measurements of O_3, CO, CH_4, and N_2O are shown in Figure 8.8 for the period of January 1, 2012 to July 1, 2013, when the most recent round of retrievals were performed. Gaps in the E-AERI dataset are explained in the Appendix and specifically outlined in Table A.1.

E-AERI 2012 and 2013 retrievals of trace gases are very similar to those performed in earlier years, indicating consistency of both the E-AERI measured radiances as well as the SFIT2+Emission retrieval algorithm. A clear seasonal cycle of O_3 and CO is measured and can be quantified in future studies; total columns of CH_4 and N_2O exhibit limited seasonal cycles, as with previous measurements. Retrievals of trace gases using SFIT2+Emission are considered on-going until implementation of the new SFIT4 retrieval algorithm is finalized (discussed in Sect. 8.6). As part of the ACE Validation Campaign, all E-AERI measurements of total columns of trace gases are submitted to the ACE data archive; more details are provided in the Appendix.

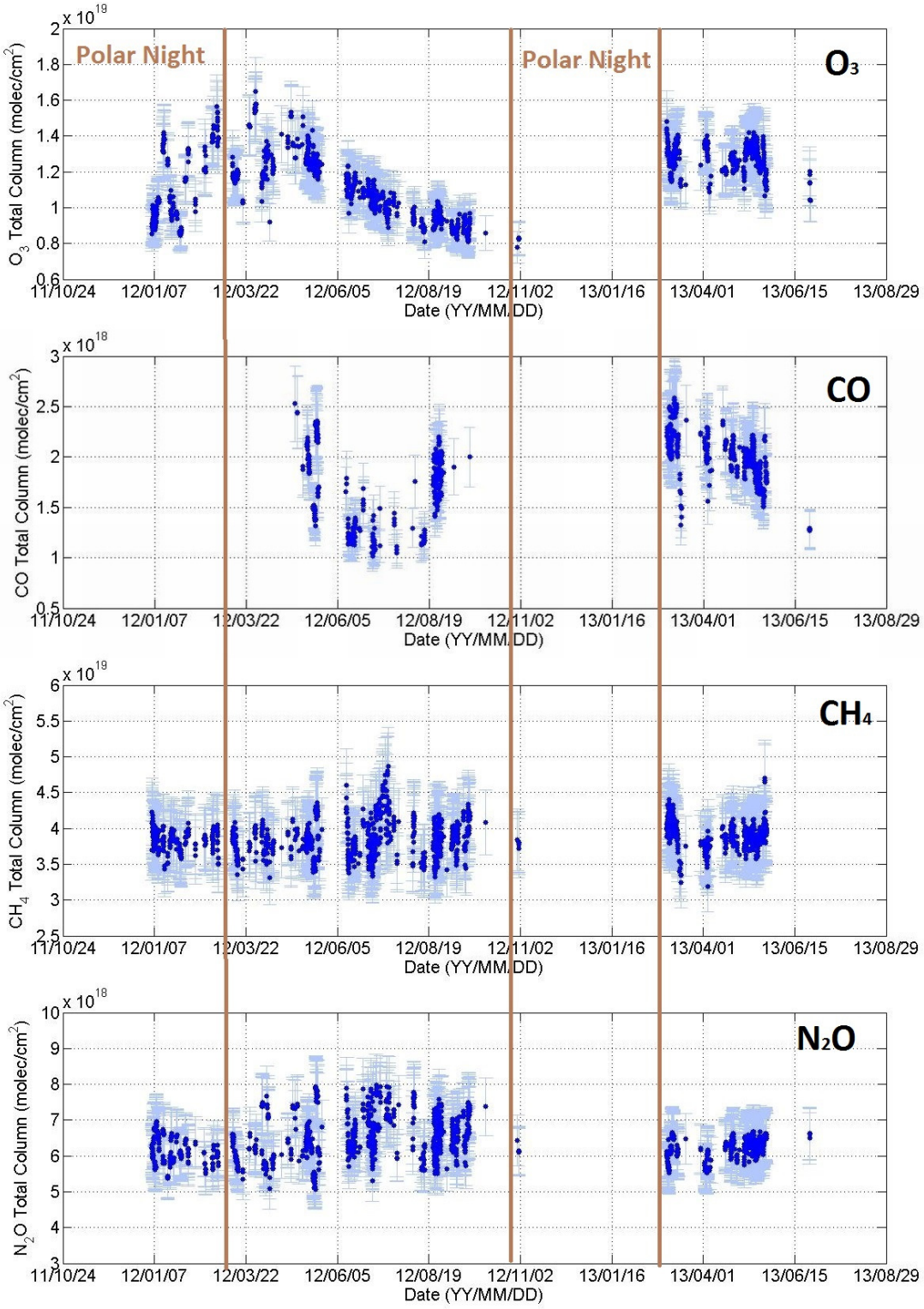

Figure 8.8: Same as in Figure 8.1, except for 2012 up to July 2013. The E-AERI was located at 0PAL (10 m altitude) and retrieved total columns are from 0.61 to 100 km. Polar night is indicated inside the brown vertical lines.

8.6 Testing the New SFIT4 Retrieval Algorithm

The successor of the SFIT2 retrieval algorithm, SFIT4, has been under development since 2011 (note there is no "SFIT3"). SFIT4 will incorporate all aspects of the modified SFIT2+Emission add-on and has these additional features:

1) Complete automation script (for SFIT2 this was called '*zephyr2*'), now called '*Layer1*'
2) Improved naming convention of output filenames
3) Streamlined input control files: now a single input file controls all aspects of the retrieval
4) Updated HITRAN database to version 2012 with improved extraction methodology
5) Ability to retrieve strength of solar lines and solar shift
6) RAYTRACE is now implemented in the SFIT4 bash script and run in conjunction with the retrieval (no longer run separately)
7) *a priori* VMR profiles that are required are generated by SFIT4 (no longer needs to be created beforehand independently)
8) All VMR and height/pressure/temperature profiles are automatically interpolated according to the specified grid in SFIT4 (no longer have to do this independently)
9) The error matrix $\mathbf{K_b}$ and gain matrix **G** are now calculated during each retrieval and can be output
10) Full error analysis is now performed (no longer an independent exercise)
11) Post-retrieval, contributions of each molecule (target trace gas and interfering trace gas species) to the spectral fit (simulated spectra) are output
12) Lunar-absorption retrievals are enabled, including necessary emission terms in the radiative transfer equation
13) Iteration scheme can be changed from Gauss-Newton to Levenberg-Marquardt for any retrieval
14) Improvements to the numerical stability when calculating the averaging kernel matrix, **A**
15) Significant improvement of retrieval speed due to streamlined input/output mechanisms and numerical stability
16) Output of spectral fitting parameters and cost function calculations

This list details some (not all) of the major improvements to the SFIT4 retrieval algorithm. Since SFIT4 is a new retrieval algorithm, a significant amount of testing has been

performed to ensure that retrievals using emission spectroscopy are numerically stable and in agreement with SFIT2+Emission's results. I have collaborated with M. Palm (U Bremen) closely on this test process; sample E-AERI spectra are the official 'test case file' for SFIT4 emission spectra for other users.

In order to run SFIT4, a considerable number of changes, technical in nature, have been be made to the E-AERI retrieval process in order to ensure compatibility: E-AERI radiance files now must be output as binary (.bnr) files, *a priori* and height/pressure/temperature radiosonde data must be interpolated onto a 61-layer grid, a "*stat.layers*" (or station layers) file must be created to specify the retrieval grid, and the SFIT4 file "*pspec*" must be altered so that SFIT4 does not estimate the amount of noise on the spectra (which it assumes is solar-absorption by default) but instead uses the NESR provided by the user. With exception of the final alteration (currently in progress), these changes have been made to the necessary E-AERI retrieval codes and permit semi-automated retrievals of trace gases using SFIT4 and *Layer 1*.

Preliminary retrievals performed using a beta version of SFIT4 (v094) were performed for June 24, 2009, 12:00-13:00 E-AERI spectra using the same set up conditions as for SFIT2; a comparison of the spectral fits with SFIT2 retrievals are shown in Figure 8.9. Note these results are preliminary until *pspec* can be altered to ensure the retrieval algorithm is using the correct value for noise, which will affect the retrieval's calculation of $\mathbf{S_m}$. These retrievals do not include the N_2 CIA model discussed in Sect. 8.4.1 as the model is not yet compatible with the current version of SFIT4; this is supposed to be included in the updated version of SFIT4. Spectral fits are very similar (change in RMS was < 0.2%) with small changes in the residual's structure, indicating consistency among retrieval versions. In all cases, the RMS error for SFIT4 residuals was smaller (albeit slightly) than with SFIT2 residuals, indicating slightly better fits.

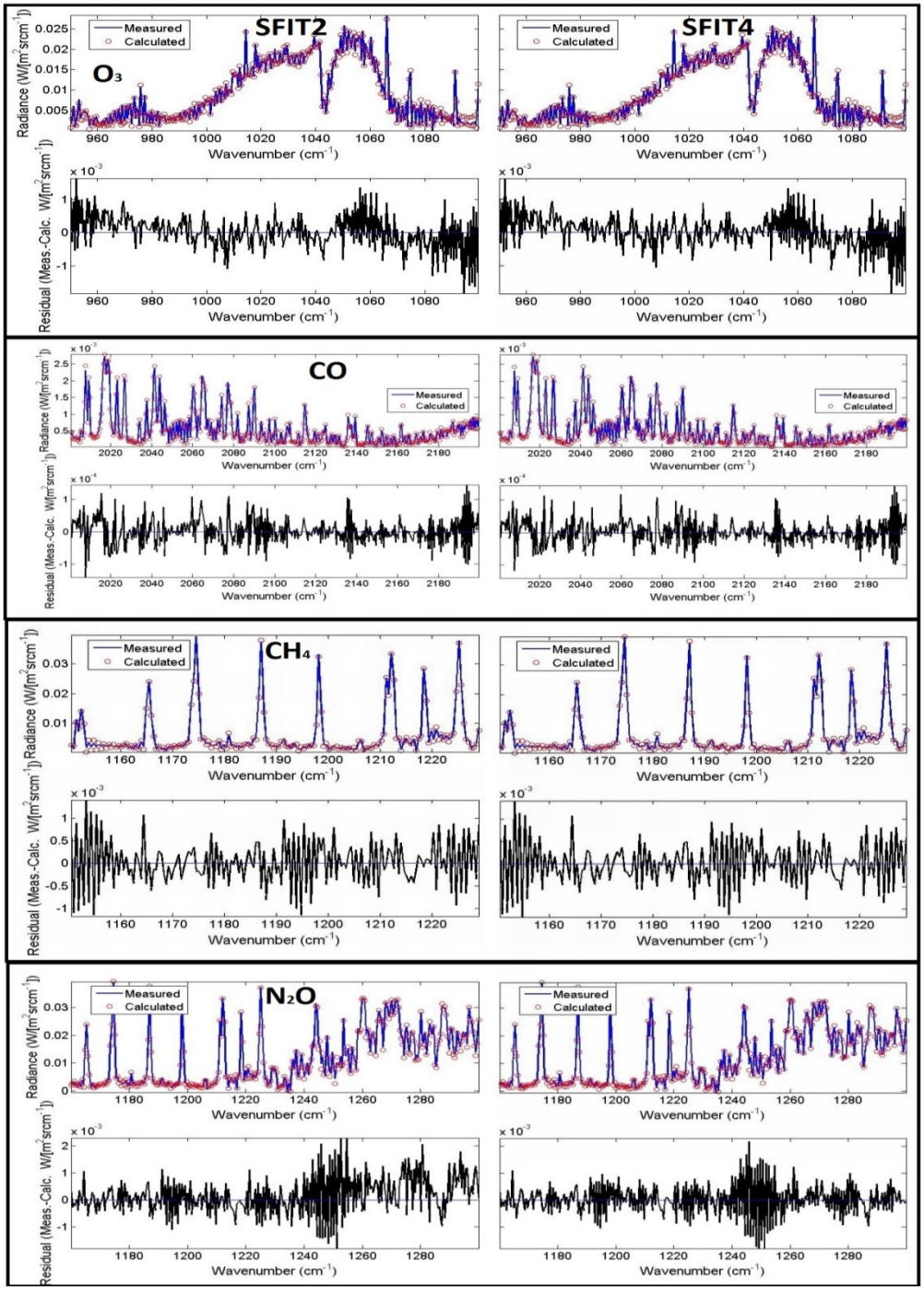

Figure 8.9: Spectral fits for O_3, CO, CH_4, and N_2O performed by SFIT2 (left column) and SFIT4 (right column). Top panels show the measured (blue) and fitted spectra (red circles), with their residuals shown in the bottom panels. Note the vertical scales are kept constant left-to-right while the residuals are on a finer scale. Retrievals were performed for spectra recorded at 12:00-13:00 UTC on June 24, 2009.

8.7 Summary of Year-round Trace Gas Measurements at Eureka

Total columns of O_3, CO, CH_4, and N_2O were retrieved using E-AERI spectra from October 2008 to September 2009 at the PEARL Ridge Lab and from February 2011 to August 2013 at 0PAL using a new version of the SFIT2 retrieval algorithm adapted for IR emission spectra. This is the first time IR emission spectra have been used to retrieve trace gases using the newly modified version of SFIT2. This Chapter also presented the first continuous ground-based polar night trace gas measurements at Eureka, which fill a gap in the PEARL dataset when the solar-viewing spectrometers are not operating.

An error analysis was performed, indicating that the uncertainty in the E-AERI total column measurements is 11.3% for O_3, 14.7% for CO, 11.0% for CH_4, and 10.9% for N_2O. E-AERI trace gas measurements agree well with those from the other spectrometers: mean relative differences are less than the uncertainties in the E-AERI total columns (1-10% differences). The 2008-2009 E-AERI and 125HR measurements of O_3 and CO were highly correlated, with a correlation coefficient of $r = 0.92$ and 0.95, respectively, which is stronger than the E-AERI O_3 correlations with the other spectrometers. The largest differences between the E-AERI and the other spectrometers for all four gases occur in the summer, indicating that the accuracy of the E-AERI's retrievals is season-dependent. This is likely due to the large (~10 x) seasonal variability of water vapour in the high Arctic and scattered solar energy by aerosols in the summer, which is not accounted for in SFIT2.

The 2011 E-AERI 0PAL retrievals are comparable to those of 2008-2009, despite the increased water vapour at 0PAL. The E-AERI vs. 125HR CO correlation is comparable to the AERI vs. convolved in-situ CO correlation ($m = 0.92$, $r = 0.76$) found in Yurganov *et al*. [2010]. Larger differences in the CO columns are due to a combination of factors, but primarily due to the effects of CIA by N_2. Preliminary tests of an ad-hoc N_2 CIA model included in the SFIT2+Emission retrievals indicate an improvement of the E-AERI CO retrievals, increasing the column amount to a level that is significantly closer (4.8 to 7.1%) to the 125HR CO measurement. This work recommends a robust N_2 CIA model be included in the new SFIT4 version to account for this. A description of the new SFIT4 retrieval algorithm, which will have

a fully-functioning emission add-on (as well as additional changes) was discussed. Preliminary tests and comparisons were performed to ensure retrievals performed using SFIT4 are comparable with SFIT2+Emission. Progress towards full implementation and automation of the new SFIT4 retrieval algorithm continues to the date of this thesis and is considered future work.

The budget of O_3 prior to, during, and after O_3 depletion events can be determined using E-AERI measurements. The 24-hour diurnal cycle of CO at Eureka has been resolved using the E-AERI measurements. The amplitude of the 24-hour diurnal cycle measured by the E-AERI is similar (~6 to 12%) to that in Oklahoma (~8%) found using AERI CO retrievals [Yurganov *et al*. 2010]; however it is likely that the Eureka amplitude is over-estimated. The amplitude of the 365-day seasonal cycle of CO at Eureka is greater (~46%) than that in Oklahoma (~40%), suggesting a stronger seasonal cycle of CO in the Arctic.

E-AERI's year-round measurements of these trace gases can provide insight when investigating biomass burning events. Although the frequency of biomass burning events is decreased in the winter, the E-AERI is the only instrument at Eureka capable of measuring emission products during this time when dynamical transport to the Arctic is enhanced, lengthening the potential period of studying such events. E-AERI retrievals can also be performed on a per-spectrum basis (every 7 minutes) as opposed to hourly-averaged in order to investigate the dynamical transport of trace gases (for instance, measuring the variability of CO as a proxy of vertical motion above Eureka) [Niwano and Shiotani, 2001]. Ongoing measurements of the trace gases discussed in this paper from 0PAL are being conducted (with only limited measurement interruptions since summer 2013) to investigate their diurnal and interanual variability and for satellite validation. E-AERI trace gas measurements will continue to be used to fill the polar night gap in the PEARL dataset, providing insight into the state of the atmosphere year-round.

The retrieval methodology used in this work can be extended to all AERI instruments (of which more than 25 are in operation across the globe) and to other spectrometers that measure IR emission. The extension of this retrieval methodology is already underway; in South Korea, I have collaborated with Tae Young Goo (National Institute of Meteorological Research) and provided SFIT2+Emission and the new SFIT4 version, which have enabled his research team to perform retrievals of CH_4 using a new 4th generation AERI for the purposes of satellite validation.

9. CONCLUSIONS

9.1 Summary

The rate at which the Arctic climate is changing is alarming. Given the sparse measurement density in this vast remote region, long-term measurements of the atmospheric state are needed to improve our understanding of how the climate is changing and why. For this reason, CANDAC has equipped PEARL for measurements during International Polar Year (IPY, project 196) and beyond. One of the instruments at PEARL is the E-AERI, installed in 2008. When combined with the P-AERI measurements taken at 0PAL, the combined Eureka dataset provides measurements of absolute downwelling IR radiation for studies of the Arctic radiation budget and atmospheric composition over the past 8+ years. The focus of this Ph.D. project was the management of the E-AERI instrument, including its operation, maintenance and repair, and analysis of its data products (including utilization of the P-AERI Eureka dataset) in order to answer the science questions outlined in Sect. 1.2. The five objectives of this thesis outlined in Sect. 1.2 have been fulfilled, with their main outcomes summarized in this section.

The power of utilizing FTS measurements as a tool for studying the atmosphere was described, including relevant theoretical background. The advantages of the FTIR spectrometer over other instrument designs presented in this work explains why this type of instrument is so commonly used for study of the Earth's - as well as other planet's - atmospheres today. A description of the E-AERI was provided, including the history of the AERI instruments, the changes pertaining to the E-AERI's new design and performance characteristics, the type of measurements the E-AERI makes, the measured spectra's quality control, and details of the BB calibration methodology (including the theoretical formulation for this calibration), and instrument certification procedure.

The validation of this new (at the time prototype) instrument's dataset ensured the reliability of the measurements used in the subsequent studies described in this thesis. The

difference between the radiative budget at two altitudes (610 m and 10 m) was investigated using these two AERIs, and comparisons between E- and P-AERI measured radiances during clear-sky conditions and simulated radiances using a FLBLRTM indicated good agreement (within error for the majority of the spectrum). Side-by-side comparisons between the two AERIs also indicated good agreement within $\pm$ 1 mW/(m^2 sr cm^{-1}) for the MCT detector and $\pm$ 0.2 mW/(m^2 sr cm^{-1}) for the InSb detector (within measurement noise when averaged over the entire spectrum). Thus measurement consistency and reliability between the P- and E-AERI validates the combination of two AERI's datasets to create a single 8+ year (9+ year and growing as of the date of this thesis) Eureka AERI dataset.

Measurements of the radiative forcing due to the presence of clouds, including a case study of a low-altitude thin-layer ice-crystal cloud, were performed. Results indicate that the impact of clouds on the radiative budget is larger for the Arctic than for more humid regions, indicating that cloud cover plays a critical role in the Arctic's radiative budget. A cloud filter was created to permit the independent identification of cloud cover (clear, thin, or thick clouds) and was shown to be highly (> 95%) accurate compared to MMCR and AHSRL data. This cloud filter was used extensively in subsequent studies to determine clear-sky scenes (for trace gas retrievals) and to characterize the radiative forcing from different types of cloud cover.

Distributions of downwelling 10 and 20 μm brightness temperatures at Eureka (the two surface cooling-to-space windows in the Arctic) were separated based on cloud cover using the cloud filter, providing a comparison to an existing 10 μm climatology from the SGP. Results indicate that the 20 μm window is closed in the summer. Statistically significant trends in seasonal averages of downwelling radiance were found in multiple microregions of interest. During the winter in Eureka, trends of downwelling radiance at 10 μm are positive, in the opposite direction, and larger (factor > 3) than the trends during any season detected at the SGP, indicating that changes in the downwelling radiance are accelerated in the high Arctic compared to lower latitudes. The large increase (> 4% / yr) in radiance at 10 and 20 μm during the winter is mainly attributed to the increased prevalence of thick clouds. This may have long-term consequences, particularly as warmer temperatures and increased water vapour "close" the 20 μm window for an extended period. These surface-based measurements of radiative forcing can be used to quantify changes in the high-Arctic energy budget and evaluate general circulation model simulations.

One of the goals of this thesis was to produce a new trace gas measurement product for the E-AERI. An overview of retrieval theory, including the theoretical description of the OEM and SFIT2 retrieval algorithm used to perform the retrievals, was provided. E-AERI total column measurements of O_3, CO, CH_4 and N_2O were retrieved from 2008 to 2013 (and are ongoing). Analysis of the E-AERI retrievals indicates high sensitivity to the troposphere. A full error analysis was performed to determine the uncertainty in the E-AERI total column measurements for each trace gas (10-15%, depending on the gas). Comparisons to other ground-based spectrometers at Eureka were performed and indicate good agreement with the E-AERI retrievals (1-9% difference, depending on the spectrometer), which serves to validate this new AERI data product. It is suggested that a N_2 CIA model be included to improve the CO retrievals (as this causes an AERI low-bias); the difference between the E-AERI and 125HR CO column was decreased from 15% to 7% when using the N_2 CIA model. A case study of the seasonal cycle of CO was performed; the seasonal cycle was found to have an amplitude of 46%. The retrieval methodology can be extended to all AERI instruments (of which more than 25 are in operation across the globe) and other spectrometers that measure IR emission. Current work has focused on implementing the retrieval methodology in the new SFIT4 retrieval algorithm, and will continue to be the basis of future work on this project.

9.2 New Knowledge Generated

The work presented in this thesis has made several contributions to scientific knowledge:

- The installation of a new FTIR spectrometer at PEARL, with the goal of calibrated, automated, and continuous long-term measurements of downwelling radiance throughout polar night. The instrument automatically measures the downwelling radiance every ~7 minutes during all weather events (except precipitation). These long-term measurements provide a dataset for trend analyses, model intercomparisons, and satellite validation studies.
- A published paper on the commissioning of the new E-AERI instrument, including a description of the design changes to the new 4th generation AERI system, side-by-side comparisons (validation of measurements), and initial measurements of downwelling

radiance. This included investigation of the difference in radiative budgets at two altitudes at Eureka using two AERIs, as well as investigation of the radiative impact of clouds. A second, non-peer-reviewed paper was published detailing the technical aspects of the new E-AERI instrument.

- Investigation of the impact of clouds and ice crystals (in a case study) on the radiative budget. Results illustrate that the impact of clouds on the radiative budget is larger for the Arctic than in other more humid regions, indicating that cloud cover plays a critical role in the Arctic's radiative budget.
- Creation of a cloud filter for E-AERI radiances. Using E-AERI spectra, clear sky/thin clouds/thick clouds can now be classified without input from any additional measurements, providing a new cloud dataset (paper in prep.).
- The first measurements of both the 10 and 20 μm surface cooling-to-space windows in the high (> 75^{o} N) Arctic. Distributions of brightness temperatures were filtered based on cloud cover, and trends in downwelling radiance were found in several microregions sensitive to these cooling-to-space windows and meteorological conditions (temperature, water vapour, cloud cover). Comparisons to an existing climatology of similar measurements for the SGP indicate that changes in the 10 μm window are accelerated in the Arctic compared to southern latitudes (paper in prep.).
- Creation of a new retrieval methodology for the E-AERI using SFIT2, providing the first dataset of total column trace gas measurements for the E-AERI. The SFIT2 retrieval algorithm, modified by M. Palm (U. Bremen), was successfully tested and implemented by me and can now be used with emission spectra, such as those produced by the E-AERI. This methodology can be extended for use with any other IR emission instrument, including the other > 25 AERIs deployed across the globe.
- Investigation and analysis of miniwindows to be used with the SFIT2 retrieval algorithm for the new emission retrievals.
- Assessment of the retrieval parameters for four trace gas species retrieved by the E-AERI. Retrievals were characterized in detail, providing the uncertainty in the column, spectral fits, sensitivity, and comparisons to other ground-based spectrometers.
- Investigation into the low-bias of AERI CO retrievals, which is not instrument- nor site-dependent (exists for more than just the E-AERI at Eureka). The importance of the N_2

CIA was determined; results indicate this spectroscopic feature should be included in the new SFIT4 version to improve the E-AERI CO retrievals.

- Submission of E-AERI trace gas total column measurements to the ACE Validation Campaign Archive. The archive is designed for satellite validation studies, which is the focus of ongoing work.
- Published paper describing the new E-AERI trace gas retrieval product. These measurements are the first continuous ground-based measurements of four trace gas species year-round (throughout polar night) at Eureka. These retrievals fill a gap in the PEARL dataset, when the other solar-absorption spectrometers are not operated.
- Investigation of the diurnal and seasonal cycle of CO (throughout polar night) to highlight the usefulness of continuous, year-round measurements at Eureka.

9.3 Recommendations for Future Work

The E-AERI requires consistent maintenance, including regular re-calibration servicing (on the order of 1-3 years, depending on the component), in order to continue operating at peak performance. Refer to the E-AERI's Standard Operating Procedure (SOP) [Mariani, 2014] for operation, maintenance, and troubleshooting guidelines. Aside from the physical operation of the E-AERI instrument, the now 9+ years of downwelling radiance measurements from the combined Eureka AERI dataset is an excellent resource to perform various scientific studies, either as a continuation of this work or as an expansion into new areas of research. Some suggestions for future work are:

- Measurement of the E-AERI's ILS
    - During trace gas retrievals it is assumed the E-AERI's ILS is an ideal sinc function – in reality this is not the case. While the sinc function offers an approximate representation of the instrument's ILS, directly measuring and characterizing the instrument's ILS should improve trace gas retrievals as it provides information on the instrument's optical alignment, scan mirror stability, and sampling errors. The E-AERI is not designed to have ILS measurements performed (as with the Bruker 125HR), hence an apparatus must first be

designed and constructed that can be temporarily mounted on top of the E-AERI's hatch and include a source (e.g., HBr gas cell) within the instrument's FOV in order to perform the ILS measurement.

- Further investigation into the difference in the radiative budget at two altitudes at Eureka (between the P- and E-AERI)
    - Several time periods of large radiance differences are shown in Figure 4.3; only one period was investigated in further detail (low-altitude ice crystal cloud described in Sect. 5.2) which explained the large radiance difference on this day. Investigation into the other days of large differences could yield interesting correlations with the meteorological conditions above Eureka.
- Create a cloud climatology
    - Using the cloud filter described in Sect. 5.3, clear-sky, thin-cloud, and thick-cloud radiances can be sorted. Over a long time period (> 10 years), this data can be used to generate a cloud cover climatology for Eureka. Trends in the change in the type of cloud cover can be quantified, compared to previous studies (e.g., Lesins *et al.* [2009], Chapter 6 of this work), and compared to other methods (satellite observations, model, LIDAR, MMCR).
- Create a climatology of downwelling radiances at surface cooling-to-space windows
    - The study presented in Chapter 6 covers an eight-year dataset. Extending this dataset to capture natural variability, fully sample the seasonal cycle, and reduce the gaps in the dataset would permit publishing a high Arctic climatology (> 10 years of measurements) of these measurements. This climatology can be compared to the existing climatology at the SGP as well as preliminary trend results found in Sect. 6 to determine whether trends are continuing. A long-term record of integrated radiances throughout the entire 20 μm window (17-25 μm) using just the E-AERI could be compared to the entire 10 μm window (8-12 μm) to determine whether a shift between these two energy regimes exists, particularly as the 20 μm window closes. This climatology would also provide additional data for comparisons to climate models.
- Compare downwelling radiances and fluxes to the other two AERIs in the Arctic (Arctic radiance climatology)

  - Two other AERIs in the Arctic (one at Barrow, Alaska, and another at Summit, Greenland) have been conducting downwelling radiance measurements over the same time period. Comparing the downwelling fluxes and radiances, such as done in Cox *et al.* [2012], between these sites can be performed. The potential for creating a climatology for Arctic measurements of this type would provide an extremely valuable dataset for model comparisons.
- Cloud-phase and composition can be investigated for the Arctic using E-AERI and LIDAR measurements, as shown in Turner *et al.* [2005].
  - The ability of AERIs to evaluate cloud properties by remote sensing can be utilized to retrieve cloud optical depth, mixed phase fraction, cloud particle size, etc. using cloud retrieval algorithms (such as MIXCRA) and combining AERI measurements with existing radiosonde, MMCR, and LIDAR measurements at Eureka. Comparisons between instruments and techniques can be performed.
- Further improvements to the CKD water vapour continuum model can be performed using E-AERI observations around 20 μm, as shown in Tobin *et al.* [1999].
- Comparisons with the far-infrared radiometer (FIRR) for the Thin Ice Clouds Far Infrared (TICFIRE) mission
  - TICFIRE is a mission proposed to the CSA for a far-infrared payload to monitor the evolution of thin-ice clouds using measurement techniques similar to the AERI, except from space. Details about the TICFIRE mission are provided in Blanchet *et al.* [2011]. Comparisons between the ground-based and space-based measurements of radiance will be of particular interest for validation and radiative-closure studies once the FIRR radiometer begins to take measurements.
- Water vapour and temperature retrievals
  - AERIPROF [Smith *et al.*, 1999] was created for retrievals of water vapour and temperature using AERI measurements at the SGP. A new *a priori* and meteorological model are required for these retrievals to work in the Arctic. Preliminary work has established the feasibility of having this retrieval algorithm work for Arctic conditions. Alternatively, a separate water retrieval code has been written by P. Rowe (U Idaho) and is currently being tested [D. Weaver; personal communication]. Comparisons between AERI water vapour retrievals and other instruments indicate good agreement, but further work is required.

- Improving the E-AERI CO retrievals
    - Refer to Sect. 8.4.1; the impact of N_2 CIA is not well published in the literature and could be the focus of a research paper.
- Ongoing trace gas retrievals using SFIT2 (with a transition to SFIT4)
    - Continue to perform trace gas retrievals using E-AERI spectra.
- Comparing SFIT2 and SFIT4 retrievals
    - Once SFIT4 has been fully implemented, a full comparison of the SFIT2 trace gas time series with the SFIT4 time series is warranted. Interesting differences can be investigated further.
- Comparisons with another retrieval algorithm
    - Comparing results generated from SFIT2/SFIT4 with other retrieval algorithms, such as that developed by P. Rowe (U. Idaho) or published in Yurganov *et al.* [2010], would provide useful insight into advantages and limitations of each algorithm.
- Retrieve trace gas total columns using other AERIs
    - The retrieval methodology outlined in this thesis can be extended to the other AERIs across the globe. Performing trace gas retrievals using the same methodology (where applicable; e.g., not the *a priori*) can produce an 'AERI measurement network' across the globe.
- Investigate new trace gas species that can be retrieved using the E-AERI
    - Other trace gas species investigated but not discussed in this thesis (additional work is required to determine correct input parameters, miniwindows, etc.) are: NO, NO_2, OH, HCOOH, HCl, CH_3OH, ClO, OCS, and NH_3. This would increase the number of retrieved trace gas products using AERI measurements.
- Investigate biomass burning events using E-AERI trace gas retrievals
    - CO enhancements are an indicator of biomass burning events, especially when they coincide with enhanced HCN and C_2H_2 columns [Viatte *et al.*, 2014]. Given the AERI's high sensitivity to tropospheric trace gases, AERI measurements can be combined with other observations of biomass burning events. Since the E-AERI operates year-round with high temporal resolution, this allows one to fill in a gap in the 125HR 'biomass burning events record' at PEARL.

- Investigate diurnal and seasonal cycles of various trace gases, with emphasis on measurements during polar night
    - Thus far only the diurnal and seasonal cycle of CO has been quantified. Similar analysis can be performed for other trace gases to better determine their chemical processes, particularly during polar night (which is a major emphasis during the new Probing the Atmosphere of the High Arctic (PAHA) research project taking place at Eureka), and over a longer time period.

APPENDIX

A.1 Additional Technical Details of the E-AERI

A.1.1 System Software Architecture

The E-AERI's software allows unattended operation of the system. The E-AERI software system performs all necessary data calibration in real-time, thereby eliminating the need for post-processing [Demirgian and Dedecker, 2005]. The software also performs a series of quality control checks in real-time and allows unattended operation of the system. The data are accessible via a digital network with an on-board storage capacity of several days. The flow structure of the E-AERI data is illustrated in Figure A.**1**. Additional details of the software architecture are provided in the Appendix.

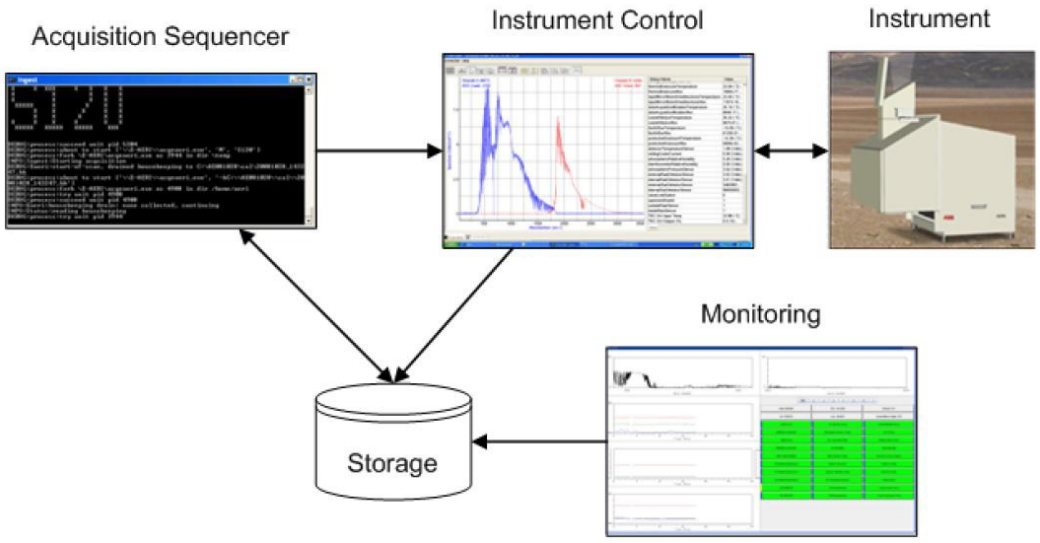

Figure A.1 Software architecture for the E-AERI. Image: ABB.

The Graphical User Interface (GUI), shown on the bottom right of Figure A.**1**, supports interactive use of the instrument and is used to monitor the state of the instrument. Calibrated spectra and some auxiliary parameters are displayed at the end of each scan. Within each window of the monitoring GUI, the radiance, air temperature, Stirling cooler current, and instrument temperature are displayed. Thirty instrument parameters are also monitored using the GUI. Table A.1 lists the variables that are used as real-time quality metrics for the E-AERI. If one of these parameters falls outside of a tolerable range, the operators are alerted.

Table A.1: Parameter metrics used when monitoring the status of the E-AERI. The normal operating range customized for operation at Eureka lies between the limits shown.

Parameter	***Normal Operating Limits***	***Description***
AB Temperature	243.15, 313.15 K	Temperature range of the given instrument components
HB Temperature	263.15, 353.15 K	
Outside Temperature	233.15, 323.15 K	
Rack Ambient Temperature	277.15, 319.15 K	
Rain Intensity	2.5, 3.2 V	Measured rain intensity range that triggers the hatch to close
AB Maximum Temperature Difference	0.1 K	Maximum allowed temperature difference between the three temperature sensors inside each blackbody
HB Maximum Temperature Difference	0.7 K	
B.B. Support Structure Temperature	233.15, 323.15 K	Temperature range of the given instrument components
Air Temperature near Blackbodies	233.15, 343.15 K	
SCE Temperature	273.15, 333.15 K	(SCE = Signal Conditioning Electronics)
Air Humidity	1, 99 %	Air humidity range
HB Stability	-0.5, 0.5 K	HB temperature variability during a scan
Mirror Motor Temperature	233.15, 363.15 K	Temperature range of the scene mirror motor
Atmospheric Pressure	750.0, 1040.0 Pa	Atmospheric pressure range
336 Kelvin (Reference)	2426.96, 2433.04 Ω	Measured resistance range for the reference temperature resistors (used to calibrate blackbody temperatures)
293 Kelvin (Reference)	10480.04, 10493.96 Ω	
249 Kelvin (Reference)	97232, 98272 Ω	
Motor Driver Temperature	273.15, 323.15 K	Temperature range of the given instrument components
Interferometer Window Temperature	293.596, 324.924 K	
Encoder Scene Confirm	-5, 5 0.01°	Confirmation of scene mirror position (range: min, max; and precision)
LW HB NEN	0, 1 mW/(m^2 sr cm^{-1})	Noise estimation (NEN) for the long- and short-wave by use of the HB
SW HB NEN	0, 0.1 mW/(m^2 sr cm^{-1})	
Air Temperature near Interferometer	293.87, 322.09 K	Temperature range of the air near the MR-300 interferometer
LW Responsivity	0.0104, 5 Counts/ mW/(m^2 sr cm^{-1})	Estimated long- and short-wave responsivity of the system during a scan
SW Responsivity	0.0112, 20 Counts/ mW/(m^2 sr cm^{-1})	
Cooler Compressor Temperature	290.398, 350.202 K	Range of the cooler compressor temperature

Cooler Current	0.03, 0.086 Amp	Range of current used by the cooler
Cooler Expander Temperature	285.0, 368.4 K	Temperature range of the hot end of the cooler
Detector Temperature	61.3, 70.4 K	Range of the detector's temperature

A.1.2 Spectral Reprocessing

Since the E-AERI's installation at PEARL, it has recorded spectra every seven minutes (weather permitting) from October 2008 onwards. In the spring of 2009, Mareile Wolff discovered several problems with the E-AERI data series. After analyzing the recorded spectra files, the following problems were found in the data series: incorrect date and location filename stamps on many files, the instrument's hatch sensor caused the recorded spectra to be deleted when it thought the hatch was closed, and duplicate spectra (or missing spectra) files were also found due to an error in the real-time processing codes.

Based on a survey of 163 days of E-AERI data from October 2008 to April 2009, about ¾ of the E-AERI data required reprocessing. A reprocessing package was developed by ABB and implemented on all 2008-2009 E-AERI spectra to fix these issues. The code was written in Fortran and Python to fix the issues listed above. Final spectra output files were re-created for every recorded spectra, for all measurement days to correct this issue. The reprocessing package was tested on spectra for each type of problem to ensure that reprocessing correctly extracted the unique spectra for that measurement. The E-AERI software package on the instrument's laptop has since undergone several updates to correct these issues (as well as other minor glitches), ensuring no further reprocessing is necessary.

A.1.3 Acquisition Software

To start an acquisition, the operator launches the E-AERI acquisition sequencer by entering a set of commands in the command prompt. Once launched, the E-AERI will automatically enter routine mode, where the instrument will record spectra approximately every seven minutes. If the instrument detects precipitation, the software automatically shuts the instrument's hatch and enters standby mode until the precipitation ends, at which point it will automatically resume taking measurements. The E-AERI data is transferred from its local storage to the Eureka Synology Cube, from where it is made available remotely to any user.

Figure A.2 illustrates this flow of E-AERI data from Eureka to anywhere on the globe. The Eureka and Toronto Cubes are managed by CANDAC.

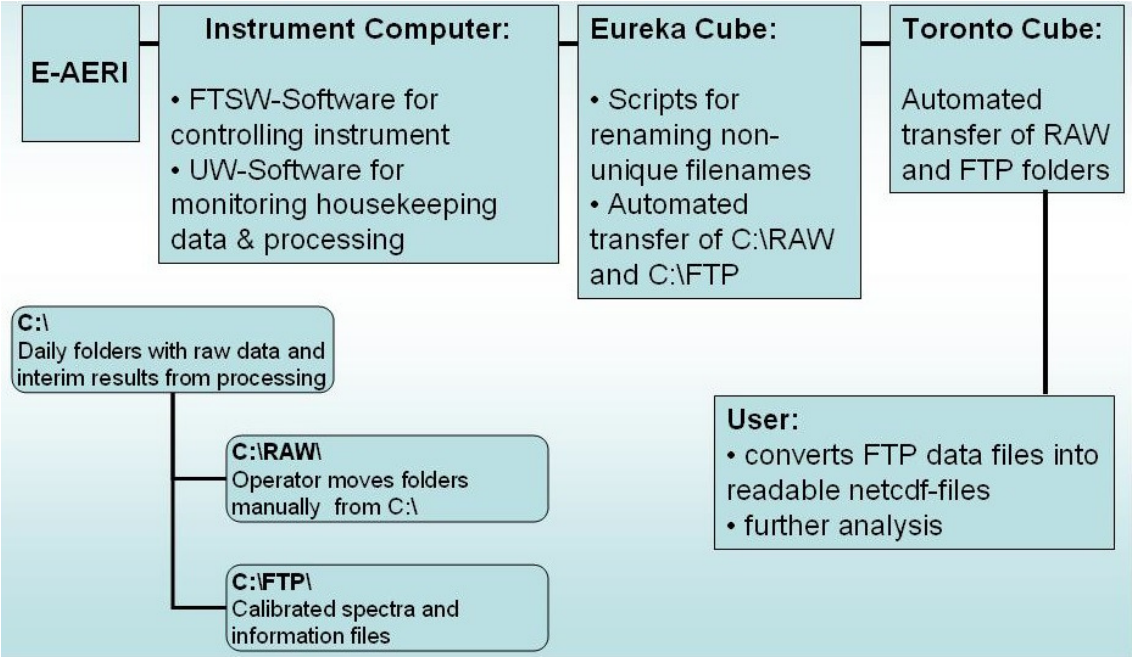

Figure A.2: Flow chart of the E-AERI data: processing, transfer and storage. Image: Mareile Wolff.

A Standard Operating Procedure (SOP) was created for the E-AERI instrument in 2009 by myself and has undergone several updates since its inception. The SOP is designed to provide all operating instructions for the E-AERI instrument intended for any CANDAC operator or researcher. Included in the SOP are basic operating guidelines, maintenance routines, troubleshooting procedures, contact lists, and repair procedures. Many elements from the E-AERI's user manual have been modified and incorporated into the SOP. The E-AERI SOP is stored on-site at 0PAL, as part of the instrument's information package, as well as on local servers (e.g., Petabit) at University of Toronto.

A.2 Repairs to the Instrument

When the University of Toronto received the E-AERI, it was the first 4th-generation AERI system constructed, and as such it was considered a prototype instrument. As with all

prototypes, it is difficult to anticipate areas of instrument failure, which has resulted in significant down-time since the E-AERI's installation in 2008. Table A.2 lists each event that caused data loss in the E-AERI dataset, including event duration, description, and resolution. Thus the gaps in the E-AERI dataset that appear in Figure 3.5 can be attributed to these issues.

In order to take measurements of the lowermost 600 m of the atmosphere, which is valuable for water vapour and temperature research, the E-AERI was moved from PEARL to 0PAL at the end of September 2009 after the P-AERI was removed. Before the E-AERI was moved, a gradual decline in the condition of both detectors was observed by operators at PEARL. Both the MCT and InSb detectors are mounted in a dewar and must be kept below 70 K in order to function properly. A Stirling cryo-cooler maintains this temperature for the detectors. When the E-AERI was moved from PEARL to 0PAL, the detectors still failed to cool below 70 K. The Stirling cooler was removed and shipped to ABB for inspection; it was determined that the Stirling cooler was damaged, and a new one was sent to Eureka on February 20, 2009.

As part of the 2010 ACE Validation Campaign, I travelled to Eureka to install the new Stirling cooler with the help of the PEARL site manager, Pierre Fogal. The installation of the new Stirling cooler into the dewar of the MR-series interferometer was completed on February 22, 2010. The E-AERI was reactivated and monitored for three days; during this time the detector temperature maintained high levels above 70 K. After further deliberation with ABB, the E-AERI was disassembled on March 2, 2010, with the MR interferometer removed from the back-end of the E-AERI. The MR, Agilent multimeter, and Stirling cooler were shipped back to ABB for further inspection. It was later discovered that the dewar inside the MR had a leak; as such it could not maintain the low temperatures generated by the Stirling cooler. Cracked glass inside the dewar was also discovered, indicating possible detector damage.

Table A.2: List of notable events (with dates and descriptions) that impacted the E-AERI dataset.

Start Date	*End Date*	*Description*	*Result*
(2006/03/12)	*(2009/05/03)*	*(P-AERI running at 0PAL)*	*(Removed from Eureka)*
2008/10/22	2009/10/30	E-AERI installed at PEARL	N/A
2009/10/12	2011/02/16	Stirling cooler and detector failure	Not running during this time
2009/10/30	N/A	E-AERI moved from PEARL to 0PAL	N/A
2010/02/20	2010/03/10	Visited Eureka during ACE campaign; installed new Stirling cooler. Detectors still did not function.	Packed up MR and Agilent multimeter, shipped back to ABB for in-house repairs
2011/02/06	2011/02/21	Visited Eureka during ACE campaign & ABB service visit. Re-installed MR with **non-extended range** detectors. Re-certified instrument.	Fully operational with limited range (520-3000 cm^{-1})
2011/03/03	2011/03/04	Laptop failure – froze; no data taken	Manual reboot
2011/03/09	2011/03/16	Laptop failure – would not restart	Manual reboot
2011/03/27	2011/03/28	Laptop failure – froze; no data taken	Manual reboot
2011/03/30	N/A	Laptop failure – would not restart	Manual reboot
2011/04/01	2011/06/02	Multiple laptop failures – crashes (blue screen)	Manual reboots, disk repairs, disk checks, start-up in safe mode
2011/06/20	2011/07/06	Laptop crashed, software errors, turned laptop off	New laptop (IBM) shipped to Eureka by ABB, software pre-installed
2011/06/24	N/A	Water leak first detected between front- and back-end of the E-AERI (thru-wall of the 0PAL container)	Bucket placed underneath back-end to collect water. Monitored, but no further action taken. Data not affected.
2011/07/06	2011/07/13	Software configuration on laptop was incorrect, not communicating properly with instrument	ABB remote accessed instrument; changed software parameters to match E-AERI correctly
2011/08/01	2011/10/29	Blackbodies and Agilent shipped to ABB for re-calibration	Not running during this time
2011/10/26	2011/11/06	Visited Eureka during ABB service visit. Installed newly calibrated blackbodies and Agilent. Installed **new extended-range** detectors. Re-certified instrument.	Fully operational, back to extended-range (400-3000 cm^{-1})
2012/03/01	2012/03/07	Laptop failure – froze; no data taken	Manual reboot
2012/03/17	2012/03/18	Laptop failure – froze; no data taken	Manual reboot
2012/05/26	2012/06/10	Laptop failure – would not restart	Manual reboot
2012/11/07	2013/02/27	Long-wave channel (Ch1, MCT; 400-1800 cm^{-1}) failure; no interferogram. Only Ch2 (InSb; 1800-3000 cm^{-1}) working.	Continued operating both channels; only Ch2 (InSb) data OK. Two possible replacement parts ordered from ABB: Analog-to-Digital Converter (ADC) and Pre-Amp.
2012/12/27	2013/01/10	Laptop failure – froze; no data taken	EC staff had to manually reboot laptop twice.
2013/02/25	2013/03/06	Visited Eureka during ACE campaign. Installed new Analog-to-Digital Converter (ADC).	Fully operational: MCT interferogram signal returned to normal. No need to replace Pre-Amp.
2013/03/01	N/A	Laptop power connected to remote power switch and configured	Remote reboot sequence for laptop now possible
2013/05/24	2013/07/03	Laptop unable to communicate with instrument	Could not take data regularly. ABB investigated

			remotely; shipped White Light bulb and laser power supply & ballast
2013/06/20	2013/07/03	P. Fogal installed laser power supply & ballast, aligned new laser	Fully operational
2014/03/4	2014/03/09	Laptop failure – froze; no data taken	Remote Laptop power cycle (reboot)
2014/03/29	2014/04/01	Laptop failure – froze; no data taken	Manual reboot
2014/05/13	2014/05/23	Laptop failure – froze; no data taken	Remote Laptop power cycle (reboot)

To construct a new extended-range detector takes a significant amount of time; hence a non-extended range detector was installed with the help of an ABB engineer, Guillaume Gamache, during the 2011 ACE Validation Campaign. The entire instrument underwent calibration and re-certification testing according to UW-SSEC standards and procedures during this time and again in November 2011 to ensure instrument performance stability and measurement reliability. This ensured the instrument's specifications and performance at 0PAL matched those at PEARL (and those of the P-AERI). The detector had the same properties as the original, with the exception that its spectral range was limited down to 520 cm^{-1}, similar to the P-AERI. In October 2011, a second visit was made to install the new extended-range detector with the help of Guillaume Gamache (ABB) and perform calibration and certification testing. In 2011, there were three periods with limited or no measurements due to minor software issues and maintenance. At the end of 2012 and beginning of 2013, the instrument's MCT channel was offline for two months until a new analog-to-digital converter was installed by me during the 2013 ACE Validation Campaign. In June 2013, a new metrology laser power supply and ballast was ordered from ABB and installed by Pierre Fogal once it was discovered that the old one had failed. Alignment of the laser was made possible by accessing the instrument's 'production mode' with the help of ABB engineers (remotely). Laser power supply failure is expected to occur at relatively frequent intervals due to the laser's relatively short lifetime (~2-3 years). These instrument-related issues have aided ABB in the development (both hardware and software) and commercial viability of their new AERI systems, several of which have since been purchased and installed at other sites, including South Korea and Germany.

A.3 Submission of E-AERI Trace Gas Measurements to the ACE Archive

As part of the ACE Validation Campaign, E-AERI measurements of total columns of trace gases are submitted to the ACE data archive. The ACE data archive, stored on a University of Waterloo server, is intended to provide a catalogue of datasets of ground-based trace gas measurements at Eureka for the Canadian Space Agency (CSA) to facilitate current and future satellite validation exercises. The first such submission to the ACE archive was conducted in July 2013 by me, in coordination with the ACE satellite validation campaign leader Prof. Kaley Walker. A MATLAB program was created by me to extract E-AERI trace gas total column measurements (which are stored on the laptop 'ZEUS' and backed up on both the petabit/GLACIER server and Alopex server) that underwent quality control (inspection of the spectral fits, removing days where non-clear-sky spectra were included, etc.) and output them in text files of a required format. Individual text files for each trace gas for each year were created, including a README file describing the measurements and how to read in the text file data. These files were included in a single .zip file, which has been uploaded to the ACE data archive. Thus researchers requiring E-AERI total column measurements can access them in numerous formats, from MATLAB to text files, from a variety of sources.

REFERENCES

ACIA (2004): Arctic Climate Impact Assessment. Cambridge University Press, pp. 1-1020.

Adams, C., K. Strong, R. L. Batchelor, P. Bernath, S. Brohede, C. Boone, D. Degenstein, W. Daffer, J. R. Drummond, P. F. Fogal, E. Farahani, C. Fayt, A. Fraser, F. Goutail, F. Hendrick, F. Kolonjari, R. Lindenmaier, G. Manney, C. T. McElroy, C. A. McLinden, J. Mendonca, J.-H. Park, B. Pavlovic, A. Pazmino, C. Roth, V. Savastiouk, K. A. Walker, D. Weaver, and X. Zhao (2012a): Validation of ACE and OSIRIS ozone and NO_2 measurements using ground-based instruments at 80° N. Atmos. Meas. Tech., 5, 927-953.

Adams, C., K. Strong, X. Zhao, M. R. Bassford, M. Chipperfield, W. Daffer, J. R. Drummond, F. Farahani, W. Feng, A. Fraser, F. Goutali, G. Manney, C. McLinden, A. Pazmino, M. Rex, and K. Walker (2012b): Severe 2011 ozone depletion assessed with 11 years of ozone, NO_2, and OClO measurements at 80^{o}N, Geophys. Res. Lett., 39, L05806, doi:10.1029/2011GL050478.

Andrews, David G. (2000): An Introduction to Atmospheric Physics. Cambridge University Press, pp. 1-211.

Austin, J., D. Shindell, S. Beagley, C. Bruhl, M. Dameris, E. Manzini, T. Nagashima, P. Newman, S. Pawson, G. Pitari, E. Rozanov, C. Schnadt, and T. Shepherd (2003): Uncertainties and assessments of chemistry-climate models of the stratosphere. Atmos. Chem. Phys., 3, 1-27.

Banwell, C. (1983): Fundamentals of Molecular Spectroscopy. McGraw-Hill, 3rd edition.

Barnes, E. (2013): Revisiting the evidence linking Arctic amplification to extreme weather in midlatitudes. Geophys. Res. Lett., 40, 1-6.

Batchelor, R., K. Strong, R. Lindenmaier, R. Mittermeier, H. Fast, J. R. Drummond, P. Fogal, (2009): A New Bruker IFS 125HR FTIR Spectrometer for the Polar Environment Atmospheric Research Laboratory at Eureka, Nunavut, Canada: Measurements and Comparison with the Existing Bomem DA8 Spectrometer. J. Atmos. Ocean. Tech., 26, 1328-1340.

Bates, D. R. and Hays, P. B. (1967): Atmospheric nitrous oxide, Planet. Space Sci., 15, 189-198.

Batchelor, R. L., Kolonjari, F., Lindenmaier, R., Mittermeier, R. L., Daffer, W., Fast, H., Manney, G., Strong, K., and Walker, K. A. (2010): Four Fourier transform spectrometers and the Arctic polar vortex: instrument intercomparison and ACE-FTS validation at Eureka during the IPY springs of 2007 and 2008. Atmos. Meas. Tech., 3, 51-66.

Bayes, T. (1763): An essay towards solving a problem in the doctrine of chances. Phil. Trans. R. Soc. Lond., 53, 370-418.

Becker, E. and J. Notholt (1997): Ground based FTIR-emission spectroscopy of the polar atmosphere during the wintertime. Proceedings of SPIE 3106, Munich, Germany, pp. 154-158.

Bekryaev, R., I. Polyakov, and V. Alexeev (2010): Role of polar amplification in long-term surface air temperature variations and modern Arctic warming. J. Climate, 23(14), 3888-3906.

Bell, R. J. (1972): Introductory Fourier Transform Spectroscopy, Academic Press, New York.

Bianchini, G., U. Cortesi, and B. Carli (2003): Emission Fourier transform spectroscopy for remote sensing of the Earth's atmosphere. Annals of Geophysics, 46(2), 205-222.

Bianchini, G., L. Palchetti, G. Muscari, I. Fiorucci, P. Di Girolamo, and T. Di Iorio (2010): Water vapor sounding with the far infrared REFIR-PAD spectroradiometer from a high-altitude ground-based station during the ECOWAR campaign. J. Geophys. Res., 116, D02310, doi:10.1029/2010JD014530.

Bintanja, R., R. Graversen, and W. Hazeleger (2011): Arctic winter warming amplified by the thermal inversion and consequent low infrared cooling to space. Nature Geosci., 4, 758-761.

Blanchet, J.P., A. Royer, F. Chateauneuf, Y. Bouzid, Y. Blanchard, J.-F. Hamel, J. de Lafontaine, P. Gauthier, N. O'Neill, O. Pancrati, and L. Garand (2011): TICFIRE – a Far Infrared Payload to Monitor the Evolution of Thin Ice Clouds. SPIE, 8176, 81761K-1.

Borysow, A., and Frommhold, L. (1986): Collision-induced rototranslational absorption spectra of N_2-N_2 pairs for temperatures from 50 to 300 K. Astrophysical Journ., 311, 1043-1057.

Bouguer, P. (1729): Essai d'Optique sur la gradation de la Lumiere. Jombert; Paris.

Brown, A., and R. Tipping (2003): Collision-induced absorption in dipolar molecule – Homonuclear diatomic pairs - Weakly interacting Molecular Pairs: Unconventional Absorbers of Radiation in the Atmosphere. NATO Science Series, 27, pp. 93-99.

Brown, R., C. Derksen, and L. Wang (2010): A multi-data set analysis of variability and change in Arctic spring snow cover extent, 1967–2008. J. Geophys. Res., 115(D16), 1-16.

Clough, S. A., F. X. Kneizys, and R. W. Davies (1989): Line shape and the water vapor continuum. Atmos. Res., 23, 229-241.

Clough, S. A., M. Iacono, and J.-L. Moncet (1992): Line-by-Line Calculations of Atmospheric Fluxes and Cooling Rates: Application to Water Vapor. J. Geophys. Res., 97(D14), 15761-15785.

Clough, S. A., M.W. Shephard, E.J. Mlawer, J.S. Delamere, M.J. Iacono, K. Cady-Pereira, S. Boukabara, and P.D. Brown (2005): Atmospheric radiative transfer modeling: a summary of the AER codes. J. Quant. Spectrosc. Ra. Trans., 91, 233-244.

Collard, A.D., S.A. Ackerman, W.L. Smith, H.E. Ma, H.E. Revercomb, R.O. Knuteson, and S.C. Lee (1995): Cirrus cloud properties derived from high spectral resolution infrared spectrometry during FIRE II. Part III: Ground-based HIS results. J. Atmos. Sci., 52, 4264-4275.

Connes, P. (1970): Astronomical Fourier spectroscopy. Ann. Rev. Astron. Astrophys., 8, 209–230.

Connes, P. (1987): Fourier's three. Mikrochim. Acta., 3, 337–352.

Cox, C., V. Walden, and P. Rowe (2012): A comparison of the atmospheric conditions at Barrow, Alaska and Eureka, Canada (2006-2008). J. Geophys. Res., 117, D12204, doi:10.1029/2011JD017164.

Cox, C., D. D. Turner, P.M. Rowe, M.D. Shupe, and V. P. Walden (2013): Cloud microphysical properties retrieved from downwelling infrared radiance measurements made at Eureka, Nunavut, Canada (2006-2009). J. Appl. Meteol. Clim., 53, 772-791.

Crutzen, P. J. (1970): The inuence of nitrogen oxides on the atmospheric ozone content, Q. J. Roy. Meteor. Soc., 96, 320-325.

Curry, J. A., W. B. Rossow, D. Randall, and J. L. Schramm (1996): Overview of Arctic cloud and radiation characteristics. J. Clim., 9, 1731-1764.

Danilin, M., and J. McConnell (1995): Stratospheric effects of bromine activation on/in sulfate aerosol. J. Geophys. Res., 100(D6), 11237-11243.

Delamere, J. S., S. Clough, V. Payne, E. Mlawer, D. Turner, R. Gamache (2010): A far-infrared radiative closure study in the Arctic: Application to water vapour. J. Geophys. Res., 115, doi:10.1029/2009JD012968.

Demirgian, J., and R. Dedecker (2005): Atmospheric Emitted Radiance Interferometer (AERI) Handbook, Atmospheric Radiation Measurement - Climate Research Facility, U.S. Department of Energy, Ref ARM TR-054.

DeSlover, D., W. Smith, P. Piironen, and E.W. Eloranta (1999): A methodology for measuring cirrus cloud visible-to-infrared spectral optical depth ratios. J. Atmos. Ocean. Tech., 16(2), 251-262.

DOE (1990): Atmospheric Radiation Measurement Program plan, U.S. Department of Energy, Washington, DC, DOE/ER-0442 and DOE/ER-0441, 135 pp.

Dong, X., B. Xi, K. Crosby, C. N. Long, R. S. Stone, and M. D. Shupe (2010): A 10 year climatology of Arctic cloud fraction and radiative forcing at Barrow, Alaska. J. Geophys. Res., 115, D17212, doi:10.1029/2009JD013489.

Ellingson, R., and W. Wiscombe (1996): The Spectral Radiance Experiment (SPECTRE): Project description and sample results. Bull. Amer. Meteor. Soc., 77, 1967-1985.

Eloranta, E. W. (2005): High spectral resolution lidar. Lidar: Range-Resolved Optical Remote Sensing of the Atmosphere, K. Weitkamp, Ed., Springer Series in Optical Sciences, Springer-Verlag, 143-163.

Erickson, M. (1979): Gas chromatography/Fourier transform infrared spectroscopy applications. Appl. Spectrosc. Rev., 15, 261-298.

Fast, H., R. Mittermeier, and Y. Makino (2011): A ten-year record of Arctic trace gas total column measurements at Eureka, Canada, from 1997 to 2006, Atmos.-Ocean, 49, 67-94.

Fellgett, P. B. (1951): The Multiplex Advantage. *PhD thesis,* University of Cambridge.

Fellgett, P. B. (1958): A propos de la th´eorie du spectrom`etre interf´erentiel multiplex, J. Phys. Radium, 19, 187-191.

Feltz, W., W. Smith, R. Knuteson, H. Revercomb, H. Woolf, and H. Howell (1998): Meteorological applications of temperature and water vapor retrievals from the ground-based Atmospheric Emitted Radiance Interferometer (AERI). J. Appl. Meteor., 37(9), 857-875.

Fisher, H., and H. Oelhaf (1996): Remote sensing of vertical profiles of atmospheric trace constituents with MIPAS limb-emission spectrometers. Applied Optics, 35(16), 2787-2796.

Fogal, P., L. LeBlanc, and J. Drummond (2013): The Polar Environment Atmospheric Research Laboratory (PEARL): Studying the atmosphere at 80^{o} North. Arctic, 66(3), 377-386.

Forster, P., V. Ramaswamy, P. Artaxo, T. Berntsen, R. Betts, D.W. Fahey, J. Haywood, J. Lean, D.C. Lowe, G. Myhre, J. Nganga, R. Prinn, G. Raga, M. Schulz and R. Van Dorland (2007): Changes in Atmospheric Constituents and in Radiative Forcing. In: Climate Change 2007: The Physical Science Basis. Contribution of Working Group I to the Fourth Assessment Report of the Intergovernmental Panel on Climate Change [Solomon, S., D. Qin, M. Manning, Z. Chen, M. Marquis, K.B. Averyt, M.Tignor and H.L. Miller (eds.)]. Cambridge University Press, Cambridge, United Kingdom and New York, NY, USA.

Francis, J. A., and E. Hunter (2007): Changes in the fabric of the Arctic's greenhouse blanket. Environ. Res. Lett., 2, 045011, doi:10.1088/1748-9326/2/4/045011.

Francis, J.A., and S. Vavrus (2012): Evidence linking Arctic amplification to extreme weather in mid-latitudes. Geophys. Res. Lett., 39(6), L06801, 1-6.

Fraser, A., C. Adams, J. R. Drummond, F. Goutail, G. Manney, K. Strong (2009): The Polar Environment Atmospheric Research Laboratory UV-visible Ground-Based Spectrometer: First measurements of O_3, NO_2, BrO, and OClO columns. J. Quant. Spectrosc. Ra. Trans., 110, 986-1004.

Fu, D., K. Walker, K. Sung, C. Boone, M.-A. Soucy, and P. Bernath (2007): The portable atmospheric research interferometric spectrometer for the infrared, PARIS-IR. J. Quant. Spectrosc. Ra., 103, 362-370.

Gallery, W., F. Kneizys, and S.A. Clough (1983). Air mass computer program for atmospheric transmittance/radiance calculation: FSCATM. Environmental research paper ERP-828=AFGL-TR-83-0065, Air Force Geophysical Laboratory, Hanscom Air Force Base, MA, USA.

Gero, P.J., and D.D. Turner (2011): Long-term trends in downwelling spectral infrared radiance over the U.S. Southern Great Plains. Bull. Amer. Meteorol. Soc., 24, 4831-4843.

Gregory, J., P. Huybrechts, S. Raper (2004): Climatology: threatened loss of the Greenland ice-sheet. Nature, 428(6983), 616.

Lorentz, H. (1906): The absorption and emission of lines of gaseous bodies. In H.A. Lorentz Collected Papers (The Hague, 1934-1939), 3, 215-238.

Hanson, D., and A. Ravishankara (1994): Reactive uptake of $ClONO_2$ onto sulfuric acid due to reaction with HCl and H_2O. J. Phys. Chem., 98, 5728-5735.

Hase, F., J. W. Hannigan, M. T. Coffey, A. Goldman, M. Hopfner, N. B. Jones, C. P. Rinsland, and S. W. Wood (2004): Inter-comparison of retrieval codes used for the analysis of high-resolution, ground-based FTIR measurements. J. Quant. Spectrosc. Ra. Trans., 87, 25-52.

Hendrick, F., J.-P. Pommereau, F. Goutail, R. Evans, D. Ionov, A. Pazmino, E. Kyr¨o, G. Held, P. Eriksen, V. Dorokhov, M. Gil, and M. Van Roozendael (2011): NDACC/SAOZ UV-visible total ozone measurements: improved retrieval and comparison with correlative ground-based and satellite observations. Atmos. Chem. Phys., 11, 5975-5995.

Hinzman, L., N. D. Bettez, W. Bolton, F. Chapin, M. Dyurgerov, C. Fastie, B. Griffith, R. Hollister, A. Hope, H. Huntington, A. Jensen, G. Jia, T. Jorgenson, D. Kane, D. Klein, G. Kofinas, A. Lynch, A. Lloyd, A. McGuire, F. Nelson, W. Oechel, T. Osterkamp, C. Racine, V. Romanovsky, R. Stone, D. Stow, M. Sturm, C. Tweedie, G. Vourlitis, M. Walker, D. Walker, P. Webber, J. Welker, K. Winker, and K. Yoshikawa (2005): Evidence and Implications of recent climate change in northern Alaska and other Arctic regions. Climate Change, 72(3), 251-298.

Houghton, J. (2002): The Physics of Atmospheres. Cambridge University Press, 3rd edition, 1-340.

Huang, X. and L. Yung (2004): A common misunderstanding about the Voigt line profile. J. Atmos. Sci., 61:1630–1632.

IGOS (2004): The Changing Atmosphere: An Integrated Global Atmospheric Chemistry Observation Theme for the IGOS Partnership. Report of the Integrated Global Atmospheric Chemistry Observation Theme Team. ESA SP-1282. Report GAW No. 159 (WMO TD No. 1235).

International Organization of Standardization (1993): Guide to the Expression of Uncertainty in Measurement. U.S. Government Printing Office, Washington, 1st ed., 101 pp.

Intrieri, J. and M.D. Shupe (2004): Characteristics and radiative effects of diamond dust over the western Arctic Ocean region, J. Climate, 17, 2953–2960.

IPCC (2007): Climate Change 2007 - Contribution of Working Group I to the Fourth Assessment Report of the Intergovernmental Panel on Climate Change. Cambridge

University Press, Cambridge, United Kingdom and New York, NY, USA, pp. 1-1007.

IPCC (2013): Climate Change 2013 – Contribution of Working Group 1 to the Fifth Assessment Report of the Intergovernmental Panel on Climate Change; The Physical Science Basis: Summary for Policymakers. Intergovernmental Panel on Climate Change, Cambridge University Press, Cambridge, United Kingdom and New York, NY, USA, 33 pp.

Jacob, D. (1999): Introduction to Atmospheric Chemistry. Princeton University Press, pp. 1-255.

Jacquinot, P. and C. Dufour (1948): Conditions optiques demploi des cellules photoélectriques dans les spectrographes et les interféromètres. *J. Rech. CNRS* (Paris), 6-91.

Jenssen, B.M. (2006): Endocrine-Disrupting Chemicals and Climate Change: A Worst-Case Combination for Arctic Marine Mammals and Seabirds? Environ. Health Perspect., 114(1), 76-80.

Kim, Y.-J. and M. Flatau (2010): Hindcasting the January 2009 Arctic sudden stratospheric warming and its influence on the Arctic Oscillation with unified parametrization of orographic drag in NOGAPS. Part I: extended-range stand-alone forecast, Weather and Forecasting, 25(6), 1628-1644.

Klein, S. and C. Jakob (1999): Validation and sensitivities of frontal clouds simulated by the ECMWF model. Mon. Weather Rev., 127(10), 2514-2531.

Knuteson, R., H. Revercomb, F. Best, N. Ciganovich, R. Dedecker, T. Dirkx, S. Ellington, W. Feltz, R. Garcia, H. Howell, W. Smith, J. Short and D. Tobin (2004a): Atmospheric Emitted Radiance Interferometer. Part I: Instrument Design. J. Atmos. Oceanic Tech., 21, 1763-1776.

Knuteson, R., H. Revercomb, F. Best, N. Ciganovich, R. Dedecker, T. Dirkx, S. Ellington, W. Feltz, R. Garcia, H. Howell, W. Smith, J. Short, and D. Tobin (2004b): Atmospheric

Emitted Radiance Interferometer. Part II: Instrument Performance. J. Atmos. Oceanic Tech., 21, 1777-1789.

Lam, K. S., V. Savastiouk, W. Fung, T. Chan, and K. Lamb (2007): Recalculation of 11-year total ozone of Brewer spectrophotometer 115, J. Geophys. Res., 112, D15104, doi:10.1029/2006JD008178.

Le Treut, H., R. Somerville, U. Cubasch, Y. Ding, C. Mauritzen, A. Mokssit, T. Peterson, and M. Prather (2007): Historical Overview of Climate Change. In: Climate Change 2007: The Physical Science Basis. Contribution of Working Group I to the Fourth Assessment Report of the Intergovernmental Panel on Climate Change [Solomon, S., D. Qin, M. Manning, Z. Chen, M. Marquis, K.B. Averyt, M. Tignor and H.L. Miller (eds.)]. Cambridge University Press, Cambridge, United Kingdom and New York, NY, USA.

Lesins, G., L. Bourdages, T. Duck, J. Drummond, E. Eloranta, and V. Walden (2009): Large surface radiative forcing from topographic blowing snow residuals measured in the High Arctic at Eureka. Atmos. Chem. Phys., 9, 1847-1862.

Lesins, G., T. Duck, and J. Drummond (2010): Climate trends at Eureka in the Canadian high Arctic. Atmos.-Ocean, 48(2), 59-80.

Lindenmaier, R., R. Batchelor, K. Strong, H. Fast, F. Goutail, F. Kolonjari, C. T. McElroy, R. Mitermeier, and K. Walker (2010): An evaluation of infrared microwindows for ozone retrievals using the Eureka Bruker 125HR Fourier transform spectrometer. J. Quant. Spectrosc. Ra., 111, 569-585.

Lindenmaier, R., K. Strong, R.L. Batchelor, M.P. Chipperfield, W.H. Daffer, J.R. Drummond, T.J. Duck, H. Fast, W. Feng, P.F. Fogal, F. Kolonjari, G.L. Manney, A. Manson, C. Meek, R.L. Mittermaier, G.J. Nott, C. Perro, and K. Walker (2012): Unusually low O_3, HCl, and HNO_3 column measurements at Eureka, Canada during spring 2011. Atmos. Chem. Phys., 12, 3821-3835.

Lindenmaier, R. (2012): Studies of Arctic Middle Atmospheric Chemistry using Infrared Absorption Spectroscopy. *PhD Thesis*, University of Toronto, 308pp.

Liou, K. (2002). An Introduction to Atmospheric Radiation. Academic Press, 2nd edition.

Manney, G., M. Santee, M. Rex, N. Livesey, M. Pitts, P. Veefkind, E. Nash, I. Wohltmann, R. Lephmann, L. Froidevaux, L. Poole, M. Schoeberl, D. Haffner, J. Davies, V. Dorokhov, H. Gernandt, B. Johnson, R. Kivi, E. Kyro, N. Larsen, P. Levelt, A. Makshtas, C.T. McElroy, H. Nakajima, M. Parrondo, D. Tarasick, P. Gathen, K.A. Walker, and N. Zinoviev (2011): Unprecedented Arctic ozone loss in 2011. Nature, 478, 469-475.

Mariani, Z., K. Strong, M. Wolff, P. Rowe, V. Walden, P. F. Fogal, T. Duck, G. Lesins, D. S. Turner, C. Cox, E. Eloranta, J. R. Drummond, C. Roy, D. D. Turner, D. Hudak, and I. A. Lindenmaier (2012a): Infrared Measurements in the Arctic using Two Atmospheric Emitted Radiance Interferometers. Atmos. Meas. Tech., 5, 329-344.

Mariani, Z., K. Strong, M. Wolff, P. Rowe, V. Walden, P. F. Fogal, T. Duck, G. Lesins, D. S. Turner, C. Cox, E. Eloranta, J. R. Drummond, R. L Lachance, C. Roy, D. D. Turner, D. Hudak, and I. A. Lindenmaier (2012b): Infrared Measurements throughout Polar Night using Two AERIs in the Arctic. SPIE, 8534, 85340H-1.

Mariani, Z., K. Strong, M. Palm, R. Lindenmaier, C. Adams, X. Zhao, V. Savastiouk, C. T. McElroy, F. Goutail, and J. R. Drummond (2013): Year-round Retrievals of Trace Gases in the Arctic using the Extended-range Atmospheric Emitted Radiance Interferometer. Atmos. Meas. Tech., 6, 1549-1565.

Mariani, Z. (2014): CANDAC/PEARL Standard Operating Procedure for the Extended-range Atmospheric Emitted Radiance Interferometer (E-AERI). V. 1.2., Technical Report, pp. 1-41.

Marty, C., R. Philipona, J. Delamere, E. G. Dutton, J. Michalsky, K. Stamnes, R. Storvold, T. Stoffel, S. A. Clough, and E. J. Mlawer (2003): Downward longwave irradiance uncertainty under arctic atmospheres: Measurements and modeling. J. Geophys. Res., 108(D12), 4358, doi:10.1029/2002JD002937.

Maslanik, J., M. Serreze, and R. Barry (1996): Recent decreases in Arctic summer ice cover and linkages to atmospheric circulation anomalies. Geophys. Res. Lett., 23(13), 1677-1680.

Meier, A., A. Goldman, P. S. Manning, T. M. Stephen, C. P. Rinsland, N. B. Jones, and S. W. Wood (2004): Improvements to air mass calculations for ground-based infrared measurements. J. Quant. Spectrosc. Ra. Trans., 83, 109-113.

Michelson, A. (1887): The relative motion of the earth and the luminiferous ether. Amer. J. Sci., 34, 333-345.

Mie, G. (1908): Beitrage zur optik truber medien, speziell kolloidaler metallosungen. Ann. Phys., 330, 377-445.

Minnett, P.J., R. Knuteson, F. Best, B. Osborne, J. Hanafin, and O. Brown (2001): The Marine-Atmospheric Emitted Radiance Interferometer (M-AERI), a high-accuracy, seagoing infrared spectroradiometer. J. Atmos. Oceanic Technol., 18, 994-1013.

Niowano, M., and M. Shiotani (2001): Quasi-biennial oscillation in vertical velocity inferred from trace gas data in the equatorial lower stratosphere. J. Geophys. Res., 106(D7), 7281-7290.

Olson, J., J. Van Allen, P. Fogal, F. Murcray, and A. Goldman (1996): Calibrated 0.1-cm^{-1} IR emission spectra from 80N. Applied Optics, 35(16), 2797-2801.

Park, J. H., J. M. Russell III, L. L. Gordley, S. R. Drayson, D. C. Benner, J. M. Mclnerney, M. R. Gunson, G. C. Toon, B. Sen, J. F. Blavier, C. R. Webster, E. C. Zipf, P. Erdman, U.

Schmidt, and C. Schiller (1996): Validation of Halogen Occultaiton Experiment CH_4 measurements from the UARS, J. Geophys. Res., 101(D6), 10183-10203.

Perrin, F. (1948): Whose absorption law? J. Opt. Soc. Am., 38, 72-74.

Pinkus, A. and Zafrany, S. (1999): Fourier Series and Integral Transforms. Cambridge University Press.

Planck, M. (1901): Ueber irreversible strahlungsvorgange. Ann. Physik, 311:818831 (English translation provided by the Smithsonian/NASA Astrophysics Data System).

Platt, U. and J. Stutz (2008): Differential Optical Absorption Spectroscopy, edited by: Guzzi, R., Lanzerotti, L. J., Imboden, D., and Platt, U., Springer, Germany, 175-285.

Pommereau, J. P. and Goutail, F. (1988): O_3 and NO_2 ground-based measurements by visible spectrometry during Arctic winter and spring 1988, Geophys. Res. Lett., 15, 891-894.

Pougatchev, N., B. Connor, and C. Rinsland (1995): Infrared measurements of the ozone vertical distribution above Kitt Peak. J. Geophys. Res., 100, D8, 16689-16697, doi:10.1029/95JD01296.

Raffalski U., G. Hochschild, G. Kopp, and J. Urban (2005): Evolution of stratospheric ozone during winter 2002/2003 as observed by ground-based millimeter wave radiometer at Kiruna, Sweden. Atmos. Chem. Phys., 5, 1399-1407.

Randel , W., M.-L. Chanin, and C. Michaut (2002): Intercomparison of Middle Atmosphere Climatologies, SPARC Report No. 3, WCRP 116, WMO/TD 1142.

Rathke, C., J. Fischer, S. Neshyba, and M. Shupe (2002): Improving IR cloud phase determination with 20 microns spectral observations. Geophys. Res. Lett., 29(8), doi: 10.1029/2001GL014594.

Ravishankara, A. R., J. S. Daniel, and R. W. Portmann (2009): Nitrous oxide (N_2O): the dominant ozone-depleting substance emitted in the 21st century, Science, 326, 123-125.

Rayleigh, L. (1871): On the light from the sky, its polarization and colour. Phil. Mag., 41, 107-120.

Rex, M., R. Salawitch, P. von der Gathen, N. Harris, M. Chipperfield, and B. Naujokat, (2004): Arctic ozone loss and climate change. Geophys. Res. Let., 31(4), L04116, doi:10.1029/2003GL018844.

Revercomb, H., H. Buijs, H. Howell, D. LaPorte, W. Smith, L. Sromovsky (1988): Radiometric calibration of IR Fourier transform spectrometers: Solution to a problem with the High-Resolution Interferometer Sounder. Appl. Opt., 27, 3210-3218.

Richter-Menge, J., J. Overland, A. Proshutinsky, V. Romanovsky, L. Bengtsson, L. Brigham, M. Dyurgerov, J.C. Gascard, S. Gerland, R. Graversen, C. Haas, M. Karcher, P. Kuhry, J. Maslanik, H. Melling, W. Maslowski, J. Morison, D. Perovich, R. Przybylak, V. Rachold, I. Rigor, A. Shiklomanov, J. Stroeve, D. Walker, and J. Walsh (2006): State of the Arctic. NOAA, pp. 1-36.

Rinsland, C. P., N. Jones, B. Connor, J. Logan, N. Pougatchev, A. Goldman, F. Murcray, T. Stephen, A. Pine, R. Zander, E. Mahieu, P. Demoulin (1998): Northern and Southern Hemisphere ground-based infrared spectroscopic measurements of tropospheric carbon monoxide and ethane. J. Geophys. Res., 103(D21), 197-217.

Rodgers, C.D. (1976): Retrieval of atmospheric temperature and composition from remote measurements of thermal radiation. Rev. Geophys., 14(4), 609-624.

Rodgers, C.D. (1990): Characterization and error analysis of profiles retrieved from remote sounding measurements. J. Geophys. Res., 95, 5587-5595.

Rodgers, C.D. (2000): Inverse methods for atmospheric sounding: theory and practice. Series on atmospheric, oceanic and planetary physics, vol. 2. New Jersey: World Scientific Publishing Co. Pte. Ltd.

Rodgers, C.D., and B. Connor (2003): Intercomparison of remote sounding instruments. J. Geophys. Res., 108(D3), 1-14.

Rothman, L.S., I.E. Gordon, A. Barbe, D.C. Benner, P.F. Bernath, M. Birk, V. Boudon, L.R. Brown, A. Camparague, J.-P. Champion, K. Chance, L.H. Coudert, V. Dana, V.M. Devi, S. Fally, J.-M. Flaud, R.R. Gamache, A. Goldman, D. Jacquemart, I. Kleiner, N. Lacome, W.J. Lafferty, J.-Y. Mandin, S. Massie, S.N. Mikhailenko, C.E. Miller, M. Moazzen-Ahmadi, O.V. Naumenko, A.V. Nikitin, J. Orphal, V.I. Perevalov, A. Perrin, A. Predoi-Cross, C. Rinsland, M. Rotger, M. Simeckova, M. Smith, K. Sung, S.A. Tashkun, J. Tennyson, A.C. Vandaele, R. Toth, and J. Vander Auwera (2009): The HITRAN 2008 molecular spectroscopic database. J. Quant. Spectrosc. Ra., 110, 533-572.

Rothrock, D., Y. Yu, and G. Maykut (1999): Thinning of the Arctic Sea-Ice Cover. Geophys. Res. Lett., 26(23), 3469-3472.

Rowe, P., L. Miloshevich, D. Turner, and V. Walden (2008): Quantification of a dry bias in radiosonde humidity profiles over Antarctica. J. Atmos. Ocean. Tech., 25, 1529-1541.

Rowe, P., S. Neshyba, and V. Walden (2011a): Responsivity-based criterion for accurate calibration of FTIR emission spectra: theoretical development and bandwidth estimation. Opt. Express 19(6), 5451-5463.

Rowe, P., S. Neshyba, C. Cox, and V. Walden (2011b): A responsivity-based criterion for accurate calibration of FTIR emission spectra: identification of in-band low-responsivity wavenumbers. Opt. Express 19(7), 5930-5941.

Savastiouk, V. and C.T. McElroy (2005): Brewer spectrophotometer total ozone measurements made during the 1998 Middle Atmosphere Nitrogen Trend Assessment (MANTRA) campaign. Atmos.-Ocean, 43, 315-324.

Schnadt, C., M. Dameris, M. Ponater, R. Hein, V. Grewe, and B. Steil (2002). Interaction of atmospheric chemistry and climate and its impact on stratospheric ozone. Clim. Dyn., 18(6), 501-517.

Schnadt, C., and M. Dameris (2003): Relationship between North Atlantic Oscillation changes and stratospheric ozone recovery in the Northern hemisphere in a chemistry-climate model. Geophys. Res. Lett., 30(9), 1487, doi:10.1029/2003GL017006.

Schneider, M., T. Blumenstock, F. Hase, M. Hopfner, E. Cuevas, A. Redondas, and J. Sancho (2005): Ozone profiles and total column amounts derived at Izana, Tenerife Island, from FTIR solar absorption spectra, and its validation by an intercomparison to ECC-sonde and Brewer spectrometer measurements. J. Quant. Spectrosc. Ra. Trans., 91, 245-274.

Schneider, M., P. Romero, F. Hase, T. Blumenstock, E. Cuevas, and R. Ramos (2010): Continuous quality assessment of atmospheric water vapour measurements techniques: FTIR, Cimel, MFRSR, GPS, and Vaisala RS92. Atmos. Meas. Tech., 3, 323-338.

Schwarzschild, K. (1914): Diffusion and absorption in the sun's atmosphere. Sitzungsberichte der Koniglichen Preussichen Akademie der Wissenschaften, pp. 1183-1200.

Screen, J., and I. Simmonds (2013): Exploring links between Arctic amplification and mid-latitude weather. Geophys. Res. Lett., 40, 959-964.

Shaw, J., P. Nugent, N. Pust, B. Thurairajah, and K. Mizutani (2005): Radiometric cloud imaging with an uncooled microbolometer thermal infrared camera. Opt. Express, 13(15), 5807-5817.

Shindell, D., D. Rind, and P. Lonergan (1998): Increased polar stratospheric ozone losses and delayed eventual recovery owing to increasing greenhouse-gas concentrations. Nature, 392(6676), 589-592.

Shindell, D., G. Schmidt, R. Miller, and D. Rind (2001): Northern hemisphere winter climate response to greenhouse gas, ozone, solar, and volcanic forcing. J. Geophys. Res., 106(D7), 7193-7210.

Shupe, M., V. Walden, E. Eloranta, T. Uttal, J. Campbell, S. Starkweather, and M. Shiobara (2011): Clouds at Arctic Atmospheric Observations. Part 1: Occurance and Macrophysical Properties. J. Appl. Meteor. Clim., 50, 626-644.

Smith, W.L., X.L. Ma, S.A. Ackerman, H.E. Revercomb, and R.O. Knuteson (1993): Remote sensing cloud properties from high spectral resolution infrared observations , J. Atmos. Sci., 50(12), 1708-1720.

Smith, W. L., W.F. Feltz, R.O. Knuteson, H. Revercomb, H. Howell, and H. Woolf (1999): The retrieval of planetary boundary layer structure using ground-based infrared spectral radiance measurements. J. Atmos. Ocean. Tech., 16, 323-333.

Solomon, S. (1999): Stratospheric ozone depletion: a review of concepts and history, Rev. Geophys., 37(3), 275-316.

Staehelin, J., R. Harris, C. Appenzeller, and J. Eberhard (2001): Ozone trends: A review, Rev. Geophys., 39, 231-290.

Stohl, A. (2001): A 1-year Lagrangian 'climatology' of air streams in the Northern Hemisphere troposphere and lower stratosphere, J. Geophys. Res., 106, 7263-7279.

Stohl, A. (2006): Characteristics of atmospheric transport into the Arctic atmosphere. J. Geophys. Res., 111, D11306, doi:10.1029/2005JD006888.

Stokes, G.M. and S.E. Schwartz (1994): The Atmospheric Radiation Measurement (ARM) Program: Programmatic background and design of the Cloud and Radiation Testbed. Bull. Amer. Meteorol. Soc., 75, 1201-1221.

Stremme, W., A. Krueger, R. Harig, and M. Grutter (2012): Volcanic SO_2 and SiF_4 visualization using 2-D thermal emission spectroscopy – Part 1: Slant-columns and their ratios. Atmos. Meas. Tech., 5, 275-288.

Tobin, D.C., F. A. Best, P.D. Brown, S.A. Clough, R. Dedecker, R. Ellingson, R. Garcia, H. Howell, R. Knuteson, E. Mlawer, H. Revercomb, J. Short, P. van Deist, and V. Walden (1999): Downwelling spectral radiance observations at the SHEBA ice station: Water vapour continuum measurements from 17 to 26 μm. J. Geophys. Res., 104(D2), 2081-2092.

Town, M., V. Walden, and S. Warren (2005): Spectral and broadband longwave downwelling radiative fluxes, cloud radiative forcing, and fractional cloud cover over the South Pole. J. Climate, 18(20), 4235-4252.

Town, M., and V. Walden (2007): Cloud cover over the South Pole from visual observations, satellite retrievals, and surface-based infrared radiation measurements. J. Climate, 20(3), 544-559.

Trenberth, K., J. Fasullo, and J. Kiehl (2009): Earth's global energy budget. Bull. Amer. Meteor. Soc., 90, 311-323.

Turner, D., W. Feltz, and R. Ferrare (2000): Continuous water vapor profiles from operational ground-based active and passive remote sensors. Bull. Amer. Meteorol. Soc., 81, 1301-1317.

Turner, D. (2003): Microphysical properties of single and mixed-phase Arctic clouds derived from ground-based AERI observations. *Ph.D. thesis*, 167 pp., Univ. of Wisconsin-Madison, Madison.

Turner, D. (2005): Arctic mixed-phase cloud properties from AERI-lidar observations: Algorithm and results from SHEBA. J. Appl. Meteor., 44, 427-444.

Turner, D. (2008): Ground-based infrared retrievals of optical depth, effective radius, and composition of airborne mineral dust above the Sahel. J. Geophys. Res., 113, doi:10.1029/2008JD010054.

Turner, D. and P.J. Gero (2011): Downwelling 10-micron infrared radiance temperature climatology for the Atmospheric Radiation Measurement Southern Great Plains site. J. Geophys. Res., 116, doi:10.1029/2010JD015135.

Turner, D.S. (1995): Absorption Coefficient Estimation Using A Two Dimensional Interpolation Procedure. J. Quant. Spectrosc. Rad. Transfer, 53, 633-637.

Uttal, T., J. Curry, M. McPhee, and 25 co-authors (2002): The surface heat budget of the Arctic Ocean, B. Am. Meteorol. Soc., 83, 255-275.

UW-SSEC (2008): UW Final Report on ABB-Bomem E-AERI-001; Certification Testing, University of Wisconsin, December 9, 2008, 1-12 pp.

Vavrus, S. (2004): The Impact of Cloud Feedbacks on Arctic Climate under Greenhouse Forcing. J. Climate, 17, 603-615.

Viatte, C., K. Strong, K. Walker, J. Drummond (2014): Five years of CO, HCN, C_2H_6, C_2H_2, CH_3OH, HCOOH, and H_2CO total columns measured in the Canadian High Arctic, Atmos. Meas. Tech., 7, 1547-1570.

Vinas, M. (July 24, 2012): Satellites see unprecedented Greenland ice sheet surface melt. NASA Earth. Date retrieved: January 13, 2014. From http://www.nasa.gov/topics/earth/features/greenland-melt.html.

Walden, V.P., M. Town, B. Halter, and J. Storey (2005): First measurements of the infrared sky brightness at Dome C, Antarctica. Publ. Astron. Soc. Pac., 117 (829), 300-308.

Waldmann, I., G. Tinetti, P. Drossart, M. Swain, P. Deroo, and C. Griffith (2012): Ground-based near infrared emission spectroscopy of HD 189733B. ApJ, 744 No. 1, 35, doi: 10.1088/0004-637X/744/1/35.

Warneke, C., K. Froyd, J. Brioude, R. Bahreini, C. Brock, J. Cozic, J. de Gouw, D. Fahey, R. Ferrare, J. Holloway, A. Middlebrook, L. Miller, S. Montzka, J. Schwartz, H. Sodermann, J. Spackman, and A. Stohl (2010): An important contribution to springtime Arctic aerosol from biomass burning in Russia. Geophys. Res. Lett., 37, L01801, doi:10.1029/2009GL041816.

Weatherhead, E., G. Reinsel, G. Tiao, X. Meng, D. Choi, W. Cheang, T. Keller, J. DeLuisi, D. Wuebbles, J. Kerr, A. Miller, S. Oltmans, and J. Frederick (1998): Factors affecting the detection of trends: Statistical considerations and applications to environmental data. J. Geosphys. Res., 103, D14, 17149-17161.

Webb, M., C. Senior, S. Bony, and J.J. Morcrette (2001): Combining ERBE and ISCCP data to assess clouds in the Hadley Centre, ECMWF and LMD atmospheric climate models. Clim. Dyn., 17, 905-922.

WMO Scientific Assessment of Ozone Depletion (2006): WMO Global Ozone Research and Monitoring Project - Report No. 50, Geneva.

Wood S., A. Goldman, P. Manning, N. Jones, J. B. Connor, and C. P. Rinsland (2000): Zephyr2: A Method for Automated Retrievals of Stratospheric and Tropospheric Molecular

Constituent Profiles From Ground-Based Infrared Solar Absorption Spectra Using SFIT2, Eos Trans. AGU, 81(48), Fall Meeting Suppl.

Yurganov, L., W. McMillan, C. Wilson, M. Fischer, S. Biraud, and C. Sweeney (2010): Carbon monoxide mixing ratios over Oklahoma between 2002 and 2009 retrieved from Atmospheric Emitted Radiance Interferometer spectra. Atmos. Meas. Tech., 3, 1319-1331.